

AN ANALYTICAL AND EXPERIMENTAL STUDY
OF THE PYROLYSIS OF COMPOSITE
ABLATIVE MATERIALS

By

JACK BRADFORD HENDERSON
II

Bachelor of Science in Mechanical Engineering
University of Tulsa
Tulsa, Oklahoma
1972

Master of Science
Oklahoma State University
Stillwater, Oklahoma
1973

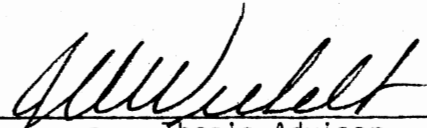
Submitted to the Faculty of the Graduate College
of the Oklahoma State University
in partial fulfillment of the requirements
for the Degree of
DOCTOR OF PHILOSOPHY
December, 1980

Thesis
1980D
H496a
cop. 2

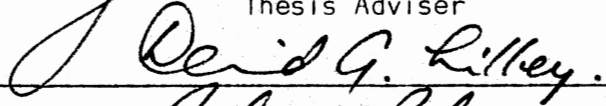


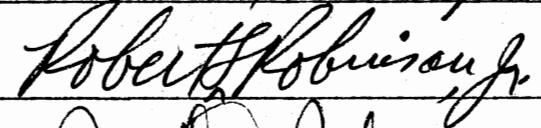
AN ANALYTICAL AND EXPERIMENTAL STUDY
OF THE PYROLYSIS OF COMPOSITE
ABLATIVE MATERIALS

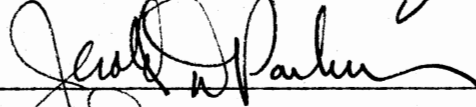
Thesis Approved:

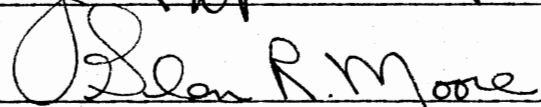


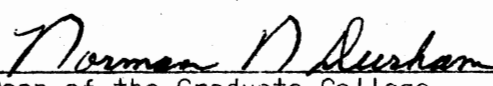
Thesis Adviser











Dean of the Graduate College

ACKNOWLEDGMENTS

During my graduate study, my philosophies with regard to engineering research and education have been greatly influenced by my friend and adviser, Professor J. A. Wiebelt. Professor Wiebelt has set an example which has been a major source of inspiration during the past seven years. Words alone cannot express my gratitude.

Also, appreciation is expressed to Dr. J. D. Parker, Dr. G. R. Moore, Dr. D. G. Lilley, and Dr. R. L. Robinson for serving as members of my graduate committee. I would especially like to thank Dr. J. D. Parker for his support and encouragement during the past seven years. My association with Professor Parker has been a valuable part of my engineering education. To him I owe more than thanks. I am also obliged to my colleague and friend, Dr. G. R. Moore, for many valuable suggestions throughout this work.

In addition, I would like to thank my friend and fellow graduate student, Mr. M. R. Tant, for our many technical discussions and his help with part of the experimental work; and Mr. Eldon Hardy for his fine work in drawing the figures.

Finally, I would like to express my gratitude to Janna, my wife and best friend, for typing the manuscript and digitizing much of the experimental data. Her encouragement and sacrifice have not waived.

TABLE OF CONTENTS

Chapter	Page
I. INTRODUCTION	1
II. REVIEW OF PREVIOUS WORK.	3
Mathematical Models	4
Kinetics of Thermal Decomposition	16
Isothermal Method.	16
Dynamic Heating Method	19
Single Heating Rate Techniques.	21
Multiple Heating Rate Techniques.	26
Specific Heat Measurements.	35
Drop Calorimetry Method.	37
Differential Scanning Calorimetry Method	39
Determination of Heat of Decomposition.	44
In Situ Measurements	44
Differential Thermal Analysis Method	45
Differential Scanning Calorimetry Method	49
Temperature Profile Measurements.	50
III. THERMAL MODEL.	59
Development	59
Method of Solution.	64
IV. DETERMINATION OF KINETIC PARAMETERS.	69
Experimental Method	70
Equipment.	70
Temperature Calibration.	72
Sample Preparation and Procedure	75
Experimental Results.	78
Method of Data Analysis	80
V. MEASUREMENT OF SPECIFIC HEAT AND HEAT OF DECOMPOSITION	114
Experimental Method	114
Equipment.	114
Calibration.	119
Sample Preparation and Procedure	121
Data Analysis and Results	127

Chapter	Page
VI. TEMPERATURE MEASUREMENTS	137
Apparatus	137
Calibration	139
Sample Preparation and Procedure.	142
VII. COMPARISON OF CALCULATED AND EXPERIMENTAL TEMPERATURE PROFILES	149
VIII. DISCUSSION AND RECOMMENDATIONS	163
Kinetic Parameters.	163
Experimental Technique and Data.	163
Data Analysis and Results.	164
Specific Heat and Heat of Decomposition	167
Theoretical Model and Temperature Measurements.	168
BIBLIOGRAPHY.	171
APPENDIX A - LISTING OF COMPUTER PROGRAM.	175
APPENDIX B - THERMOGRAVIMETRIC DATA	183

LIST OF TABLES

Table		Page
I.	Activation Energies for Weight Loss of Wood Samples by Thermal Degradation.	18
II.	Activation Energy of Decomposition of Wood and Its Major Components.	20
III.	Summary of Kinetic Parameters Determined by the Ratio Method.	25
IV.	Summary of Kinetic Parameters	29
V.	Summary of Heat of Pyrolysis and Combustion	49
VI.	Giant Planet Pilot Facility Test Results.	51
VII.	Properties Used in Sample Calculations.	67
VIII.	Magnetic Standards Used for TGS Calibration	74
IX.	Composition of Materials Tested	79
X.	Results of Thermogravimetric Analysis	110
XI.	Statistical Analysis of Errors in Computed Versus Experimental w/w_0	113
XII.	Calibration Standards Used for DSC Calibration.	120
XIII.	Results of Specific Heat Measurements	136
XIV.	Heat Flux Distribution Relative to Center Position.	145
XV.	Summary of Dimensions and Density of Materials Used in Temperature Profile Measurements.	147
XVI.	Properties Used in Temperature Calculations for H41NE and MXBE-350.	150
XVII.	Statistical Analysis of Calculated Versus Experimental Temperatures for H41NE.	155

Table	Page
XVIII. Statistical Analysis of Calculated Versus Experimental Temperatures for MXBE-350, 255-Second Run	157
XIX. Statistical Analysis of Calculated Versus Experimental Temperatures for MXBE-350, 1200-Second Run.	160
XX. Weight Loss and Rate of Weight Loss Data for H41NE.	184
XXI. Weight Loss and Rate of Weight Loss Data for H41D	186
XXII. Weight Loss and Rate of Weight Loss Data for MXBE-350	188
XXIII. Weight Loss and Rate of Weight Loss Data for MXB-360. . . .	191
XXIV. Weight Loss and Rate of Weight Loss Data for FR-1	192
XXV. Weight Loss and Rate of Weight Loss Data for FR-2	195

LIST OF FIGURES

Figure	Page
1. Schematic of Pyrolysis in a One-Dimensional Slab	5
2. Time-Temperature Curve for a 2.0-Cm Sheet of Deal Wood [1] . .	7
3. Time-Temperature Curve for a 4.0-Cm Sheet of Deal Wood [1] . .	7
4. Effect of Char Thermal Conductivity on Rate of Weight Loss [9]	14
5. Effect of Heat of Decomposition on Rate of Weight Loss [9] . .	15
6. Plot Used to Determine Activation Energy and Order of Reaction for Three Separate Weight Loss Regions for Calcium Oxalate Monohydrate [17]	23
7. Effect of Sample Geometry on Rate of Decomposition in an Inert Isothermal Environment [19].	27
8. Comparison of Data for High Heating Rate Tests with Predictions from TGA Model [20].	28
9. Thermogram for CTL91-LD Fiberglass-Phenolic [22]	32
10. Slopes Used to Determine Average Activation Energy [22]. . . .	33
11. Plot to Determine the Pre-Exponential Factor and Order of Reaction [22]	34
12. Specific Heat of a 5000°F Precharred Carbon Phenolic [25]. . .	38
13. Qualitative Diagram of a Programmed Temperature Scan for Empty Pan, Virgin and Char Material [28]	41
14. Specific Heat of Oak Wood as a Function of Temperature in a Nitrogen Atmosphere [12]	43
15. Idealized DTA Scan [29].	47
16. DTA Thermogram of BRP5549 Phenolic Resin [30].	48
17. NASA's Giant Planet Pilot Facility [34].	52

Figure	Page
18. Comparison Between Calculated and Predicted In-Depth Temperature Profiles [35].	54
19. Time-Temperature Profiles at Various Radii of a Cellulose Cylinder Burning in Free Convection [36]	56
20. Comparison of Havens' Experimental and Brown's Computed Temperature Profiles for White Pine Cylinders [29]	58
21. Comparison of the Results of Kung's and Henderson's Computations for a 1.0-Cm Thick Slab of Pyrolyzing Wood.	68
22. Perkin-Elmer TGS-2 Thermogravimetric System.	71
23. Schematic of TGS-2 Analyzer Unit	73
24. Magnetic Standard Temperature Calibration for TGS at 80°C/Min	76
25. Magnetic Standard Temperature Correction for TGS at 80°C/Min	77
26. Fraction of Weight Remaining for Six Heating Rates for H41NE.	81
27. Fraction of Weight Remaining for Six Heating Rates for H41D	82
28. Fraction of Weight Remaining for Six Heating Rates for MXBE-350	83
29. Fraction of Weight Remaining for Six Heating Rates for MXB-360.	84
30. Fraction of Weight Remaining for Six Heating Rates for FR-1	85
31. Fraction of Weight Remaining for Six Heating Rates for FR-2	86
32. Derivatives of Weight Loss for Six Heating Rates for H41NE.	87
33. Derivatives of Weight Loss for Six Heating Rates for H41D	88
34. Derivatives of Weight Loss for Six Heating Rates for MXBE-350	89
35. Derivatives of Weight Loss for Six Heating Rates for MXB-360.	90

Figure	Page
36. Derivatives of Weight Loss for Six Heating Rates for FR-1. . .	91
37. Derivatives of Weight Loss for Six Heating Rates for FR-2. . .	92
38. Plot of Slopes Used to Determine the Activation Energy for H41NE.	93
39. Plot of Slopes Used to Determine the Activation Energy for H41D	94
40. Plot of Slopes Used to Determine the Activation Energy for MXBE-350	95
41. Plot of Slopes Used to Determine the Activation Energy for MXB-360.	96
42. Plot of Slopes Used to Determine the Activation Energy for FR-1	97
43. Plot of Slopes Used to Determine the Activation Energy for FR-2	98
44. Activation Energy and Intercept as a Function of Degree of Conversion for H41NE.	99
45. Activation Energy and Intercept as a Function of Degree of Conversion for MXBE-350	100
46. Plot to Determine the Pre-Exponential Factor and Order of Reaction for Two Regions of Weight Loss for H41NE	102
47. Plot to Determine the Pre-Exponential Factor and Order of Reaction for Two Regions of Weight Loss for H41D.	103
48. Plot to Determine the Pre-Exponential Factor and Order of Reaction for Two Regions of Weight Loss for MXBE-350. . .	104
49. Plot to Determine the Pre-Exponential Factor and Order of Reaction for Two Regions of Weight Loss for MXB-360 . . .	105
50. Plot to Determine the Pre-Exponential Factor and Order of Reaction for Two Regions of Weight Loss for FR-1.	106
51. Plot to Determine the Pre-Exponential Factor and Order of Reaction for Two Regions of Weight Loss for FR-2.	107
52. Plot of Slopes Used to Determine the Activation Energy for H41NE by the Method of Flynn and Wall.	108
53. Plot of Slopes Used to Determine the Activation Energy for MXBE-350 by the Method of Flynn and Wall	109

Figure	Page
54. Comparison of Calculated Versus Experimental Weight Loss for H41NE	111
55. Comparison of Calculated Versus Experimental Weight Loss for MXBE-350.	112
56. Perkin-Elmer DSC-1B Differential Scanning Calorimeter.	116
57. Schematic of DSC-1B Sample Holder.	117
58. Idealized DSC Thermogram [33].	118
59. Temperature Calibration for DSC.	122
60. 20°C/Min DSC Scan for MXBE-350	124
61. Perkin-Elmer AD-2Z Microbalance.	125
62. Specific Heat and Heat of Decomposition of H41NE	130
63. Specific Heat and Heat of Decomposition of H41D.	131
64. Specific Heat and Heat of Decomposition of MXBE-350.	132
65. Specific Heat and Heat of Decomposition of MXB-360	133
66. Specific Heat and Heat of Decomposition of FR-1.	134
67. Specific Heat and Heat of Decomposition of FR-2.	135
68. Tungsten Lamps and Sample Holder	138
69. Thermogage, Inc. Blackbody Standard.	140
70. Calibration Curve for Gardon Heat Flux Transducer.	141
71. Calibration Curve for Tungsten Filament Lamps.	143
72. Sample Dimensions and Thermocouple Locations	144
73. Sample of MXBE-350 Virgin Material with Thermocouples.	146
74. Sample of MXBE-350 After Pyrolysis.	148
75. Calculated and Experimental Temperatures and Calculated Active Material Densities for H41NE.	151
76. Calculated Spatial Dependent Temperatures and Active Material Densities for H41NE	152

Figure	Page
77. Calculated and Experimental Temperatures and Calculated Active Material Densities for MXBE-350, 255-Second Run . . .	154
78. Calculated Spatial Dependent Temperatures and Active Material Densities for MXBE-350, 255-Second Run.	156
79. Calculated and Experimental Temperatures and Calculated Active Material Densities for MXBE-350, 1200-Second Run. . .	158
80. Calculated Spatial Dependent Temperatures and Active Material Densities for MXBE-350, 1200-Second Run	159
81. Experimental Temperatures for FR-1	162
82. Comparison of Thermograms for H41NE Calculated Using Two Methods.	166

CHAPTER I

INTRODUCTION

There is a large group of materials which undergo thermal-chemical decomposition, pyrolysis, when exposed to high temperatures. Some of these include wood, cellulose, fabric, plastics, and composite ablative materials. The pyrolysis phenomenon which occurs in these materials has been of interest for many years. Wood and cellulose have been studied in order to understand the rate of flame spread in building and forest fires. This knowledge has been valuable in evaluating fire retardant coatings and fire prevention systems. Composite ablative materials, which are used for thermal protection of re-entry vehicles, rocket motor nozzles and areas exposed to impingement from rocket motor exhausts have been the subject of study during recent years. Knowledge of the thermal response of ablative materials is required to optimize the amount and type of thermal protection required for a given application.

One particular class of ablative materials which has become of interest is the glass- and asbestos-phenolics. These materials consist primarily of a continuous or chopped strand fiber such as asbestos, silica or fiberglass combined with a phenol-formaldehyde resin. This type of ablative, known as a charring ablative, is relatively inexpensive and displays remarkable resistance to ablation/erosion. Applications for these materials have been found in such areas as blast shields

for rocket motor exhausts, liners for missile plenums, and in the chemical industry as corrosion resistant piping and storage tanks. Even though use of this particular class of ablative is widespread, little effort has been expended to study its thermal characteristics.

Although the pyrolysis phenomenon has been the subject of intensive research, the exact process by which it occurs is still not well understood. Consequently, efforts to model the thermal response of pyrolyzable materials have had limited success. The problem is compounded for the charring ablatives described above because of the lack of accurate thermal and kinetic property data.

The object of this research was to characterize the thermal behavior of the low cost charring ablaters; specifically to (1) measure the virgin and char specific heats, (2) estimate the heat of decomposition, (3) determine the kinetic parameters from experimental data, (4) incorporate this property data into a thermal model, and (5) compare the time dependent temperatures calculated using the model with experimental data obtained from pyrolyzing samples of charring ablatives.

CHAPTER II

REVIEW OF PREVIOUS WORK

Charring ablative materials consist of an inert fiber and/or powder filler and a volatile, catalyst or thermal setting resin. The thermal resins are mixed with the other constituents, molded to the desired geometry and cured in an autoclave for a specified amount of time. In contrast, the catalyst setting resins utilize a catalyst and are usually cured at room temperature for 2 to 3 days. In either case the result is a heterogenous composite solid with resin contents ranging from 25 to 60 percent.

When a heat flux is applied to a one-dimensional slab of pyrolyzable material, the initial temperature rise is a function of the rate of heat conduction into the material and the boundary conditions. The temperature response for this initial heating period is described by the one-dimensional, nonsteady heat conduction equation. When the surface temperature reaches the pyrolysis temperature at some time, t_p , chemical reactions begin to occur and the resin component begins to degrade to form volatile gases. As time increases, the pyrolysis zone widens and progresses further into the virgin solid. At time t_c , the active material at the surface is consumed leaving only a char residue containing the volatile gases. As time goes on, the pyrolysis front progresses through the slab consuming all of the active material.

Finally at time t_f , only the inactive char residue remains. This process is depicted qualitatively by Figure 1.

Once the pyrolysis process begins at time t_p , until its completion at time t_f , the thermal response of the material is altered by chemical reactions and/or the presence of pyrolysis gases. In order to predict the thermal response of the material, the energy liberated or consumed by these processes must be considered.

Mathematical Models

Several analytical models have been proposed which consider the pyrolysis phenomenon. They range from models which predict the rate of decomposition of wood, in which the char structure remains intact, to those which predict the surface recession of the subliming ablators used in re-entry applications. In general these models are similar. They consist primarily of the unsteady one-dimensional heat conduction equation with additional terms to account for the energy associated with the decomposition of the material. They differ primarily in their geometry, boundary conditions, and method of solution. Several of these models and their solutions will be discussed.

Bamford, Crank, and Malan [1] were the first to propose a mathematical model for the decomposition of a pyrolyzing material. These researchers proposed that the transient response and the rate of mass loss from a one-dimensional slab of wood undergoing pyrolysis could be described by the following equation:

$$k \frac{\partial^2 T}{\partial x^2} - Q_p \frac{\partial w}{\partial t} = C_p \rho \frac{\partial T}{\partial t} \quad (1)$$

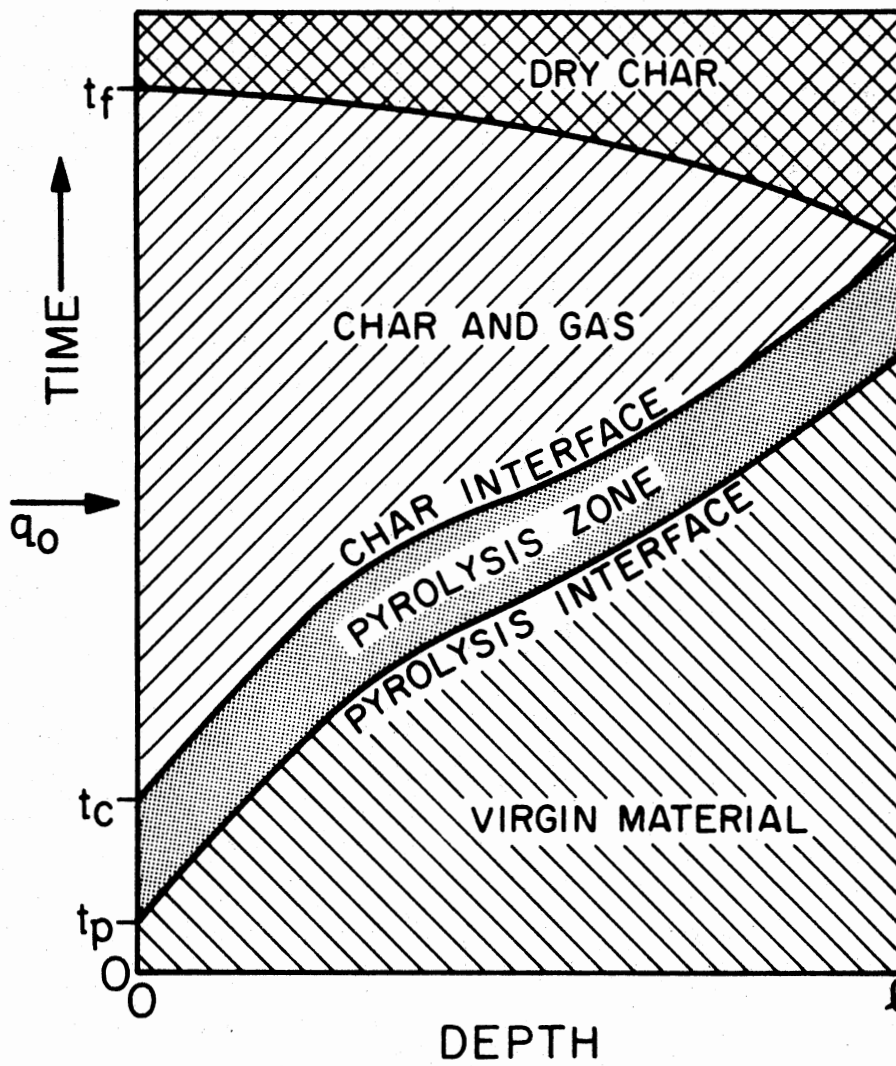


Figure 1. Schematic of Pyrolysis in a One-Dimensional Slab

where T = temperature of the slab ($^{\circ}\text{C}$)
 x = spatial variable (cm)
 t = time (sec)
 w = weight of pyrolyzable material (gm)
 k = thermal conductivity (cal/cm-sec- $^{\circ}\text{C}$)
 C_p = specific heat (cal/gm- $^{\circ}\text{C}$)
 ρ = density (gm/cm 3)
 Q_p = heat of decomposition of the material (cal/gm).

The weight loss term, $\partial w/\partial t$ in Equation (1), was determined by assuming a first order decomposition reaction given by the kinetic rate equation:

$$\frac{\partial w}{\partial t} = -Awe^{-E/RT} \quad (2)$$

where A = pre-exponential factor (sec $^{-1}$)
 E = activation energy (cal/gm-mole)
 R = gas constant (1.986 cal/gm-mole- $^{\circ}\text{K}$).

Bamford et al. heated both faces of 23-cm 2 samples by a gas flame. The center temperature of both 2.0 and 4.0-cm thick samples was monitored until complete pyrolysis of the sample had occurred.

Equation (1) was solved by a finite difference technique, using the appropriate boundary conditions. The assumption of constant thermal properties and a first order decomposition reaction of Equation (2) was made. The results of these calculations and the experimental measurements are shown in Figures 2 and 3. Figure 2 depicts both the calculated and experimental central temperatures as well as the calculated surface temperature of the 2-cm thick samples. Figure 3 depicts only the comparison of computed and experimental central temperatures

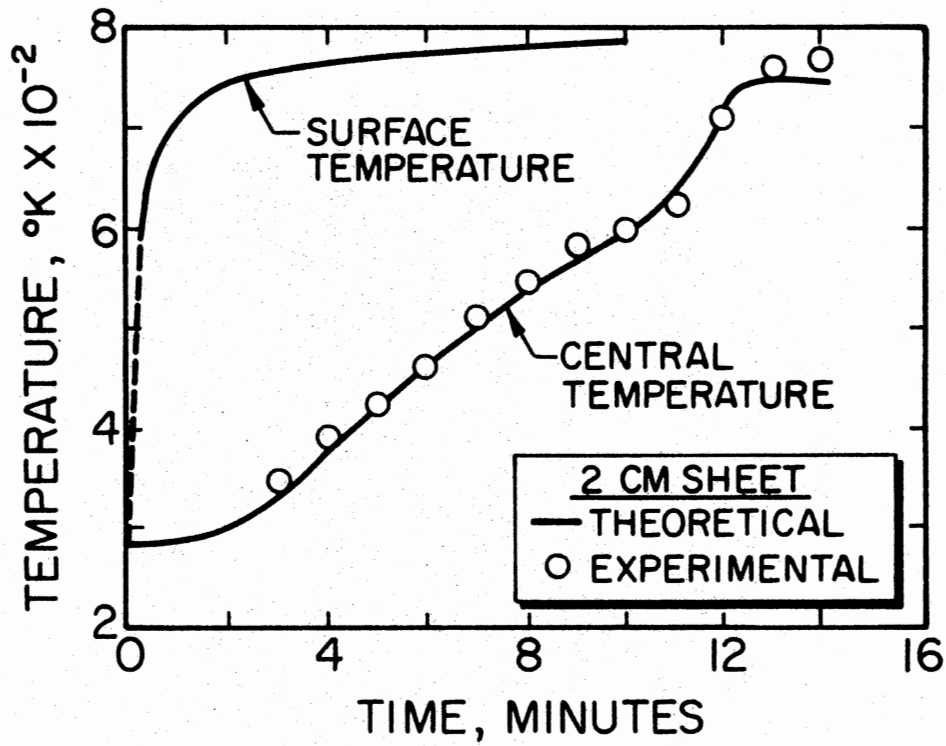


Figure 2. Time-Temperature Curve for a 2.0-Cm Sheet of Deal Wood [1]

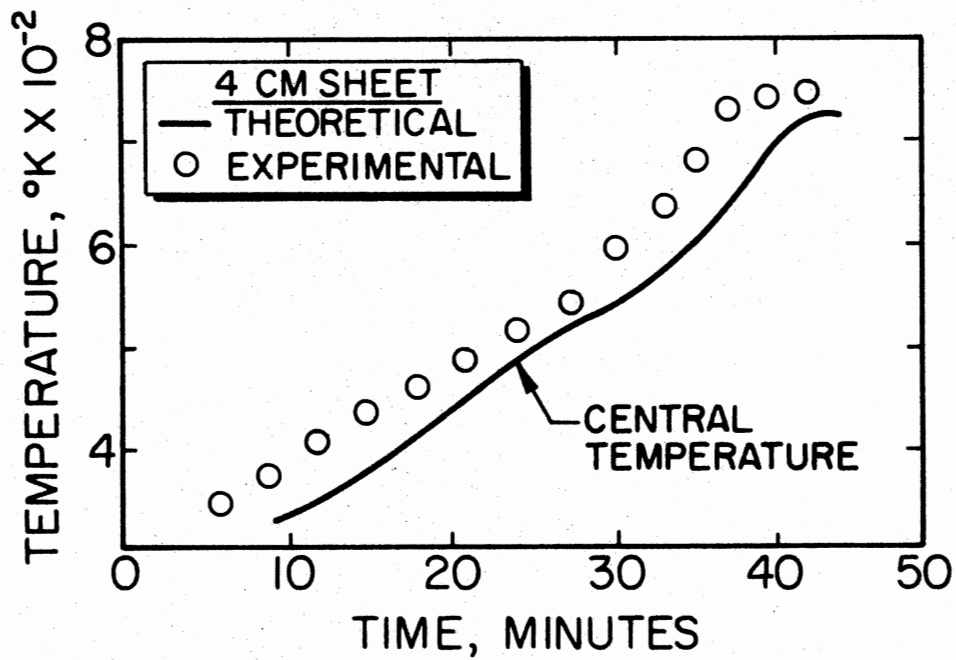


Figure 3. Time-Temperature Curve for a 4.0-Cm Sheet of Deal Wood [1]

of the 4-cm thick samples. The lack of good agreement between measured and calculated temperatures in Figure 3 is due, in part, to the pyrolysis gas flowing out through the char structure.

Panton and Rittman [2] included the variations in physical and thermal properties and multiple decomposition reactions in the heat conduction equation. These researchers described the thermal conductivity of wood as a function of the percent of active virgin material. That is:

$$k = k_0 \rho / \rho_0 \quad (3)$$

where k_0 = thermal conductivity of the material at ρ_0
(cal/cm-sec-°C)

ρ_0 = density of the virgin material (gm/cm³).

Equation (1) written for variable thermal conductivity and heat effects from multiple decomposition reaction results in:

$$\rho C_p \frac{\partial T}{\partial t} = \frac{\partial}{\partial x} \left(k \frac{\partial T}{\partial x} \right) + \sum_i Q_i \quad (4)$$

where Q_i = heat of reaction from the i^{th} reaction.

Substituting the definition of thermal conductivity from Equation (3) into Equation (4) yields:

$$\frac{\partial T}{\partial t} = \frac{k_0}{\rho_0 C_p} \frac{\partial^2 T}{\partial x^2} + \frac{k_0}{\rho_0 \rho C_p} \frac{\partial \rho}{\partial x} \frac{\partial T}{\partial x} + \frac{\sum Q_i}{\rho C_p} \quad (5)$$

This model is significant since Panton and Rittman were the first researchers to account for the change in thermal conductivity during thermal decomposition. The specific heat was assumed to be constant

through pyrolysis and the effect of the gas flow back through the char structure was neglected. Equation (5) was solved by an Integral technique.

The effect of gas flow on the temperature history was neglected not only by Panton and Rittman [2], but in similar models by Bamford et al. [1], Weatherford [3], Thomas and Bowes [4], and Murty Kanury [5]. Murty Kanury and Blackshear [6] suggested that the effect of the gas flow is a function of the thickness of the material and used the ratio of conduction and convection to evaluate its importance. That is:

$$\frac{\text{energy flux by convection}}{\text{heat transfer by conduction}} = \frac{C_{pg} (\rho_g v_g) \frac{\partial T}{\partial x}}{\frac{\partial}{\partial x} \left(k_0 \frac{\partial T}{\partial x} \right)} \quad (6)$$

which takes the form of the Peclet Number:

$$Pe = \frac{C_{pg} (\rho_g v_g) L}{k_0} \quad (7)$$

where L = characteristic length (cm)

v_g = gas velocity (cm/sec)

C_{pg} = specific heat of the gas products (cal/gm-°C)

ρ_g = gas density (gm/cm³)

Other terms were previously defined.

Murty Kanury and Blackshear arrived at the criterion of $C_{pg} \rho_g v_g L / k_0 < 0.1$ necessary to neglect the convection effects for times greater than $\rho C_p L^2 / k$. In general, this criterion implies that if $Pe \ll 1.0$, convection effects will be small and the analyses of [1,2,3,4,5] will be correct.

Munson [7] and Murty Kanury [8] proposed models which accounted for the variable thermal properties, gas flow back through the char structure, and took into account the variable heat of gasification at different temperatures. The model proposed by Munson is:

$$\frac{\partial}{\partial t} (\rho h) = \frac{\partial}{\partial x} \left(k \frac{\partial T}{\partial x} \right) - C_{pg} \dot{m}_g \frac{\partial T}{\partial x} - \frac{\partial \rho}{\partial t} (C_{pg} T + Q_p) \quad (8)$$

where \dot{m}_g = mass flux of the pyrolysis gas flowing through the char structure (gm/cm²-sec)

h = enthalpy of solid material (cal/gm).

The mass flux of the volatiles is given by the continuity equation

$$\frac{\partial \rho}{\partial t} = \frac{\partial \dot{m}_g}{\partial x} \quad (9)$$

Kung [9] proposed a model which not only accounted for variable heat of gasification, but separated the material into active and residual components. These additions to Equation (8) result in Equation (10).

$$\frac{\partial}{\partial t} (\rho_a h_a + \rho_r h_r) = \frac{\partial}{\partial x} \left(k \frac{\partial T}{\partial x} \right) + \frac{\partial}{\partial x} (\dot{m}_g h_g) + Q_p \frac{\partial \rho}{\partial t} \quad (10)$$

where ρ_a = density of the active material (gm/cm³)

h_a = enthalpy of the active material (cal/gm)

ρ_r = density of the residual material (gm/cm³)

h_r = enthalpy of the residual material (cal/gm)

h_g = enthalpy of the gaseous material (cal/gm)

Q_p = the heat of reaction associated with decomposition at an ambient reference temperature T_∞ (cal/gm).

The enthalpy of the various components is given by:

$$h_i = \int_{T_\infty}^T C_{pi} dT \quad (11)$$

where i represents the component of interest, i.e. gas phase (g), active material (a), and residual material (r).

Kung proposed that the rate of change of the density is given by a first order kinetic rate equation

$$\frac{\partial \rho}{\partial t} = -A \rho_a(T) e^{-E/RT} \quad (12)$$

in which the active material density, $\rho_a(T)$ is given by:

$$\rho_a(T) = \frac{\rho(T) - \rho_f}{1 - \rho_f/\rho_0} \quad (13)$$

where ρ_f = final density of the char material (gm/cm³).

The total instantaneous density of the partially pyrolyzed material is related to the active material density by

$$\rho(T) = \rho_a(T) + \rho_r(T). \quad (14)$$

Substituting Equation (13) into Equation (12) yields the relationship for the decomposition equation used by Kung:

$$\frac{\partial \rho}{\partial t} = -A \frac{\rho(T) - \rho_f}{1 - \rho_f/\rho_0} e^{-E/RT}. \quad (15)$$

The thermal properties were calculated by a linear interpolation between the properties of ρ , k , and C_p of virgin and wood char. That is:

$$\rho C_p = \rho_a C_{pa} + \rho_r C_{pr} \quad (16)$$

and

$$\rho k = \rho_a k_a + \rho_r k_r \quad (17)$$

where k_a = thermal conductivity of the active material
(cal/cm-sec-°C)

k_r = thermal conductivity of the residual material
(cal/cm-sec-°C).

Equations (9), (10), and (15) form a set of nonlinear partial differential equations. The following boundary conditions apply:

$$T = T_\infty, \rho = \rho_0, \dot{m}_g = 0, \text{ at } t = 0, 0 \leq x \leq \ell \quad (18)$$

$$k \frac{\partial T}{\partial x} = \alpha_s q_0 - \epsilon_s \sigma T_s^4, \text{ at } t > 0, x = 0 \quad (19)$$

$$\frac{\partial T}{\partial x} = 0, \dot{m}_g = 0, \text{ at } t \geq 0, x = \ell \quad (20)$$

where T_∞ = ambient temperature (°C)

T_s = surface temperature (°K)

q_0 = incident energy (cal/cm²-sec)

ℓ = half thickness of the material (cm)

α_s = absorptivity of the material

ϵ_s = emissivity of the material

σ = Stefan-Boltzmann constant (1.369×10^{-12} cal/sec-cm²-°K⁴).

Kung solved the set of equations using (18), (19), and (20) as boundary conditions with the implicit method of Crank-Nicolson. The most interesting of Kung's computations were those which illustrated the

effect of the char material thermal conductivity and heat of decomposition on the rate of mass loss in a pyrolyzing sample. The results of these computations are shown in Figures 4 and 5. Kung's calculations were not compared to experimental data.

Kratsch, Hearne, and McChesney [10] modeled the thermal decomposition of organic charring ablators similar to the ones of interest in this work. This model was similar to that of Kung [9]. Kratsch et al. however determined the gas enthalpy by summing the enthalpies of each of the individual species evolved during decomposition. This results in the following equation for the gas enthalpy:

$$h_g = \sum_j K_j \left(\int_0^T C_{pj} dT + \Delta h_{fj} \right) \quad (21)$$

where j = species of interest
 K = mass fraction of j^{th} gas species
 Δh_f = heat of formation of the gas species (cal/gm).

Arai [11] developed a one-dimensional model to predict the ablation values of Teflon exposed to intense radiative and conductive environments. This model is unique because it includes the optical transmittance of the material.

Perhaps the most unique model encountered was proposed by Havens [12]. Havens based his analysis on a model developed for predicting the transient temperature profiles in frozen soils. In this method the region of interest is divided into a set of cells of finite dimensions and an energy balance is written for each cell.

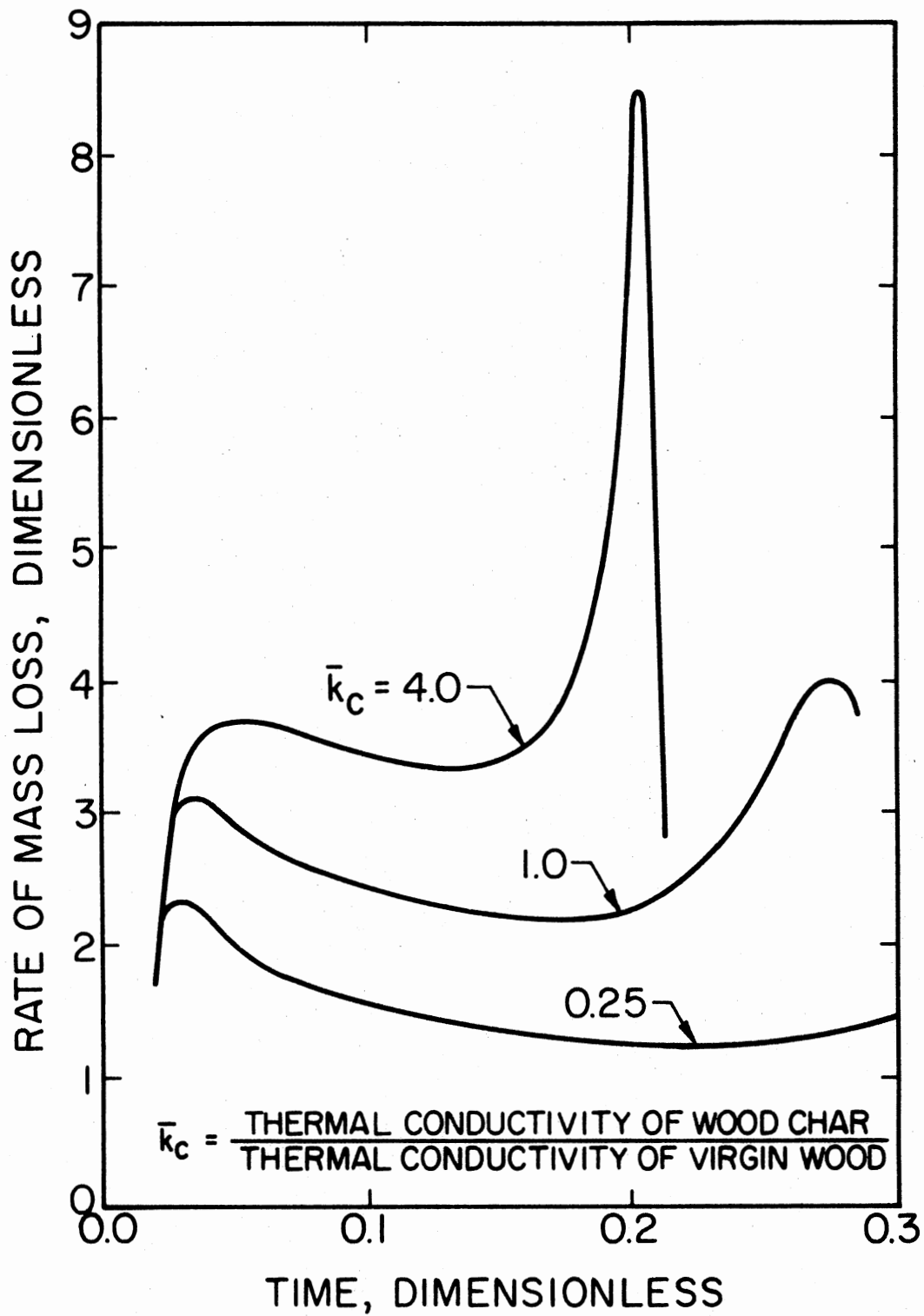


Figure 4. Effect of Char Thermal Conductivity on Rate of Weight Loss [9]

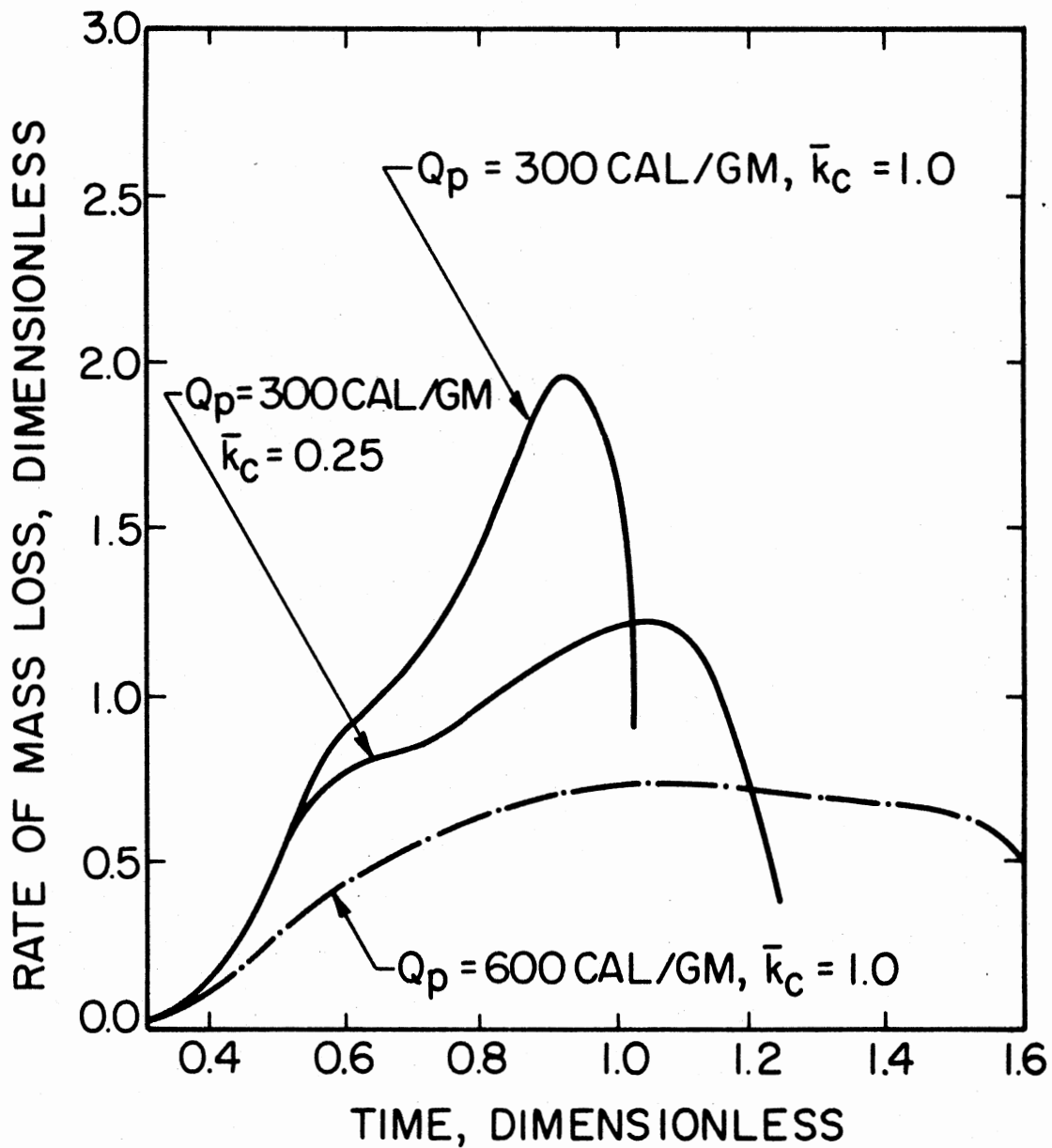


Figure 5. Effect of Heat of Decomposition on Rate of Weight Loss [9]

Kinetics of Thermal Decomposition

The rate of decomposition of a pyrolyzable material is modeled by the kinetic rate equation. If it is assumed that the material dimensions are constant, the rate equation determines the density of the remaining char. Both the rate of decomposition and the char density affect the thermal performance of the material. In order to predict the thermal response, accurate values of the kinetic parameters over the entire range of decomposition are required for use in the thermal model. These parameters include the pre-exponential factor and activation energy in Equations (2) and (15), and the order of reaction which will be defined later.

Several methods have been devised to extract the kinetic parameters from experimental data. Two standard techniques of obtaining this data are the measurement of the weight loss of a sample heated in an isothermal environment and the measurement of the weight loss of a sample exposed to a preprogrammed increasing temperature environment.

Isothermal Method

Several researchers have determined the kinetic parameters from data taken by the isothermal method. This is accomplished by placing a material sample, at ambient temperature, in an isothermal environment and measuring the sample weight as a function of time.

If the kinetics of thermal decomposition are described by a first order reaction similar to Equation (2), that is:

$$\frac{dw}{dt} = -Bw = -Awe^{-E/RT} \quad (22)$$

Equation (22) can be integrated to yield:

$$\ln w = Bt + \ln w_0 \quad (23)$$

where w_0 = initial weight of sample (gm).

If the reaction is first order, then a plot of $\ln w$ against time at each isothermal condition will yield a straight line with slope B . Repeating this procedure for several different isothermal conditions yields a plot with a series of straight lines, each with a different slope. The temperature dependence may then be obtained by plotting $\ln B$ vs $1/T$, at the same weight loss, for each furnace temperature. This results in a straight line with slope $-E/R$ and intercept A .

This method was used by Stamm [13] to determine the kinetic parameters for spruce, fir and pine samples. The samples were heated in ovens or beneath the surface of molten metal. Temperature ranges were varied from 93.5 to 300°C and heating times ranged from 1 minute to 2.4 years. A summary of these data is presented in Table I.

McNaughton [14] used a technique similar to Stamm [13] to obtain weight loss data for hardwood maple samples. McNaughton heated the specimens for periods ranging from 16 to 1,050 days at temperatures of 107 to 150°C. He obtained values of the pre-exponential factor and activation energy of $1.2 \times 10^{10} \text{ sec}^{-1}$ and 33.1 kcal/gm-mole-°C, respectively.

Akita [15] also investigated the decomposition of wood using an isothermal method. Temperatures ranged from 200 to 400°C. Akita heated samples in a Pyrex vessel immersed in a molten metal bath at pressures ranging from 1 atmosphere to 2 mm Hg. The sample weights were continuously monitored during decomposition, while remaining in

TABLE I
ACTIVATION ENERGIES FOR WEIGHT LOSS OF WOOD SAMPLES
BY THERMAL DEGRADATION*

Material	Heating Condition	Time Range	Temperature Range (°C)	Pre-Exponential Factor (sec ⁻¹)	Activation Energy (kcal/gm-mole)
Southern and white pine, Sitka spruce, Douglas fir sticks, and Sitka spruce veneer [†]	Oven	1 hr-2.4 yr	94-250	5.1×10^{11}	29.5
Douglas fir sawdust	Under molten metal	1 min-6 days	167-300	2.3×10^{11}	29.8
α -cellulose from Douglas fir	Oven	16 hr-64 days	110-220	1.9×10^9	25.0
Hemicellulose from Douglas fir	Oven	16 hr-64 days	110-220	4.8×10^9	26.0
Lignin from Douglas fir	Oven	2 hr-64 days	110-220	3.6×10^{10}	26.7
	Oven	16 hr-64 days	110-220	1.4×10^{10}	23.0

[†]Average value of activation energy and pre-exponential factor are listed for these samples.

*Data from Ref. [13]

the bath. This method of weighing eliminated the error induced, in Stamm's work, while removing the samples from the oven for weighing.

Akita postulated that the majority of wood is composed of cellulose, lignin and hemicellulose, and that the rate constants differed for each component. He further postulated that the rate of isothermal decomposition could be described by considering only these three constituents in the following equation.

$$\frac{dN}{dt} = \sum_j B_j (N_{\infty j} - N_j) \quad (24)$$

where N = total number of moles of gas evolved at time t

N_j = number of moles of gas evolved at time t , by the j^{th} component

$N_{\infty j}$ = number of moles of gas evolved at $t=\infty$, by the j^{th} component

B_j = rate constant for the j^{th} component (sec^{-1}).

Akita found that an apparent change of mechanism for cellulose pyrolysis occurred at approximately 340°C , which resulted in two activation energies. These data are shown in Table II.

Dynamic Heating Method

Several researchers have studied the thermal decomposition of various materials by the method known as thermogravimetric analysis (TGA). This method consists of measuring the weight of a very small sample which is heated at a preprogrammed linearly increasing temperature.

TABLE II
 ACTIVATION ENERGY OF DECOMPOSITION OF WOOD AND
 ITS MAJOR COMPONENTS*

Material	Temperature Range (°C)	Activation Energy (kcal/gm-mole)
Lignin	270-400	26.0
Hemicellulose	270-400	17.0
Cellulose	270-340	36.0
Cellulose	340-370	24.0
Wood (Japanese Cypress)	270-340	26.0 (avg)
	340-370	23.0 (avg)

*Data from Ref. [15]

This method is particularly attractive for the following reasons: (1) it is much faster than the isothermal technique, (2) effect of heating rate on decomposition may be studied easily, (3) weight loss and rate of weight loss may be obtained simultaneously, (4) with accurate microbalances, very small samples may be studied, and (5) the transient response effect of placing a sample at ambient temperature in an isothermal furnace is eliminated. Despite these advantages, several potential problems may arise: (1) decomposition rates may be significantly affected by sample geometry due to thermal gradients and gas diffusion through the char, (2) the furnace temperature rate may lead

or lag the programmed rate, and (3) differences in the indicated furnace temperature may differ from the true sample temperature.

The kinetic parameters may be extracted from TGA data based on a single weight loss curve taken at one heating rate, or on multiple curves obtained from several heating rates. The limitations and advantages of each are discussed in detail by Flynn and Dickens [16].

Single Heating Rate Techniques. The difference method of Freeman and Carroll [17] was one of the first developed for the dynamic heating method and has been widely used. The kinetic parameters obtained by this method are based on a single weight loss and differential weight loss curve. The kinetic model is described by:

$$-\frac{dw}{dt} = Bw^n = Aw^n e^{-E/RT} \quad (25)$$

where n = order of reaction.

Solving for B yields:

$$Ae^{-E/RT} = -\frac{dw/dt}{w^n} \quad (26)$$

Taking the log of both sides and differentiating with respect to T gives:

$$\frac{E}{RT^2} = \frac{d \log(-dw/dt)}{dT} - n \frac{d \log w}{dT} \quad (27)$$

Integrating Equation (27) over a finite temperature range and dividing by $\Delta(\log w)$ yields

$$\frac{(-E/R)\Delta(T^{-1})}{\Delta(\log w)} = \frac{\Delta \log(-dw/dt)}{\Delta(\log w)} - n \quad (28)$$

If $\Delta(T^{-1})/\Delta(\log w)$ is plotted vs $\Delta[\log(-dw/dt)]/\Delta(\log w)$ a straight line of slope $-E/2.303R$ and intercept n is obtained.

Freeman and Carroll used this technique to determine the kinetic parameters for calcium oxalate monohydrate. Samples weighing 423.0 mg were heated in an air atmosphere to 1000°C at a 10°C/min heating rate. A plot of $\Delta(T^{-1})/\Delta(\log w)$ vs $\Delta[\log(-dw/dt)]/\Delta(\log w)$ is shown in Figure 6.

Freeman and Carroll found that three separate sets of kinetic data were required to describe the thermal degradation at a single heating rate. The order of reaction was found to be 1.0, 0.7, and 0.4 for each of the three regions of weight loss. The activation energy was 22, 74, and 39 kcal/mole for each region.

Anderson and Freeman [18] later modified the Freeman and Carroll method. The modified procedure utilizes constant intervals of $1/T$ rather than increasingly larger intervals of $1/T$. The result of this modification is presented as Equation (29).

$$\Delta \log(dw/dt) = n \Delta \log w - \frac{E}{2.303R} \Delta(1/T). \quad (29)$$

$\Delta \log(dw/dt)$ may be plotted against $\Delta \log w$ if $\Delta(1/T)$ is kept constant. The order of reaction, n , is obtained from the slope and the activation energy is obtained from the intercept at $\Delta \log w=0$. This method was applied to the study of polystyrene and polyethylene. Experiments were carried out in a spring type vacuum thermobalance at 1 mm of Hg pressure. Samples of 100 mg were heated from ambient temperature to 500°C at 5°C/min. The polystyrene followed a zero-order reaction for the first 15 percent of the degradation. The initial

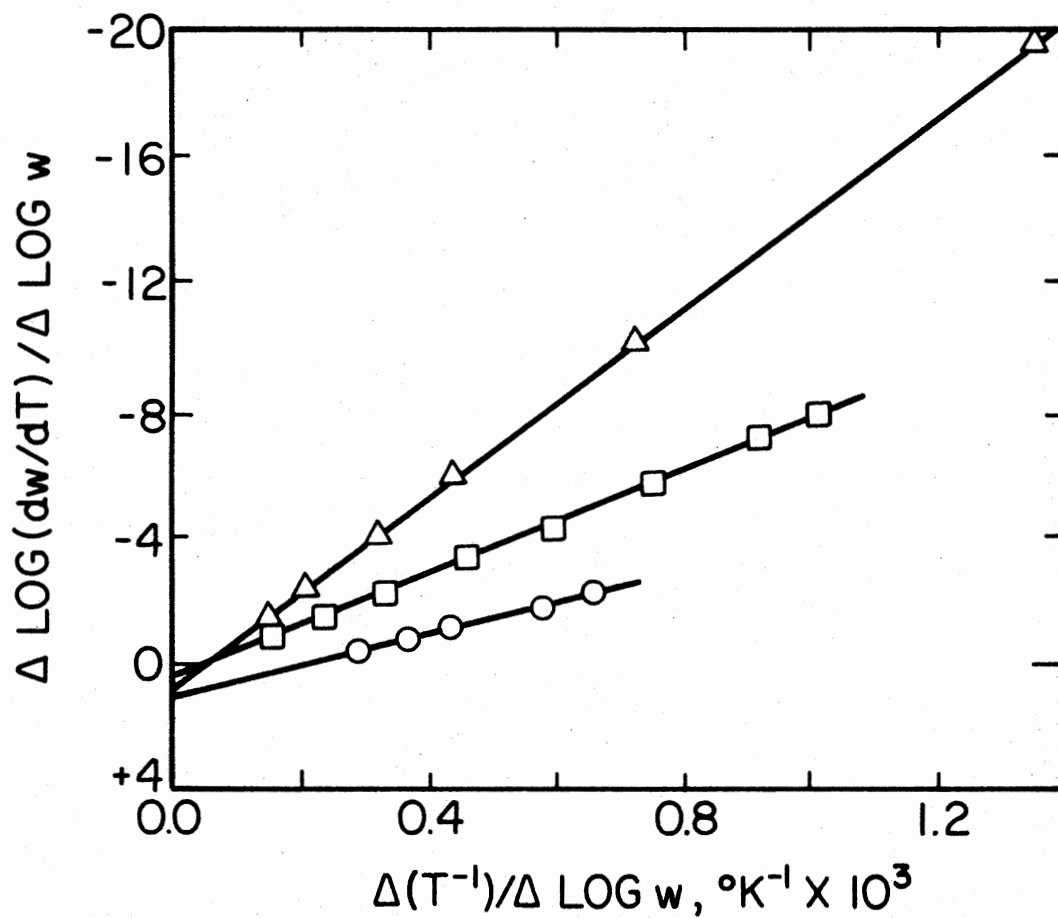


Figure 6. Plot Used to Determine Activation Energy and Order of Reaction for Three Separate Weight Loss Regions for Calcium Oxalate Monohydrate [17]

three percent had an activation energy of 48 kcal/mole and 61 kcal/mole from 3 to 15 percent. The order of reaction and activation energy for weight losses between 35 and 95 percent were approximately 1 and 67 kcal/mole. The weight loss between 15 and 35 percent was considered to be transition from zero to first order.

Mickelson and Einhorn [19] developed the ratio method to extract the kinetic parameters from a single thermogram taken at one heating rate. This method is attractive because it does not require rate of weight loss data. These researchers used the following form of the kinetic rate equation:

$$\frac{dy}{dt} = A\gamma^n e^{-E/RT} \quad (30)$$

and

$$\gamma = \frac{w-w_f}{w_0-w_f} \quad (31)$$

where w_f = final weight (mg).

If Equation (30) is written for two different temperatures, denoted by i and j , taking the ratio of the two results in

$$\frac{(dy/dt)_i}{(dy/dt)_j} = \exp\{-E/R[(T_j-T_i)/T_i T_j]\} (\gamma_i/\gamma_j)^n. \quad (32)$$

Taking the logarithm of both sides yields

$$\log\left(\frac{(dy/dt)_i}{(dy/dt)_j}\right) = \{E/2.303R[(T_j-T_i)/T_i T_j]\} - n \log(\gamma_i/\gamma_j)^n. \quad (33)$$

Providing $\gamma_i/\gamma_j = \text{constant}$, a plot of $\log[(d\gamma/dt)_i/(d\gamma/dt)_j]$ vs $(T_j - T_i)/T_i T_j$ will result in a straight line in which the slope is the activation energy and the intercept is the order of reaction.

These researchers decomposed 6.8 mg samples of shredded urethane polymer in a Mettler thermobalance. Samples were run in an argon atmosphere at heating rates of 4°C/min and 10°C/min. The results are summarized in Table III.

TABLE III
SUMMARY OF KINETIC PARAMETERS DETERMINED
BY THE RATIO METHOD*

Heating Rate (°C/min)	Activation Energy (cal/gm-mole)	Reaction Order	Pre-Exponential Factor (min ⁻¹)
4	33,200	0.46	1.32×10^{12}
10	33,200	0.55	1.51×10^{12}
10	30,500	0.61	1.55×10^{11}
10 [†]	33,200	0.49	1.91×10^{12}

[†]Sample weight was 4.0 mg

*Data from Ref. [19]

The effect of sample geometry on the rate of decomposition was studied by Mickelson and Einhorn as well. Samples weighing 6.8 mg were decomposed in an isothermal argon environment at 243°C. Two samples

were cast with different surface areas and one sample was shredded. The rate of decomposition of the thick cast sample was significantly reduced, thus illustrating the importance of sample geometry. The results of these tests are shown in Figure 7.

Baer, Hedges, Seader, Jayakar, and Wojcik [20] studied the pyrolysis of three reinforced polymeric materials. The materials were decomposed at heating rates from $10^{\circ}\text{C}/\text{min}$ to $4200^{\circ}\text{C}/\text{min}$, in a nitrogen atmosphere. A Mettler thermobalance was used for the $10^{\circ}\text{C}/\text{min}$ heating rate and the data were reduced using the Mickelson and Einhorn method. The Higher Heating Rate (HHR) tests were carried out by applying thin films of the polymers to preoxidized stainless steel plates and passing a current through them. The HHR data was reduced by a quasilinearization technique developed by Burningham and Seader [21]. The most startling result of this work is the lack of agreement between the predicted results using the kinetic parameters calculated from the $10^{\circ}\text{C}/\text{min}$ heating rate and the experimental data taken using the HHR technique. The lack of agreement leads to the conclusion that kinetic parameters calculated from data taken at a single heating rate will not accurately predict kinetic behavior of a material at higher heating rates. This is illustrated by the data presented in Figure 8. A summary of the results of this work is shown in Table IV.

Multiple Heating Rate Techniques. The multiple heating rate methods have the capability of utilizing thermogravimetric data taken over a wide range of heating rates. Friedman [22] developed a technique based on the multiple heating rate technique where the Arrhenius equation is combined with an arbitrary function of weight. This allows

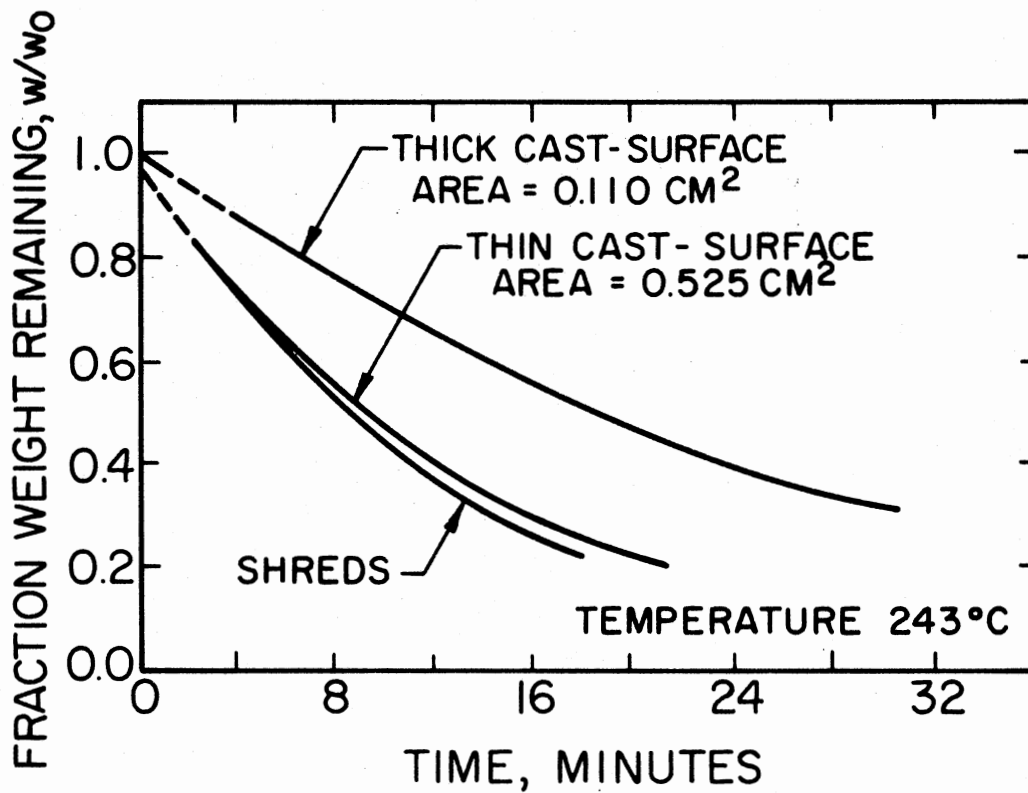


Figure 7. Effect of Sample Geometry on Rate of Decomposition in an Inert Isothermal Environment [19]

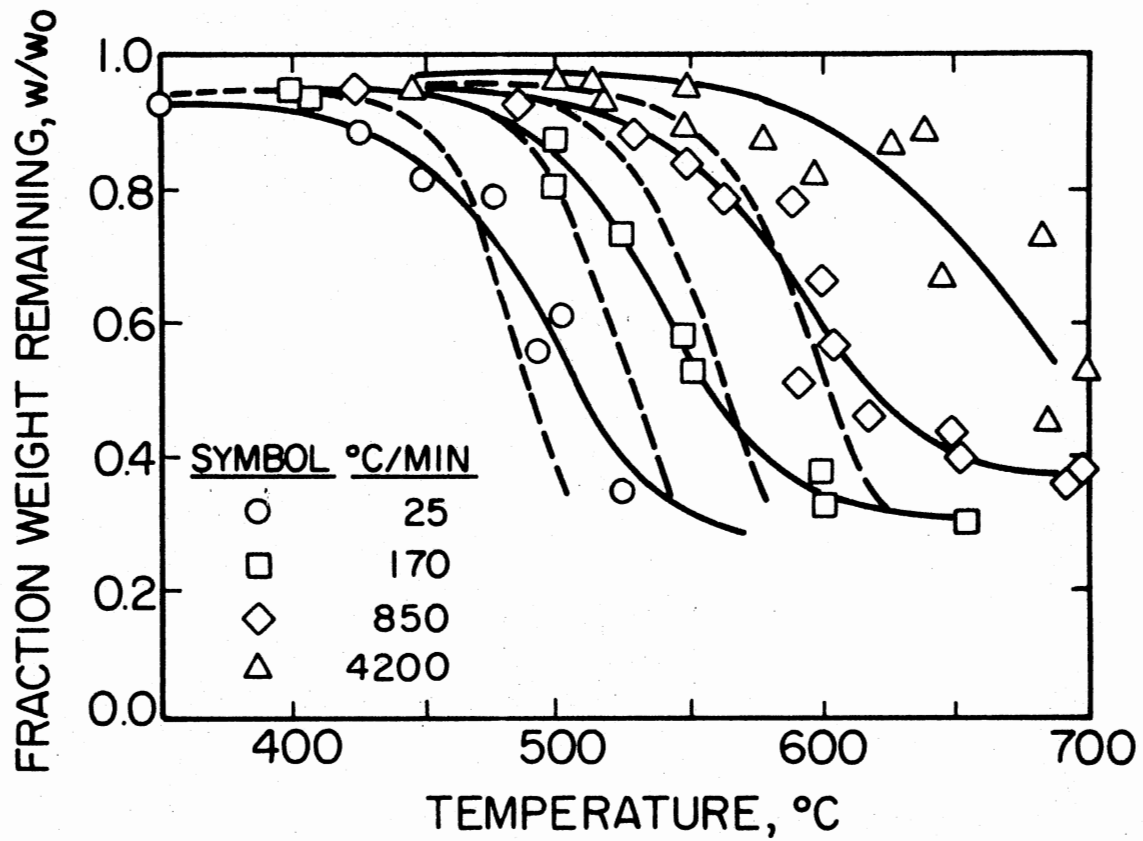


Figure 8. Comparison of Data for High Heating Rate Tests with Predictions from TGA Model [20]

TABLE IV
SUMMARY OF KINETIC PARAMETERS*

Material	Type of Test [†]	Fraction Retained at		Reaction Order	Activation Energy (kcal/gm-mole)	Pre-Exponential Factor (min ⁻¹)
		350°C	T _{max} [‡]			
EPDM/Neoprene	TGA	0.95	0.32	0.58	58.0	0.47 × 10 ¹⁷
Acrylonitrile Butadiene Resin	TGA	0.96	0.338	0.74	25.7	0.13 × 10 ⁸
BKR 2620 Phenolic and Acrylonitrile Butadiene Resin	TGA	0.92	0.484	2.12	39.2	0.37 × 10 ¹²
EPDM/Neoprene	HHR	0.96	0.26	1.56	36.0	0.18 × 10 ¹¹
Acrylonitrile Butadiene Resin	HHR	0.93	0.39	1.82	38.5	0.76 × 10 ¹²
BKR 2620 Phenolic and Acrylonitrile Butadiene Resin	HHR	0.89	0.48	2.48	59.0	0.36 × 10 ¹⁸

[†] TGA refers to test using the Mettler thermoanalyzer at a heating rate of 10°C/min. HHR refers to high heating rate tests.

[‡] For TGA tests, T_{max} was 1000°C. For the HHR tests, T_{max} was 700°C achieved at a heating rate of 170°C/min.

*Data from Ref. [20]

more flexibility, since no prior knowledge of the function is required. This method does, however, require measurement of the weight loss and rate of weight loss as a function of temperature at several different heating rates.

The general form of the rate equation proposed by Friedman is

$$-\frac{1}{w_0} \frac{dw}{dt} = Af(w/w_0)e^{-E/RT} \quad (34)$$

where $f(w/w_0)$ = undefined function of weight.

A dimensionless form of Equation (34) can be obtained by multiplying both sides by unit time. Taking the natural logarithm of both sides results in

$$\ln\left(-\frac{1}{w_0} \frac{dw}{dt}\right) = \ln[Af(w/w_0)] - E/RT. \quad (35)$$

A linear equation may be fit to $\ln[(-1/w_0)(dw/dt)]$ as a function of $1/T$ at constant parametric values of w/w_0 . These equations will have slopes of $-E/R$. Each intercept is the value of $\ln[Af(w/w_0)]$ at the parametric value of w/w_0 . Then, by defining

$$f(w/w_0) = [(w-w_f)/w_0]^n \quad (36)$$

and multiplying Equation (36) by A and taking the natural logarithm results in

$$\ln[Af(w/w_0)] = \ln A + (n)\ln[(w-w_f)/w_0]. \quad (37)$$

The final ratio, w_f/w_0 , is taken from the original thermograms. Since

$\ln[Af(w/w_0)]$ is known for various w/w_0 ratios, Equation (37) can be used to obtain values of A and n .

Friedman used this technique to calculate the kinetic parameters for CTL91-LD fiberglass-phenolic. Flaked samples weighing 200 mg were heated at rates of 50, 100, 180, and 360°C/hr in a stream of dry nitrogen. The thermograms obtained from these measurements are shown in Figure 9. Rate of weight loss data was calculated from Figure 9 using a derivimeter. One activation energy was calculated for each of the 12 values of weight loss ranging from 0.675 to 0.95 (on a glass-free basis). These data are shown in Figure 10. The average activation energy was calculated from these data. By eliminating the early weight loss ($\approx 4\%$) and dropping the data points above $w/w_0=0.875$ and using $w_f/w_0=0.61$, the linear curve shown in Figure 11 was fit to the data. Thus, the effective range covered by the curvefit was approximately $0.65 \leq w/w_0 \leq 0.85$, which accounted for about 50 percent of the total weight loss. This resulted in a rather poor fit of the data at both ends of the weight loss curve. Friedman calculated values of 57.7 kcal/gm-mole, $5.98 \times 10^{18} \text{ hr}^{-1}$, and 5.0 for the average activation energy, pre-exponential factor, and order of reaction, respectively.

Friedman's technique was later modified by Henderson, Wiebelt, Tant, and Moore [23], in order to cover a larger percentage of the weight loss curve. Application of this method required calculating an average activation energy for the entire thermal decomposition. The decomposition reaction required two models, one for the initial decomposition and another for the remainder. For these two regions, separate pre-exponential factors and apparent orders of reaction were

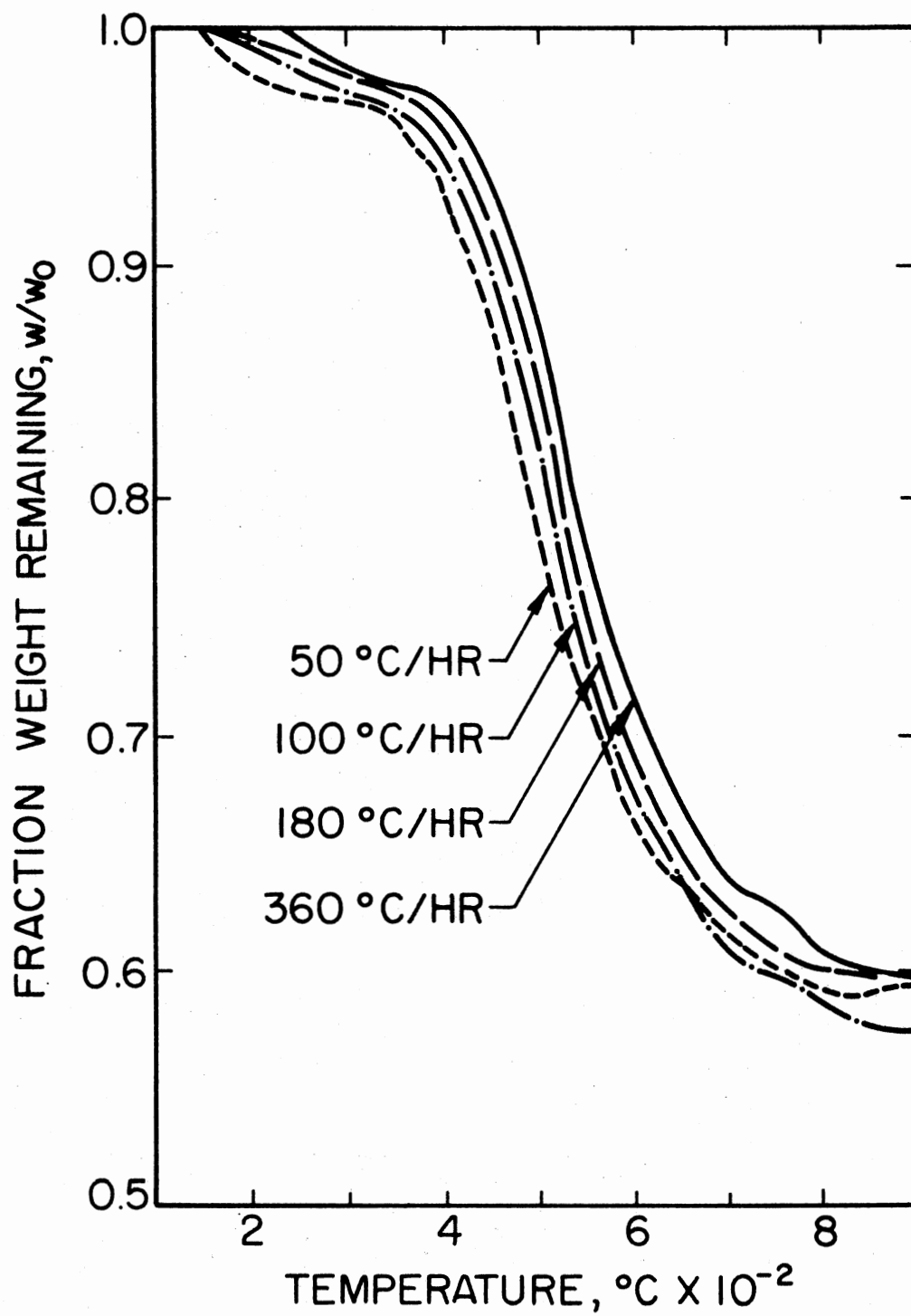


Figure 9. Thermogram for CTL91-LD Fiberglass-Phenolic [22]

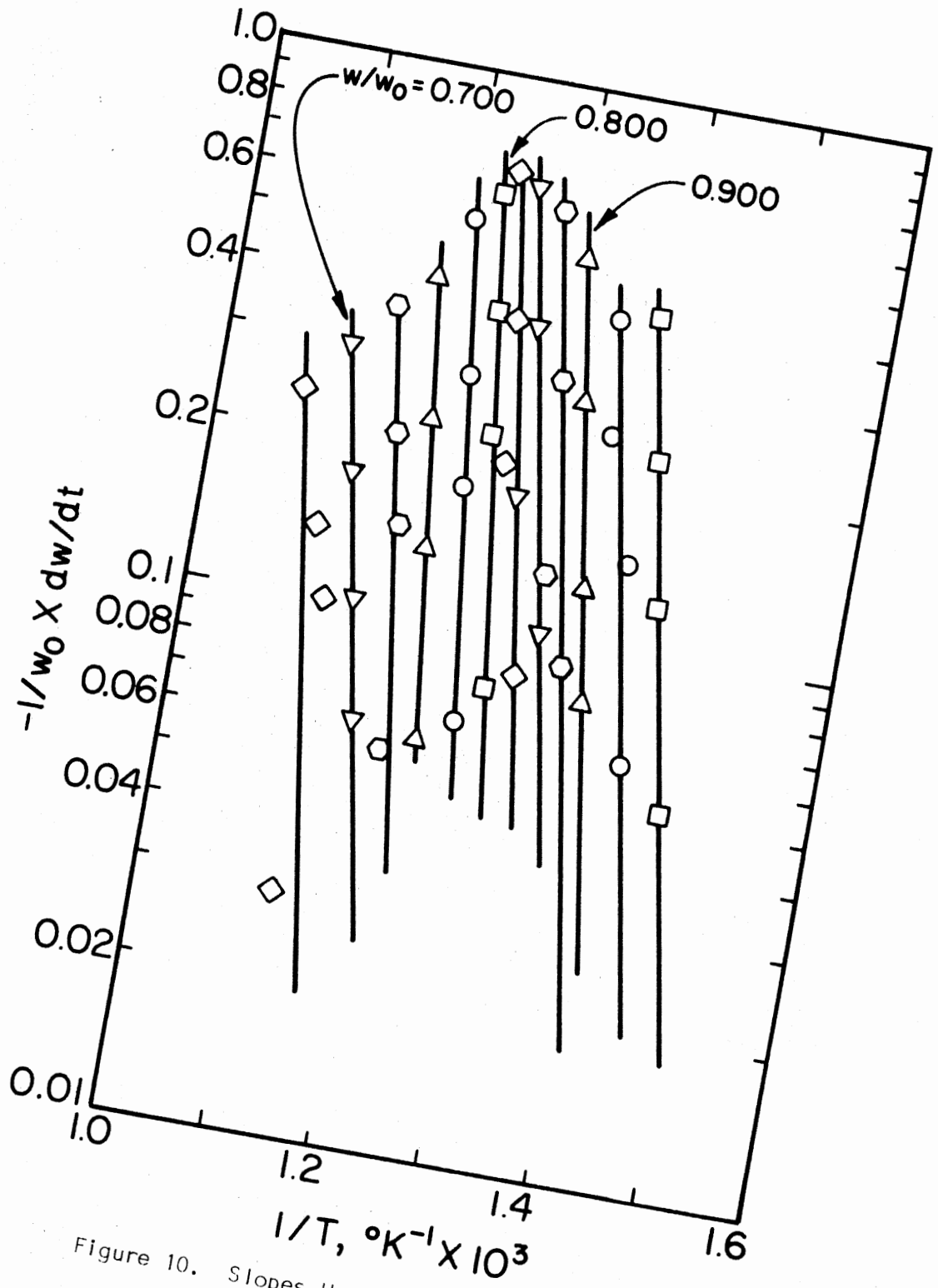


Figure 10. Slopes Used to Determine Average Activation Energy [22]

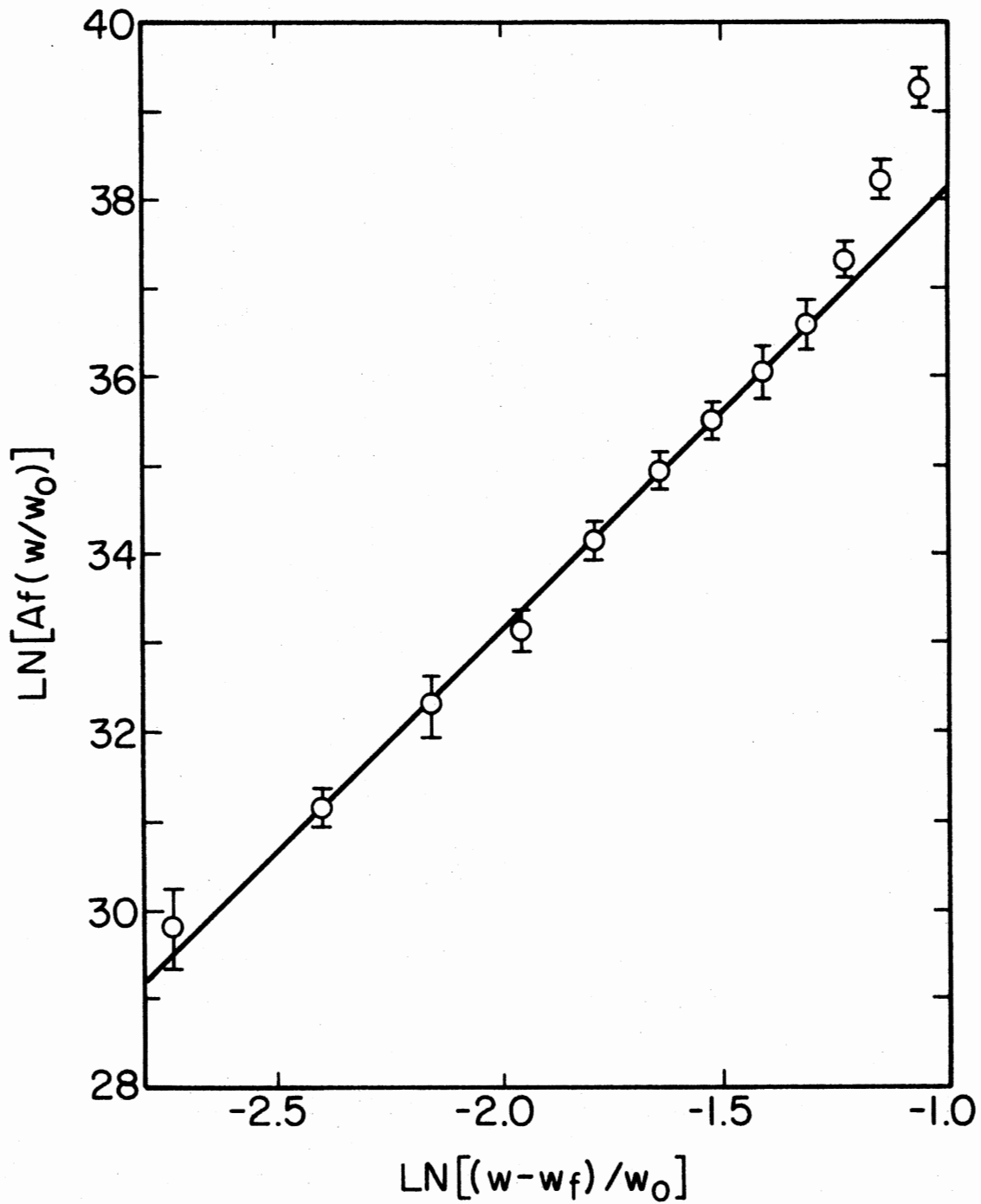


Figure 11. Plot to Determine the Pre-Exponential Factor and Order of Reaction [22]

calculated by the technique developed by Friedman. This method will be discussed in detail later.

Flynn and Wall [24] developed a convenient method to determine the activation energy from weight loss curves measured at several heating rates. The following relationship is used to calculate the activation energy.

$$E \approx -(R/C) d \log \beta / d(1/T) \quad (38)$$

where β = heating rate ($^{\circ}\text{C}/\text{min}$)

$$C = C(E/RT).$$

Plotting $1/T$ versus $\log \beta$ at several weight loss ratios results in a series of straight lines with slope $\Delta \log \beta / \Delta(1/T)$. Using the slope and the appropriate value of C , the activation energy can be calculated by Equation (38). Since C is a function of E/RT , the calculation of E from Equation (38) is an iterative process. Flynn and Wall constructed a table of values for C over the range from $7 \leq E/RT \leq 60$. The variation of C over this range is approximately ± 3 percent. This method is extremely attractive, since it involves only reading the temperature at a constant weight loss from a series of thermograms at different heating rates. The feasibility of this method was demonstrated using a hypothetical set of data.

Specific Heat Measurements

The rate of energy storage in a pyrolyzable material is a function of both the density and specific heat of the virgin and char components. As is the case with the kinetic parameters, accurate values of these properties are necessary to characterize the thermal response. The

time dependent density of the material is given by the kinetic rate equation. The specific heat may be determined by experimental techniques.

Despite the importance of the specific heat, there is a dearth of experimental data in the literature for all pyrolyzable materials. A limited amount of data are available for both wood and phenolic ablative materials below 400°C. However, no data were found for residual char or partially pyrolyzed glass- or asbestos-phenolic ablatives. The problem is compounded by the fact that the magnitude of specific heat of both the virgin and char components is sensitive to the type and amount of the filler or fiber. Thus the published data are of limited usefulness for the materials considered in this work.

The specific heat of the phenolic ablatives is a function of the temperature and the decomposition history. Measurement of the temperature dependent specific heat up to incipient pyrolysis and after its completion is a rather straightforward procedure. However, determination of these properties during pyrolysis is somewhat more difficult. This is primarily because the mass of the sample is changing and the energy liberated or consumed, as a result of the decomposition, is difficult to separate from the sensible energy added to the sample.

Several methods have been used to measure specific heats. The two most widely used are drop calorimetry and differential scanning calorimetry. The drop calorimetry method is extremely accurate; however, it is slow and tedious. In contrast, differential scanning calorimetry is quick and reasonably straightforward, but lacks the accuracy of the drop method. Both methods are applicable to the materials of interest in this work.

Drop Calorimetry Method

The drop ice calorimeter consists primarily of a furnace and an ice calorimeter. The method of operation is straightforward. Samples are heated in the isothermal furnace and then dropped into the ice calorimeter. The calorimeter is a sealed vessel which contains a cup surrounded by an ice mantle and an annulus containing an ice water bath. The enthalpy of the specimen is sensed as a change in volume of the water-ice system as the ice melts. The change in the volume of the water-ice system is then related to the change in height of a column of mercury. The temperature dependent enthalpy can be determined by a series of drops at different temperatures. The specific heat can be determined from the slope of the enthalpy curve, that is

$$C_p = \frac{d}{dT} (h_T - h_{273.15}). \quad (39)$$

The overall error in this method is less than ± 1.0 percent.

The specific heat of precharred CCA3/SC1008 carbon phenolic was measured to 5000°F by Pears [25] using an ice bath calorimeter. A plot of the data is shown in Figure 12. No details of the measurements were given.

Several values of specific heat of phenolic ablatives below 400°C were found in Reference 26. Most of these were measured by Southern Research Institute, a commercial testing laboratory.

Dunlap [27] measured the specific heat of wet and dry woods by ice bath calorimetry. He reported specific heats for 20 different species of wood in the temperature range 0 to 106°C with densities ranging from

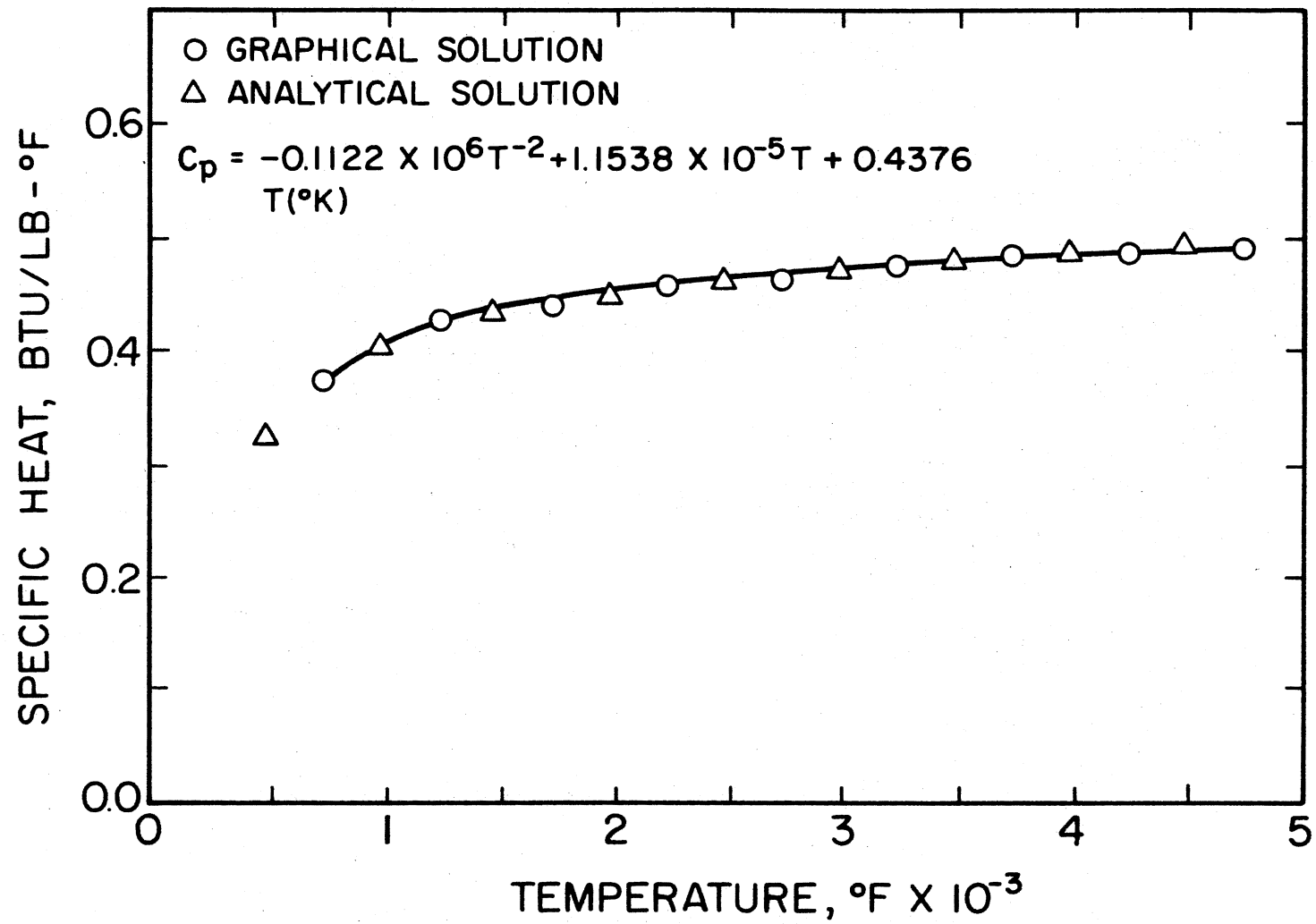


Figure 12. Specific Heat of a 5000°F Precharred Carbon Phenolic [25]

0.23 to 1.10 gm/cm³. The data were fitted to the linear equation

$$C_p = 0.266 + 0.00116T. \quad (40)$$

Differential Scanning Calorimetry Method

The technique of differential scanning calorimetry was developed in the early 1960's and has been used for the measurement of specific heats and enthalpy of fusion for temperatures under 800°C. The DSC method maintains a sample and reference pan at very nearly the same temperature as it scans a predetermined temperature range. The DSC simply measures the differential energy required to maintain the reference pan and the sample at the same temperature. From this data the specific heat before and after any chemical reactions occur can be extracted, i.e. virgin and char material specific heat. The following equation may be used to calculate the specific heat:

$$C_p = \frac{dq/dt}{m dT/dt} \quad (41)$$

where dq/dt = measured differential heat input (cal/sec)
 dT/dt = scan speed (°C/sec)
 m = mass of sample (gm).

During the decomposition process the combined specific heat and heat of decomposition results. Details of the operation and calibration of a differential scanning calorimeter will be discussed in a later chapter.

Brennan, Miller, and Whitwell [28] developed a technique to separate the sensible energy from the heat effects due to a decomposition reaction. This was accomplished through a DSC scan of both the virgin material, through pyrolysis, and the residual char. These scans are

depicted qualitatively by Figure 13. Lines two and three represent the virgin and char material scans, respectively. Line one represents the empty sample and reference pan baseline scan. The extrapolated line, AE, represents the curve for the reactant as if no thermal decomposition were occurring. The area contained by AMB represents the estimated heat of decomposition based on the assumed sensible energy, AB. The sensible energy added to the combination of the active and char components is given by:

$$\frac{dq}{dt} = f m_a C_{pa} \frac{dT}{dt} + (1-f) m_c C_{pc} \frac{dT}{dt} \quad (42)$$

where $f = \text{fraction reacted} = \frac{A_1}{A_1 + A_2}$

$m_a = \text{mass of active material (mg)}$

$m_c = \text{mass of char material (mg)}$

$A_1 = \text{area contained by AMO}$

$A_2 = \text{area contained by BMO.}$

The procedure outlined by Brennan is as follows:

1. assume line AB represents the sensible energy component
2. calculate f at any point
3. calculate dq/dt from Equation (42)
4. repeat steps 2 and 3 at increasing values of temperature until decomposition is complete
5. iterate on steps 2, 3, and 4 until convergence is achieved and a new line AB is established.

Once the new baseline, AB, is established, the area contained by AMB should represent the heat of decomposition of the material.

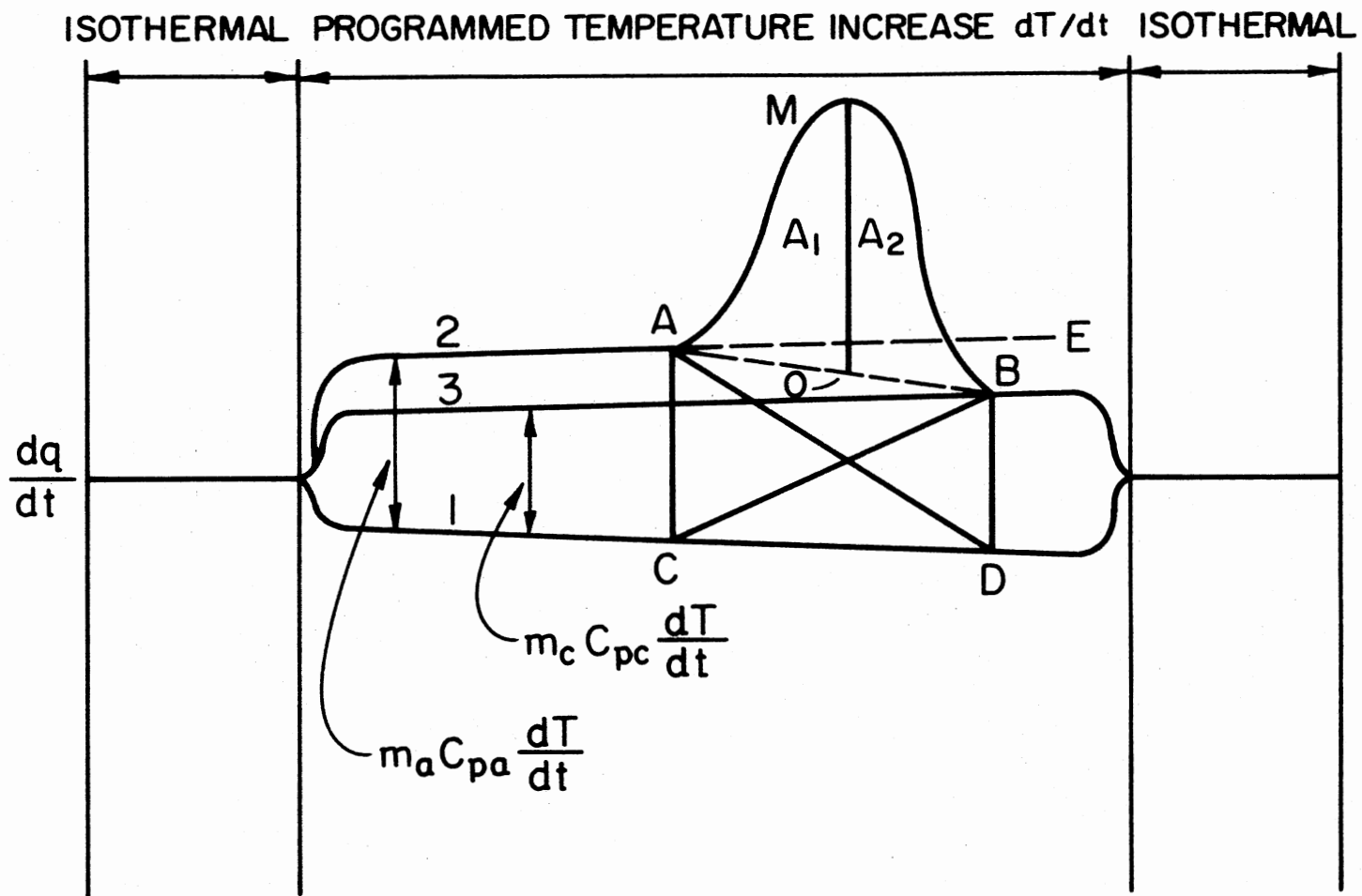


Figure 13. Qualitative Diagram of a Programmed Temperature Scan for Empty Pan, Virgin and Char Material [28]

The feasibility of this technique was demonstrated by determining the heat of decomposition and specific heat of cotton and poly(methyl methacrylate). No details of the measurements or resulting values from the calculations were given.

This method is unique in that no values for the mass of the virgin material components are required during decomposition. The method does, however, require the assumption that the fraction of mass reacted at a given temperature is equal to the fraction of energy liberated or consumed at the same temperature. Additionally, the assumption that $m_a C_{pa} dT/dt$ may be extrapolated along line AE is required.

Havens [12] used the DSC technique to determine the specific heat and estimate the heat of decomposition of wood. Havens measured the specific heat of samples of white pine and oak from 100 to 420°C. During decomposition the heat of pyrolysis was estimated by extrapolating the specific heat curve through the decomposition region. A plot of the specific heat of oak is shown in Figure 14. Havens' estimates resulted in values of 47.5 and 26.6 cal/gm for the heat of pyrolysis for white pine and oak, respectively.

Havens was the first researcher to attempt to determine the specific heat and heat of decomposition of wood by the DSC technique. However, the calculated apparent specific heat during pyrolysis was based on the original weight of the sample. This resulted in values of apparent specific heat appearing much lower than the true value. Havens' TGA work shows that $w_f/w_0=0.2$. If this ratio of initial to final weight were used in Equation (41) after pyrolysis is complete, it would yield a value for the final char specific heat of ≈ 0.5 cal/gm-°C

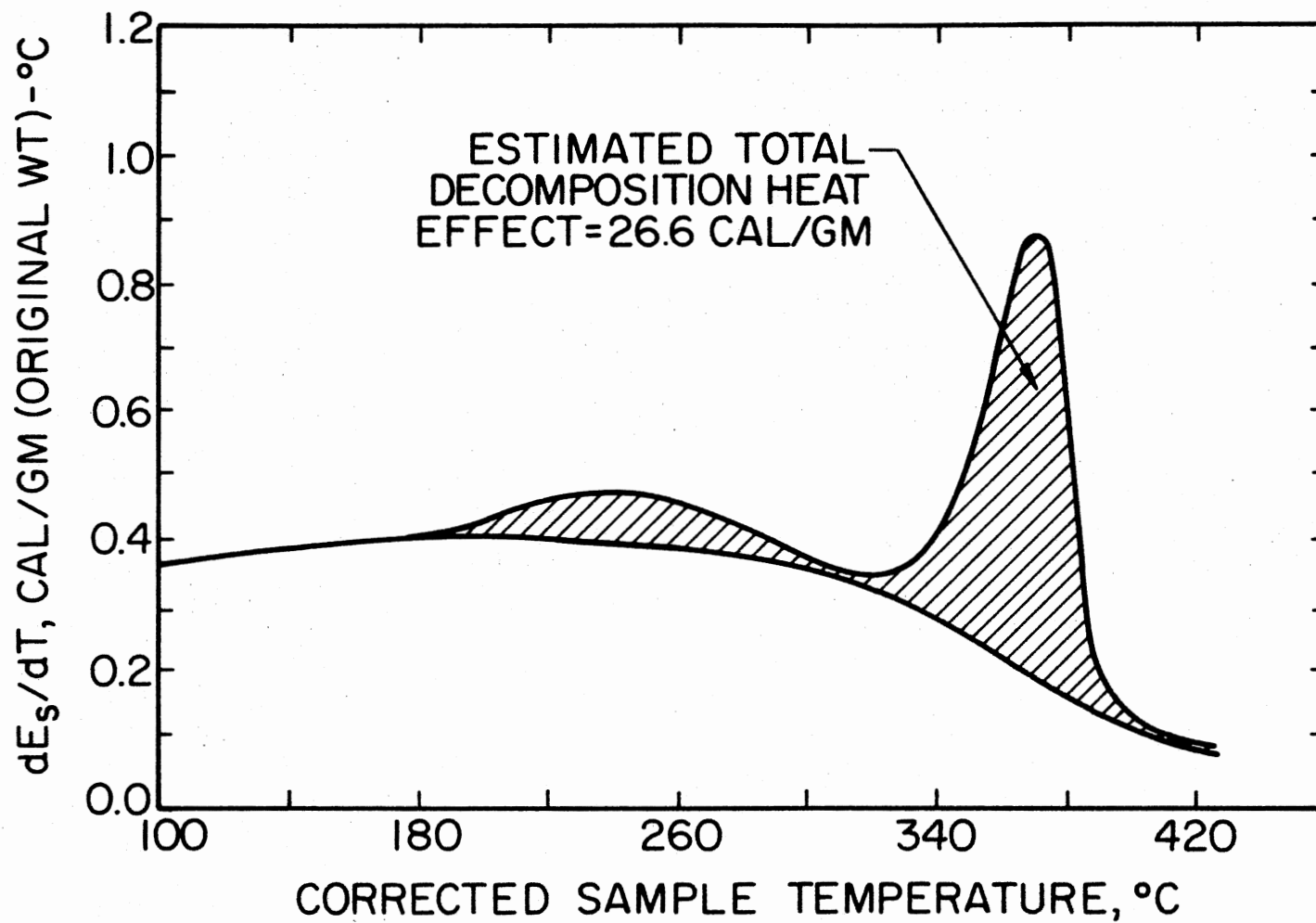


Figure 14. Specific Heat of Oak Wood as a Function of Temperature in a Nitrogen Atmosphere [12]

rather than the 0.1 cal/gm-°C reported. The area calculated as the heat of decomposition is in error as well.

Determination of Heat of Decomposition

The magnitude of the heat of decomposition or heat of pyrolysis of pyrolyzable materials has eluded researchers for years. Both endothermic and exothermic values have been reported. Brown [29] attributes the lack of agreement to the different experimental methods used to measure these values. Laboratory measurements of the heats of decomposition, using differential scanning calorimetry and differential thermal analysis (DTA), have been largely endothermic, whereas values calculated from in situ measurements have been exothermic. Murty Kanury [6] suggested that the confusion is due largely to secondary exothermic reactions of the pyrolysis gases, catalyzed by the hot outer char layer.

In Situ Measurements

Bamford et al. [1] calculated the heat of decomposition using the sudden rise which occurs in the center of the sample during decomposition. The assumption was made that the sudden rise in temperature was due to the exothermic reaction and that no heat was conducted away. With these assumptions an energy balance can be written as follows:

$$\rho_V C_p \Delta T = Q_p (\rho_V - \rho_C) \quad (43)$$

where ΔT = sudden temperature rise (°C).

This sudden central temperature rise is apparent in Figure 1. Using a value of 98°C for ΔT , Bamford et al. calculated a heat of decomposition for deal wood of 86 cal/gm exothermic.

Akita [14] used a similar technique to calculate the heat of decomposition for sawdust and cypress. The central transient temperature of spheres was used as input to an approximate solution of the heat conduction equation for a sphere with heat generation.

The heat of pyrolysis was assumed to be liberated at a rate proportional to the rate of change of density, that is:

$$Q_p \frac{d\rho}{dt} = Q_p A(\rho - \rho_f) e^{-E/RT} \quad (44)$$

The value of Q_p , the only unknown, was adjusted until there was agreement between the calculated and measured central temperature. Akita calculated values of 32 and 30 cal/gm exothermic for sawdust and cypress, respectively. Constant thermal properties were assumed.

Murty Kanury [8] proposed that the heat of decomposition could be computed by Equation (9) or (10) using variable thermal and physical properties. Kung [29] used this method to calculate the heat of pyrolysis of the Bamford et al. [1] data. The value which yielded the best fit was 180 cal/gm endothermic. There is significant disagreement between the results of Kung and Bamford.

Differential Thermal Analysis Method

Differential thermal analysis (DTA) differs from differential scanning calorimetry (DSC) in that both the sample and reference pans are heated by a single source. The difference in temperatures is measured by a differential thermocouple imbedded in the sample and reference material. The temperature difference is defined as:

$$\Delta T = T_s - T_r \quad (45)$$

where T_s = sample temperature ($^{\circ}\text{C}$)
 T_r = reference temperature ($^{\circ}\text{C}$).

If ΔT is plotted against temperature or time, any type of chemical reaction occurring in the sample will show up as a deviation from a straight line. This is shown qualitatively in Figure 15.

The DTA data can be converted to energy units by comparing the sample thermogram to one for a calibration material which has a well defined heat of fusion.

Sykes [30] measured the heat of decomposition of Union Carbide Corporation BRP5549 phenolic resin using DTA. Samples weighing 60 mg were filed from a molded disk and heated from ambient to 900°C , at $10^{\circ}\text{C}/\text{min}$, in an helium atmosphere. The results are presented in Figure 16. The exothermic peaks extend above the baseline $\Delta T=0$ and the endothermic peaks extend downward. Section A is a combination of both endothermic and exothermic reactions. Section B is primarily endothermic. Sykes attributed the first endothermic reaction, at 100°C , to the vaporization of water which remained in the sample after post curing. The exothermic peak, at 265°C was 16 cal/gm exothermic. Gas chromatography identified water vapor again as the major gas constituent. Finally, the 70 cal/gm endothermic reaction is the energy associated with decomposition of the material.

Tang and Neill [32] studied the effect of flame retardants on α -cellulose using DTA. Both the heat of decomposition and heat of combustion were measured. Samples weighing 100 mg were heated to 555°C at $12^{\circ}\text{C}/\text{min}$ in both helium and oxygen atmospheres. The heat of pyrolysis measured in an inert atmosphere was found to be 88 cal/gm, endothermic,

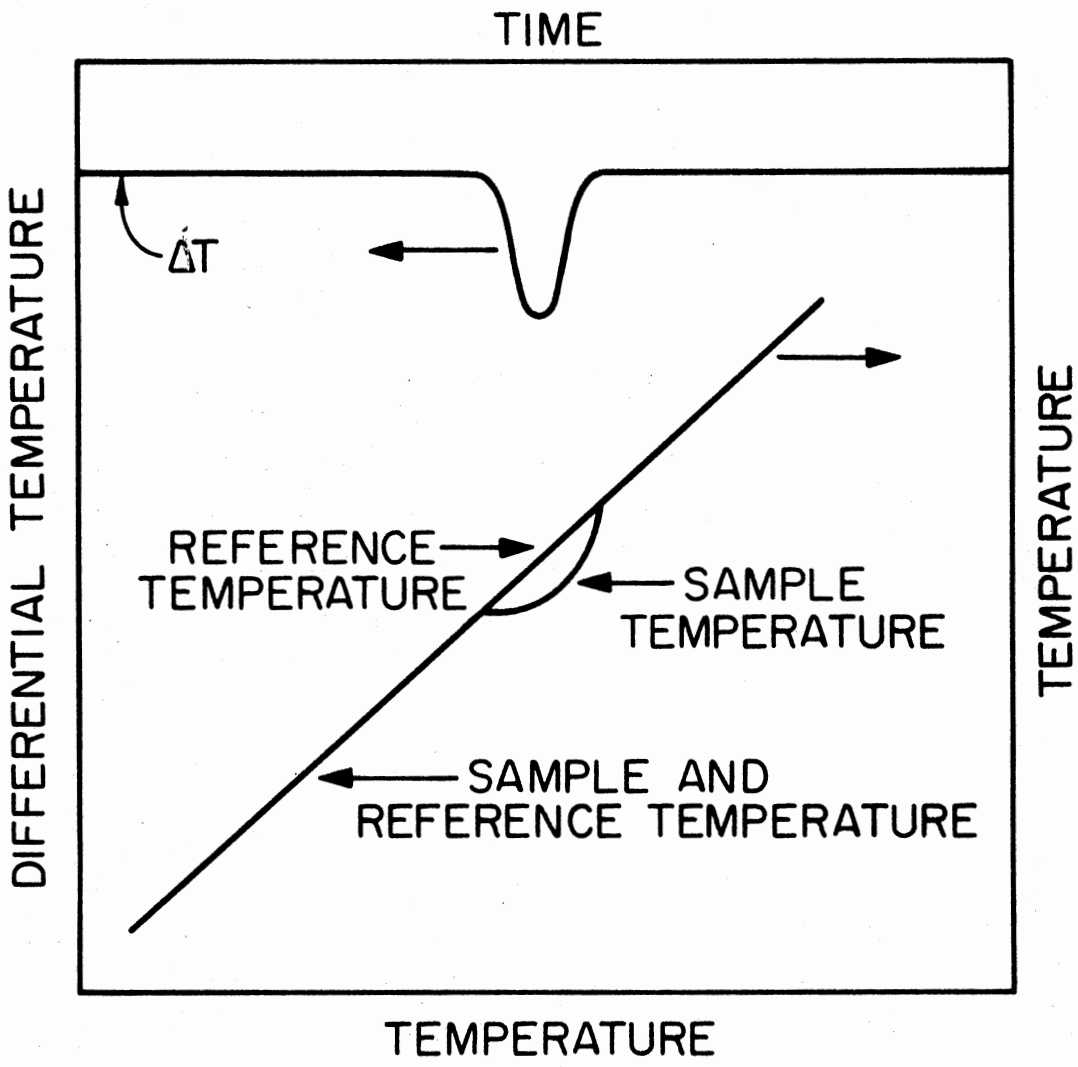


Figure 15. Idealized DTA Scan [29]

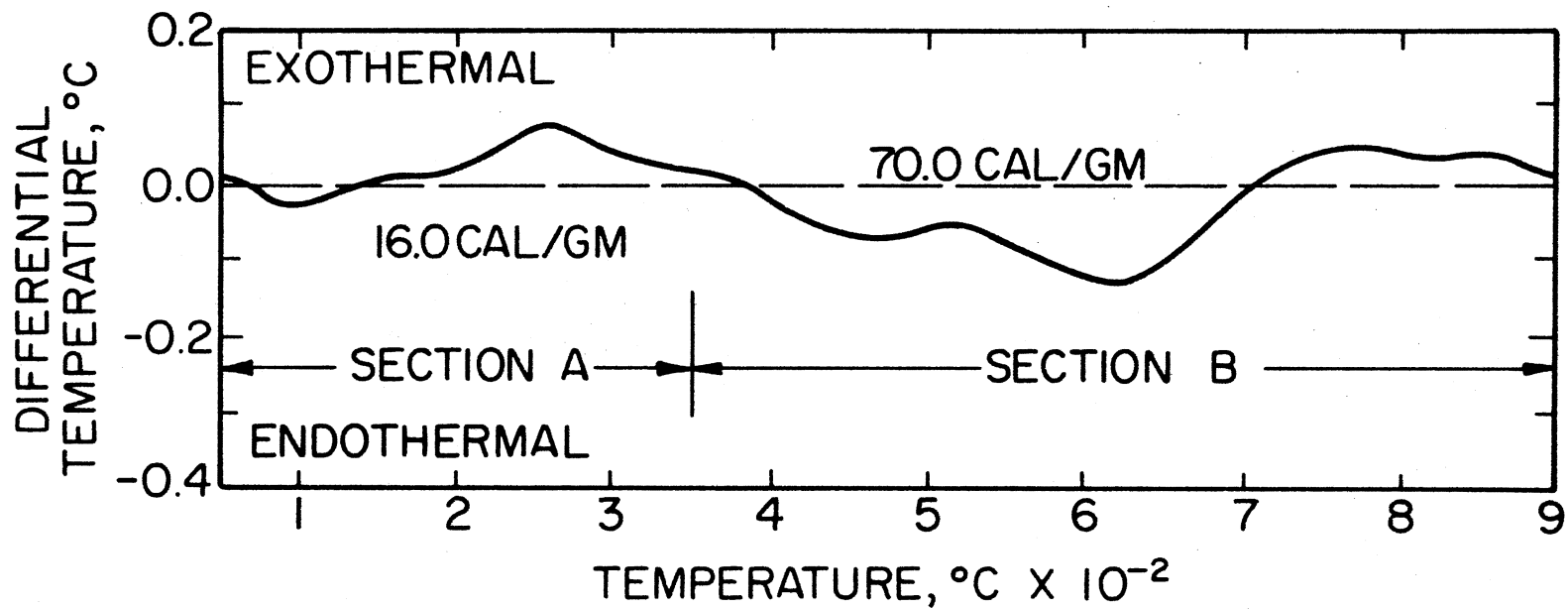


Figure 16. DTA Thermogram of BRP5549 Phenolic Resin [30]

while the heat of combustion was 3540 cal/gm, exothermic. Tang and Neill's results are summarized in Table V.

TABLE V
SUMMARY OF HEAT OF PYROLYSIS AND COMBUSTION*

α -Cellulose with:	Heat of Pyrolysis (cal/gm)	Heat of Combustion (cal/gm)
No treatment	88 \pm 3.6	-3540 \pm 140
2% Na ₂ B ₄ O ₇ ·10H ₂ O	58 \pm 2.4	-3630 \pm 146
2% AlCl ₃ ·6H ₂ O	87 \pm 3.4	-3560 \pm 142
2% KHCO ₃	72 \pm 3.0	-3500 \pm 140
2% NH ₄ H ₂ PO ₄	78 \pm 3.2	-3520 \pm 140
8% NH ₄ H ₂ PO ₄	64 \pm 2.6	-3520 \pm 140

*Data from Ref. [32]

Differential Scanning Calorimetry Method

The use of DSC to measure enthalpies of fusion and vaporization for various substances has been widespread. An excellent discussion of some of these applications is given by McNaughton and Mortimer [33]. The application of DSC to the measurement of heats of decomposition or combustion of a pyrolyzable material is limited. This is thought to be due to the difficulty of separating the sensible energy from that

associated with the chemical reaction. The only references located were the previously discussed work of Havens [12] and Brennan [28].

Temperature Profile Measurements

Techniques to measure the surface recession, pyrolysis rate, ignition time, and temperature profiles of combustible materials have been of interest for many years. A variety of experimental devices have been built to accomplish this task. The differences are due, in part, to the type of investigation being undertaken.

Ablation rates of phenolic ablative materials have been of concern in the aerospace industry during recent years. As a result, various types of experimental devices have been built which test the capability of materials to withstand severe heating/erosive environments. They consist mainly of devices which simulate re-entry conditions for various types of vehicles and those which simulate direct impingement from solid rocket motors. This particular class of simulators are, in general, extremely high heating rate facilities in which ablative samples are heated by both radiation and convection. Many have the capability of injecting particles into the flow in order to simulate various erosive conditions which range from atmospheric dust or rain to Al_2O_3 particles contained in solid rocket motors. In general these devices produce boundary conditions which are not easily quantified. The result is data which are usually not well suited for comparison with analytical solutions. For the sake of completeness, however, some of these experimental devices will be discussed.

Davy, Menees, Lundell, and Dickey [34] used experimental data obtained from NASA Ames Giant Planet Pilot Facility to compare with

calculated ablation rates for carbon materials. Carbon-phenolic and ATJ graphite samples of 4.0-cm diameter were heated at rates up to 21.0 kW/cm² in a hydrogen-helium atmosphere to simulate Jupiter entry conditions. Davy et al. measured the surface recession for run times of 2.0-5.0 seconds. The surface recession and exposure time data for the tests are given in Table VI. A schematic of the GPPF facility is shown in Figure 17. In-depth temperature profiles were not reported.

TABLE VI
GIANT PLANET PILOT FACILITY TEST RESULTS*

Material	Diameter (mm)	Test Time (sec)	Surface Recession (mm)
Carbon-phenolic	45	3.3	0.19
Carbon-phenolic	35	3.3	0.25
Graphite	40	2.0	0.13
Graphite	40	3.3	0.16
Graphite	40	4.9	0.26
Graphite	40	5.0	0.33
Graphite	40	5.0	0.29
Graphite	40	5.0	0.30
Graphite	40	5.0	0.31
Graphite	40	5.0	0.29

*Data from Ref. [34]

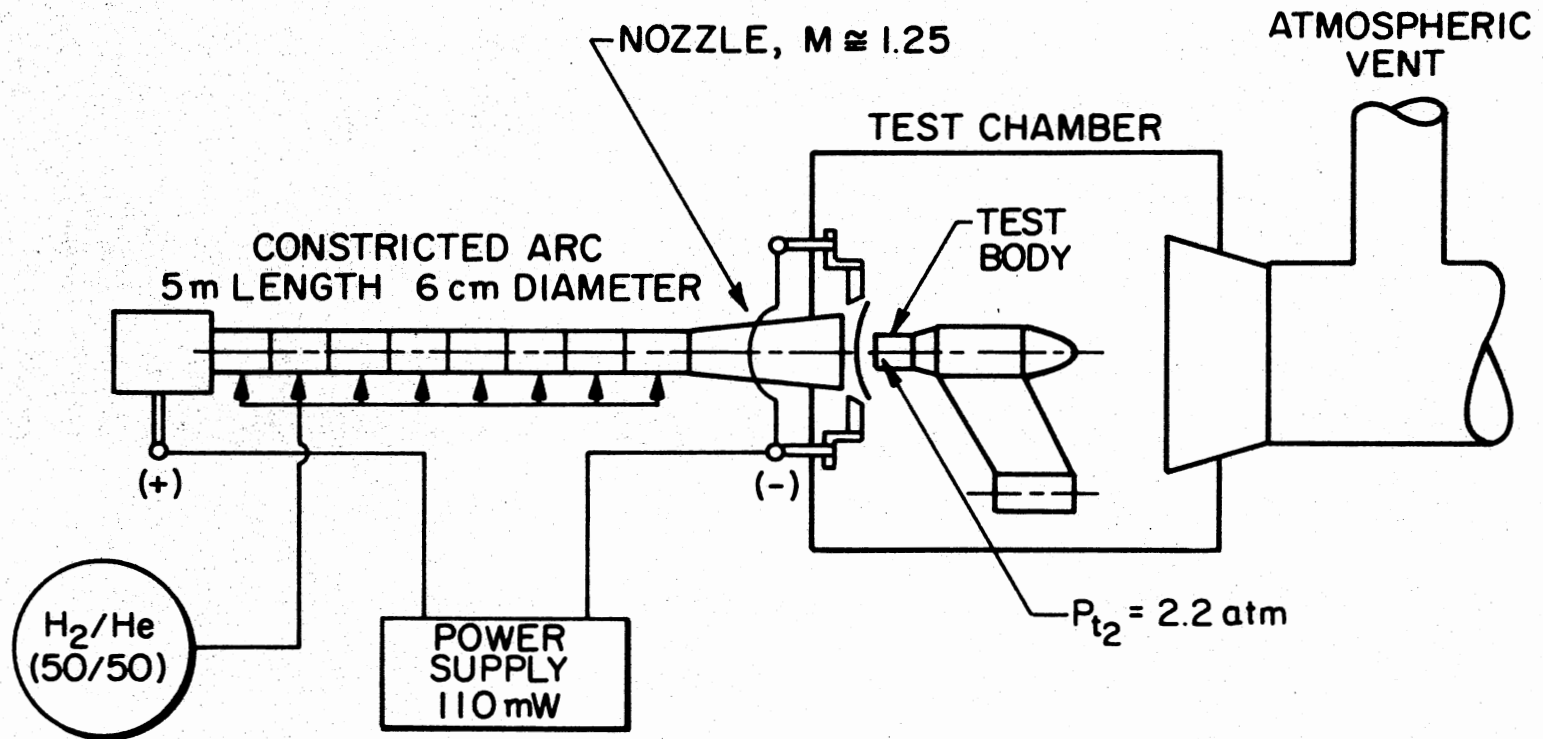


Figure 17. NASA's Giant Planet Pilot Facility [34]

Schaefer, Dahm, Rodriguez, Reese, and Wool [35] used an arc-plasma generator to study the ablation rates of three types of silica-phenolic materials. Schaefer et al. used a 1-megawatt arc-plasma generator in which the energy was added to the primary gas stream by a steady electric arc discharge.

The heat flux to the ablative samples was measured with a Gardon-type calorimeter and the total gas enthalpy was determined by performing an energy balance on the plasma generator. In-depth temperature profiles were measured using 0.005-inch diameter Tungsten-Rhenium and Chromel-Alumel thermocouples. Surface temperatures were measured with an optical pyrometer. Surface recession rates and char thickness were measured as well. The measured temperature profiles were input into a charring materials ablator (CMA) program which was used to calculate the temperature dependent thermal conductivity. This method produced excellent agreement between the experimental and predicted temperature profiles since the thermal conductivity was varied to force the curve through the experimental data. The results of one of these tests are presented in Figure 18.

More common and less expensive techniques have been developed by researchers whose primary concern has been the pyrolysis of wood and cellulosic materials. These methods have been designed for much lower heating rates and thus create boundary conditions which are easier to quantify.

Bamford et al. [1] heated both 2 and 4-cm thick sheets of deal wood by gas flames from batswing burners. The flames were large enough to cover the entire face of the samples. The results of these measurements are shown in Figures 1 and 2. It is interesting to note

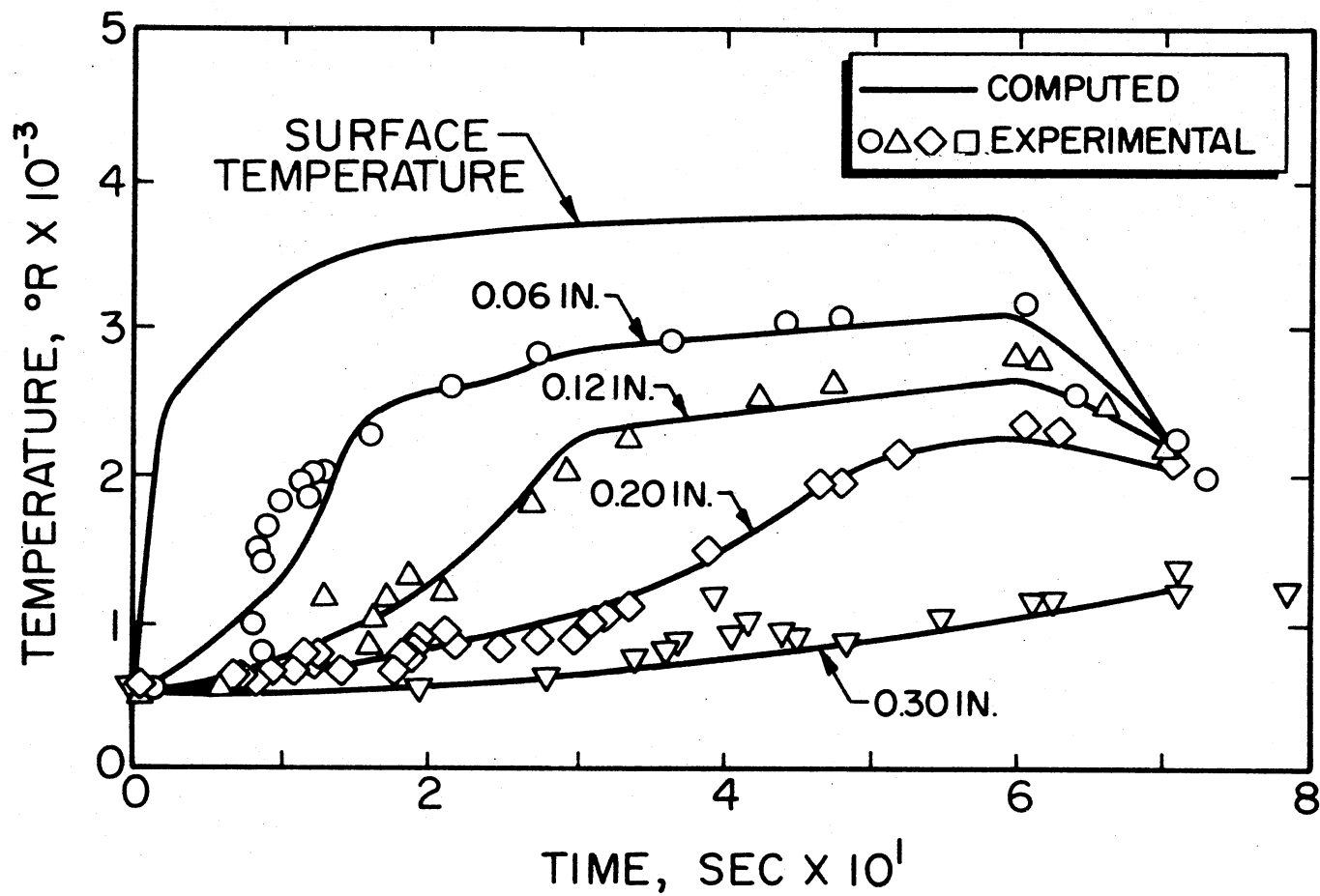


Figure 18. Comparison Between Calculated and Predicted In-Depth Temperature Profiles [35]

that the temperature rise is nearly linear to approximately 550°K. Then a slight endothermic depression occurs prior to the sharp temperature rise resulting from the exothermic reaction near 600°K. This phenomenon has been observed by other researchers.

Murty Kanury [36] presented experimental temperature profiles for the interior of cellulose cylinders burning in free convection. The results are presented in Figure 19. Again the depressed temperature profiles are evident near 100°C and 300°C, just prior to a large exothermic reaction. Murty Kanury suggests that the 100°C depression is due to moisture diffusion, condensation and re-evaporation, as a result of volatile products diffusing into the cooler interior of the material. As they diffuse, they carry energy from the high temperature outer char layer and condense in the cooler region, thus preheating the virgin material. As time progresses, conduction overtakes the preheated zone and re-evaporates the condensed volatiles. The recondensation of the volatiles corresponds to the temperature depressions in Figure 19.

Havens [12] heated cylindrical samples of white pine and oak in a nitrogen atmosphere using a resistance wire heater located at the center of the specimen. Heat fluxes of 0.34 cal/cm²-sec were applied to the samples. Temperature profiles were measured by 36-gauge chromel-alumel thermocouples and the energy input was determined by

$$p = I^2R \quad (46)$$

where p = power per cm of wire length (watts/cm)

I = current (amps)

R = resistance (ohms/cm).

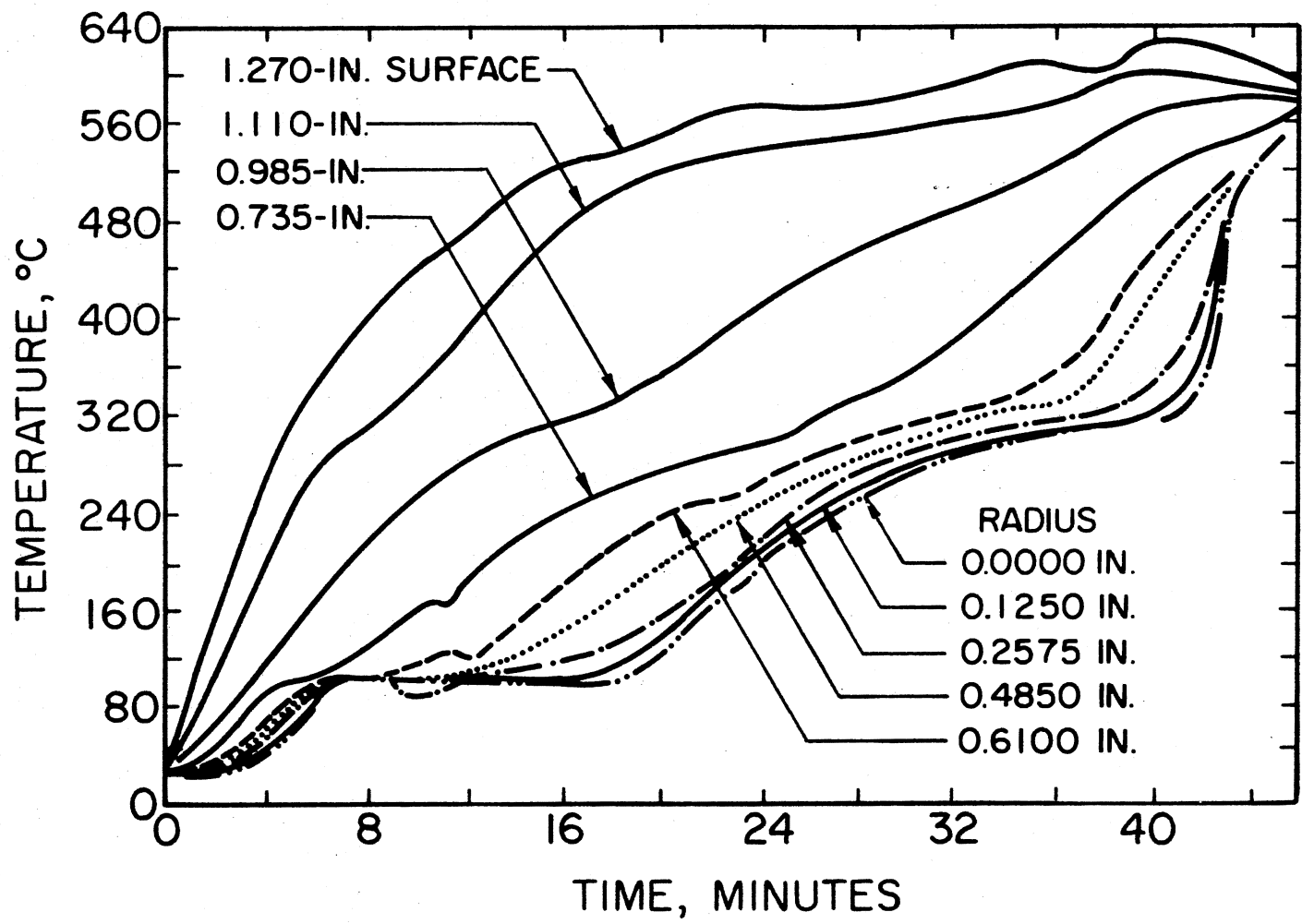


Figure 19. Time-Temperature Profiles at Various Radii of a Cellulose Cylinder Burning in Free Convection [36]

Brown [29] compared Havens' experimental data to computed values at four different radial positions in samples of white pine. The results are shown in Figure 20. The 100°C temperature depressions are not evident in Havens' data. This is thought to be due primarily to the fact that the samples were preheated for 24 hours at 110°C, thus removing all traces of water. Havens' experimental technique is extremely attractive because it provides well defined boundary conditions.

Wiebelt and Henderson [37] measured the temperature profiles and pyrolysis rates in 0.145-cm sheets of α -cellulose using two 1000-watt tungsten filament lamps as a heat source. Samples were heated in air from ambient through material decomposition. Heating rates were varied from 0.5 to 0.8 cal/cm²-sec.

Martin [38] used the same method to heat α -cellulose samples at much higher heating rates. Samples were irradiated at levels up to 22.0 cal/cm²-sec. Martin measured temperature profiles, surface temperatures, and rate of production of volatile pyrolysis products. This method is particularly attractive because of the wide range of irradiances and the radiant boundary conditions which are easily quantified.

Perhaps the most unique method of heating samples was reported by Ulrich [39]. He used 144 13.0-cm² solar mirrors to heat 20.0-cm² white pine samples. Lincoln [40] used a helical xenon flash tube which yielded up to 3000 cal/cm²-sec in 30-millisecond pulses.

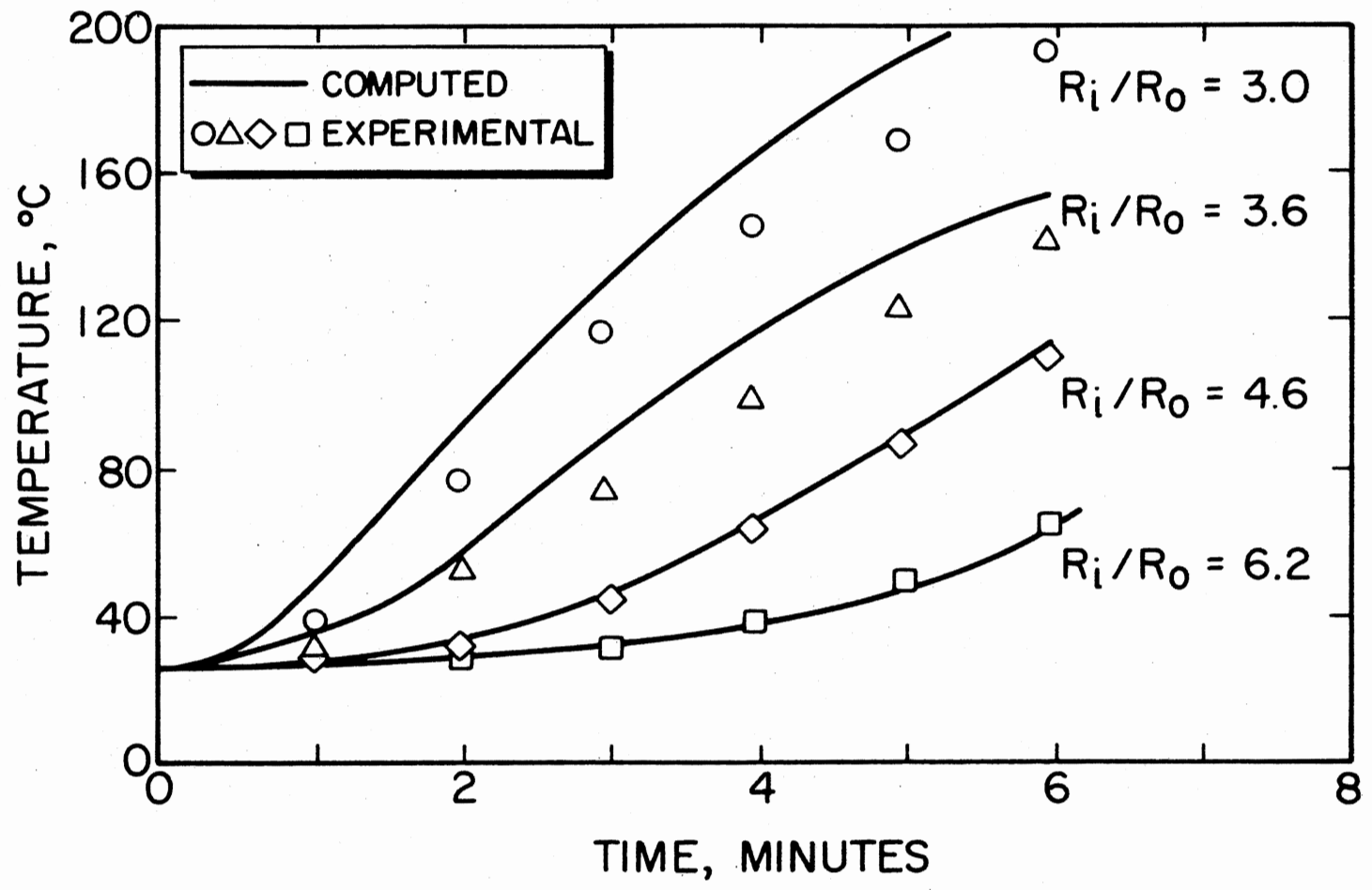


Figure 20. Comparison of Havens' Experimental and Brown's Computed Temperature Profiles for White Pine Cylinders [29]

CHAPTER III

THERMAL MODEL

The thermal model proposed by Kung [9] was the most complete of those found in the literature. The basic model is considered appropriate for this work because the following factors were considered in its formulation:

1. the variation in thermal properties during decomposition
2. flow of pyrolysis gases back through the char zone
3. variation in the heat of gasification with decomposition temperature and
4. local heat of gasification using active and char material properties.

The shortcomings of the model are that it does not account for the low temperature endothermic reactions in which no significant mass loss occurs, and no secondary reactions between the char and pyrolysis gases are considered.

Development

One can gain insight to the relevance of each term in the proposed model if Equation (10) is rearranged. An expanded version of Equation (10) is presented as Equation (47).

$$\frac{\partial}{\partial t} (\rho_a h_a + \rho_r h_r) = k \frac{\partial^2 T}{\partial x^2} + \frac{\partial k}{\partial x} \frac{\partial T}{\partial x} + h_g \frac{\partial \dot{m}_g}{\partial x} + \dot{m}_g \frac{\partial h_g}{\partial x} + Q_p \frac{\partial \rho}{\partial t} \quad (47)$$

The energy storage term on the left side of Equation (47) may be rewritten as:

$$\frac{\partial}{\partial t} (\rho_a h_a + \rho_c h_c + \rho_g h_g)$$

where $\rho_r h_r = \rho_c h_c + \rho_g h_g$
 ρ_c = density of the char material (gm/cm³)
 h_c = enthalpy of the char material (cal/gm)

In general $\rho_g h_g \ll \rho_c h_c + \rho_a h_a$ and the accumulation of energy of the gaseous species can be neglected. Therefore Equation (47) can be rewritten as:

$$\frac{\partial}{\partial t} (\rho_a h_a + \rho_c h_c) = k \frac{\partial^2 T}{\partial x^2} + \frac{\partial k}{\partial x} \frac{\partial T}{\partial x} + h_g \frac{\partial \dot{m}_g}{\partial x} + \dot{m}_g \frac{\partial h_g}{\partial x} + Q \frac{\partial \rho}{\partial t} \quad (48)$$

Expanding the left side of Equation (48) results in:

$$\frac{\partial}{\partial t} (\rho_a h_a + \rho_c h_c) = h_a \frac{\partial \rho_a}{\partial t} + \rho_a \frac{\partial h_a}{\partial t} + h_c \frac{\partial \rho_c}{\partial t} + \rho_c \frac{\partial h_c}{\partial t} \quad (49)$$

Differentiation of Equation (11) results in Equations (50) and (51) for the active and char material, respectively.

$$\frac{\partial h_a}{\partial t} = C_{pa} \frac{\partial T}{\partial t} \quad (50)$$

$$\frac{\partial h_c}{\partial t} = C_{pc} \frac{\partial T}{\partial t} \quad (51)$$

Substituting Equations (50) and (51) into Equation (49) yields:

$$\frac{\partial}{\partial t} (\rho_a h_a + \rho_c h_c) = \rho C_p \frac{\partial T}{\partial t} + h_a \frac{\partial \rho_a}{\partial t} + h_c \frac{\partial \rho_c}{\partial t} \quad (52)$$

where $\rho C_p = \rho_c C_{pc} + \rho_a C_{pa} \approx \rho_r C_{pr} + \rho_a C_{pa}$.

Substitution of Equations (9) and (52) into Equation (48) and rearranging results in:

$$\begin{aligned} \rho C_p \frac{\partial T}{\partial t} = & k \frac{\partial^2 T}{\partial x^2} + \frac{\partial k}{\partial x} \frac{\partial T}{\partial x} + \dot{m}_g \frac{\partial h_g}{\partial x} + \frac{\partial \rho}{\partial t} (h_g + Q_p) \\ & - h_a \frac{\partial \rho_a}{\partial t} - h_c \frac{\partial \rho_c}{\partial t} \end{aligned} \quad (53)$$

Differentiation of Equation (13) yields:

$$\frac{\partial \rho_a}{\partial \rho} = \frac{\rho_0}{\rho_0 - \rho_f} \quad (54)$$

Combining Equations (13) and (14) and differentiating results in:

$$\frac{\partial \rho_c}{\partial \rho} = - \frac{\rho_f}{\rho_0 - \rho_f} \quad (55)$$

where $\rho_c \approx \rho_r$.

Substituting Equations (54) and (55) and the result of $\partial h_g / \partial x$ into Equation (53) gives:

$$\begin{aligned} \rho C_p \frac{\partial T}{\partial t} = & k \frac{\partial^2 T}{\partial x^2} + \frac{\partial k}{\partial x} \frac{\partial T}{\partial x} + \dot{m}_g C_{pg} \frac{\partial T}{\partial x} \\ & + \frac{\partial \rho}{\partial t} \left(h_g + Q_p - \frac{h_a \rho_0}{\rho_0 - \rho_f} + \frac{h_c \rho_f}{\rho_0 - \rho_f} \right). \end{aligned} \quad (56)$$

Equation (56) is the basic nonlinear partial differential equation which should predict the thermal response of a one-dimensional pyrolyz-

ing slab. The term on the left represents the rate of temperature increase due to the sensible energy added to an element in the solid. The first term on the right is the excess conductive flux into the element. The second term represents the effect of variable thermal conductivity on the conductive flux. The third term represents the energy attenuation as a result of gaseous volatiles flowing through the char structure. The local heat of vaporization of the element is given by the last term.

The third term in Equation (56) represents the convection resulting from the mass flux of volatiles flowing back through the char. This term opposes the conductive flux into an element and attenuates the energy reaching the virgin zone. Local temperature equilibrium between char and gas was assumed.

The last set of terms in Equation (56),

$$L(T) = h_g + Q_p + \frac{h_c \rho_f}{\rho_0 - \rho_f} - \frac{h_a \rho_0}{\rho_0 - \rho_f}, \quad (57)$$

is the energy per unit mass of generated volatiles of an element at temperature T . The rate of change of the char material with respect to the total density change, that is, the mass of char produced per unit mass of generated volatiles is $\rho_f / \rho_0 - \rho_f$. The energy consumed per unit mass of generated volatiles is $h_c \rho_f / \rho_0 - \rho_f$. Similarly, $\rho_0 / \rho_0 - \rho_f$ represents the mass of active material consumed per unit mass of total material consumed and $h_a \rho_0 / \rho_0 - \rho_f$ is the energy released as a result of this consumption. The energy consumed as a result of the production of the volatiles is represented by h_g . Finally, Q_p represents the basic energy supplied to the element.

Equation (57) is extremely sensitive to the enthalpy of the char and active material components. $L(T)$ may increase or decrease with temperature, depending upon the temperature dependence of the specific heats. Therefore, accurate values of these quantities are required.

The first order kinetic rate equation used by Kung does not adequately represent the rate of decomposition of a composite material. As a result, a form similar to that proposed by Friedman was chosen and is presented as Equation (58).

$$\frac{\partial \rho}{\partial t} = -A\rho_0 \left(\frac{\rho - \rho_f}{\rho_0} \right)^n e^{-E/RT} \quad (58)$$

Equation (58) results in a closer approximation of the actual decomposition, primarily as a result of the addition of the order of reaction, n . This is discussed more thoroughly in Chapter IV.

The mass flux varies with depth as a function of the rate of gas generation at each spatial location. The magnitude of the flux may be obtained by integrating Equation (9) which yields:

$$\dot{m}_g(x,t) = \int_{\ell}^x \frac{\partial \rho(x,t)}{\partial t} dx. \quad (59)$$

Accumulation of gases due to internal pressures is ignored.

Equations (56), (58), and (59) form a set of nonlinear partial differential equations and must be solved numerically. The appropriate boundary conditions are:

$$T = T_{\infty}, \rho = \rho_0, \dot{m}_g = 0, \text{ at } t = 0, 0 \leq x \leq \ell \quad (60)$$

$$\alpha_s q_0 - \epsilon_s \sigma T_s^4 - k \frac{\partial T}{\partial x} - \dot{m}_g C_{pg} dT + \frac{L(T)\Delta x}{2} \frac{\partial p}{\partial t} = \frac{\rho C_p \Delta x}{2} \frac{\partial T}{\partial t}, \quad (61)$$

$$\text{at } t > 0, x = 0$$

$$\frac{\partial T}{\partial x} = 0, \dot{m}_g = 0, \text{ at } t > 0, x = l. \quad (62)$$

Method of Solution

The set of nonlinear partial differential equations (PDE's) presented as Equations (56), (58), and (59) were solved by finite difference techniques. Both implicit and explicit computer programs were developed.

The Crank-Nicolson method was used to solve the PDE's implicitly. For the case of a linear PDE the implicit technique is stable for any size time step. Nonlinear PDE's, however, require iteration at each interval of time. If the time step chosen is too large, instabilities will result. Although limited by the nonlinearities, the time interval required for the implicit technique is larger than the explicit method. However, the iterations required at each time interval with the implicit technique offset any savings in computer time. For this reason, the explicit form of the equations and computer program will be presented.

The numerical technique is presented using the notation T_i^j , where i represents the spatial node and j represents the time node or interval. Time derivative terms are represented by forward difference and the spatial variables by central difference, with the exception of the mass flux term which is represented by backward difference.

Using this notation, each term in Equation (56) can be represented as follows:

$$\frac{\partial T}{\partial t} = \frac{T_i^{j+1} - T_i^j}{\Delta t} \quad (63)$$

$$\frac{\partial^2 T}{\partial x^2} = \frac{T_{i+1}^j - 2T_i^j + T_{i-1}^j}{\Delta x^2} \quad (64)$$

$$\frac{\partial k}{\partial x} \frac{\partial T}{\partial x} = \frac{k_{i+1}^j - k_{i-1}^j}{2\Delta x} \frac{T_{i+1}^j - T_{i-1}^j}{2\Delta x} \quad (65)$$

$$\frac{\partial T}{\partial x} = \frac{T_i^j - T_{i-1}^j}{\Delta x} \quad (66)$$

$$\frac{\partial \rho}{\partial t} = \frac{\rho_i^{j+1} - \rho_i^j}{\Delta t} \quad (67)$$

Substitution of Equations (63) through (67) into Equation (56) results

in:

$$\begin{aligned} \frac{T_i^{j+1} - T_i^j}{\Delta t} &= \frac{k}{\rho C_p} \left(\frac{T_{i+1}^j - 2T_i^j + T_{i-1}^j}{\Delta x^2} \right) \\ &+ \frac{1}{\rho C_p} \left(\frac{k_{i+1}^j - k_{i-1}^j}{2\Delta x} \right) \left(\frac{T_{i+1}^j - T_{i-1}^j}{2\Delta x} \right) \\ &+ \frac{\dot{m}_g C_{pg}}{\rho C_p} \left(\frac{T_i^j - T_{i-1}^j}{\Delta x} \right) \\ &+ \frac{1}{\rho C_p} \left(\frac{\rho_i^{j+1} - \rho_i^j}{\Delta t} \right) \left(Q_p + h_g + \frac{h_c \rho_f}{\rho_0 - \rho_f} - \frac{h_a \rho_0}{\rho_0 - \rho_f} \right). \quad (68) \end{aligned}$$

Equation (58) can be represented by:

$$\frac{\rho_i^{j+1} - \rho_i^j}{\Delta t} = -A\rho_0 \left(\frac{\rho_i^j - \rho_f}{\rho_0} \right)^n e^{-E/RT_i^j} \quad (69)$$

Equation (59) is approximated by:

$$\dot{m}_{(g)i}^{j+1} = \sum_{i=N}^1 \left(\frac{\rho_i^{j+1} - \rho_i^j}{\Delta t} \right) \Delta x_i \quad (70)$$

where N = number of spatial nodes.

Equations (68), (69), and (70) form a set of nonlinear algebraic equations in T , ρ , and \dot{m}_g . The solution is straightforward and progresses as follows:

1. calculate $\dot{m}_{(g)i}^{j+1}$ and ρ_i^{j+1} based on T_i^j
2. calculate T_i^{j+1} using values of $\dot{m}_{(g)i}^{j+1}$ and ρ_i^{j+1} from step 1 and
3. repeat steps 1 and 2 until maximum time is reached.

The numerical solutions of Equations (68) through (70), using the boundary and initial conditions presented as Equations (60) through (62) were carried out on a digital computer. A listing of the program is shown in Appendix A.

To ensure that the computer program was functioning properly, a set of sample calculations were performed for a 1.0-cm thick slab using Kung's data and boundary conditions. For the comparison run, the Fourier modulus was chosen as 0.1, with $\Delta x = 0.01$ cm. The net surface heat flux was 0.9 cal/cm²-sec. The properties used in the calculations are presented in Table VII. Also, Kung ignored the temperature dependence of the active and char components of the specific heat and thermal conductivity. Therefore, $C_{pa} = C_{p0}$, $C_{pc} = C_{pf}$, $k_a = k_0$, and $k_c = k_f$.

TABLE VII
 PROPERTIES USED IN SAMPLE CALCULATIONS

Pre-exponential factor	$A = 5.25 \times 10^7 \text{ sec}^{-1}$
Activation energy	$E = 30 \text{ kcal/mole}$
Ambient temperature	$T_{\infty} = 300^{\circ}\text{K}$
Thermal conductivity (virgin)	$k_0 = 3 \times 10^{-4} \text{ cal/cm-sec-}^{\circ}\text{C}$
Final thermal conductivity (char)	$k_f = 7.5 \times 10^{-5} \text{ cal/cm-sec-}^{\circ}\text{C}$
Specific heat (virgin)	$C_{p0} = 0.6 \text{ cal/gm-}^{\circ}\text{C}$
Final specific heat (char)	$C_{pf} = 0.6 \text{ cal/gm-}^{\circ}\text{C}$
Specific heat (volatiles)	$C_{pg} = 0.24 \text{ cal/gm-}^{\circ}\text{C}$
Density (virgin)	$\rho_0 = 0.5 \text{ gm/cm}^3$
Final density (char)	$\rho_f = 0.125 \text{ gm/cm}^3$
Heat of decomposition	$Q_p = 125 \text{ cal/gm}$

Figure 21 depicts the temperatures and active material densities as a function of depth. The symbols represent the values calculated in the present work, while the lines represent Kung's computations. The calculated temperatures and densities agreed to within 15% in the worst case and were generally within 7%. These variations are thought to be due primarily to the difference in the boundary conditions and the method of calculating the mass flux of volatiles.

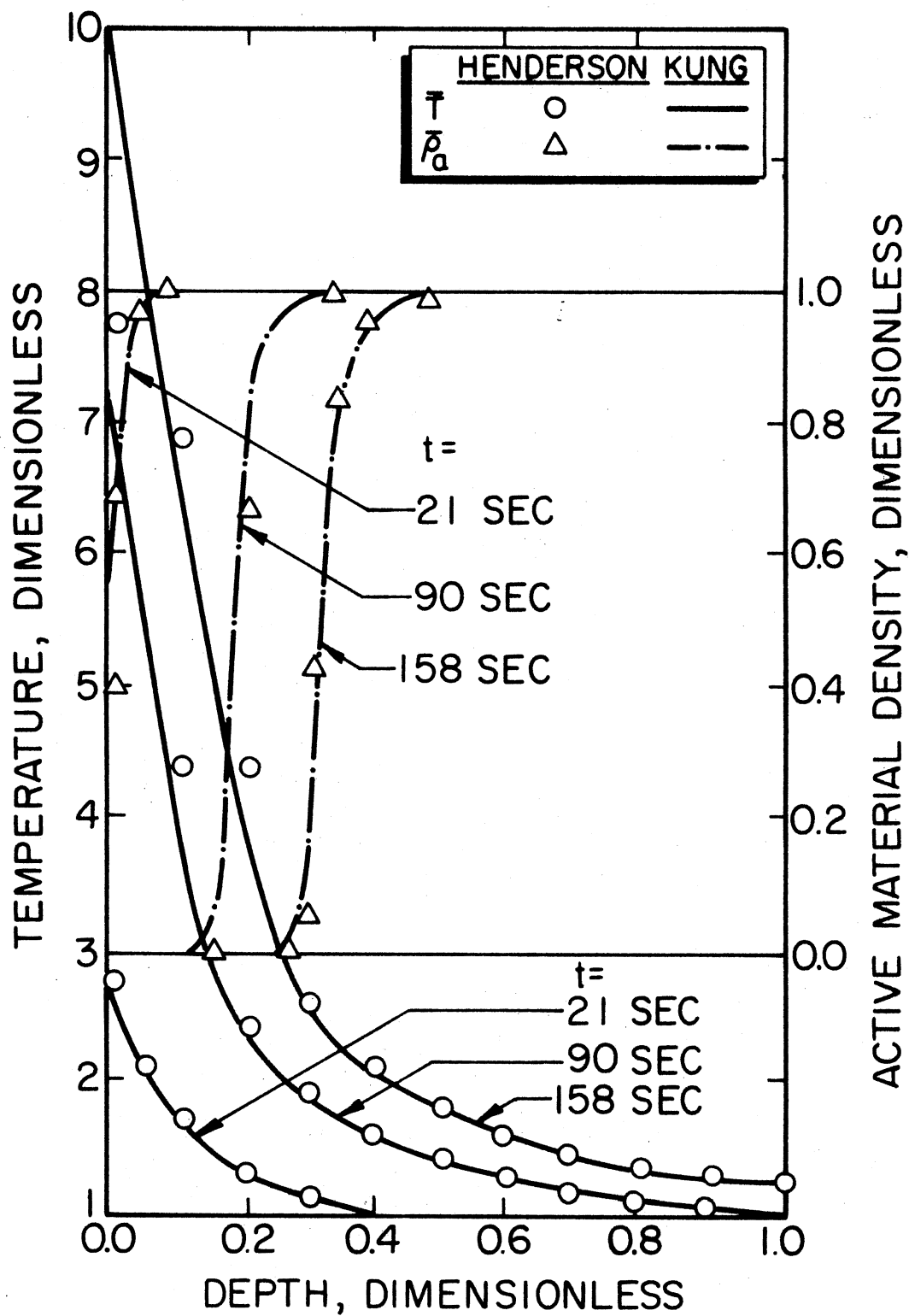


Figure 21. Comparison of the Results of Kung's and Henderson's Computations for a 1.0-Cm Thick Slab of Pyrolyzing Wood

CHAPTER IV

DETERMINATION OF KINETIC PARAMETERS

The thermal model is sensitive to the density, ρ , and the rate of decomposition, $\partial\rho/\partial t$, predicted by the kinetic rate equation. This is due to three factors; (1) the contribution of the heat of gasification, $L(T)$, (2) the mass flux of the volatiles, and (3) the density dependent thermal properties of the char and active material components. The combination of these can completely change the character of the predicted thermal response of the material. It is therefore of paramount importance that the kinetic parameters used in the rate equation be determined as accurately as possible. Further, the materials of interest in this work may be exposed to a wide range of heat fluxes. Therefore, the effect of the heating rate on the kinetic parameters must be known as well.

Brown [29] showed that the kinetics of decomposition for wood are independent of heating rate up to $160^{\circ}\text{C}/\text{min}$. Therefore, the only effect of increasing the heating rate is to displace the weight loss curve to higher temperatures. As a result, kinetic parameters calculated based on lower heating rates are applicable to the higher values. Friedman's work [22] substantiated Brown's findings for phenolic ablative materials at much lower heating rates. In contrast, Baer et al. [20] showed that kinetic parameters of phenolic ablatives calculated from data taken at a single heating rate are not reliable when

used for high heating rates. Although the experimental technique used by Baer et al. is not well proven, their assessment is at least partially correct. There is an upper limit of heating rates in which the kinetics of decomposition are governed by the heat transfer rate to the sample. The limit is a function of the sample geometry and the thermal properties of the material. Regardless, it is advisable to calculate the kinetic parameters based on as wide a range of heating rates as possible. For this reason, the multiple heating rate technique was chosen for this study.

Experimental Method

Equipment

The data required for extraction of the kinetic parameters by the dynamic heating method are temperature, weight loss, and the rate of weight loss. These data were obtained with a Perkin-Elmer TGS-2 Thermogravimetric System, with temperature control provided by a Perkin-Elmer System 4 microprocessor. Figure 22 is a photograph of the instrument.

The TGS-2 system consists of an analyzer, balance control unit, heater control, first derivative computer, and System 4 controller. The sample pan, microbalance, and heater are housed in the TGS-2 analyzer unit. The electronic microbalance employs a platinum-nickel torque motor in a high gain servo system which amplifies the current required to balance the sample weight. The balance generates a continuous signal proportional to the sample weight during a test. The unit is capable of weighing samples ranging from 1.0×10^{-4} mg to 5.0 g, with an accuracy of 0.1 μ g at 2 mg. The 50.0 μ l sample pan is immersed in a

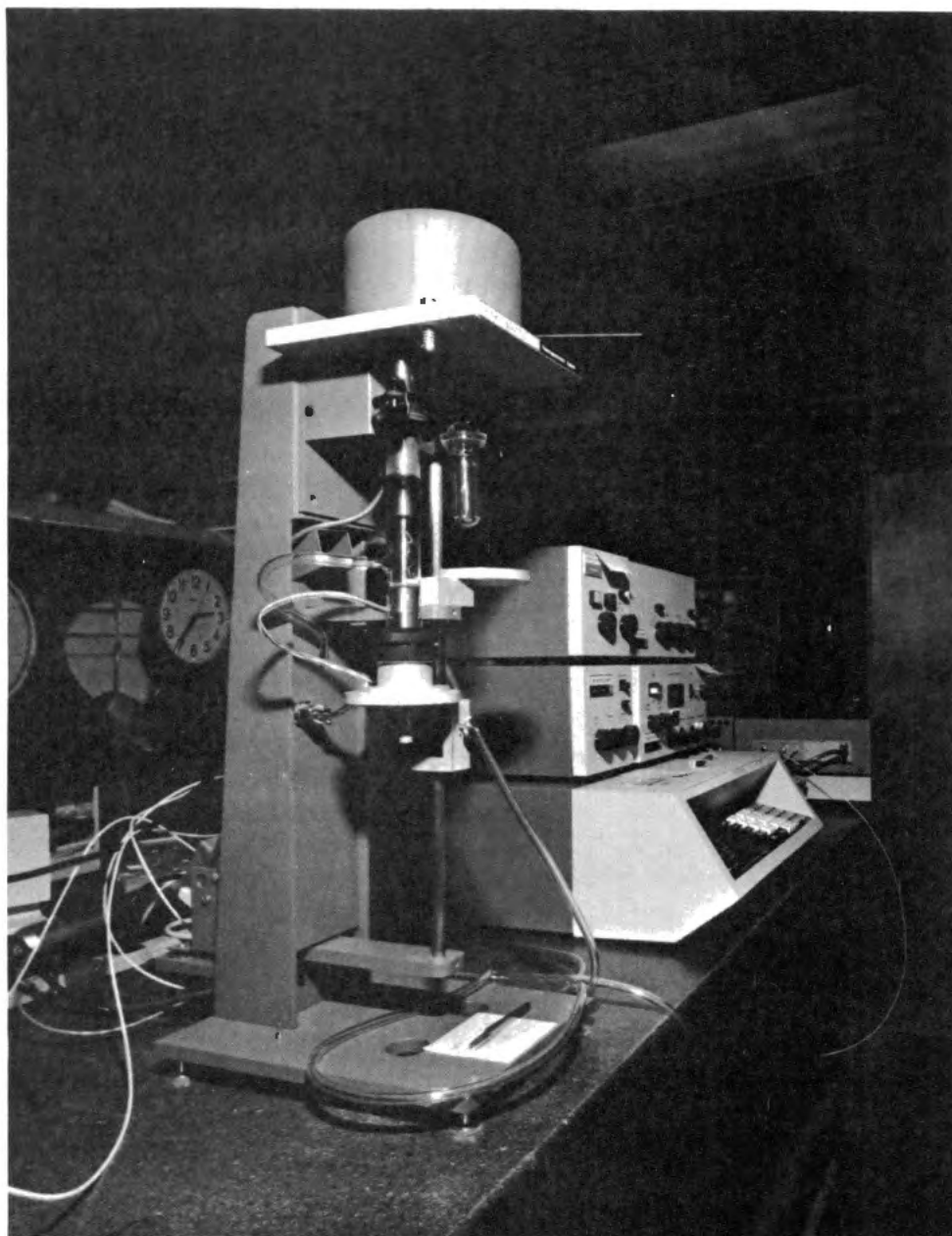


Figure 22. Perkin-Elmer TGS-2 Thermogravimetric System

platinum wound furnace which is capable of heating rates up to 160°C/min to a maximum temperature of 1000°C. Apparent sample temperatures are measured with a chromel-alumel thermocouple located inside the furnace, directly under the sample pan. These components are contained in a sealed unit which can be purged with one or more inert gases. A schematic of this arrangement is shown in Figure 23.

The System 4 microprocessor controls the temperature limits, heating rate, and gas switching valves. The controller can be programmed for a variety of tasks ranging from simple heat-cool mode to multiple heat-hold cycles. It also has a permanently programmed temperature calibration routine which matches the furnace temperature to the apparent sample temperature.

The output from the system is plotted as temperature, fraction weight remaining, and rate of weight loss on a Soltec Model VP-6432P x-y₁-y₂ plotter.

The TGS-2 system proved to be relatively trouble free with the exception of the furnace. Volatiles condensing on the furnace walls caused the platinum heater to fail. It was found that burning the condensates off after each run extended the furnace life. This was accomplished by switching to oxygen at the end of the programmed temperature scan.

Temperature Calibration

Due to the physical separation of the thermocouple and sample pan, the indicated and actual sample temperatures differ. This required calibration of the instrument. Norem, O'Neill, and Gray [41] developed a calibration method based on the use of ferromagnetic metals. The

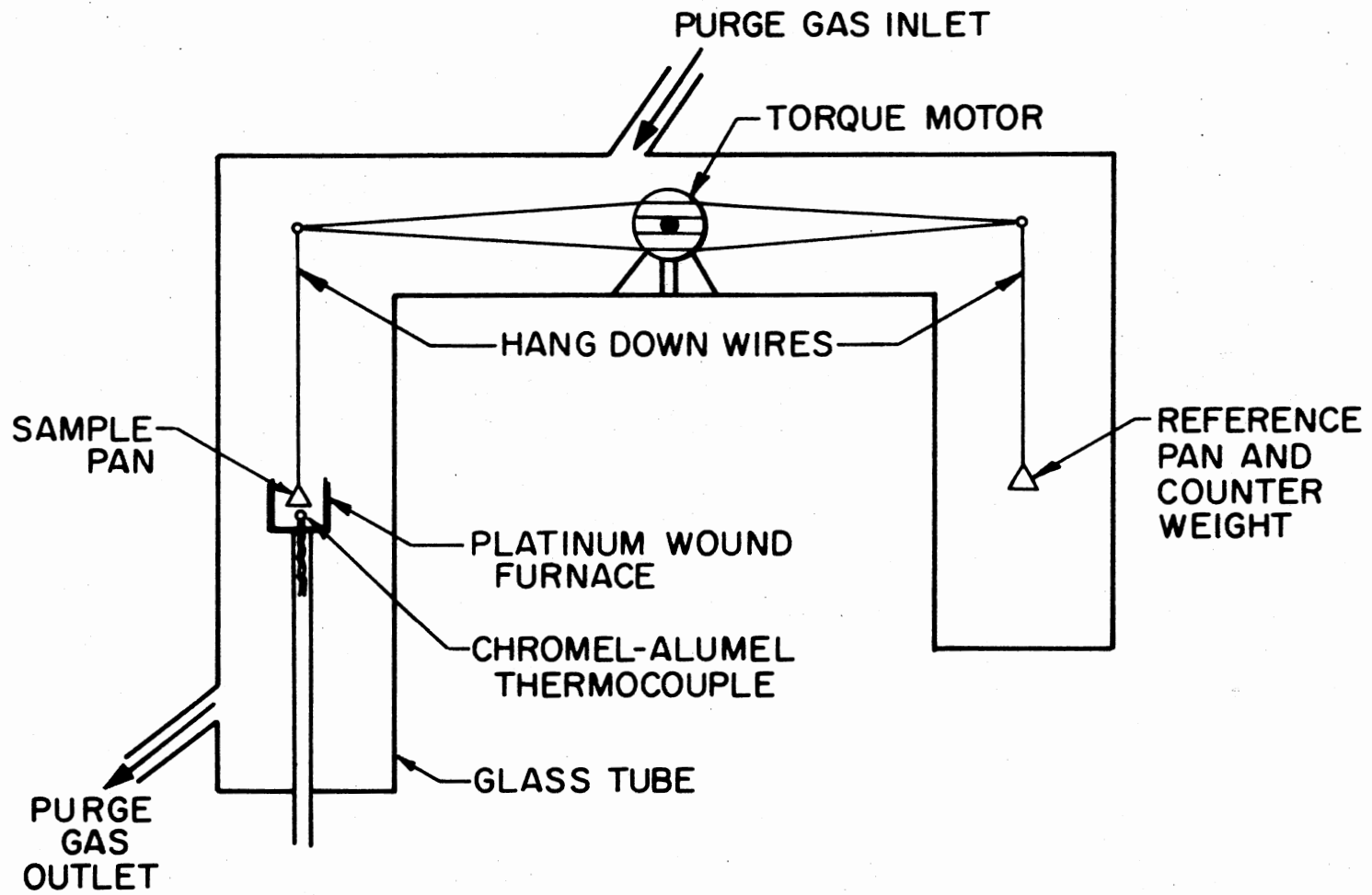


Figure 23. Schematic of TGS-2 Analyzer Unit

magnetic domains in these metals become disoriented over certain temperature ranges where the materials sharply transform to the paramagnetic state. This transformation occurs at a well defined temperature or Curie point where the apparent weight drops to zero. These materials and their Curie points are shown in Table VIII.

TABLE VIII
MAGNETIC STANDARDS USED FOR
TGS CALIBRATION

Standard	Curie Point (°C)
Alumel	163
Nickel	354
Perkalloy	596
Iron	780
Hisat 50	1000

The calibration procedure is simple. A small sample weight of each material is placed in the sample pan. A permanent magnet is placed around the furnace tube to create an apparent "magnetic mass". The furnace is then heated at the desired rate. As the Curie point of each material is reached, the sample undergoes an apparent weight loss. From these data, the difference between the indicated and actual temper-

atures may be determined. A typical calibration run at 80°C/min is shown in Figure 24. A plot of the temperature correction for this run is presented as Figure 25.

The calibration procedure was carried out each time the heating rate was changed and at the beginning of each day. If the temperature correction at any Curie point was more than $\pm 10^\circ\text{C}$, the limits on the temperature control unit were changed, the System 4 calibration routine was rerun, and the Curie standard calibration repeated. This was seldom necessary, except when new thermocouples were installed. Generally this required adjusting the location of the thermocouples in addition to the above procedure.

Sample Preparation and Procedure

Powdered samples were used in order to minimize errors resulting from heat transfer effects. The samples were obtained from cuttings while machining larger slabs for the temperature profile measurements. After the baked outer crust was machined off, the machine was cleaned and clear plastic sheets were placed under the sample. Cuttings were removed from the plastic, screened through a 20-mesh sieve, and stored in sealed glass containers. The day before testing, samples were placed in an open beaker and stored in a vacuum oven at 30°C for 12-24 hours. If the samples were not run within 24 hours after being placed in the oven, they were discarded. This procedure was adapted after observing "aging" of the samples left in the oven over a period of time. This aging significantly altered the decomposition characteristics of the materials.

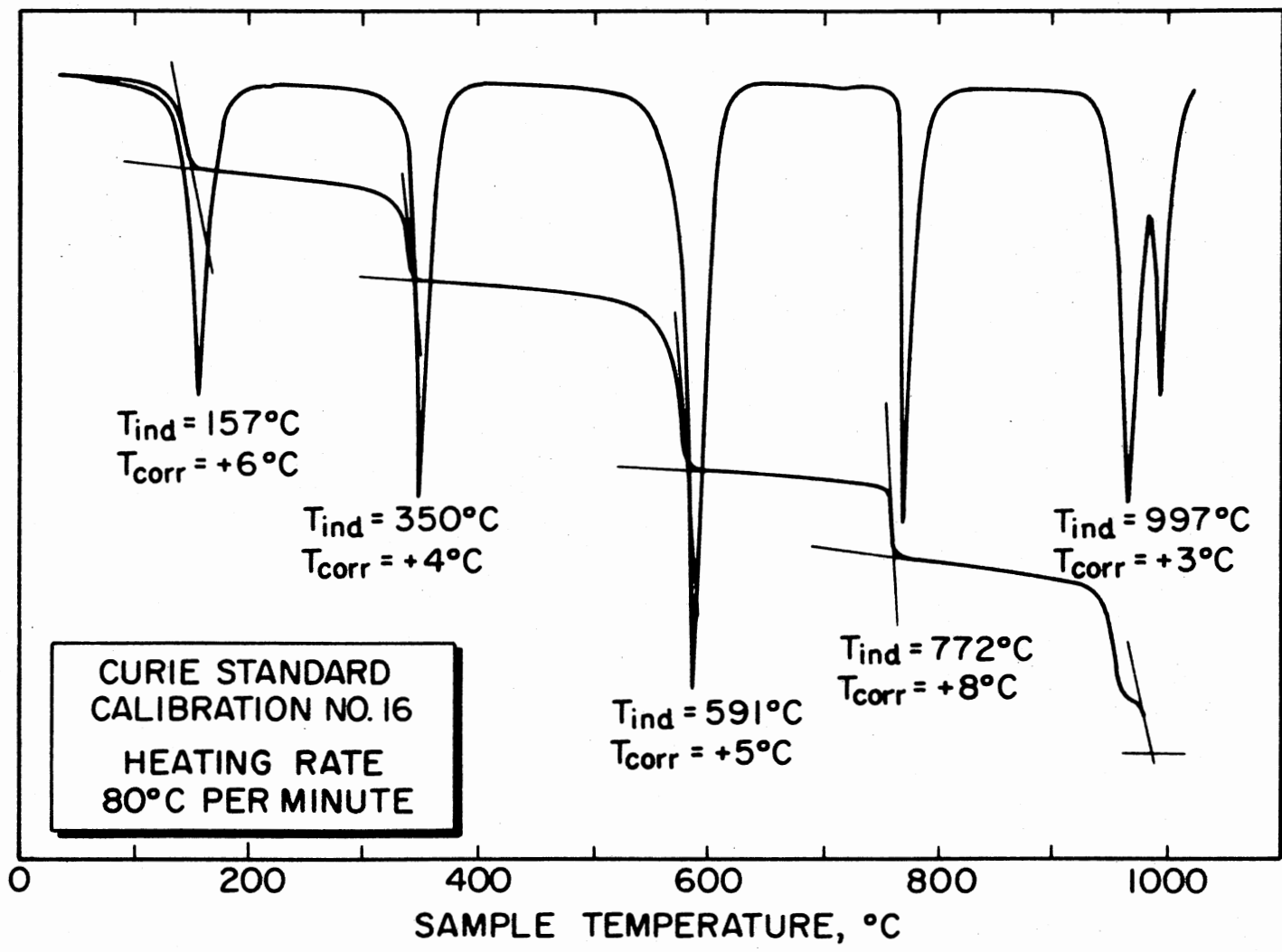


Figure 24. Magnetic Standard Temperature Calibration for TGS at 80°C/Min

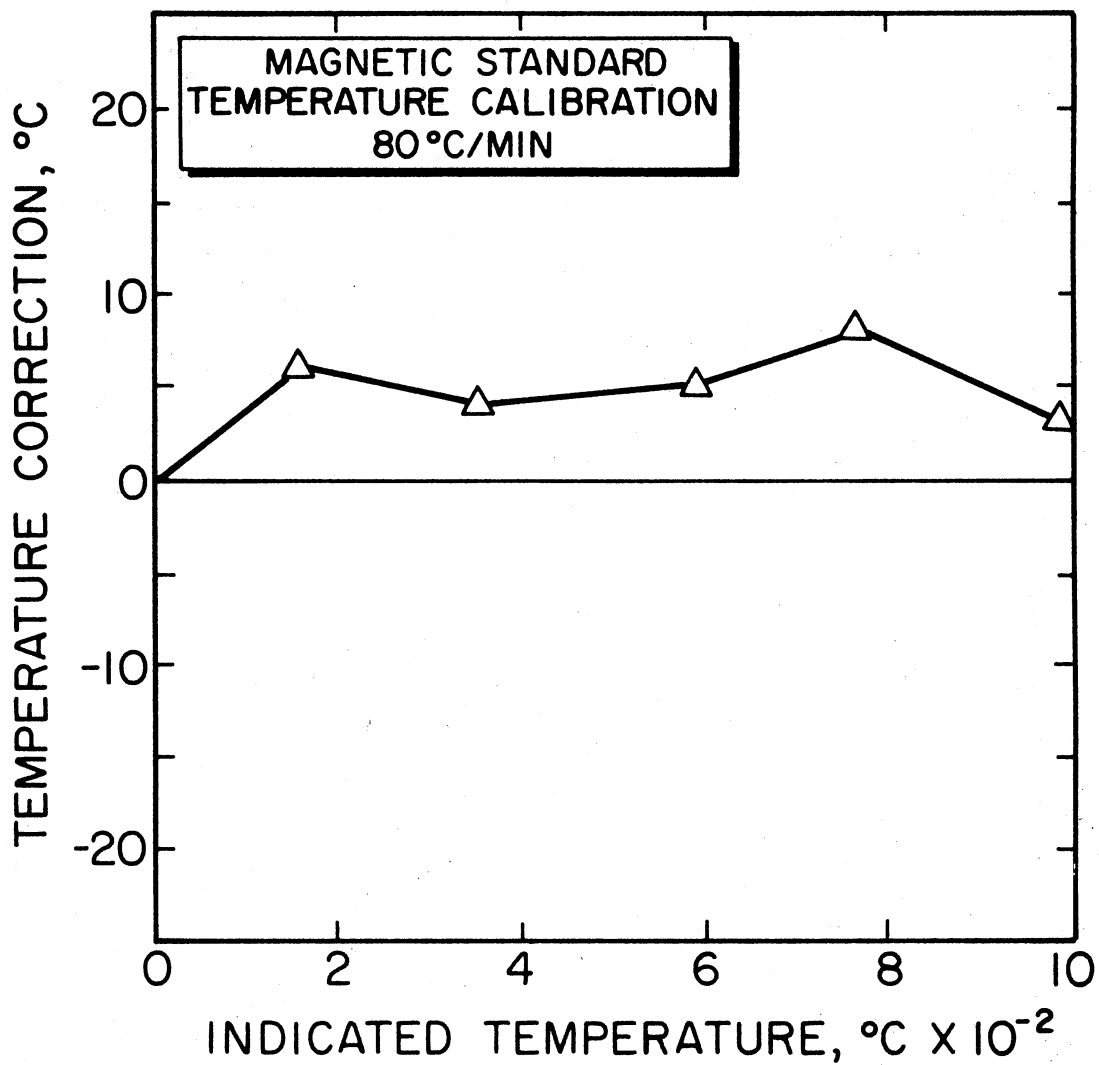


Figure 25. Magnetic Standard Temperature Correction for TGS at 80°C/Min

At the beginning of each day the balance was calibrated using the standard recommended techniques. Additionally, the recorder was checked using a Leeds and Northrup Model 8686 Millivolt Potentiometer. As discussed previously, the temperature calibration was checked at least once daily. After completion of the calibrations, powdered samples weighing 7.5 ± 0.5 mg were placed in the sample pan. The system was sealed, held at 40°C , and purged with nitrogen at 100 mL/min to remove all traces of air. This condition was maintained at least 10 minutes prior to initiating the run. The programmed temperature scan was then run at the desired heating rate to approximately 950°C . At the end of the programmed scan the temperature was held at 950°C and the purge gas was automatically switched to oxygen to oxidize the remaining resin. This condition was held until the resin had completely oxidized. If the ratio of initial to final weight, w_f/w_0 , varied more than $\pm 2\%$ for any of the six heating rates, the data were discarded and a new sample was run.

Experimental Results

Six types of ablative materials containing various amounts and types of fillers and resins were tested. A wide cross section of the low cost ablatives are represented by these selections. The materials and their compositions are shown in Table IX.

Thermogravimetric data for the six materials were obtained at heating rates of 10, 20, 40, 80, 100, and $160^{\circ}\text{C}/\text{min}$. The original thermograms contained temperature, fraction of weight loss, and derivative of weight loss. These data were digitized at 0.01 intervals of the fraction of weight remaining. The experimental temperatures were

TABLE IX
COMPOSITION OF MATERIALS TESTED

Contents	Material Composition (percent)					
	Haveg Ind. H41NE	Haveg Ind. H41D	Fiberite Corp. MXBE-350	Fiberite Corp. MXB-360	Fiber Materials, Inc. FR-1	Fiber Materials, Inc. FR-2
Asbestos	--	52.0	--	--	--	--
Glass Powder (SiO ₂)	--	--	15.5	14.5	--	--
Glass Fiber (SiO ₂)	61.0	--	--	--	42.0	--
Talc (Magnesium Silicate)	--	--	--	--	--	--
Fiberglass	--	--	41.0	59.0	--	--
Carbon	--	--	--	--	--	40.0
Total Filler Content	61.0	52.0	56.5	73.5	42.0	40.0
Phenol-Formaldehyde Resin	39.0	48.0	--	26.5	58.0	60.0
Acrylonitrile-Butadiene Resin	--	--	43.5	--	--	--

corrected using the Curie standard temperature calibration for each heating rate. For temperatures between the calibration points, a linear interpolation was used to obtain the correction factor. The thermograms were reproduced from the digitized data using Calcomp plotting routines on a CDC 6700 computer. Figures 26 through 31 show the fraction of weight remaining as a function of the corrected sample temperature for all six heating rates. Rate of weight loss data are depicted by Figures 32 through 37. The digitized data for all six materials are shown in Appendix B.

Method of Data Analysis

The method of Friedman was chosen to calculate the kinetic parameters. However, the technique was altered in order to cover a larger portion of the weight loss curve. As previously discussed, this was accomplished by calculating the pre-exponential factor and order of reaction for each of two regions of weight loss. For comparison, the average activation energy for each material determined by this method was compared to the value obtained by the method of Flynn and Wall.

From Equation (35) a plot of $\ln[(-1/w_0)(dw/dt)]$ as a function of $1/T$ yields a straight line for each value of weight loss. The slope of each line is $-E/R$ and the intercept is $\ln[Af(w/w_0)]$. These plots are shown in Figures 38 through 43 for all six materials. The slope of each line was determined by a least squares fit of the data. Figure 44 shows the corresponding activation energy and intercept at each value of weight loss from $0.84 \leq w/w_0 \leq 0.98$ for H41NE. Figure 45 presents the same information for MXBE-350 over the range from $0.73 \leq w/w_0 \leq 0.99$. The range of each data point in Figures 44 and 45 is the range of error

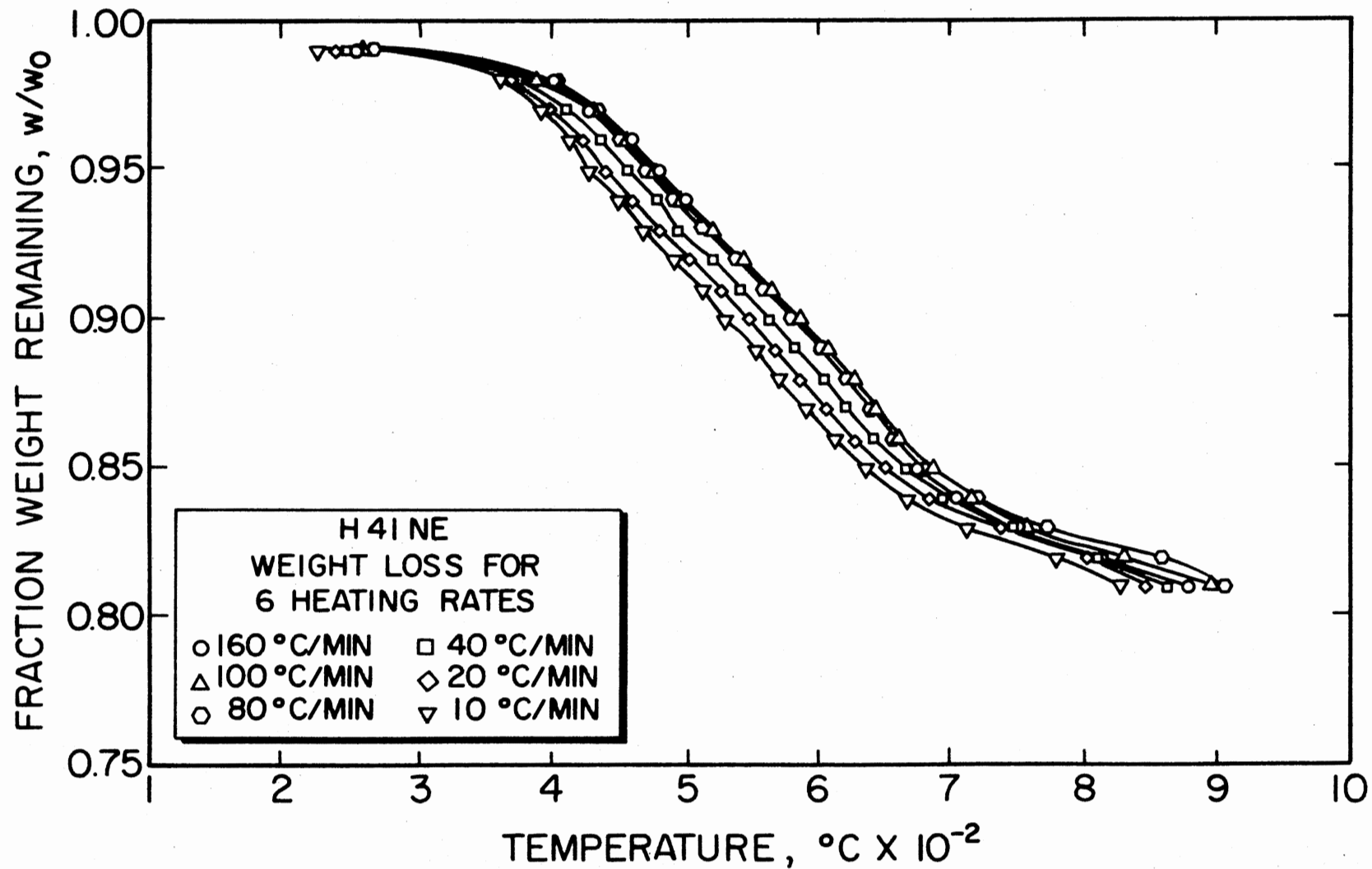


Figure 26. Fraction of Weight Remaining for Six Heating Rates for H41NE

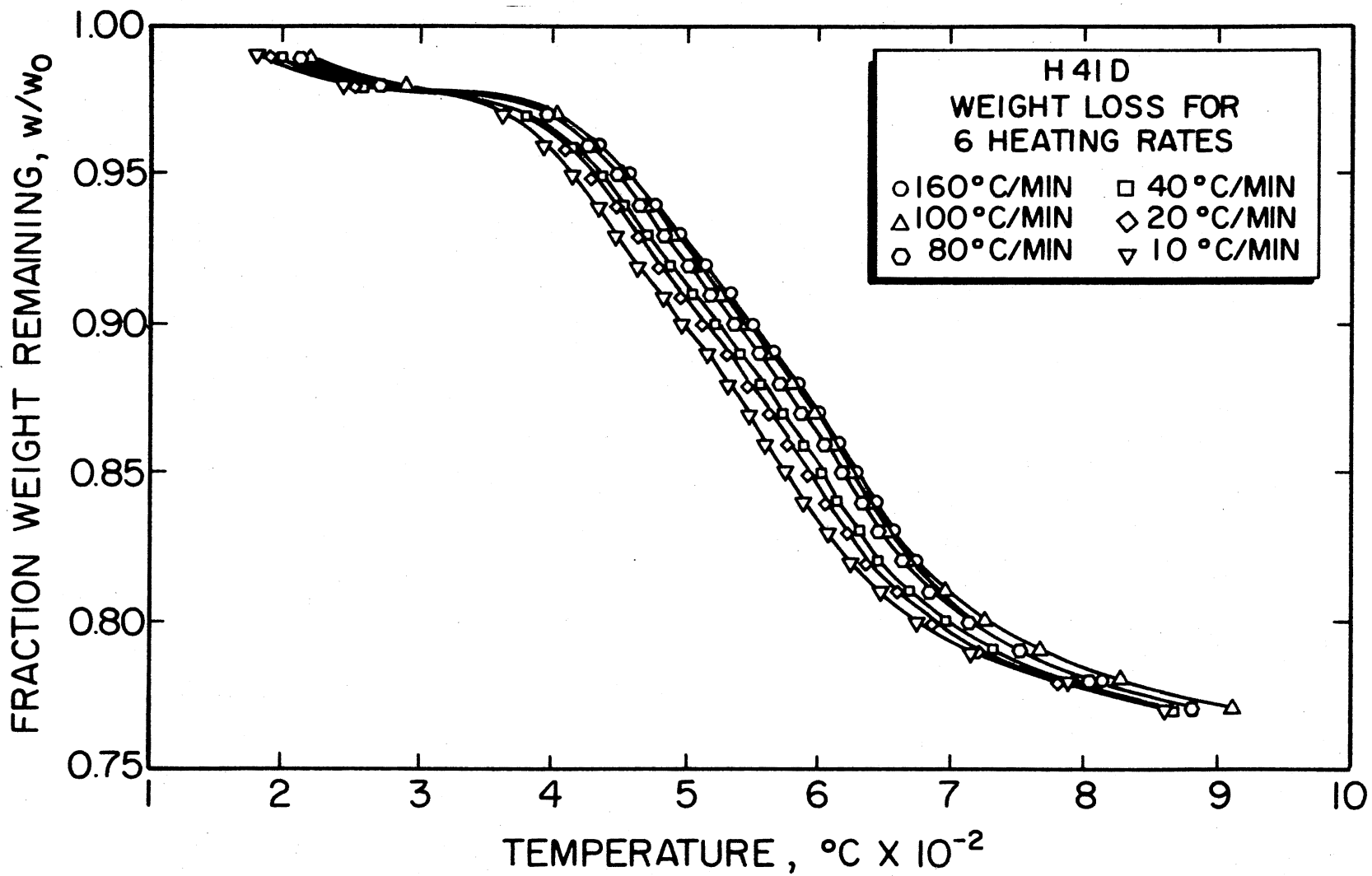


Figure 27. Fraction of Weight Remaining for Six Heating Rates for H41D

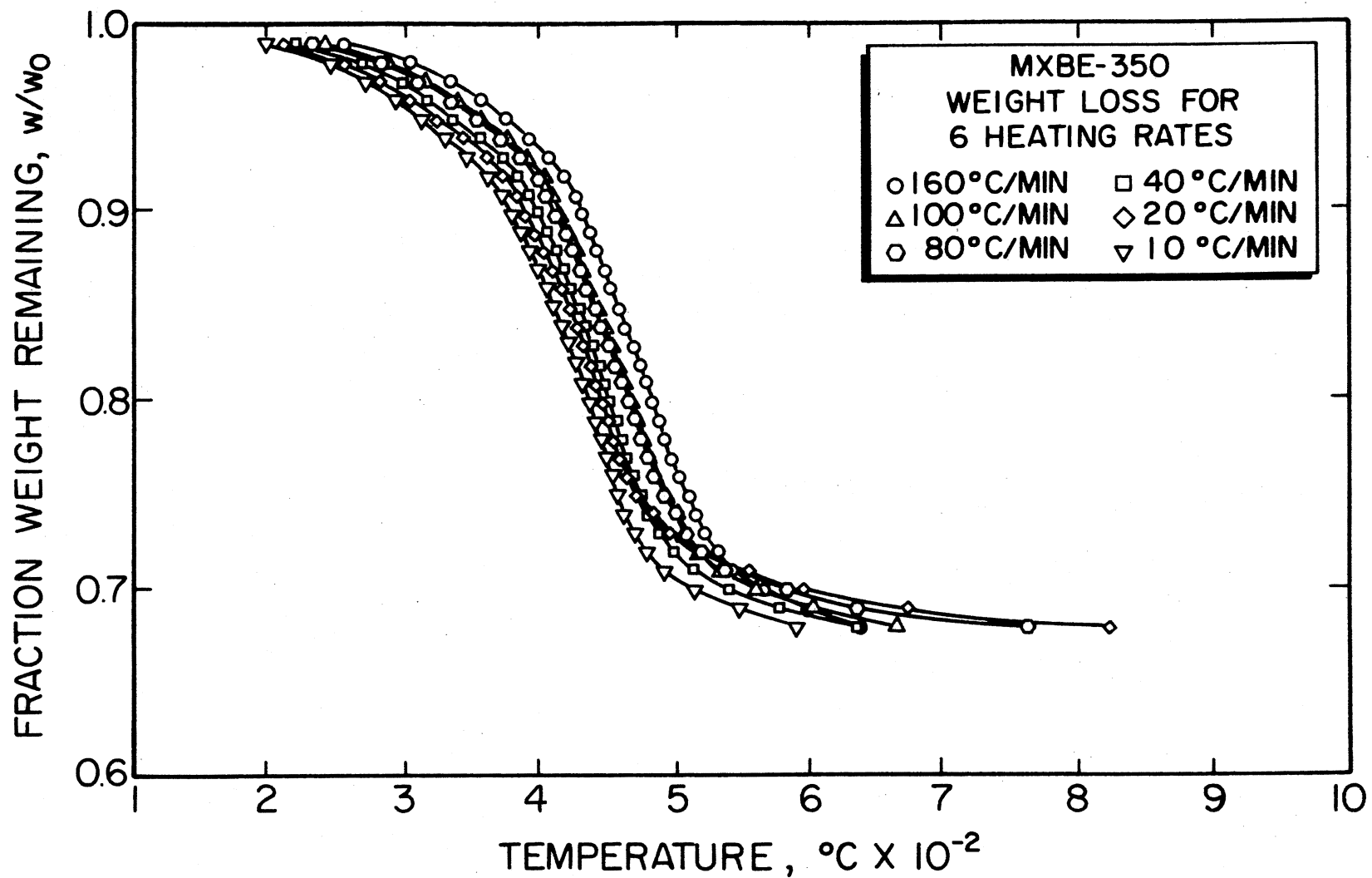


Figure 28. Fraction of Weight Remaining for Six Heating Rates for MXBE-350

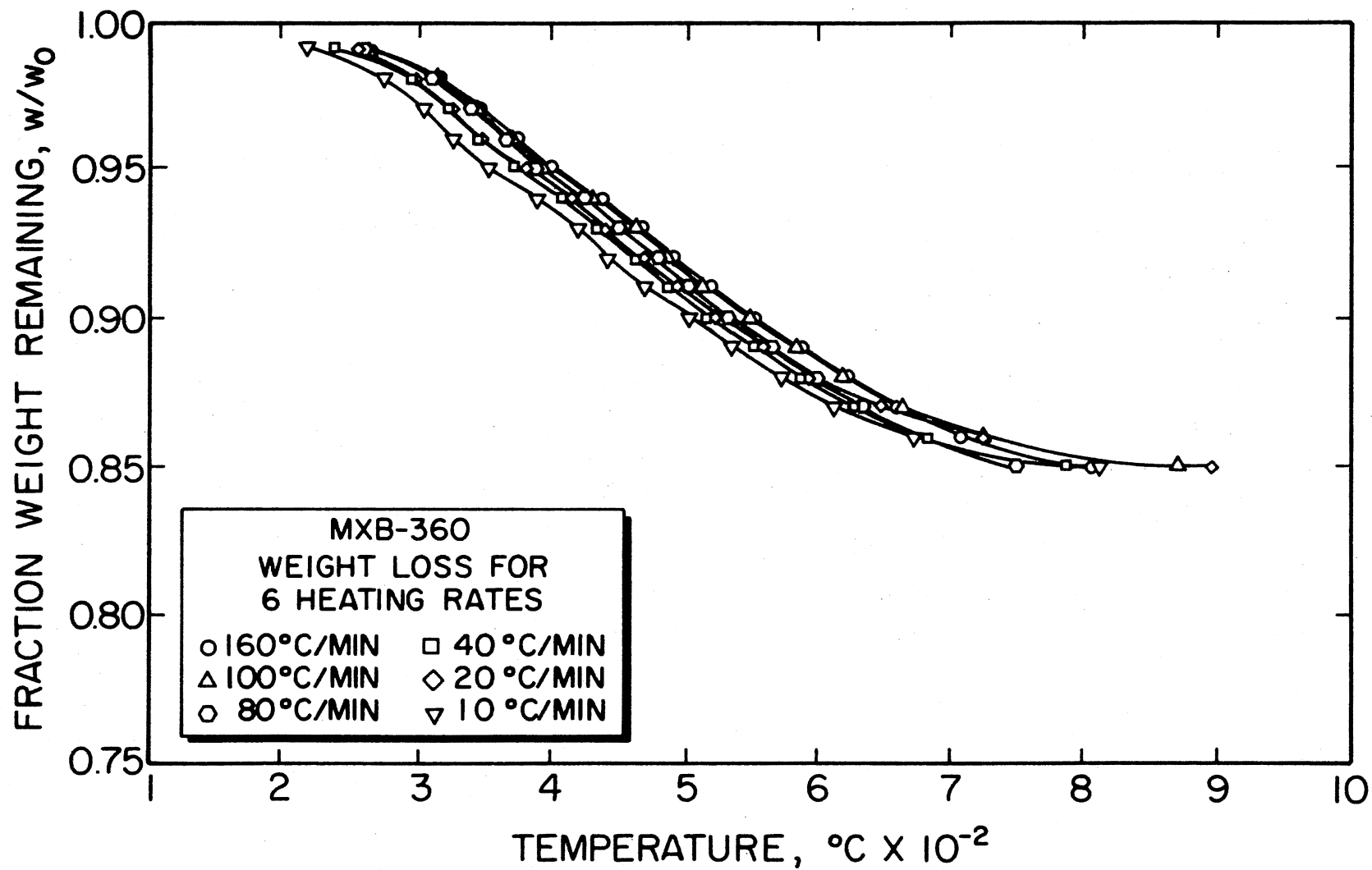


Figure 29. Fraction of Weight Remaining for Six Heating Rates for MXB-360

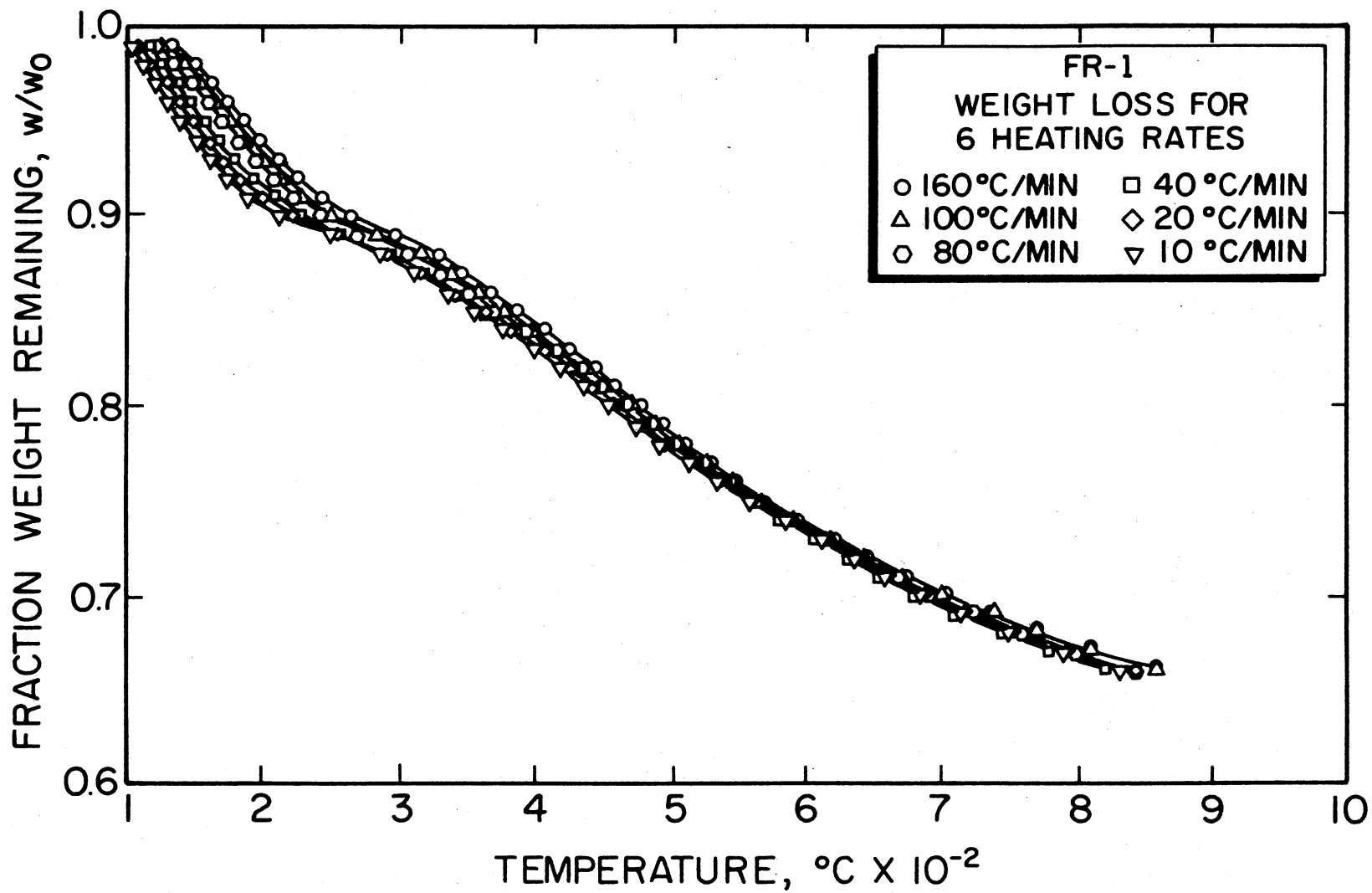


Figure 30. Fraction of Weight Remaining for Six Heating Rates for FR-1

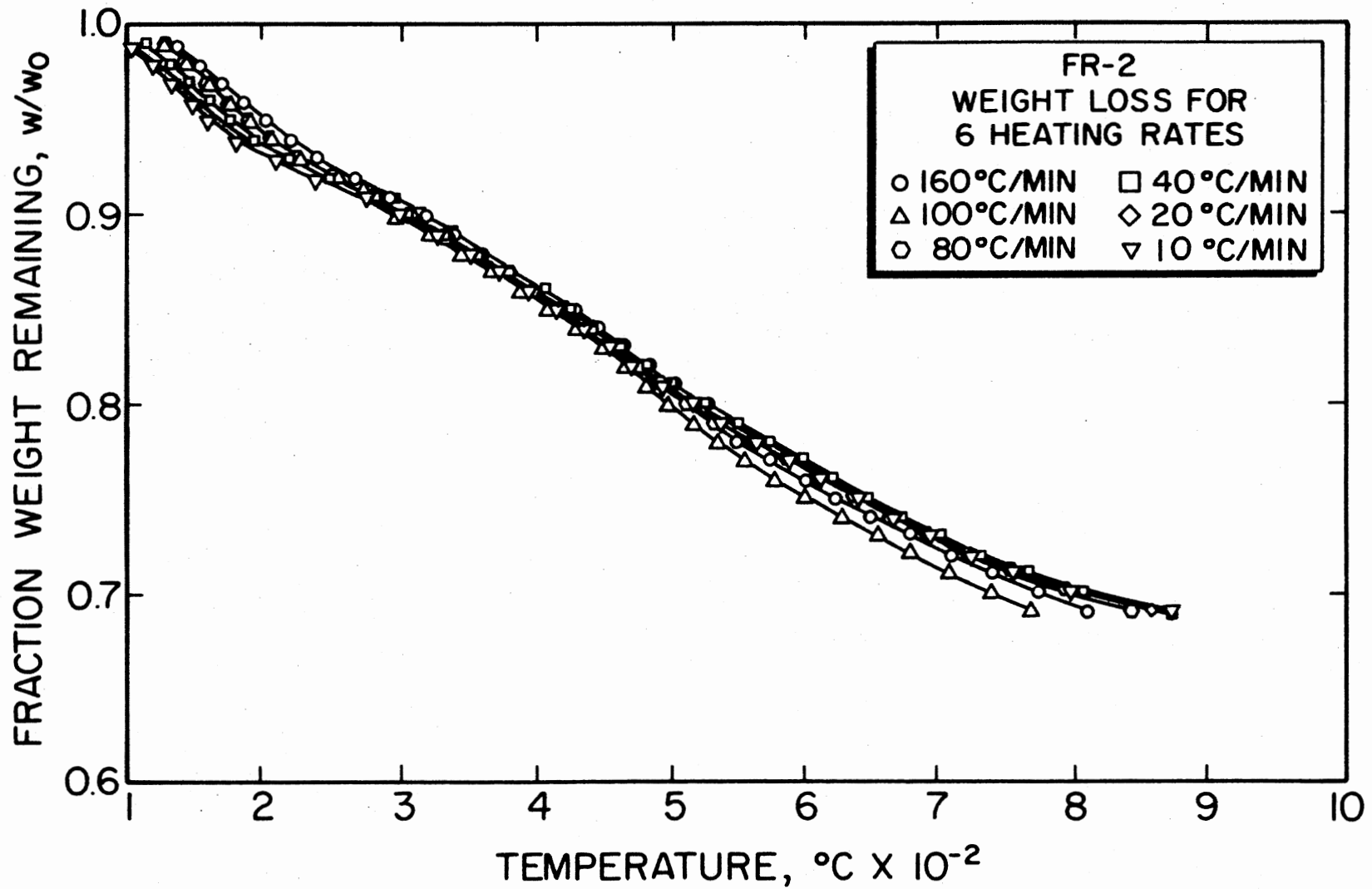


Figure 31. Fraction of Weight Remaining for Six Heating Rates for FR-2

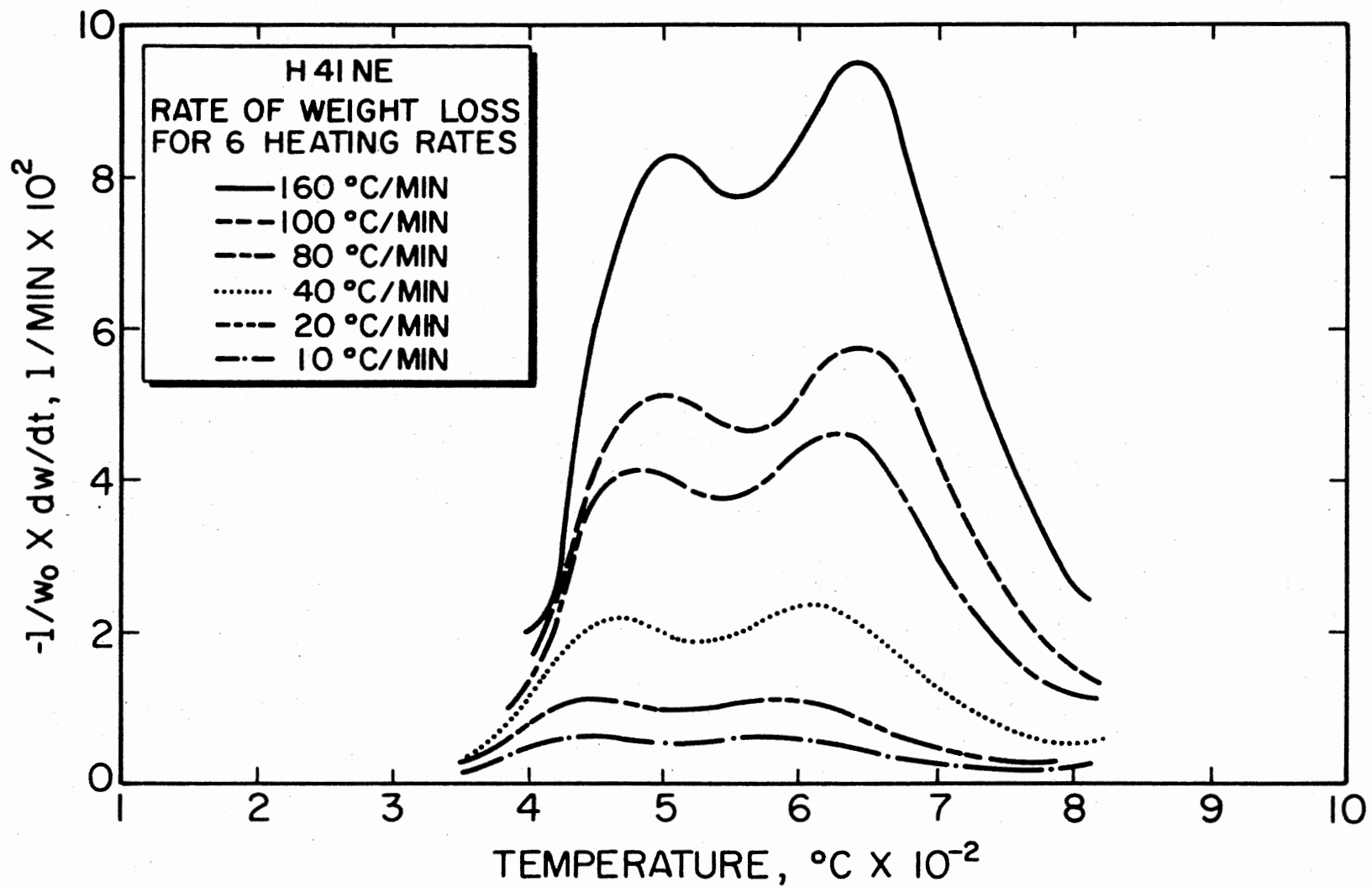


Figure 32. Derivatives of Weight Loss for Six Heating Rates for H41NE

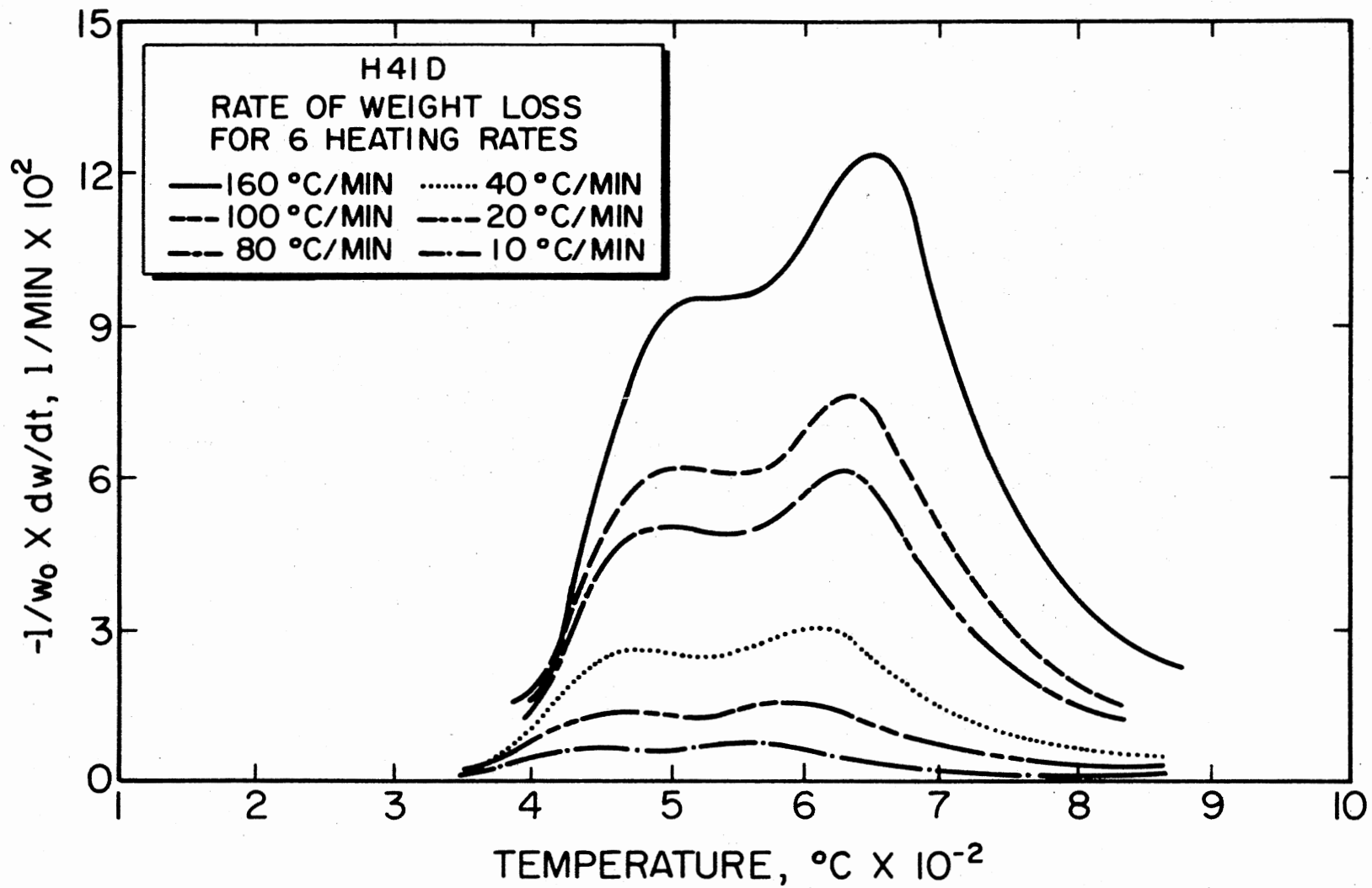


Figure 33. Derivatives of Weight Loss for Six Heating Rates for H41D

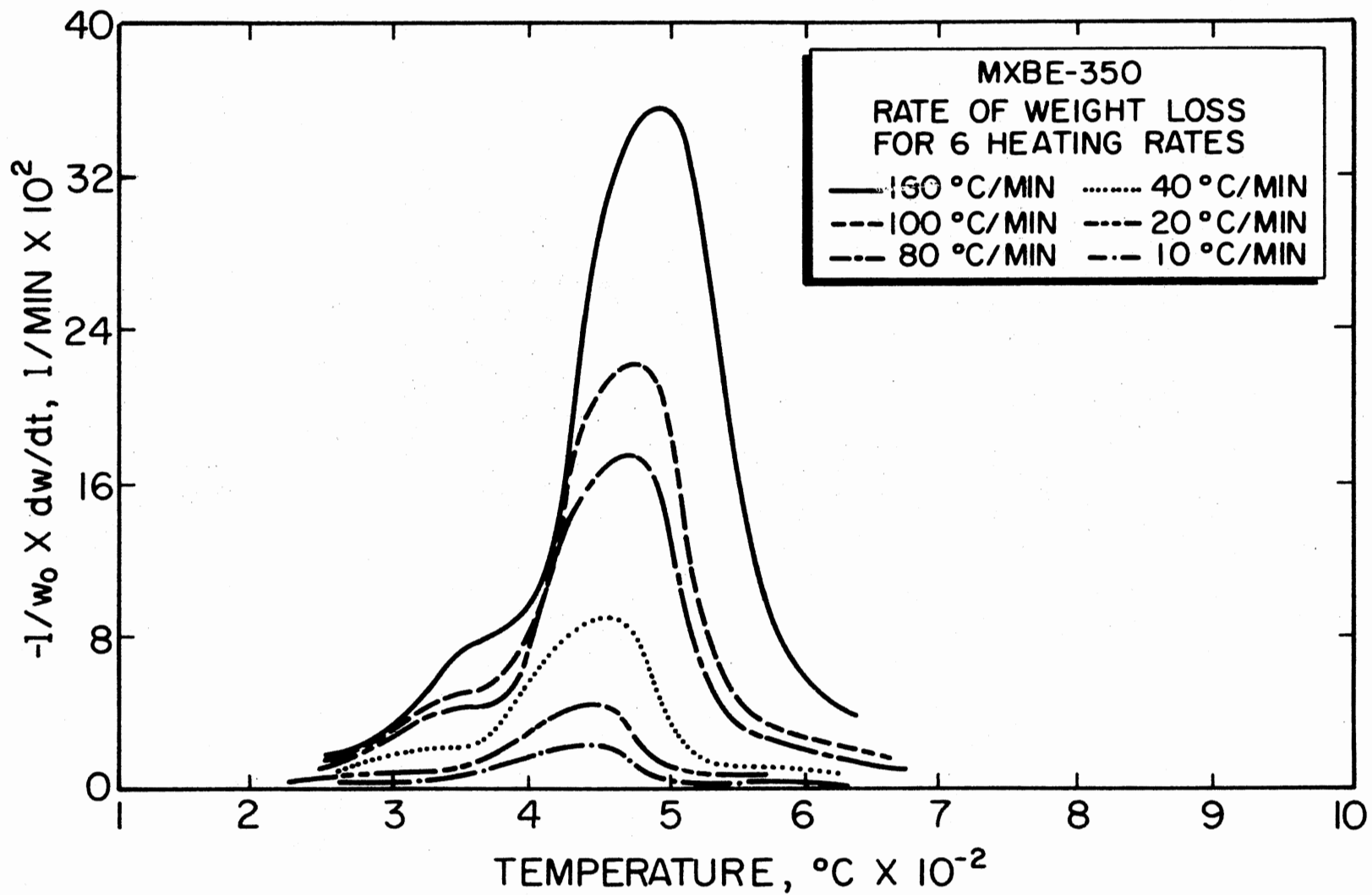


Figure 34. Derivatives of Weight Loss for Six Heating Rates for MXBE-350

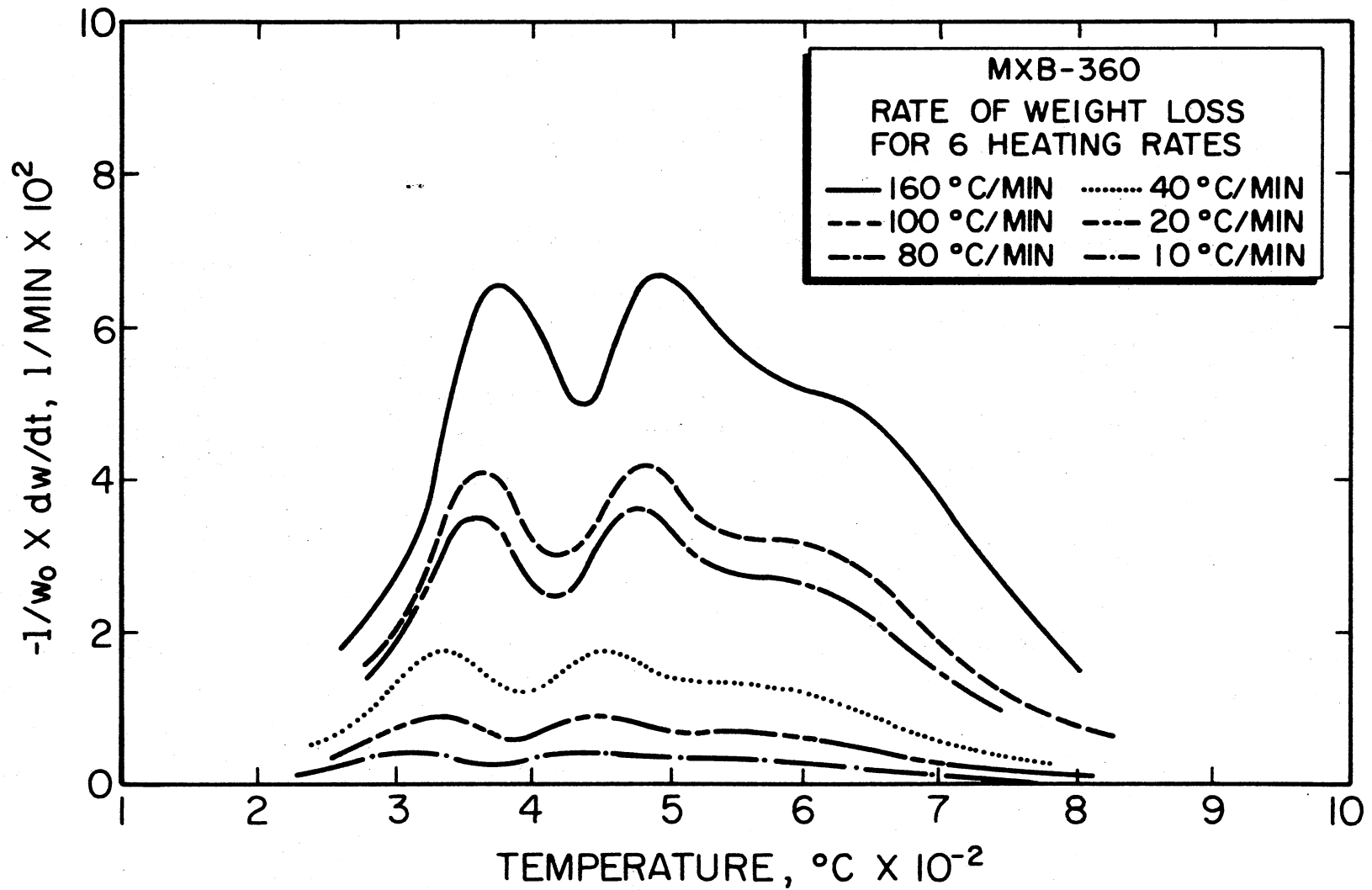


Figure 35. Derivatives of Weight Loss for Six Heating Rates for MXB-360

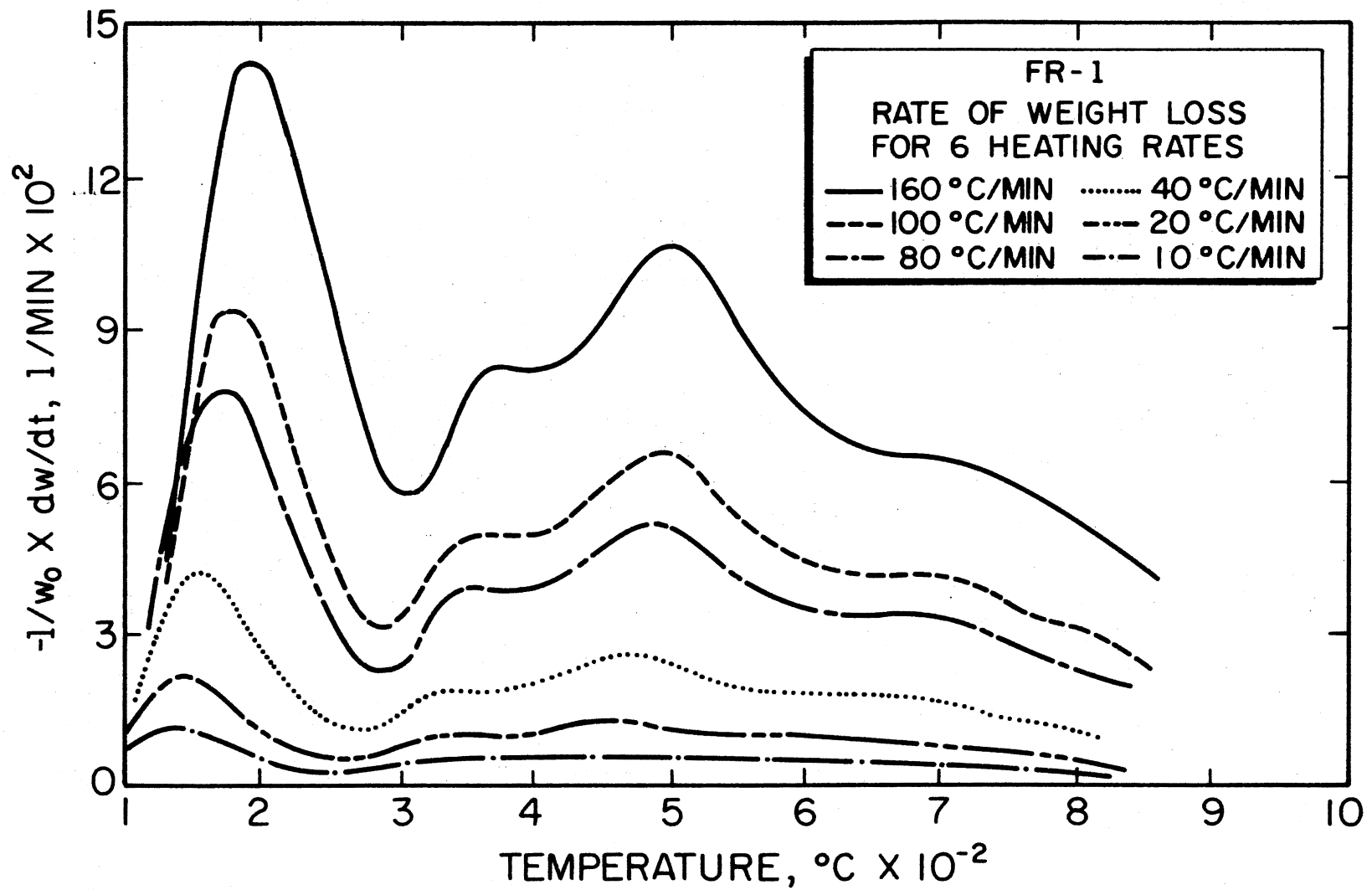


Figure 36. Derivatives of Weight Loss for Six Heating Rates for FR-1

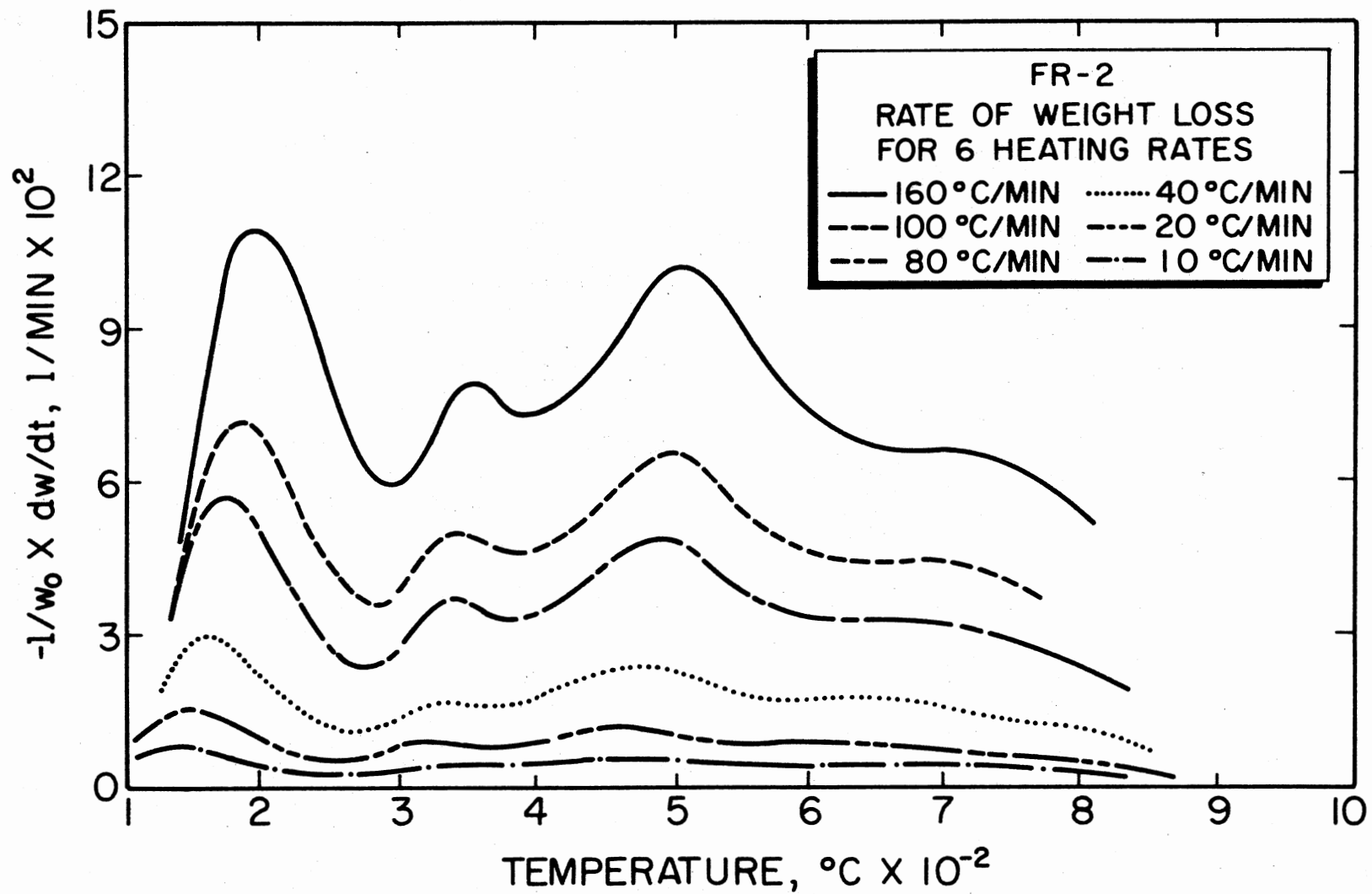


Figure 37. Derivatives of Weight Loss for Six Heating Rates for FR-2

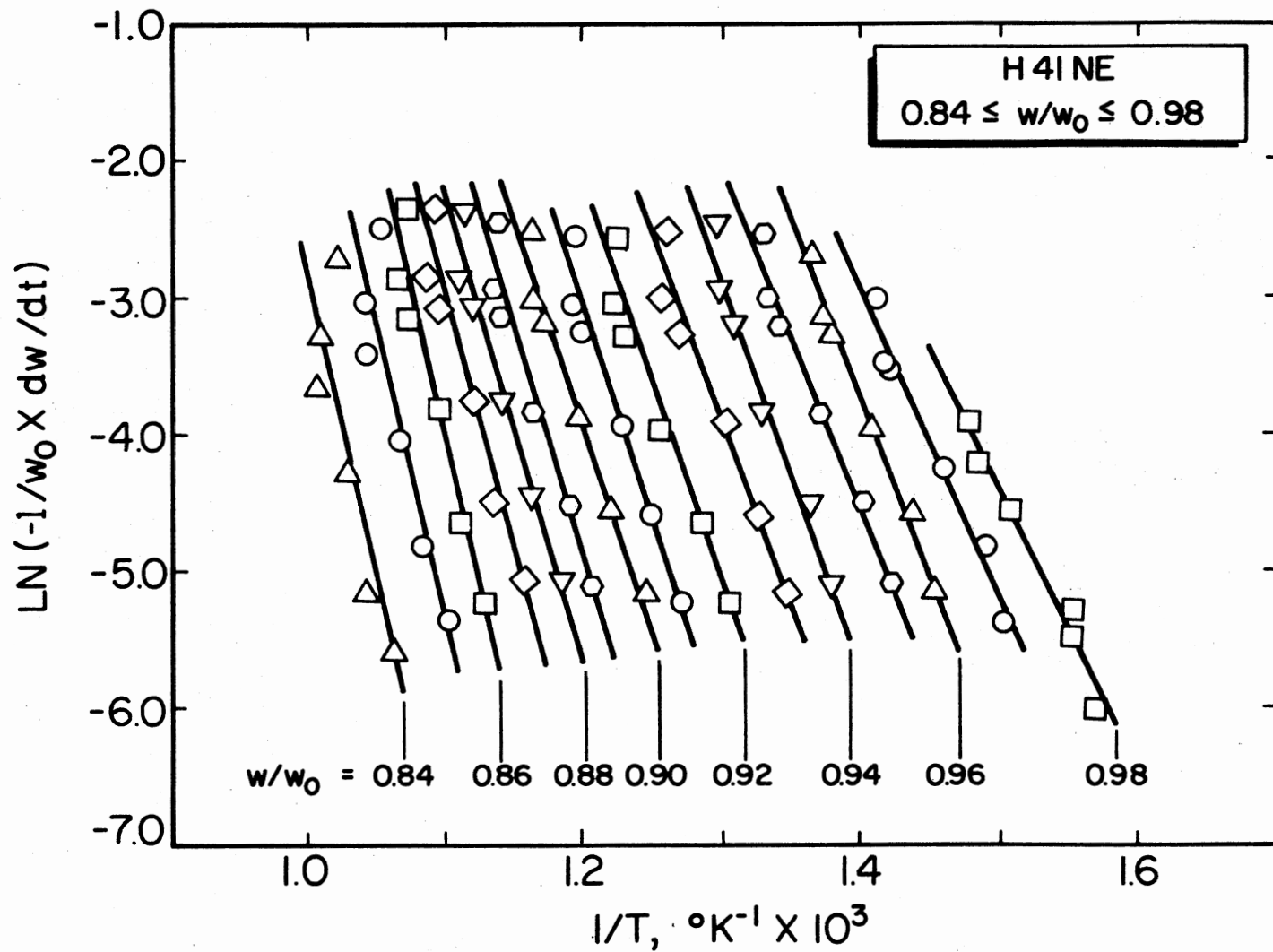


Figure 38. Plot of Slopes Used to Determine the Activation Energy for H41NE

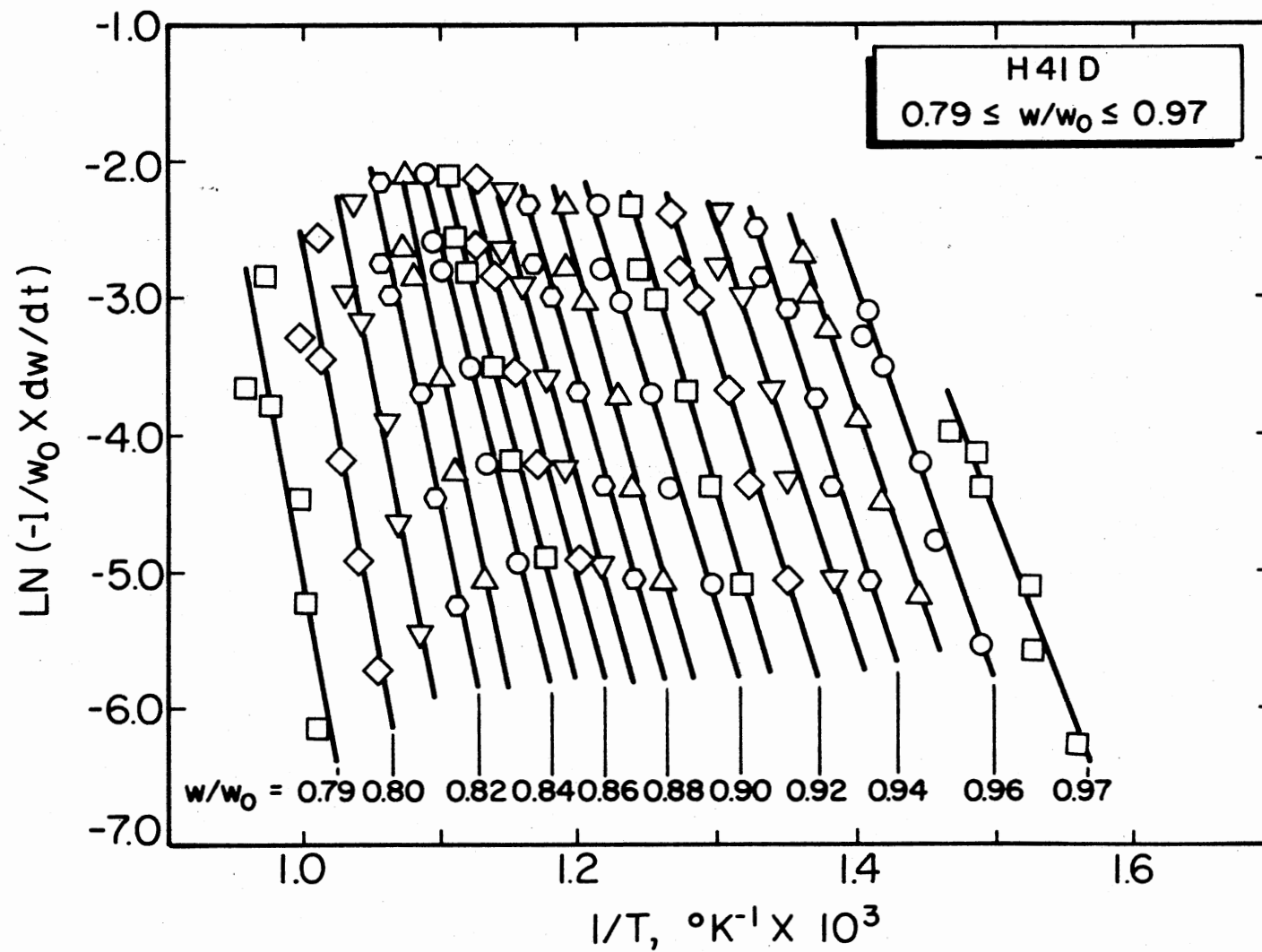


Figure 39. Plot of Slopes Used to Determine the Activation Energy for H41D

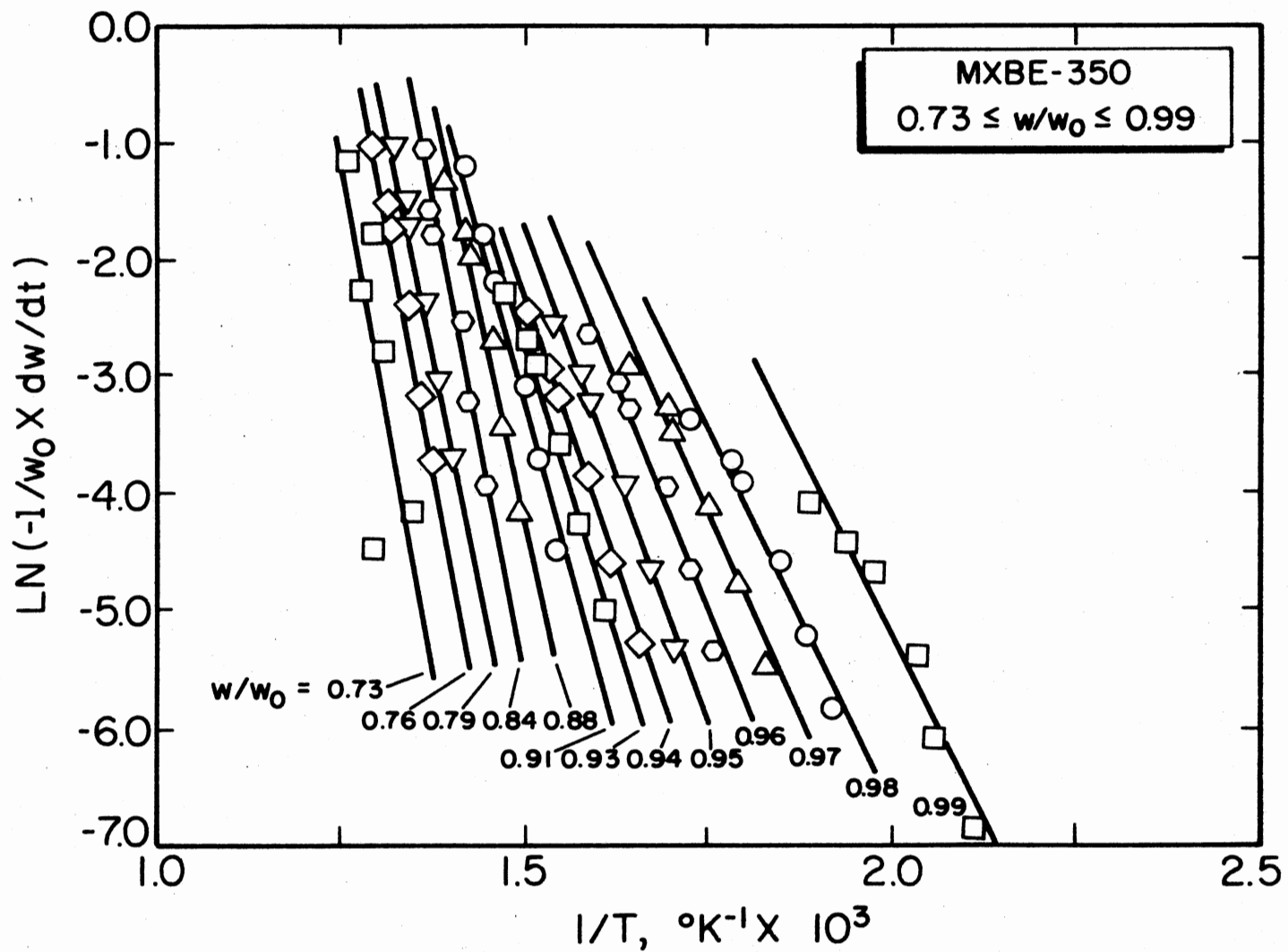


Figure 40. Plot of Slopes Used to Determine the Activation Energy for MXBE-350

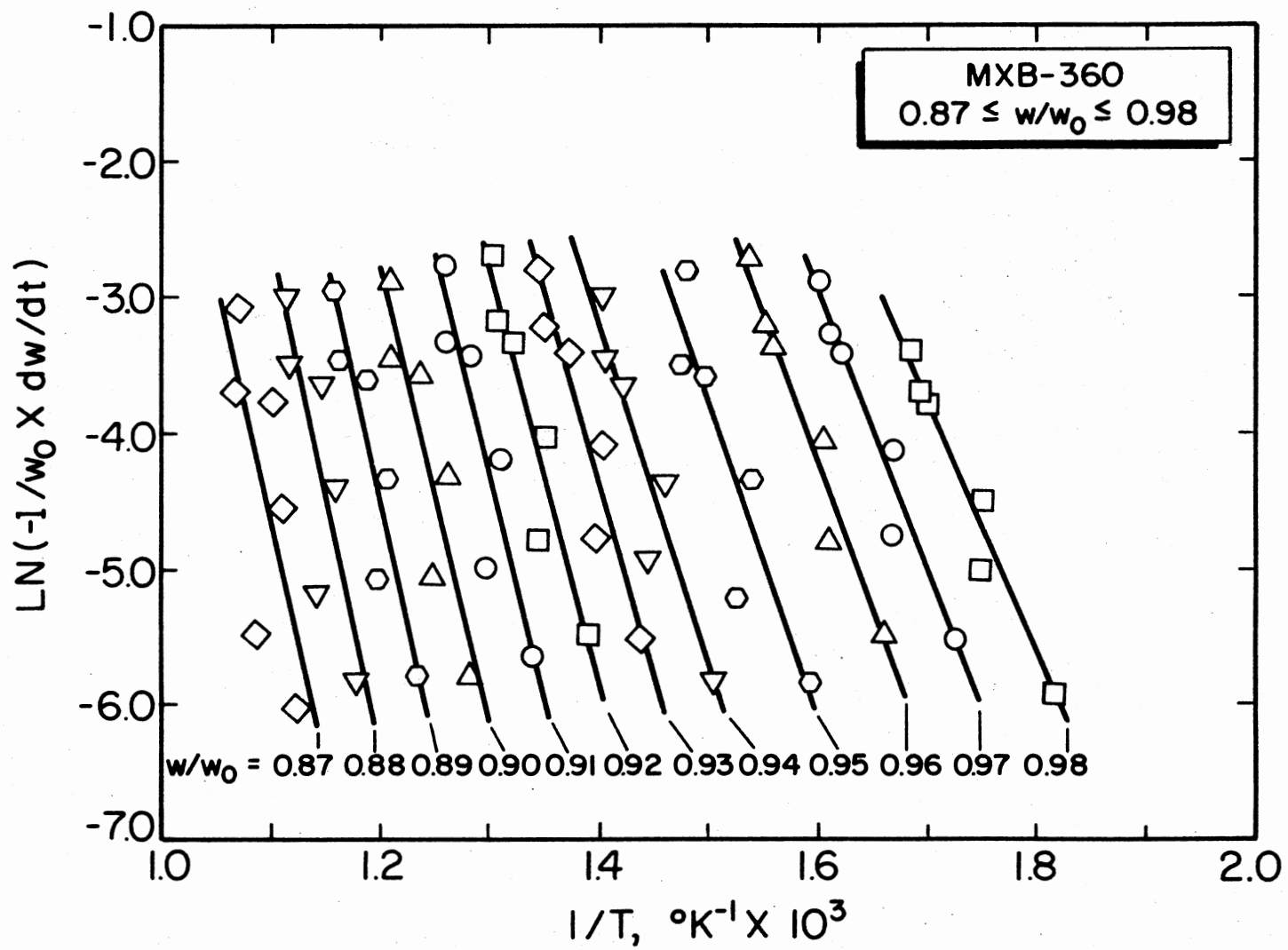


Figure 41. Plot of Slopes Used to Determine the Activation Energy for MXB-360

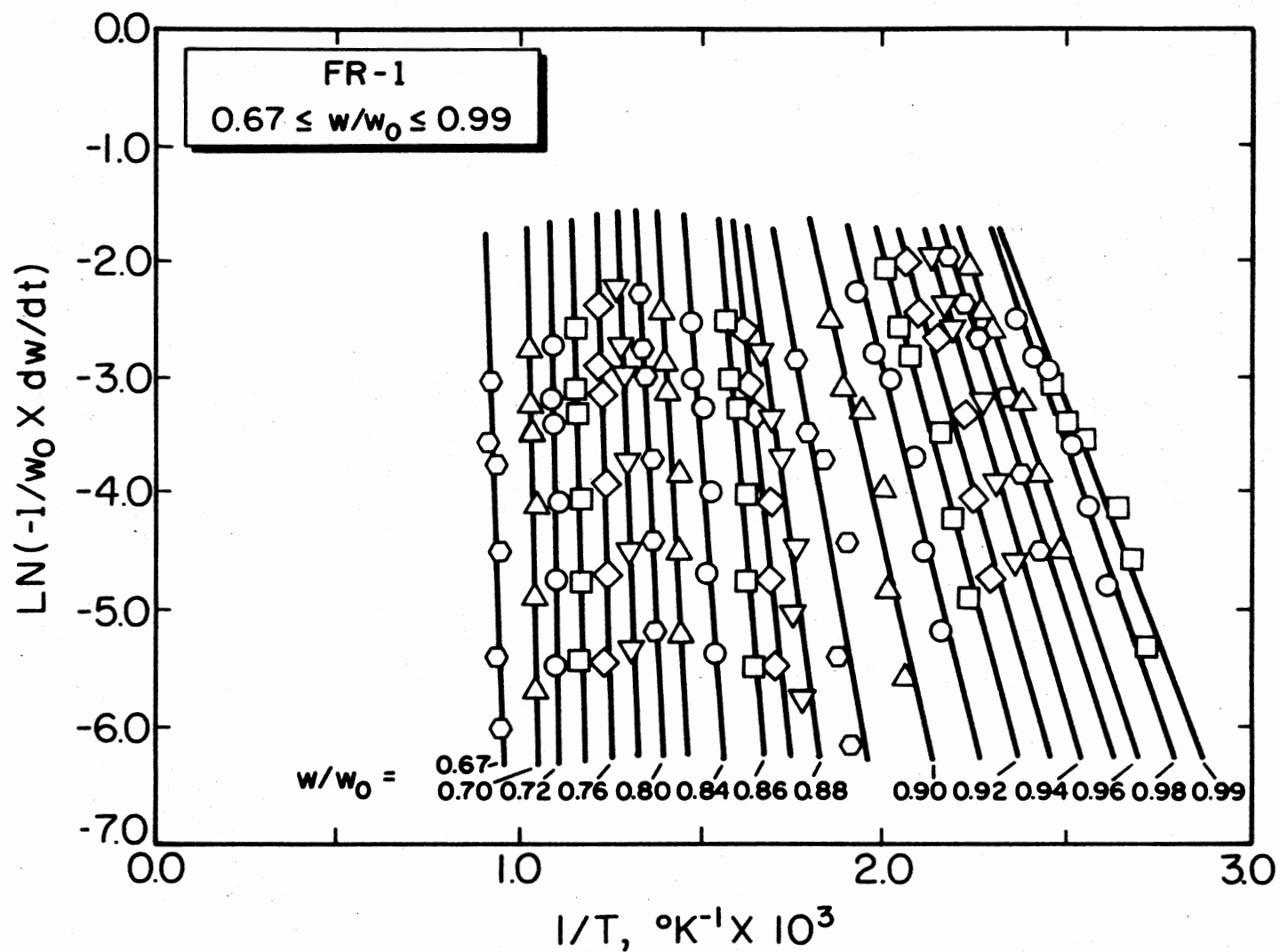


Figure 42. Plot of Slopes Used to Determine the Activation Energy for FR-1

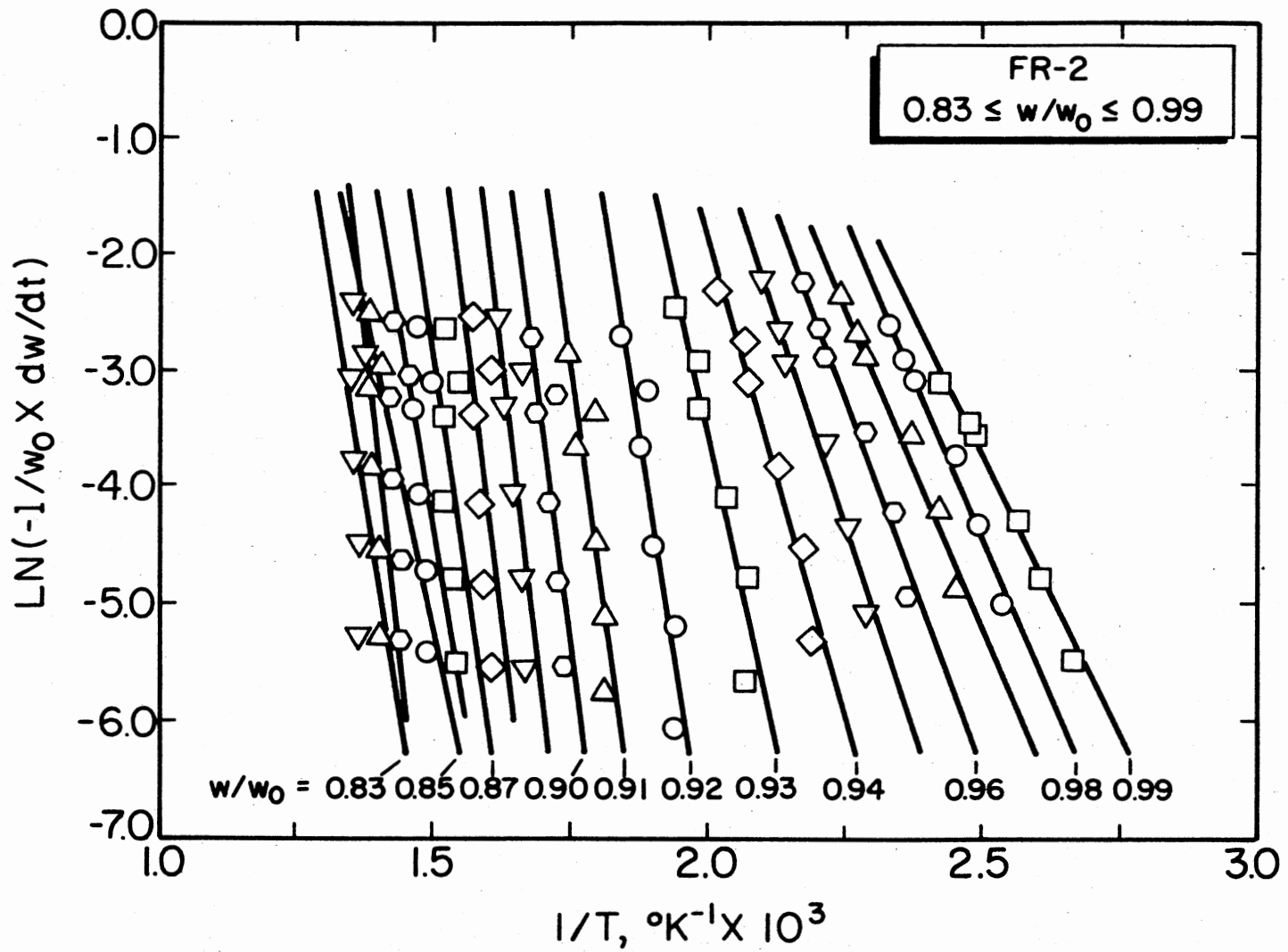


Figure 43. Plot of Slopes Used to Determine the Activation Energy for FR-2

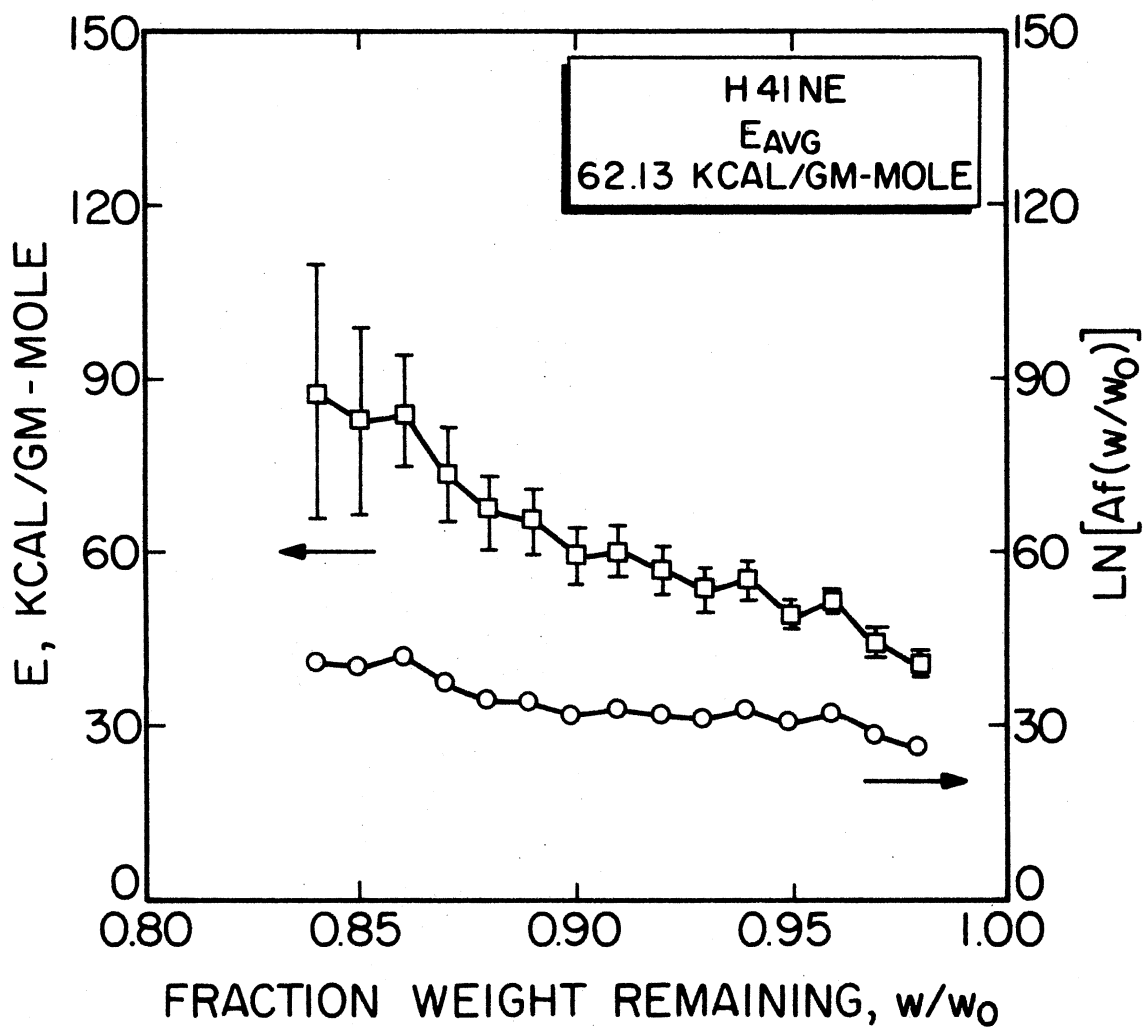


Figure 44. Activation Energy and Intercept as a Function of Degree of Conversion for H41NE

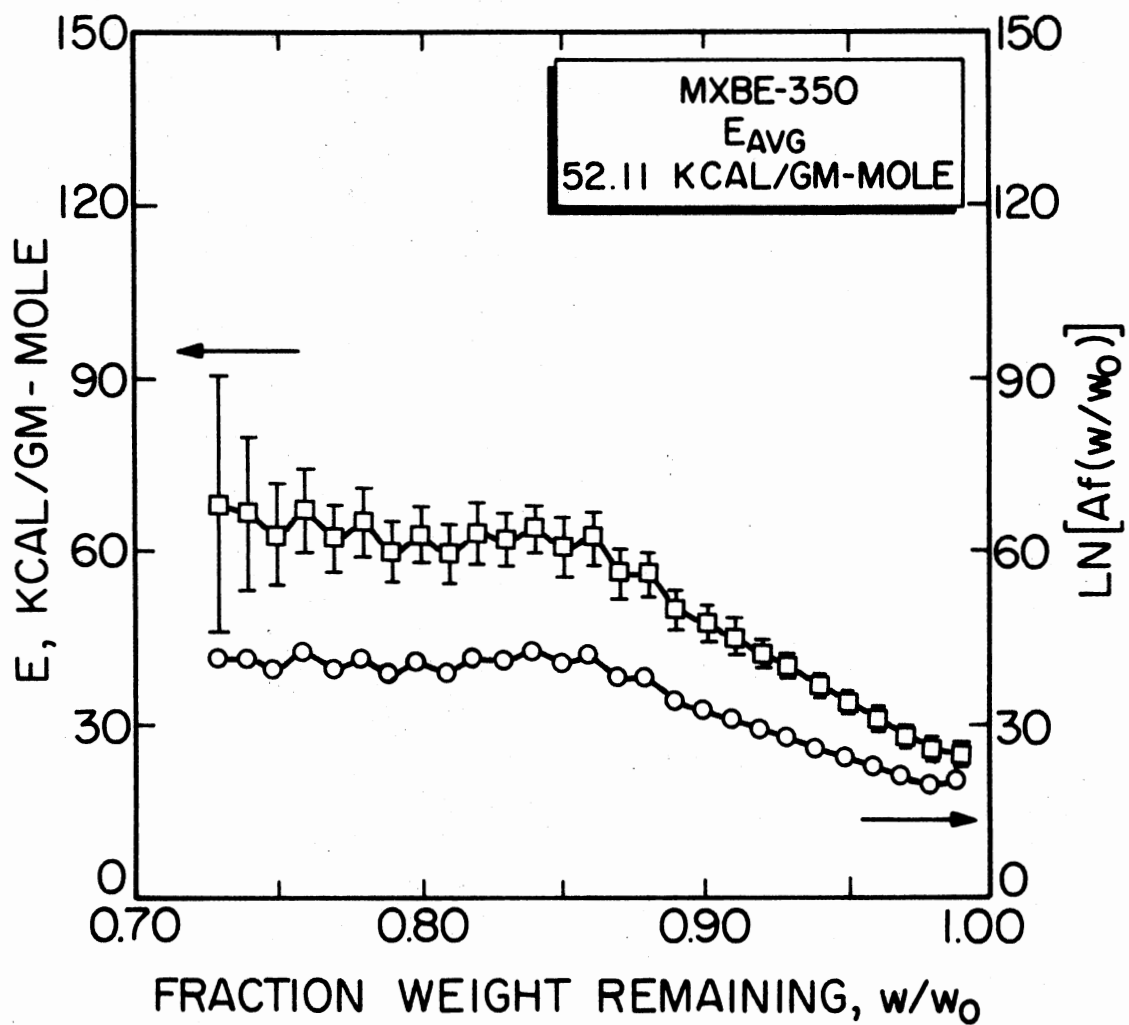


Figure 45. Activation Energy and Intercept as a Function of Degree of Conversion for MXBE-350

based on the least squares fit of the slopes. From Equation (37), plotting $\ln[Af(w/w_0)]$ versus $\ln[(w-w_f)/w_0]$ yields a straight line with slope n and intercept $\ln A$. These values were plotted for all six materials and are shown in Figures 46 through 51. These figures depict the separation of the reaction into the two regions of weight loss and the corresponding least squares fit over each region. The range of each data point is the range of each intercept resulting from using the average activation energy. A pre-exponential factor, A , and order of reaction, n , were determined for each of these two regions. The average activation energies determined from Figures 38 through 43 were used for both regions. Using the Flynn and Wall method described in Chapter II, the average activation energy for all six materials was calculated based on plots of $\log \beta$ versus $1/T$. The plots for H41NE and MXBE-350 are shown in Figures 52 and 53. The results of all the calculations are summarized in Table X.

The kinetic parameters calculated by the modified version of Friedman's method were used in the appropriate form of Equation (34) to calculate the fraction of weight remaining versus temperature. That is:

$$\frac{dw}{dt} = -w_0 A [(w-w_f)/w_0]^n e^{-E/RT}. \quad (71)$$

Each set of parameters was applied to that portion of the weight loss curve from which it was determined. A comparison of the results of these calculations and the experimental data for $10^\circ\text{C}/\text{min}$ and $160^\circ\text{C}/\text{min}$ heating rates for H41NE and MXBE-350 are shown in Figures 54 and 55, respectively. The average error, standard deviation of errors, and the 95 percent confidence interval were calculated for the experimental

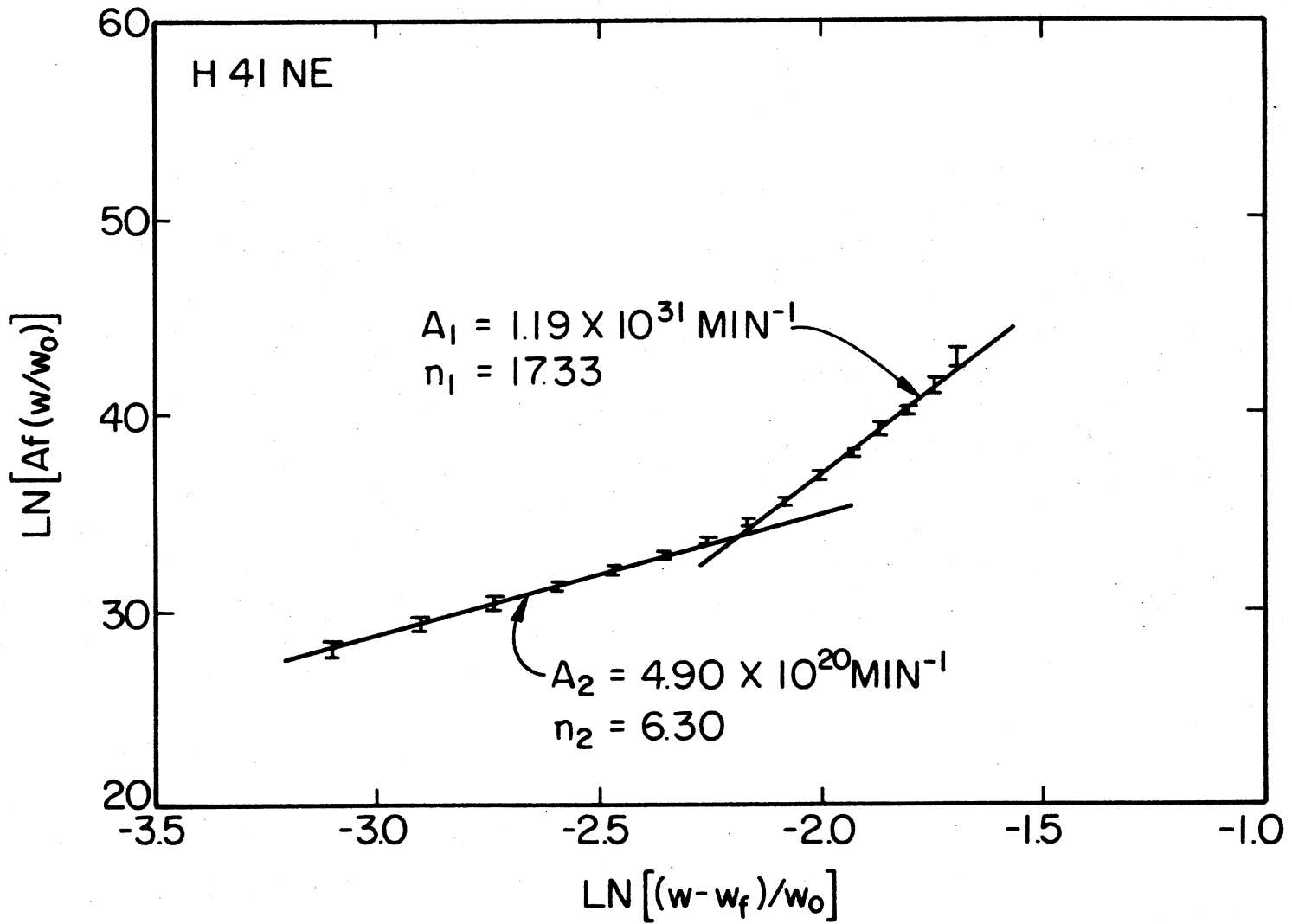


Figure 46. Plot to Determine the Pre-Exponential Factor and Order of Reaction for Two Regions of Weight Loss for H41NE

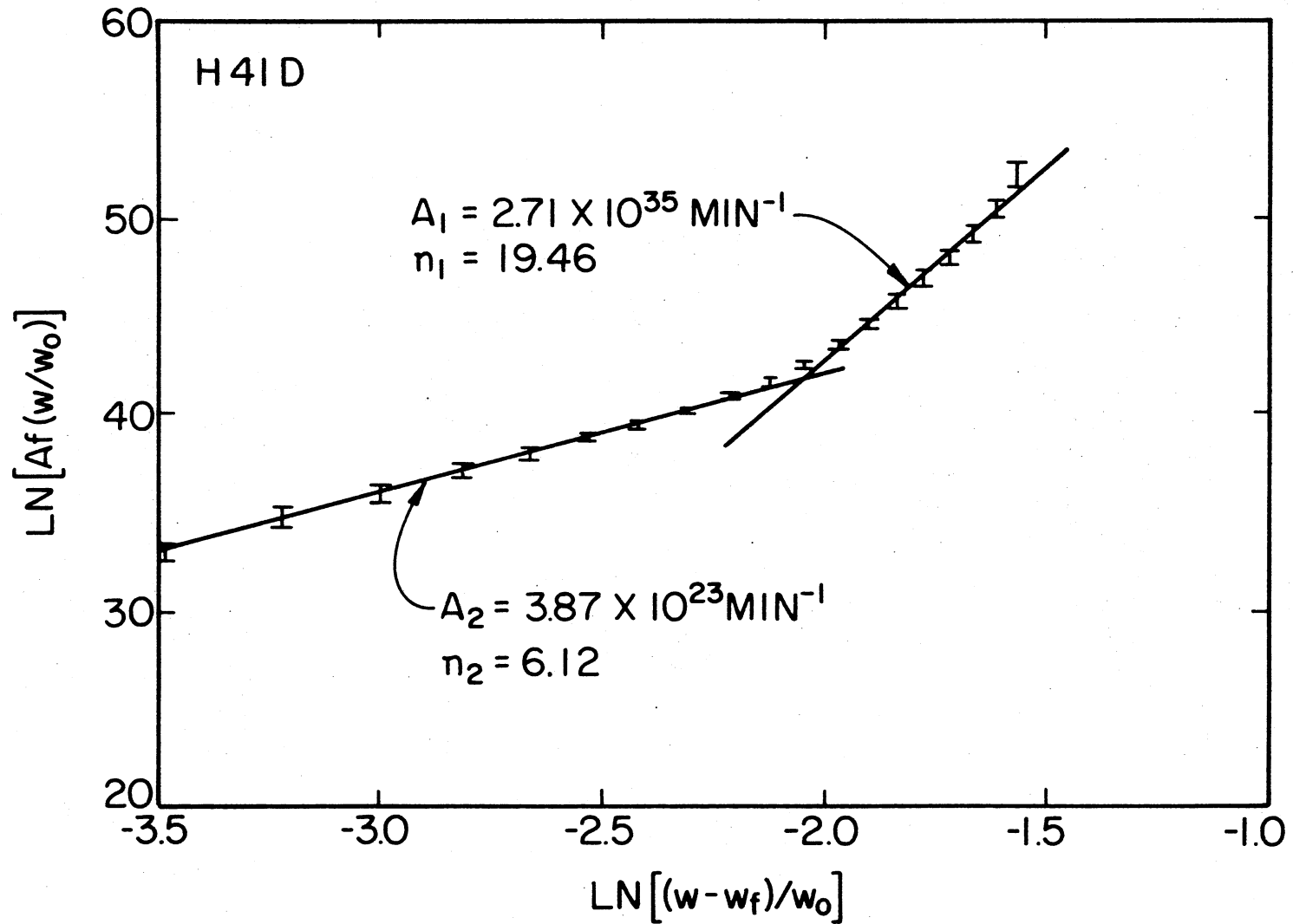


Figure 47. Plot to Determine the Pre-Exponential Factor and Order of Reaction for Two Regions of Weight Loss for H41D

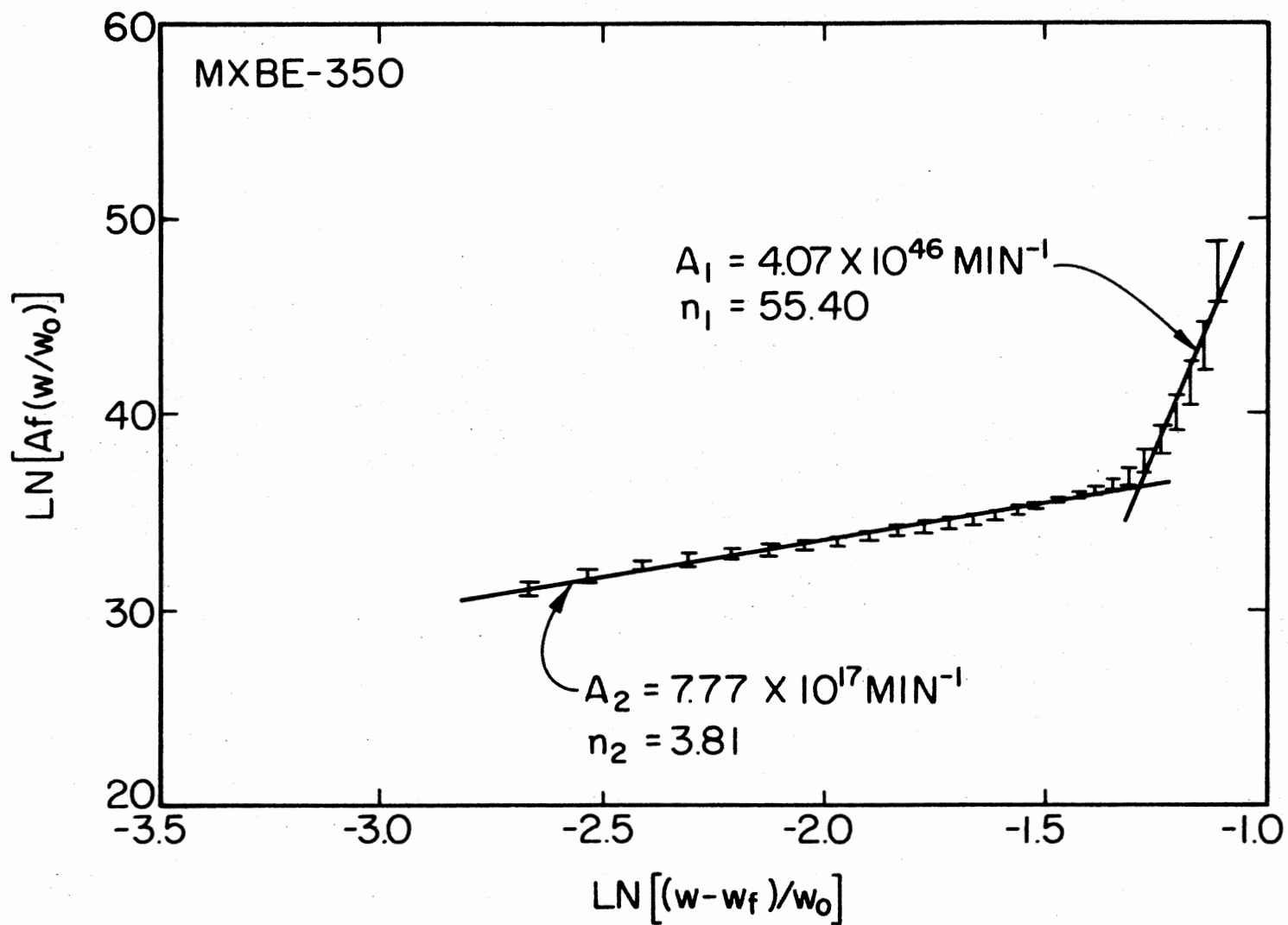


Figure 48. Plot to Determine the Pre-Exponential Factor and Order of Reaction for Two Regions of Weight Loss for MXBE-350

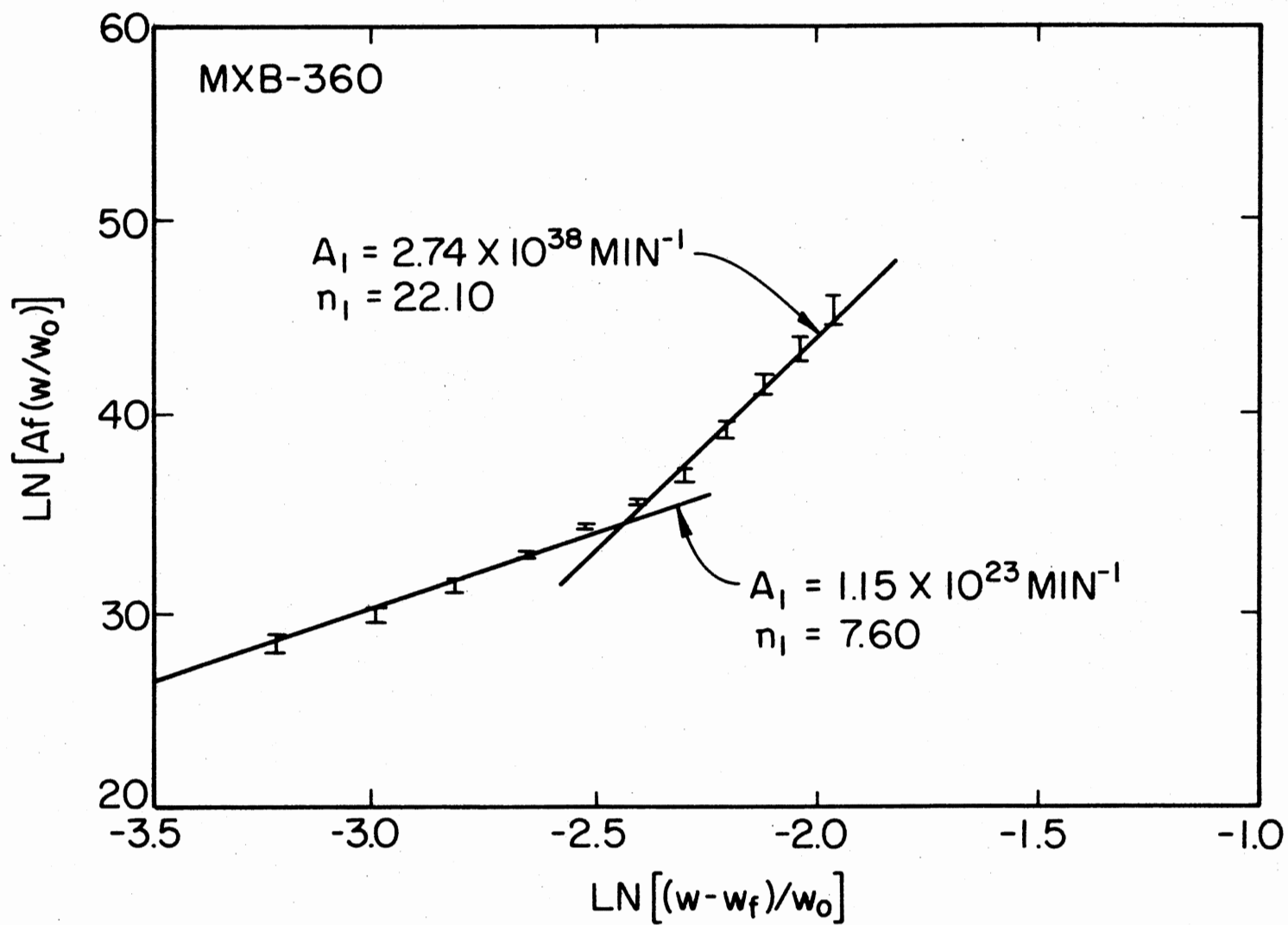


Figure 49. Plot to Determine the Pre-Exponential Factor and Order of Reaction for Two Regions of Weight Loss for MXB-360

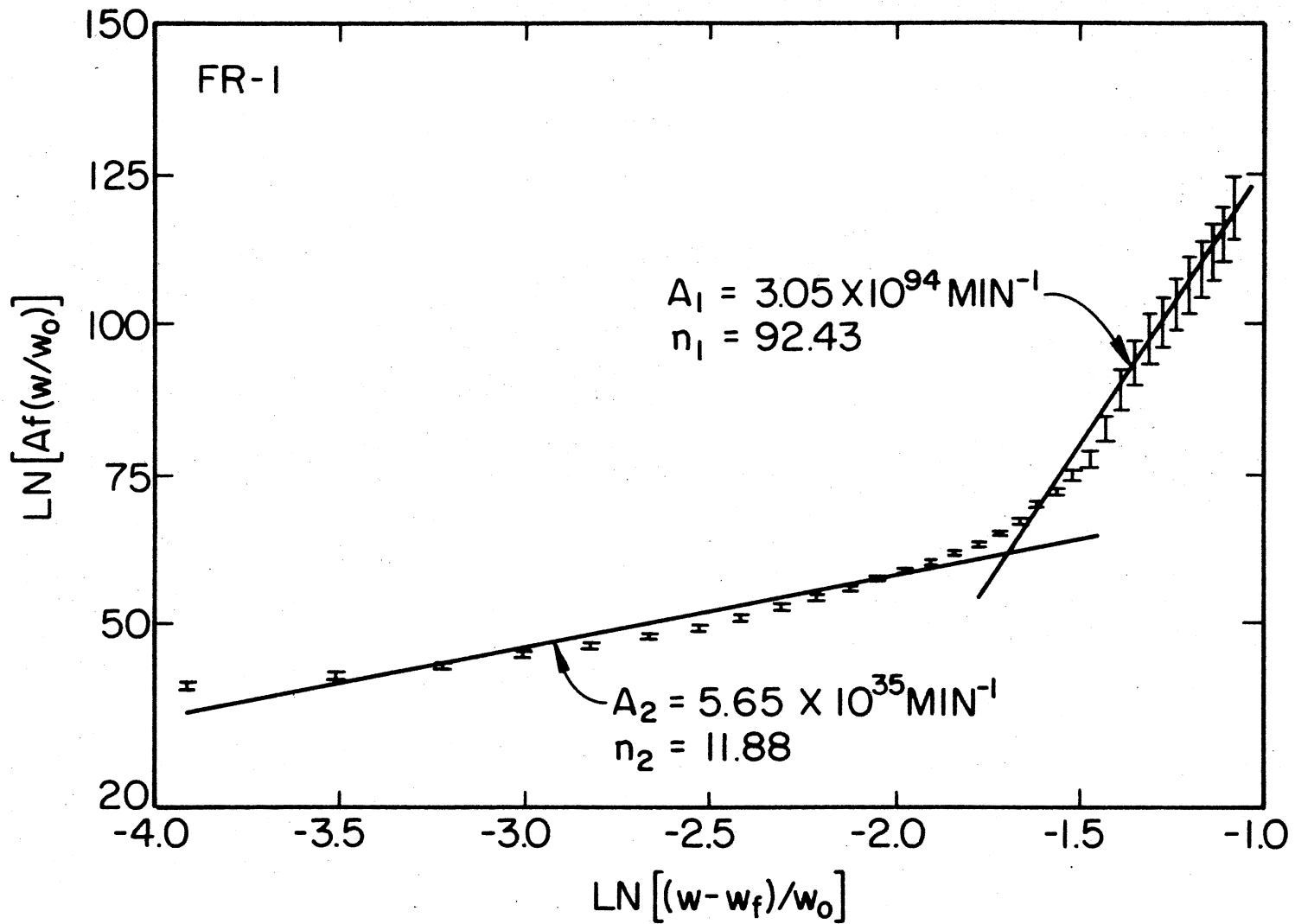


Figure 50. Plot to Determine the Pre-Exponential Factor and Order of Reaction for Two Regions of Weight Loss for FR-1

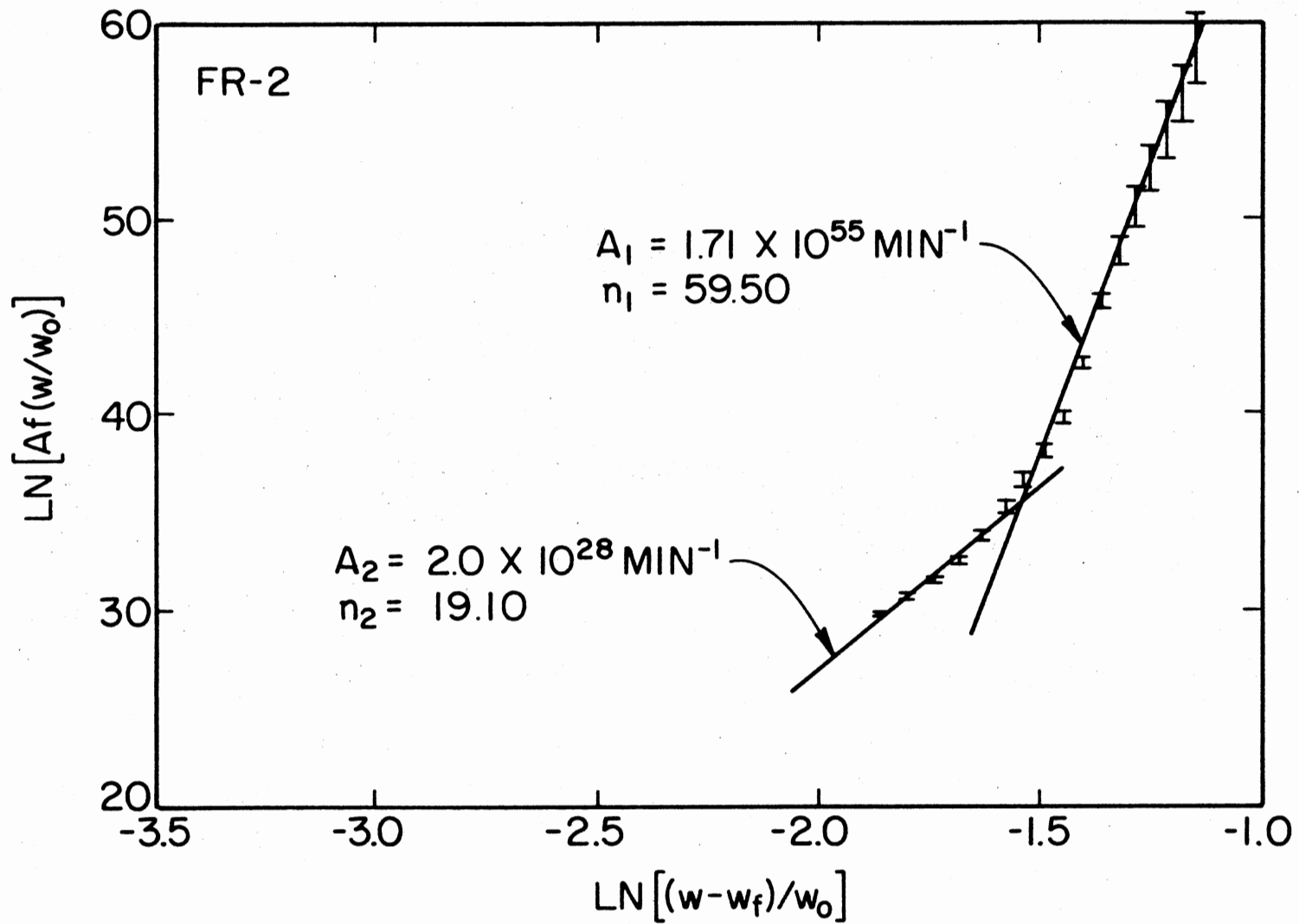


Figure 51. Plot to Determine the Pre-Exponential Factor and Order of Reaction for Two Regions of Weight Loss for FR-2

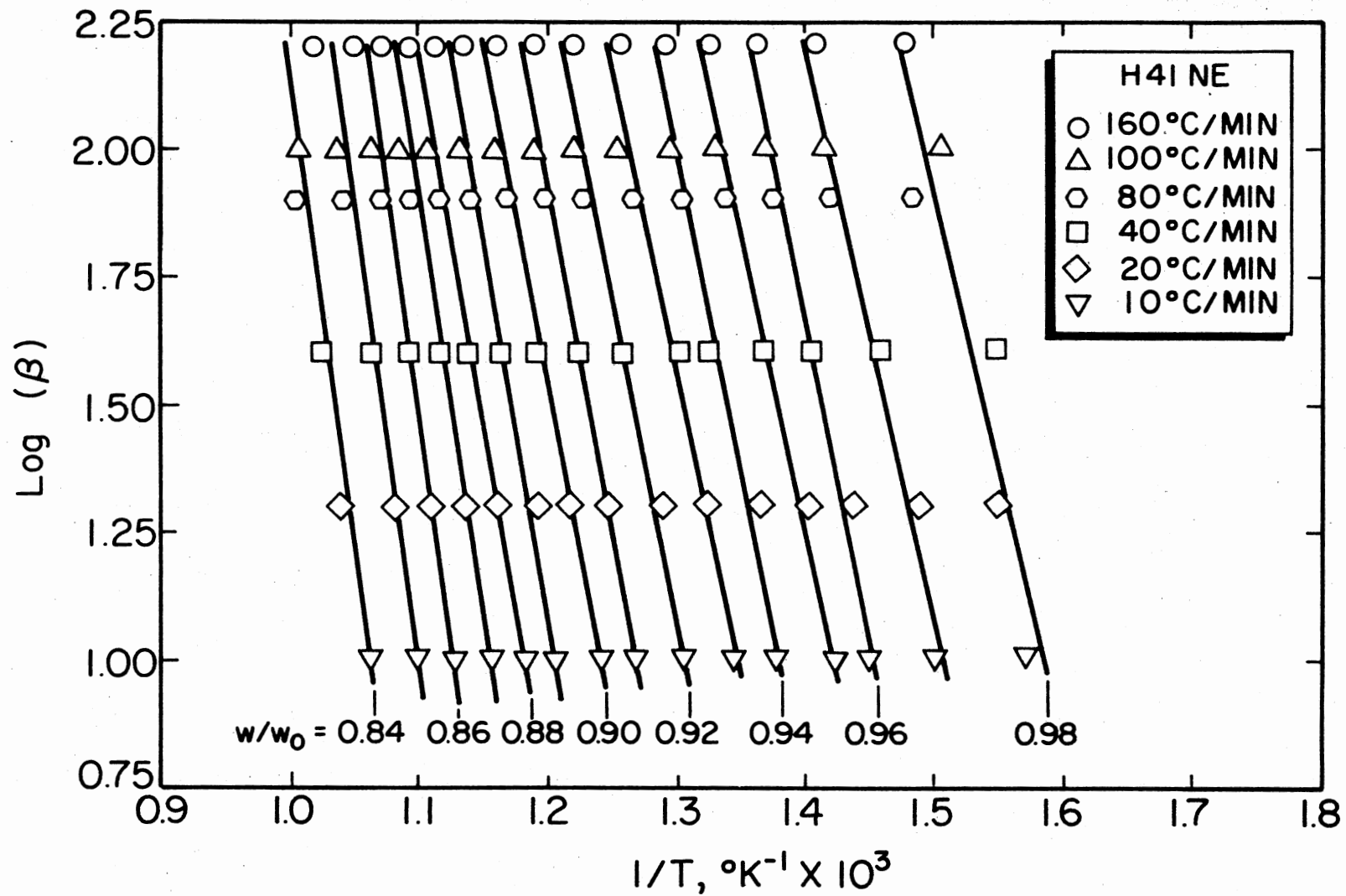


Figure 52. Plot of Slopes Used to Determine the Activation Energy for H41NE by the Method of Flynn and Wall.

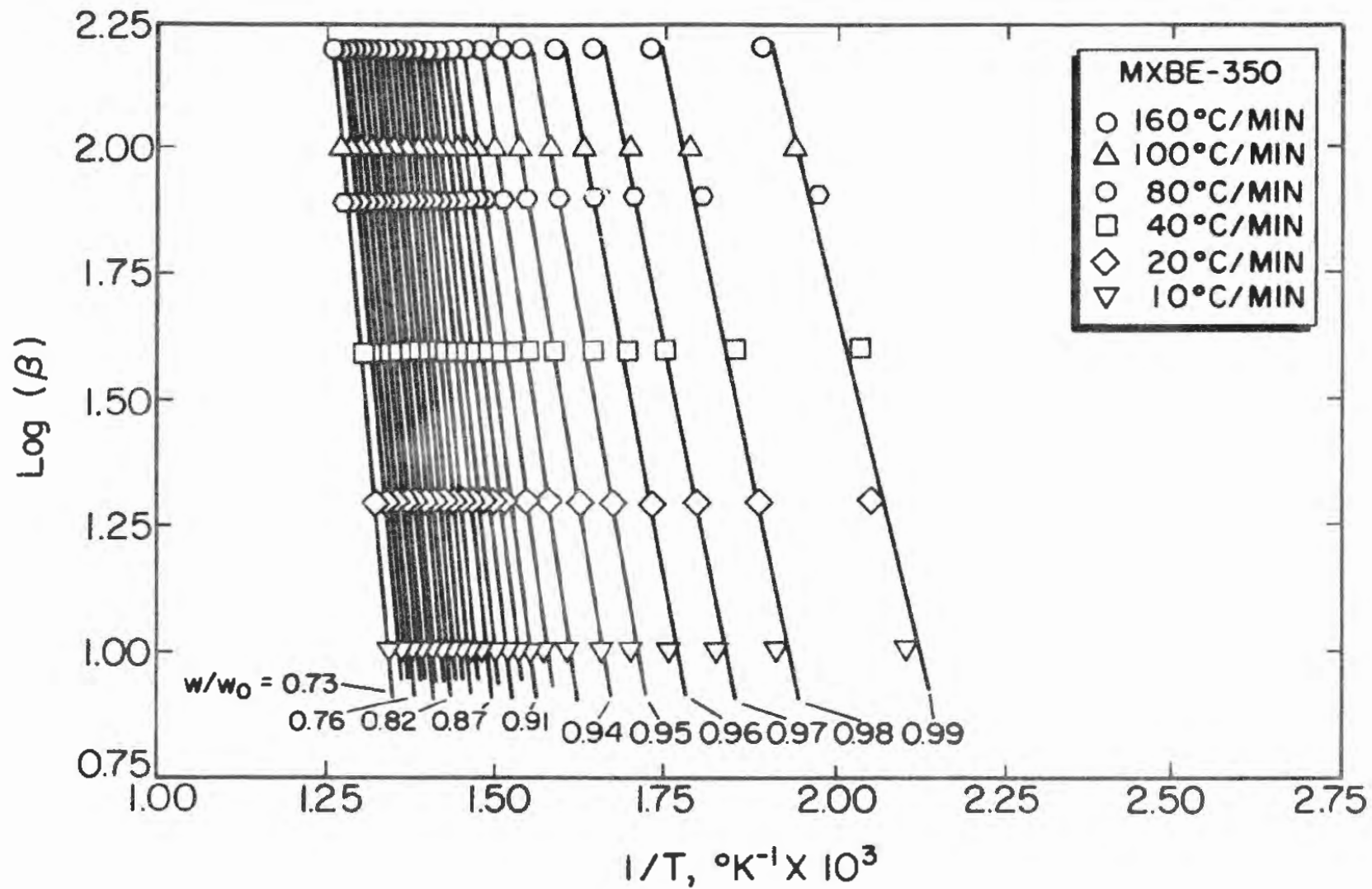


Figure 53. Plot of Slopes Used to Determine the Activation Energy for MXBE-350 by the Method of Flynn and Wall

TABLE X
RESULTS OF THERMOGRAVIMETRIC ANALYSIS

Material	w_f/w_0	Range of w/w_0	E_{avg} (kcal/gm-mole)		A (min^{-1})	n	w/w_0
			Friedman	Flynn & Wall			
Haveg H41NE	0.795	.98 - .84	62.13	62.15	1.19×10^{31} 4.90×10^{20}	17.33 6.30	$\geq .91$ $< .91$
Haveg H41D	0.760	.97 - .79	74.97	71.52	2.71×10^{35} 3.87×10^{23}	19.46 6.12	$\geq .89$ $< .89$
Fiberite MXBE-350	0.660	.99 - .73	52.11	50.22	4.07×10^{46} 7.77×10^{17}	55.40 3.81	$\geq .94$ $< .94$
Fiberite MXB-360	0.840	.98 - .87	56.87	53.70	2.74×10^{38} 1.15×10^{23}	22.10 7.60	$\geq .93$ $< .93$
Fiber Materials FR-1	0.650	.99 - .67	94.62	88.49	3.05×10^{94} 5.65×10^{35}	92.43 11.88	$\geq .84$ $< .84$
Fiber Materials FR-2	0.675	.99 - .83	49.05	45.38	1.71×10^{55} 2.00×10^{28}	59.50 19.10	$\geq .89$ $< .89$

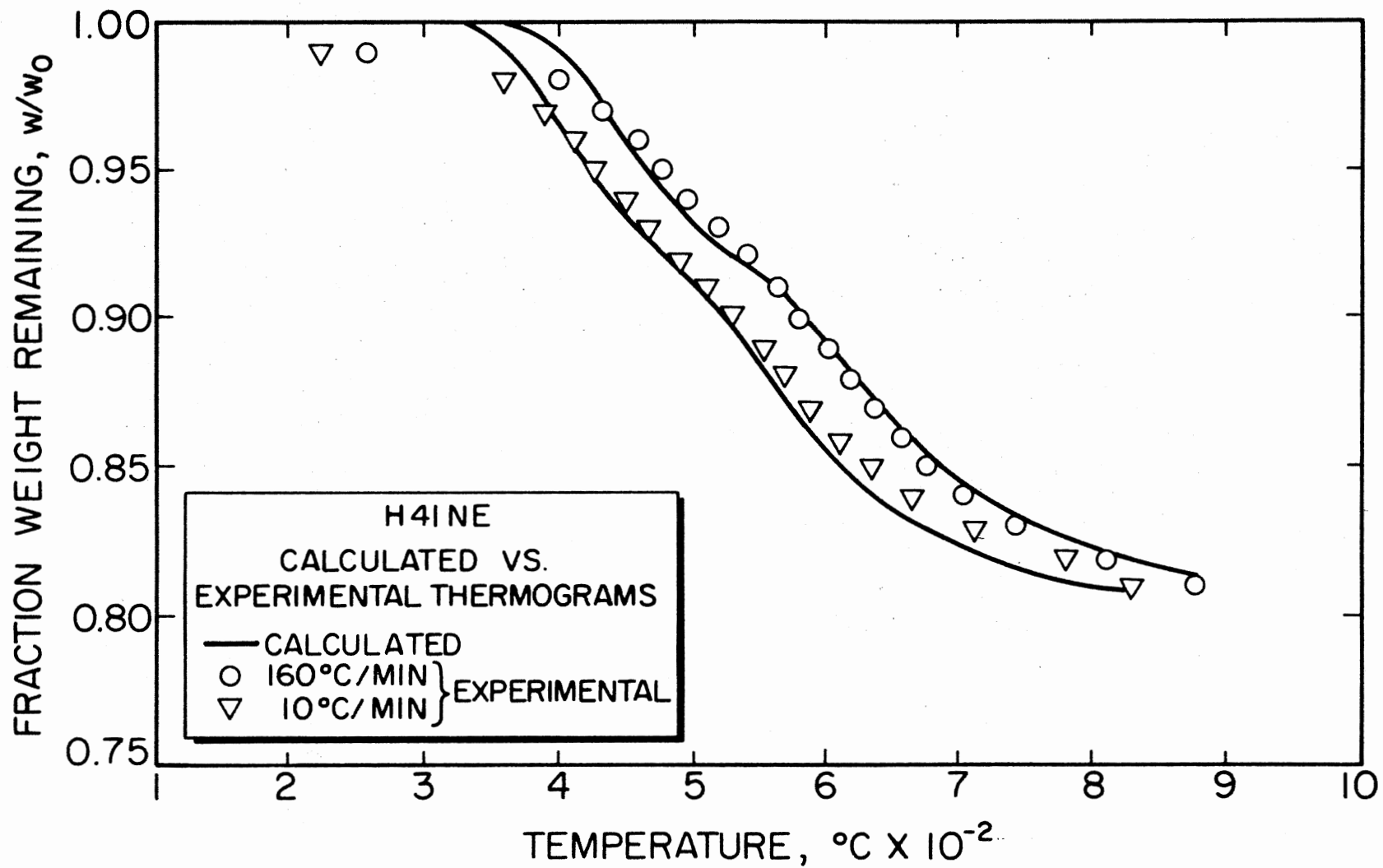


Figure 54. Comparison of Calculated Versus Experimental Weight Loss for H41NE

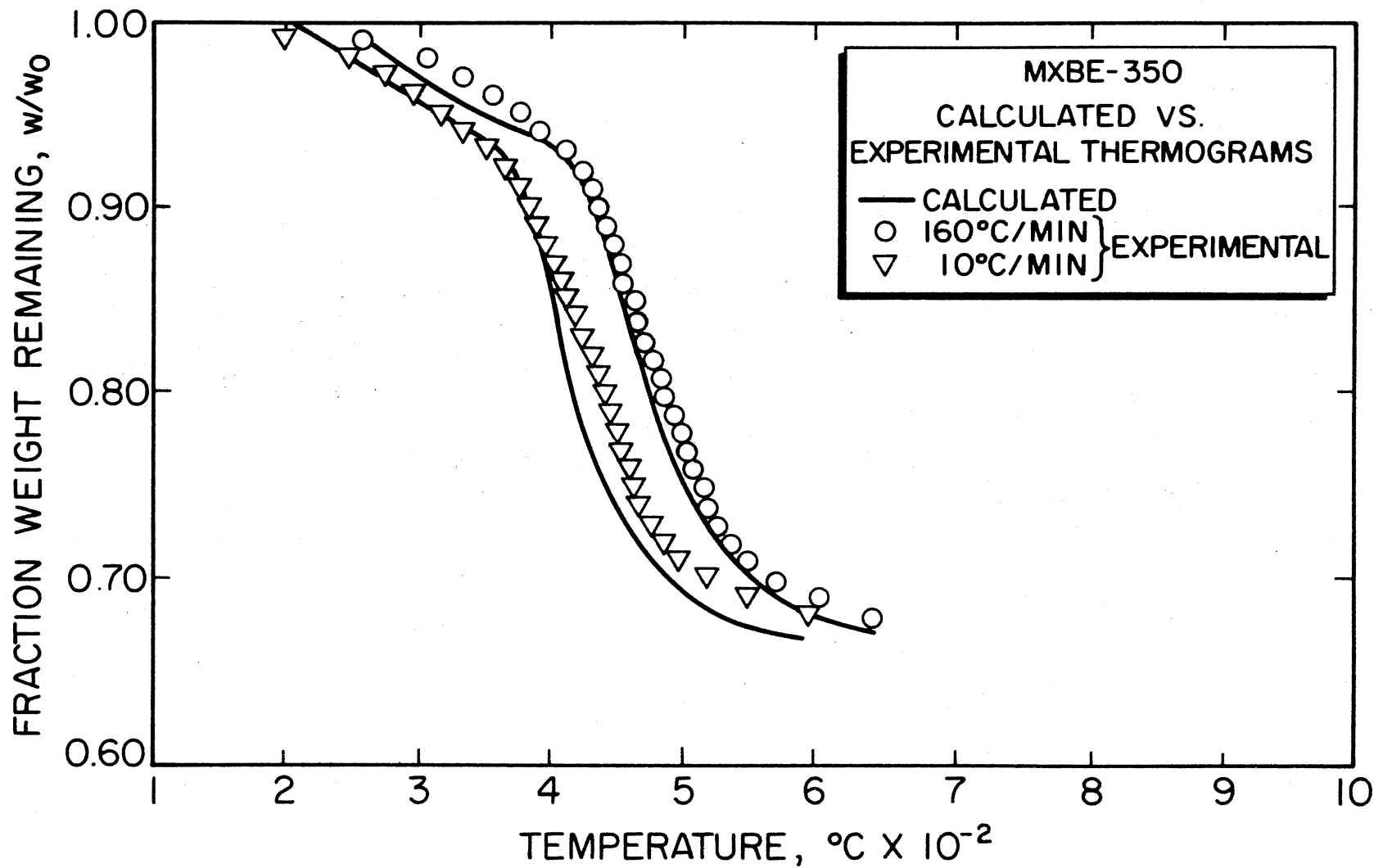


Figure 55. Comparison of Calculated Versus Experimental Weight Loss for MXBE-350

versus calculated points for all six materials. These results are presented in Table XI.

TABLE XI
STATISTICAL ANALYSIS OF ERRORS IN COMPUTED
VERSUS EXPERIMENTAL w/w_0

Material	Average Error (percent)	Standard Deviation (percent)	95 Percent Confidence Interval	Number of Data Points
H41NE	0.33	0.58	0.22 - 0.44	90
H41D	0.28	0.84	0.14 - 0.42	114
MXBE-350	1.36	1.41	1.17 - 1.55	162
MXB-360	0.18	0.48	0.08 - 0.29	72
FR-1	0.50	1.22	0.38 - 0.72	198
FR-2	1.07	2.30	0.74 - 1.41	90

CHAPTER V

MEASUREMENT OF SPECIFIC HEAT AND HEAT OF DECOMPOSITION

Both the specific heat and heat of decomposition are required as input to the thermal model. The specific heat of the char and active components are important from the standpoint of energy storage in the element. Equally important is their impact on Equation (57) which represents the local heat of gasification of the material. The energy released as a result of the consumption of the active material is a function of the active material specific heat. Similarly, the char component specific heat substantially affects the energy consumed as a result of the char production. As with the kinetic parameters, the character of the predicted thermal response of a material is altered by these values. Both the magnitude and sign of the heat of decomposition are important as well.

Differential scanning calorimetry (DSC) was chosen for this work. This was primarily because of the ease of measuring both the specific heat and heat of decomposition simultaneously.

Experimental Method

Equipment

The specific heat of a nonvolatile sample can be calculated by Equation (41). The data required are the energy input to the sample,

the mass of the sample, and the heating rate. The temperature dependent specific heat can be calculated if dq/dt is measured as a function of temperature. In this work, these data were obtained with a Perkin-Elmer Differential Scanning Calorimeter Model DSC-1B. The unit consists of an analyzer module and control unit. A photograph of the instrument is presented as Figure 56.

The control module contains the electronics associated with the system. This includes the scan speed, range, and slope control. The sensitivity of the range, dq/dt , can be adjusted from 1 mcal/sec to 32 mcal/sec full scale on a 10-mv recorder. Heating rates can be varied from 0.625 to 80°C/min with an upper limit of 500°C.

The analyzer module contains the sample holder and the average and differential temperature control. The sample holder assembly is shown schematically in Figure 57. This unit forms the basis of the system. The DSC operates on a "null balance" principle. That is, the sample and reference pans are maintained at very nearly the same temperature. The differential power required to maintain this equality is calibrated directly in millicalories per second, dq/dt . The "null balance" is accomplished by a platinum heater and resistance thermometer located in the floor of both the sample and reference holders. As the system temperature is increased at a predetermined rate, any difference in sample and reference temperatures is sensed by the platinum thermometers. A closed loop control system then adjusts the power input to remove this difference. This is shown qualitatively by the DSC thermogram presented as Figure 58. The departure of the thermogram from the baseline represents an endothermic event requiring additional energy to maintain the sample temperature.

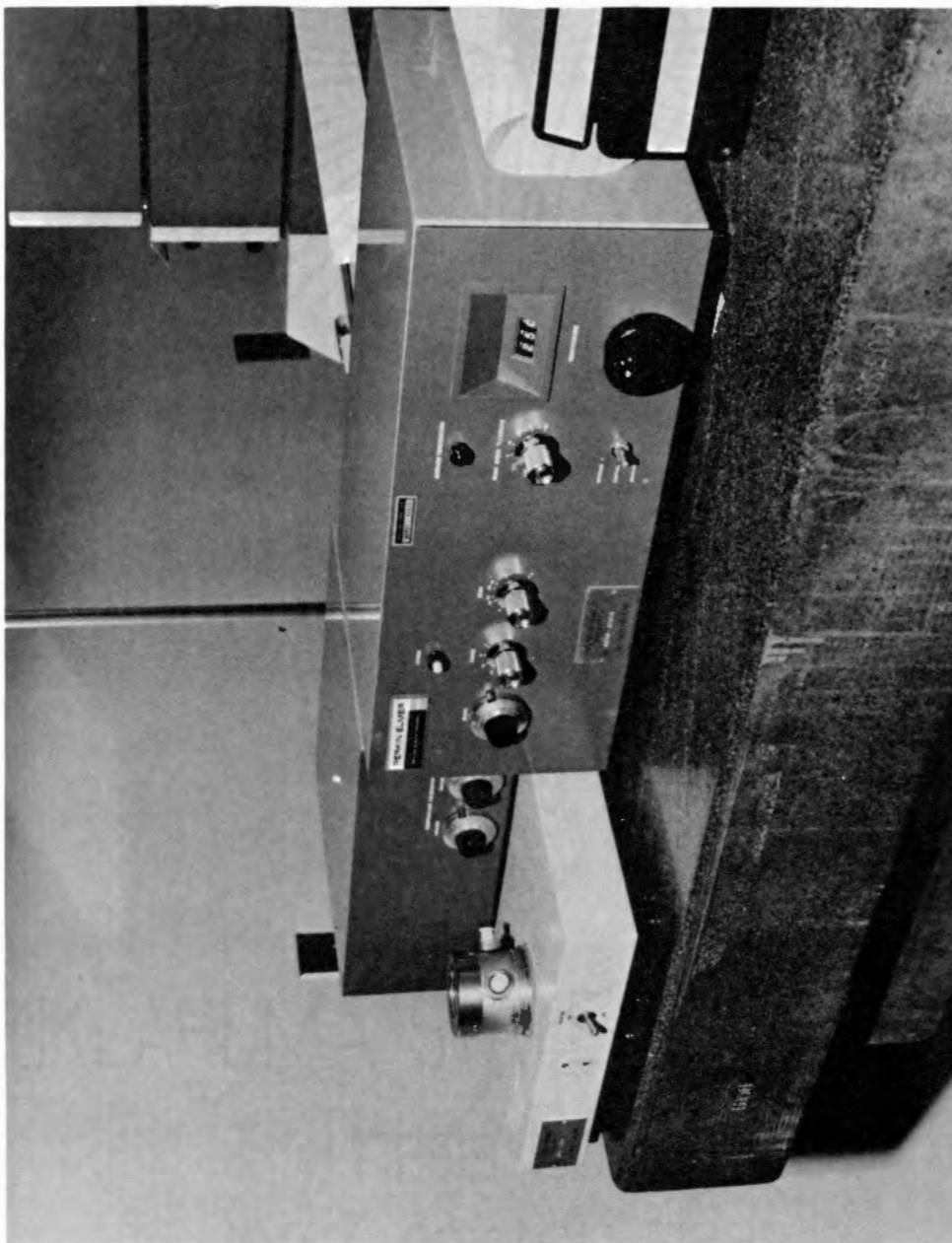


Figure 56. Perkin-Elmer DSC-1B Differential Scanning Calorimeter

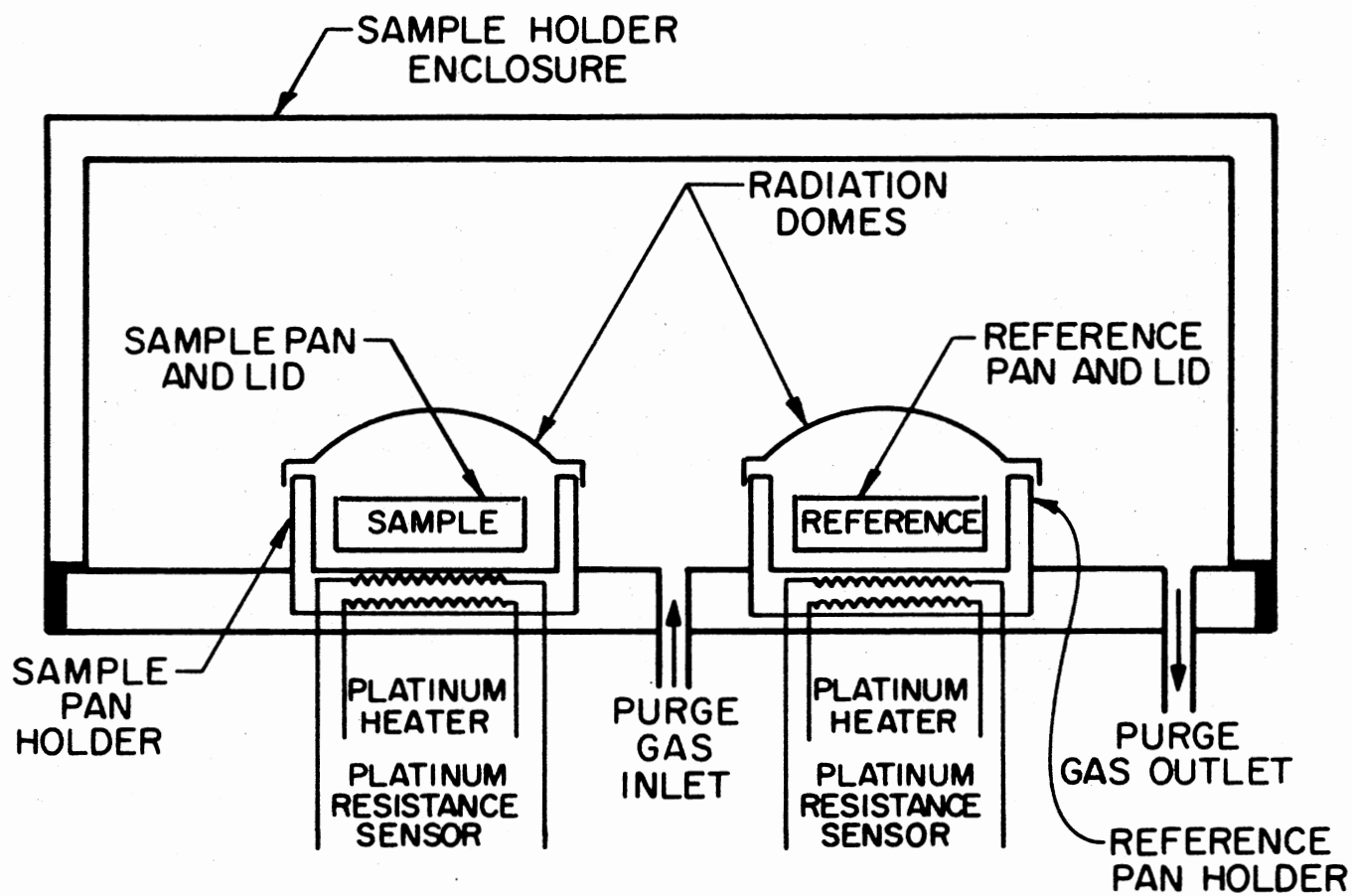


Figure 57. Schematic of DSC-1B Sample Holder

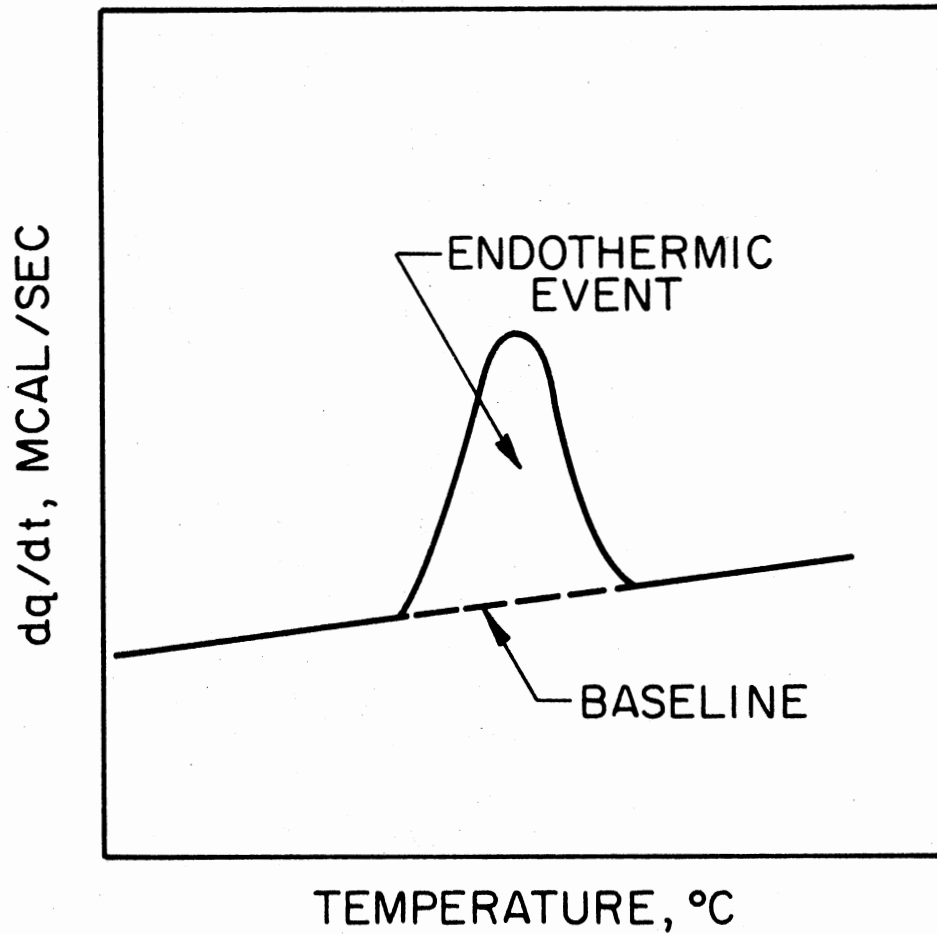


Figure 58. Idealized DSC Thermogram [33]

The DSC output was recorded as temperature and differential energy on a Linear Instruments Model 598 3-channel strip chart recorder.

Calibration

Two calibrations are required for the DSC-1B. These are temperature and differential temperature. Additionally, a power calibration is required if the instrument is to be used for heat of fusion measurements.

The differential temperature calibration is required to ensure that the sample and reference pans are maintained at approximately the same temperature over the temperature range of interest. This is accomplished through the use of a set of four standards, each with a well defined melting point and heat of fusion. These standards are listed in Table XII. The procedure is to place a sample of one of the standards in both sample holders. The isothermal temperature is set 25°C below the melting point. The standard is then heated at 10°C/min through its melting point. If two peaks occur (exothermic and endothermic) the differential temperature calibration is adjusted and the process repeated. When the correct setting is reached only one peak will occur. It should be noted that it is all but impossible to get the differential temperatures to coincide over the entire temperature range of the instrument. Therefore, the calibration should be optimized over the temperature range of interest. In this work, the calibration was optimized over the range of 156°C to 420°C. The differential temperatures over this range were within $\pm 2^\circ\text{C}$.

This particular calibration procedure was carried out when a new sample holder assembly was installed. Initially the calibration was

checked regularly. However, it was found that only slight variations occurred and frequent calibration was not necessary.

TABLE XII
CALIBRATION STANDARDS USED FOR DSC CALIBRATION

Standard	Melting Point (°C)	Heat of Fusion (cal/gm)
Indium	156.60	6.80
Tin	231.88	14.45
Lead	327.47	5.50
Zinc	419.47	25.90

Because of nonlinearities in the platinum sensors, the actual and indicated temperatures differ. The necessary corrections may be determined using the standards listed in Table XII. The procedure is similar to the differential temperature calibration. The isothermal temperature is set approximately 25°C below the melting point of the standard. The scan speed is set at the rate to be used in the actual measurements. A standard is then placed in the sample pan holder and is heated through the melting point of the standard. If the indicated temperature and melting point of the standard (actual temperature) do not coincide, the average temperature calibration must be adjusted.

Again, it is virtually impossible to get perfect agreement between the indicated and actual temperatures over the entire range of the instrument.

This calibration was carried out more frequently than the differential temperature calibration. However, little change occurred over the course of the measurements, except when a new sample holder was installed. A plot of a temperature calibration is shown in Figure 59.

Sample Preparation and Procedure

Obtaining a straight and reproducible baseline over the entire temperature range of the DSC-1B is virtually impossible. For this reason, the experiments were run over three separate temperature ranges with overlap occurring at each interface. The following ranges were selected: (1) 50°C to 190°C, (2) 170°C to 320°C, and (3) 300°C to 470°C.

Because three temperature ranges were used, some difficulty in preparing the samples was encountered. Testing virgin material samples at the two higher temperature ranges required using samples which had been "prerun" up to the lower limit of the temperature range of interest. These samples were obtained by preheating the material in the TGS-2 system in a nitrogen atmosphere at 20°C/min. When the temperature limit had been reached, the samples were quenched in a flowing nitrogen atmosphere. The samples were removed from the TGS-2 and placed directly in the DSC. If they were not run within 30 minutes, they were discarded and a new sample prepared.

The powdered samples of virgin material were prepared the same as for the thermogravimetric analysis. The char material samples were

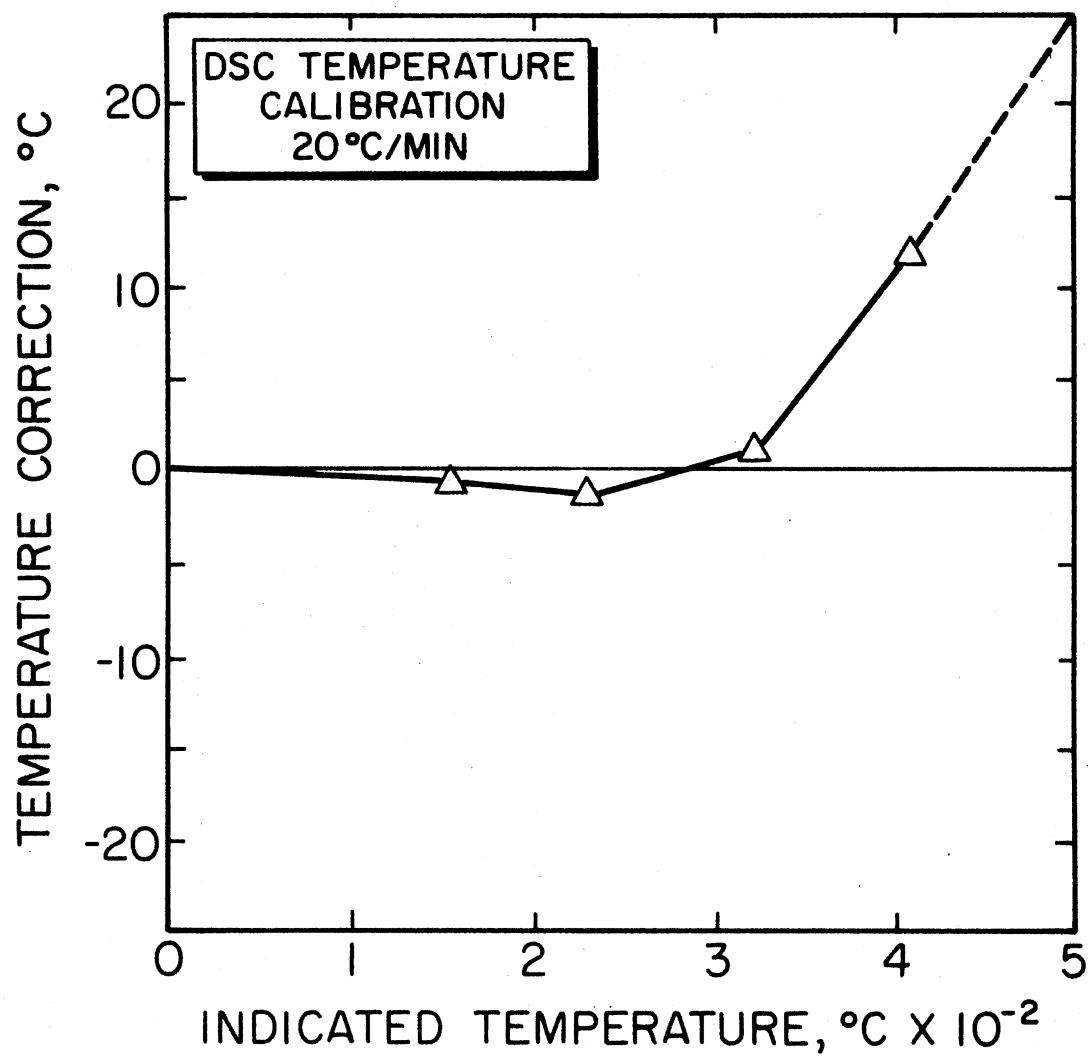


Figure 59. Temperature Calibration for DSC

obtained by precharring powdered samples of the virgin material in the thermogravimetric system. Samples were run at 160°C/min heating rate in a nitrogen atmosphere to 950°C. The pre-experimental handling of both the virgin and char material was identical to that used in the thermogravimetric analysis, described in Chapter IV.

Four scans were necessary for each material over each temperature range. The virgin and char materials required one scan each. Empty sample pan scans were run in order to establish a baseline and a sapphire standard was run with each set of data. The use of the sapphire standard will be discussed later.

Before running a sample, the baseline was established. This was accomplished by scanning through the temperature range of interest with empty sample pans in both the sample and reference side. The procedure was to raise the isothermal temperature to 10°C below the lower temperature limit of the temperature range of interest. Empty sample and reference pans were then placed in the sample holder. The radiation domes were placed over the pans and the sample cover was replaced. The purge gas was allowed to flow for 3-5 minutes at 60 mL/min before initiating the run. The program temperature scan was run at 20°C/min to the upper limit of the temperature range of interest. The unit was then cooled down to the initial temperature and the process repeated for the sapphire, char, and virgin materials. The DSC run for the lower temperature range for MXBE-350 is shown in Figure 60.

Sample weights ranged between 5 and 15 mg and were weighed on a Perkin-Elmer AD-2Z microbalance. The accuracy of this unit is the same as the TGS-2 microbalance. The balance is shown in Figure 61.

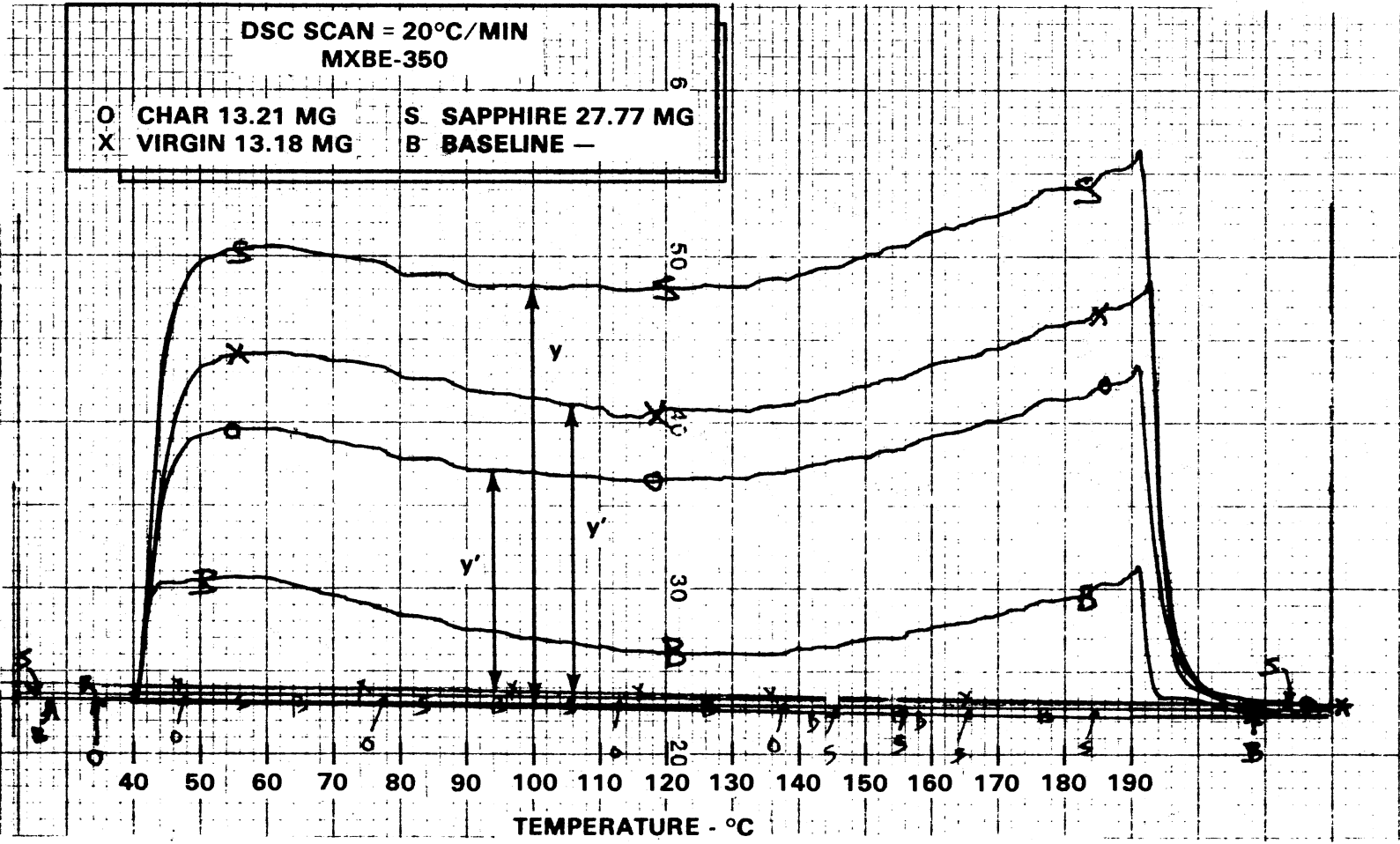


Figure 60. 20°C/Min DSC Scan for MXBE-350



Figure 61. Perkin-Elmer AD-22 Microbalance

Several points regarding the operation of the DSC-1B are in order. First, the system is extremely sensitive to the radiation exchange between the sample pans, sample holder, and radiation domes. A slight change in the position of one of these components will result in large discrepancies between the isothermal baselines. Once the baseline is run, each component must be replaced as closely as possible to the original position. This can be accomplished by marking the pans and lids and taking care to realign them. This procedure cannot be overemphasized. Also, care must be taken to match radiation domes as closely as possible. This results in much flatter and more reproducible baselines.

Second, the sample head must be kept clean. Any deposits of volatiles or soil will render the data useless. This was found to be a major problem at the higher temperatures where volatiles were condensing on the heating unit and radiation dome. To overcome this difficulty, the sample head was cleaned with acetone between each run. Additionally, the radiation domes were stored in containers of acetone to remove the condensates.

Havens [12] showed the importance of the radiative characteristics of the sample holder. He calculated that a 0.1 change in the surface emissivity of a sample pan surface containing a material with a specific heat of $0.35 \text{ cal/gm-}^\circ\text{C}$ would result in differential power inputs of 23 times those normally required.

Finally, the mass of the sample and reference pans should be matched as closely as possible. The baseline shown in Figure 60 could have been inverted by more closely matching the empty pan weights. This can be accomplished by adding or removing sample pan lids to the

reference pan. The baseline can be more closely reproduced if the weights are evenly matched.

Also, the range of the DSC-1B was insufficient to get completely through the decomposition of the ablatives. Therefore, the high temperature range scan was stopped at an indicated temperature of 470°C and held isothermally until the sample had completely degraded. This event was evidenced by the return to the isothermal baseline.

Data Analysis and Results

The specific heat of a volatile sample can be determined by the method proposed by Brennan [28]. This requires the assumption that the fraction of mass reacted is proportional to the fraction of energy liberated at the temperature of interest. An alternate technique involves using Equation (41), where the temperature dependent mass of the sample is known. These data were obtained by decomposing samples in the TGS system at the same heating rate used in the DSC measurements. Equation (41) may be rewritten with the temperature dependent mass as:

$$C_p = \frac{dq/dt}{m(T) dT/dt} \quad (72)$$

Equation (72) could be used to calculate the specific heat directly. However, any errors in dq/dt or dT/dt would reduce the accuracy of the results. By using data obtained from a known mass of sapphire in conjunction with sample data, the need for accurate calibration of dq/dt is eliminated. Further, any errors in dT/dt will be cancelled out. Writing Equation (72) for the sapphire standard results in:

$$C_{pstd} = \frac{(dq/dt)_{std}}{m_{std} (dT/dt)} \quad (73)$$

where the subscript std indicates sapphire standard.

Taking the ratio of Equations (72) and (73) yields:

$$\frac{C_{ps}}{C_{pstd}} = \left(\frac{(dq/dt)_s}{m(T)_s dT/dt} \right) / \left(\frac{(dq/dt)_{std}}{m_{std} (dT/dt)} \right) \quad (74)$$

where the sample is indicated by the subscript s. Rearranging and eliminating dT/dt results in Equation (75):

$$C_{ps} = \frac{(dq/dt)_s}{(dq/dt)_{std}} \frac{m_{std}}{m(T)_s} C_{pstd} \quad (75)$$

Equation (75) may be used to determine the temperature dependent specific heat directly from the thermogram. Only the two ordinate deflections, dq/dt, and m(T), from the thermogravimetric data are required. The temperature dependent specific heat of artificial sapphire is well defined and is given by Ginnings and Furukawa [42]. The ordinate deflections for the sapphire and sample are shown as y and y' respectively, in Figure 60.

This technique was applied to the six materials listed in Table IX. DSC data were obtained at a heating rate of 20°C/min from 50°C to 470°C. These data were digitized at 10°C intervals. The temperatures were corrected using temperature calibration data similar to those presented in Figure 59. As with the thermogravimetric data, temperatures were corrected by a linear interpolation between the calibration points. For the materials, m(T) was taken from the 20°C/min thermogravimetric

runs presented in Figures 26 through 31. Equation (75) was used to convert the data to temperature dependent specific heat and heat of decomposition. The results of these calculations for all six materials are presented as Figures 62 through 67.

The range of the DSC-1B was not sufficient to cover the entire decomposition process. Therefore, the curves had to be extrapolated over the last 50 to 200°C. The remainder of the curves were completed using a technique similar to that proposed by Brennan [28]. The area enclosed by the char and apparent specific heat was numerically integrated up to approximately 500°C, i.e., the upper limit of the experimental data. The fraction of the mass reacted at this point was known and the total heat of decomposition was calculated by:

$$Q_p = Q_R / \left(\frac{1 - \gamma_R}{1 - \gamma_f} \right) \quad (76)$$

where Q_R = total heat of pyrolysis up to γ_R
 γ_R = fraction of pyrolyzable material reacted
 γ_f = final fraction remaining.

Using the calculated value for Q_p and the shape of the thermogravimetric weight loss and derivative of weight loss curves, the apparent specific heat curves were completed. The char specific heat was extrapolated from a linear least squares fit of the experimental data. The average specific heat of the virgin material was calculated over a temperature range of 200 to 390°C. A summary of the DSC measurements for all six materials is given in Table XIII.

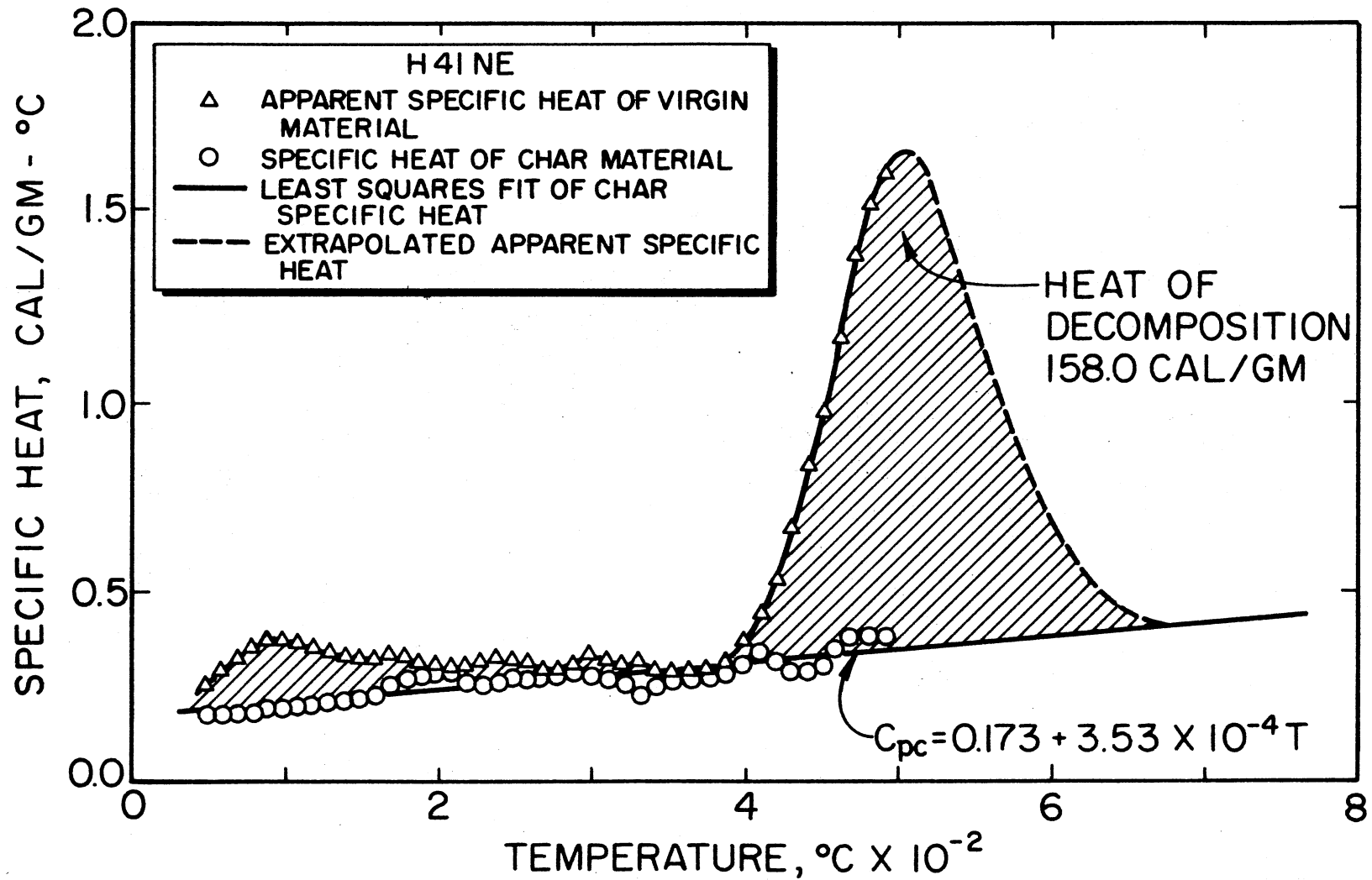


Figure 62. Specific Heat and Heat of Decomposition of H41NE

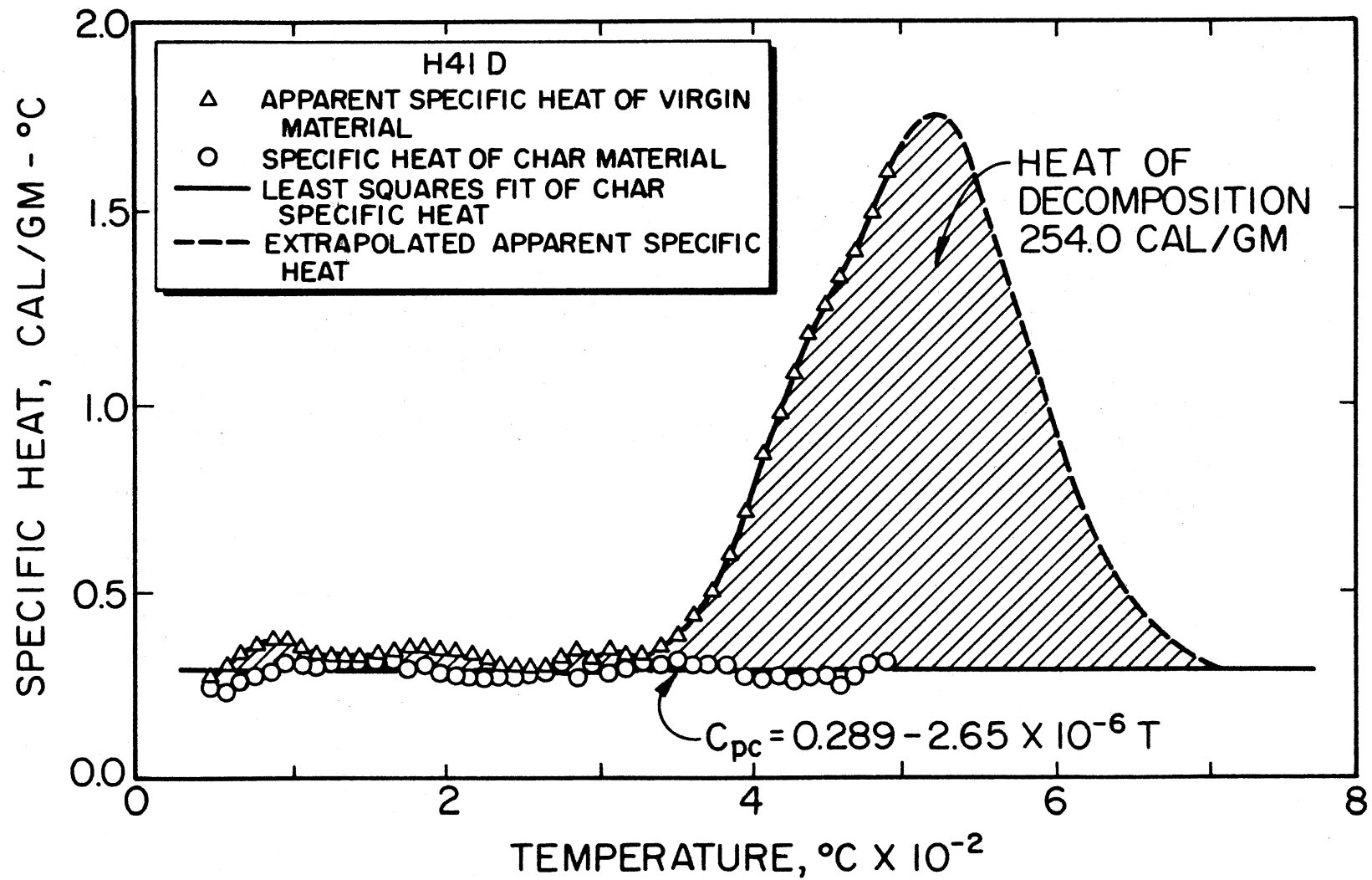


Figure 63. Specific Heat and Heat of Decomposition of H41D

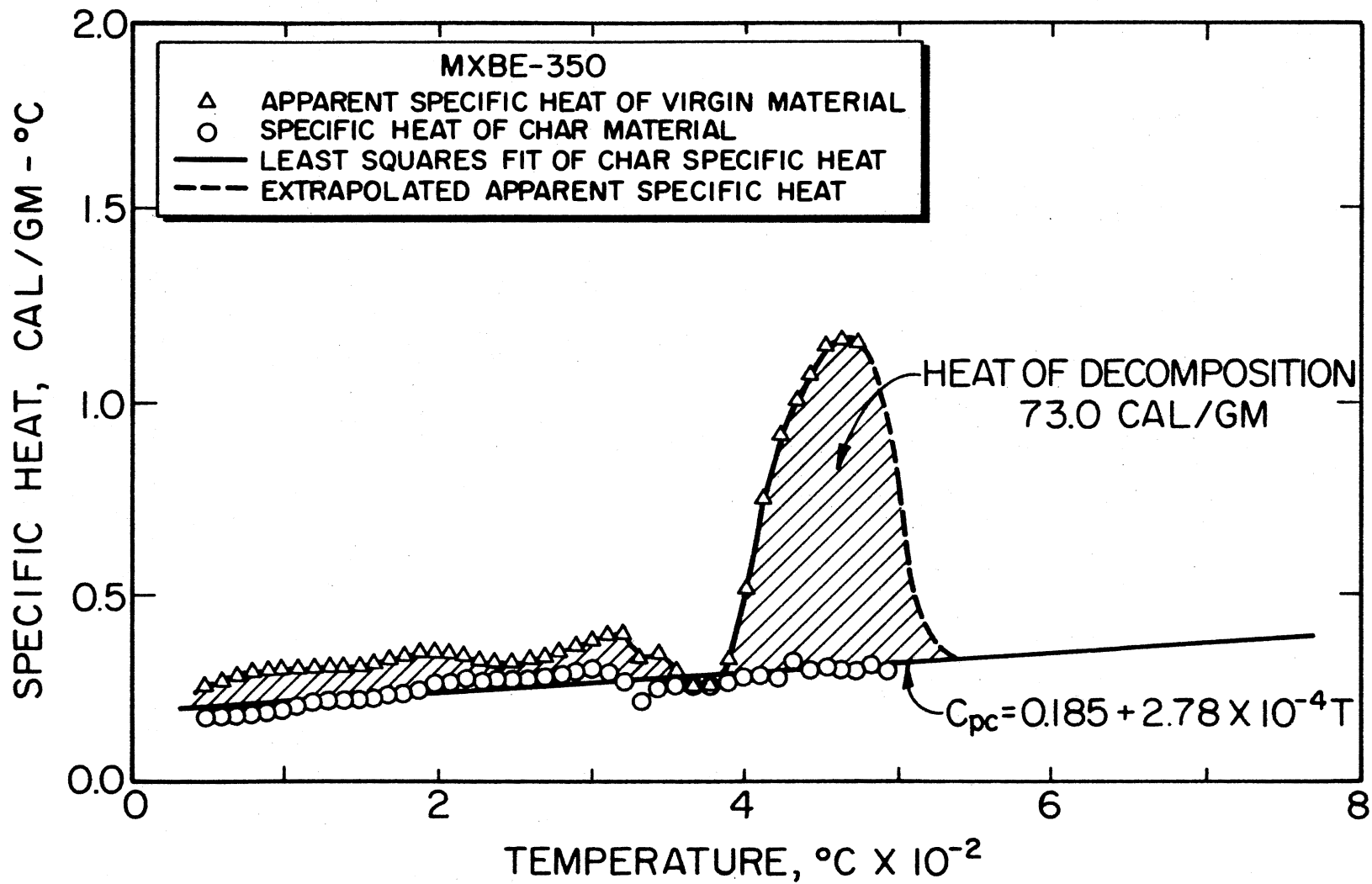


Figure 64. Specific Heat and Heat of Decomposition of MXBE-350

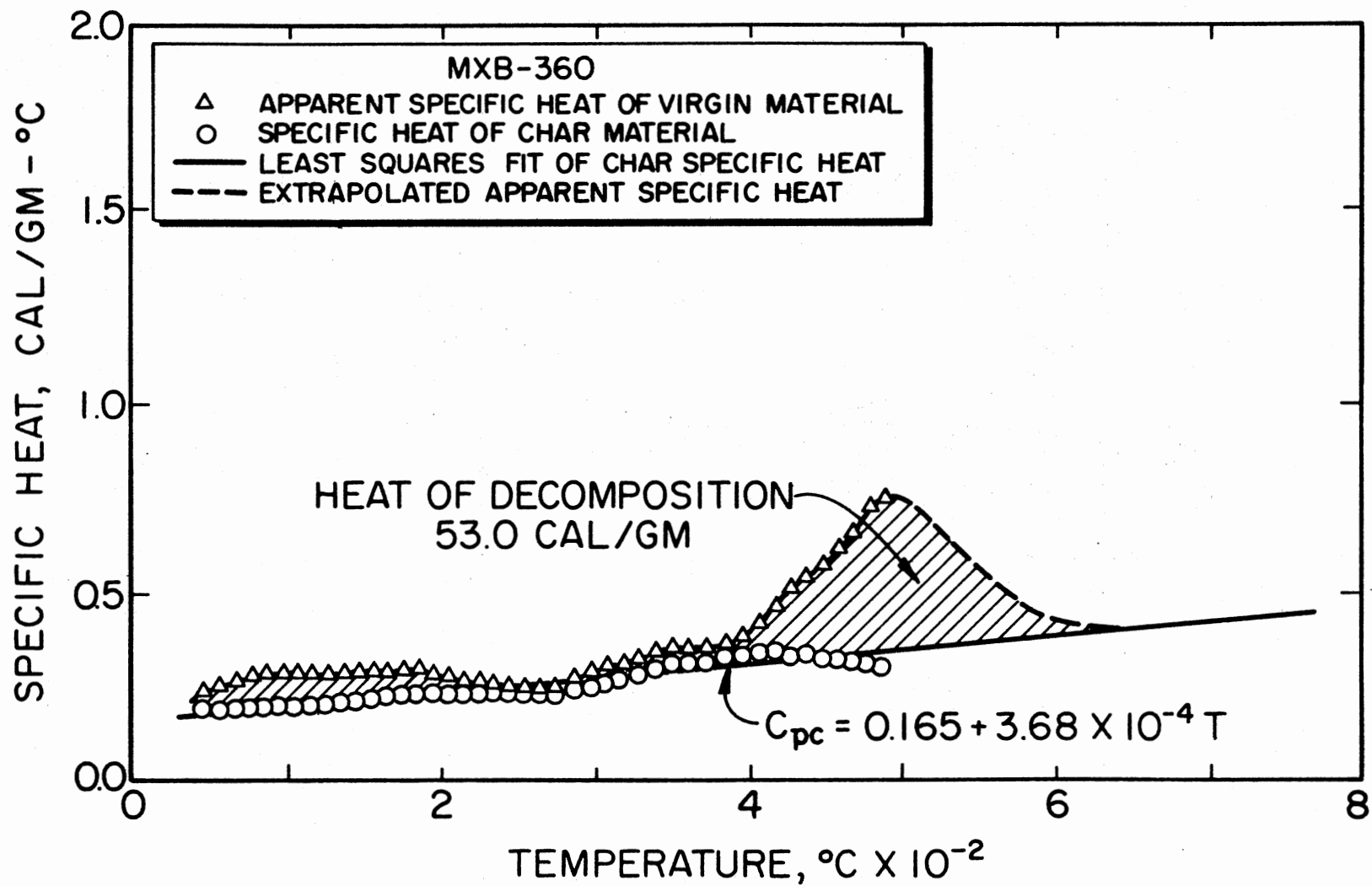


Figure 65. Specific Heat and Heat of Decomposition of MXB-360

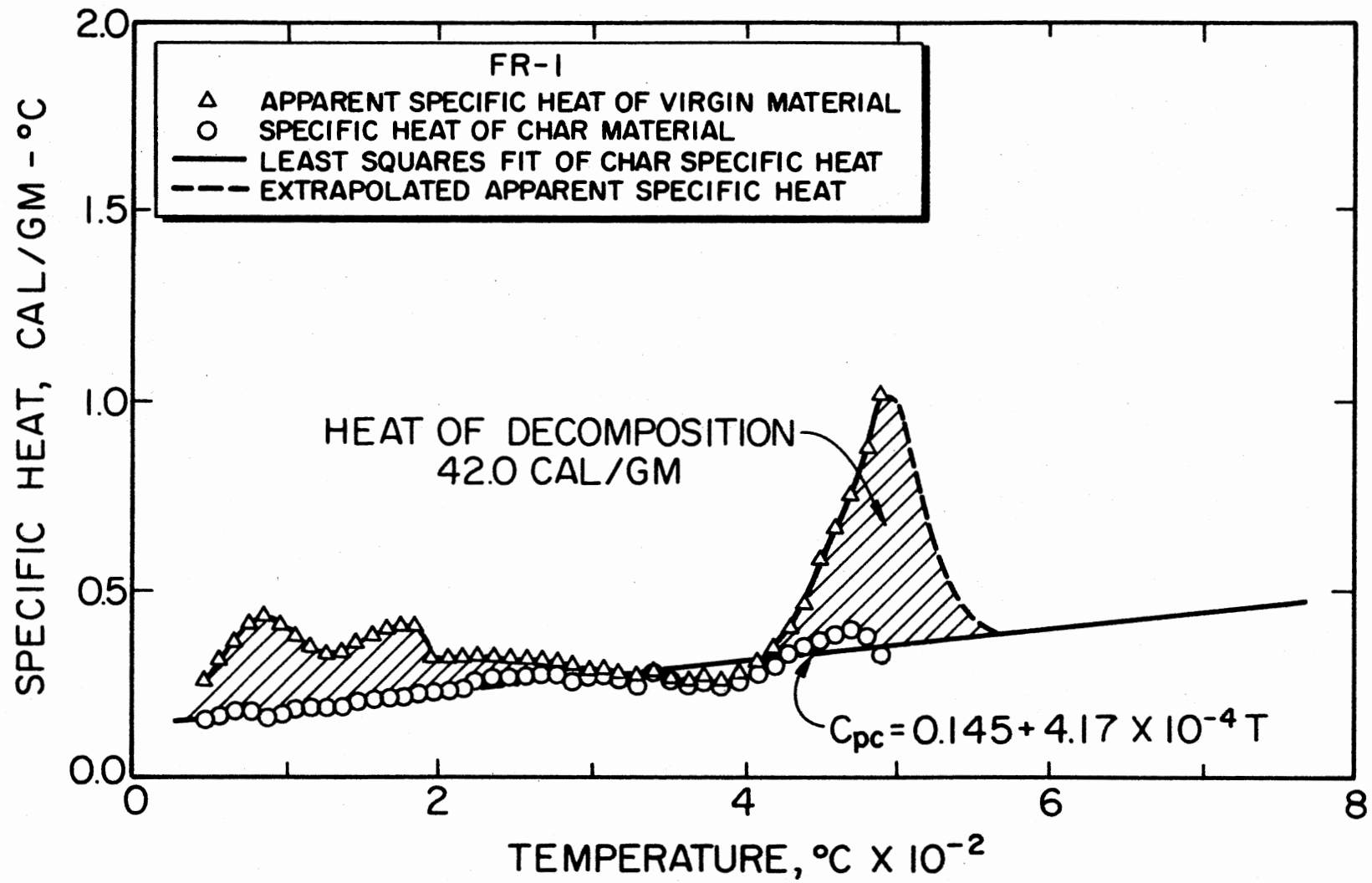


Figure 66. Specific Heat and Heat of Decomposition of FR-1

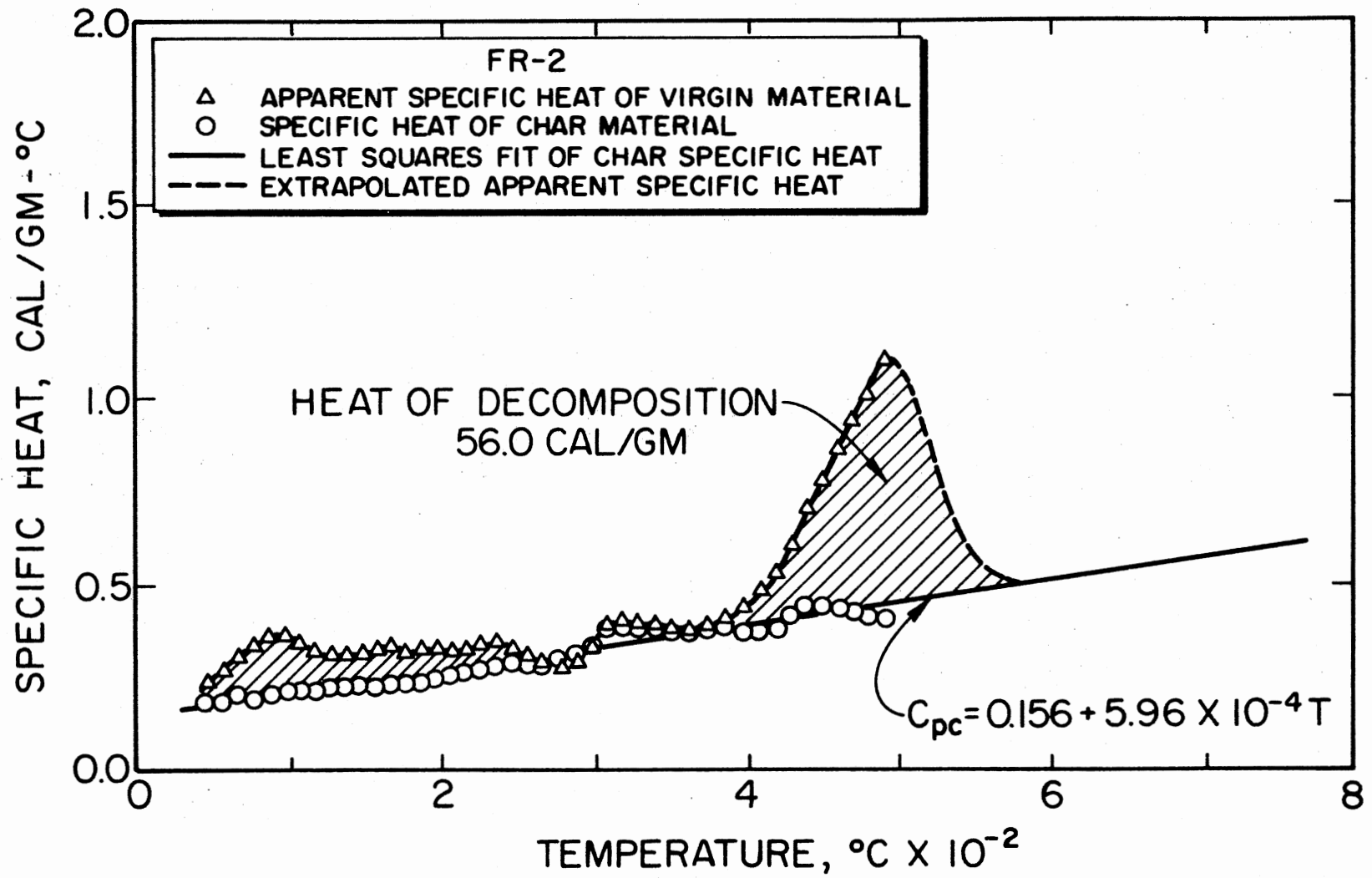


Figure 67. Specific Heat and Heat of Decomposition of FR-2

TABLE XIII
RESULTS OF SPECIFIC HEAT MEASUREMENTS

Material	Average Specific Heat of Virgin Material (cal/gm-°C)	Linear Temperature Dependent Specific Heat of Char Material (cal/gm-°C)		Estimated Heat of Pyrolysis (cal/gm)
		Intercept at 0°C	Slope	
Haveg 41NE	0.307	0.173	3.53×10^{-4}	158.0
Haveg 41D	0.331	0.289	-2.56×10^{-6}	254.0
Fiberite MXBE-350	0.332	0.185	2.78×10^{-4}	73.0
Fiberite MXB-360	0.303	0.165	3.68×10^{-4}	53.0
Fiber Materials FR-1	0.294	0.145	4.17×10^{-4}	42.0
Fiber Materials FR-2	0.360	0.156	5.96×10^{-4}	56.0

CHAPTER VI

TEMPERATURE MEASUREMENTS

The temperature measurement portion of this study was undertaken to provide sufficient experimental data to evaluate the accuracy of the predictions of the model. An experiment was designed to measure the in-depth temperature profiles in a one-dimensional slab of pyrolyzing material exposed to a radiative heat flux.

Apparatus

Two banks of water cooled tungsten lamps capable of producing heat fluxes up to $50 \text{ cal/cm}^2\text{-sec}$ were used to irradiate the samples. Power to the lamps was controlled by a Robicon Corporation Model 401-328-5 power controller. A photograph of the lamps and sample holder is presented as Figure 68.

Each bank of lamps contained 21 tungsten filament bulbs connected for three-phase delta, 480-volt operation. Each lamp was equipped with a water cooled copper shroud. The 15-cm long shroud reduced the outlet to $15.24 \text{ cm} \times 15.24 \text{ cm}$. Both the inside of the shrouds and lamp reflectors were coated with gold to increase the heat flux and improve the energy distribution. The cooling water flow rate was approximately 55 ℓ/min through each unit. The outlet of each shroud was covered with a quartz lens to prevent volatiles from coating the inside surfaces of the lamp unit. The entire unit was mounted on a 110-cm long, 12-cm

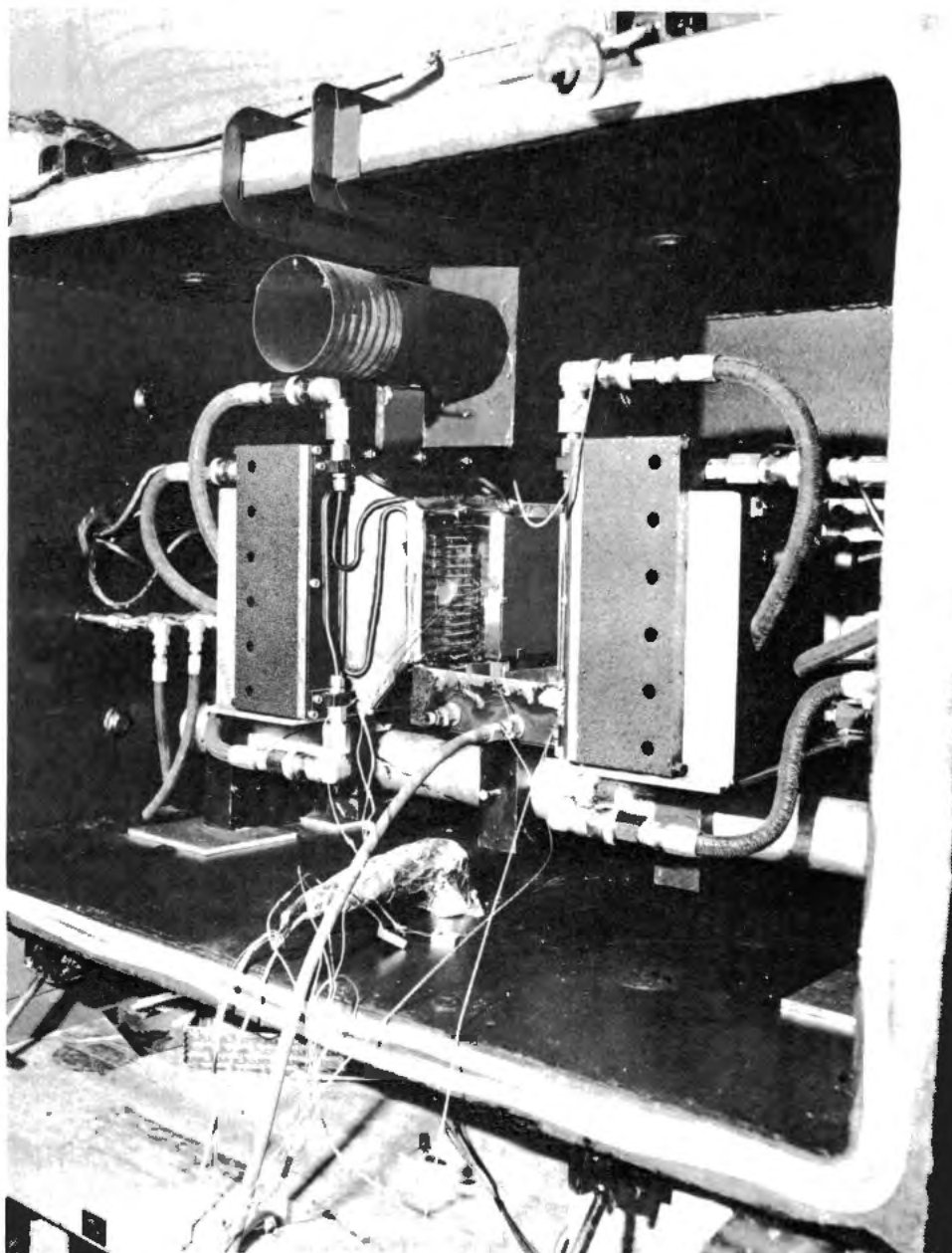


Figure 68. Tungsten Lamps and Sample Holder

diameter aluminum shaft to allow the distance between the sample and lamps to be varied. Also, the lamps could be rotated around the tube to allow easy access.

The sample holder was constructed to rotate around the same shaft on which the lamps were mounted. The holder consisted of a tantalum strap mounted on an aluminum block. The strap was 2 cm wide and covered approximately 5 cm on each vertical edge of the sample. This is depicted in Figure 68.

The power to the lamps was monitored with a Weston Model 2044 Iron vane meter used in conjunction with a current transformer. Temperatures were monitored using 40-gage chromel-alumel thermocouples. The thermocouples were contained in 15-cm long, 0.10-cm diameter 304-stainless steel sheaths. The thermocouples were referenced to 0°C using Omega Model CJ-K cold junctions. The thermocouple output was recorded on two Linear Instruments Model 598 3-channel strip chart recorders.

Calibration

The lamps were calibrated using a Medtherm Model 64-50-20 Gardon type heat flux transducer. The calibration of the Gardon transducer was performed with a Thermogage, Inc. blackbody standard capable of producing 0-100 cal/cm²-sec. The instrument operates by heating a 4-cm × 7.5-cm pyrolytic graphite plate held between two water cooled copper blocks. The instrument is pictured in Figure 69. The blackbody temperature of the graphite plate was measured with a Leeds and Northrup Model 8630 optical pyrometer. The calibration for the heat flux transducer is shown in Figure 70.

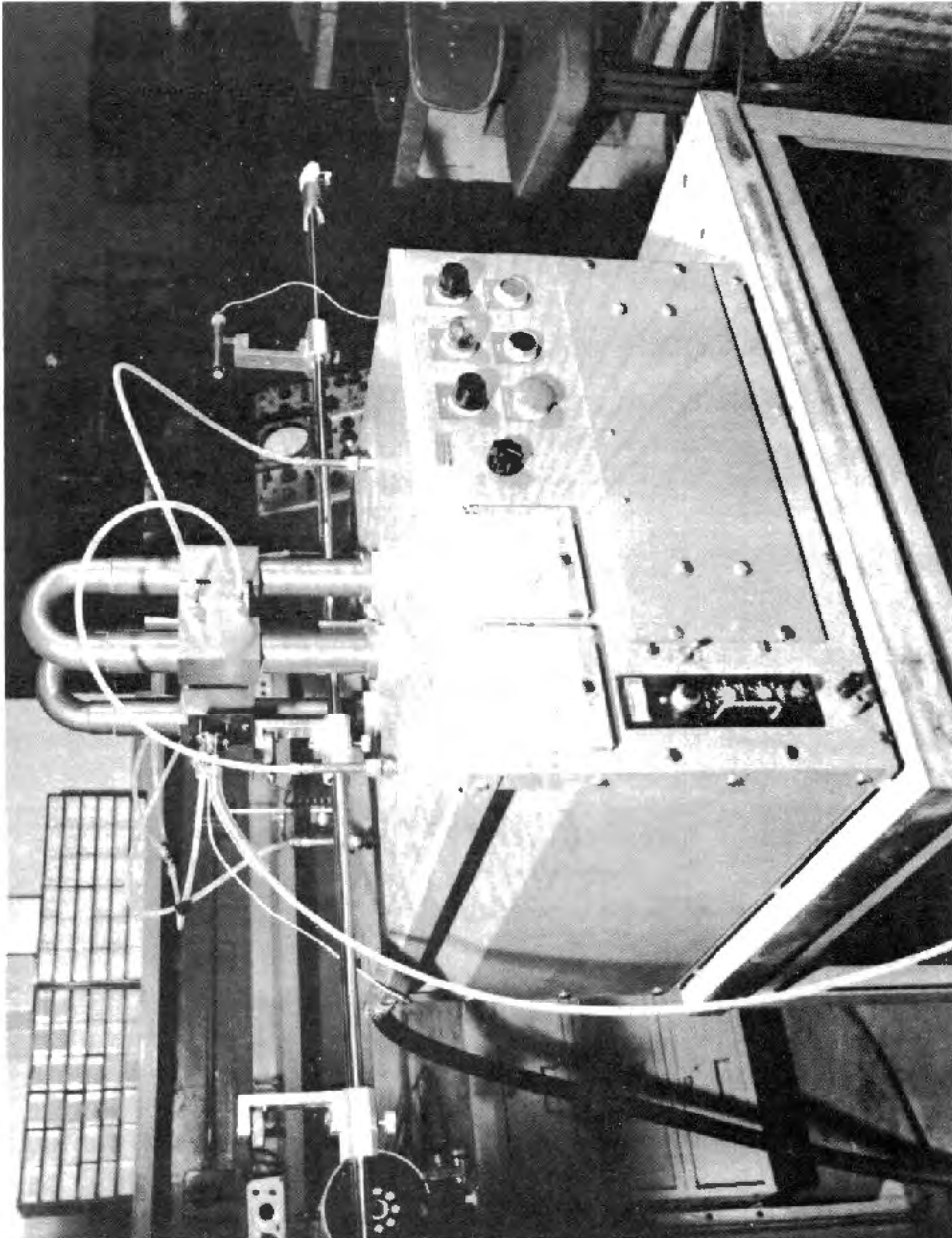


Figure 69. Thermo-gage, Inc. Blackbody Standard

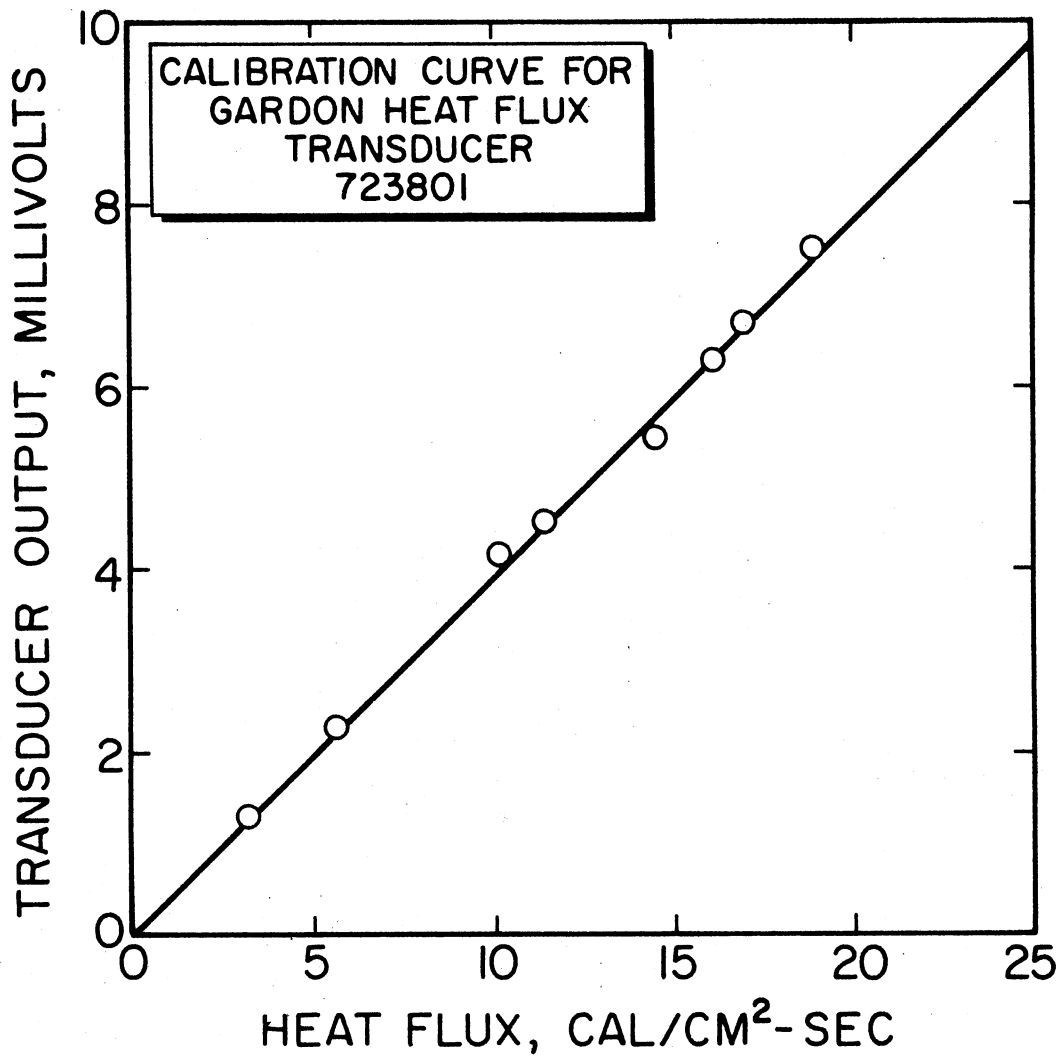


Figure 70. Calibration Curve for Gardon Heat Flux Transducer

The lamps were calibrated with the heat flux transducer mounted in a copper block held by the sample holder. The dimensions and position of the copper block were identical to the material samples. The energy distribution over the surface of the sample is important. Therefore, the copper block was constructed to allow the heat flux transducer to be mounted in five locations. The mounting positions were located in each corner and in the center of the block. The calibration curves for the heat flux transducer located in the center position are shown in Figure 71. The difference in the heat flux due to the hot and cold lenses is depicted by this figure as well.

The energy distribution over the surface of the sample was determined by measuring the heat flux at five different locations. The results are listed in Table XIV. The distribution is within 9 percent with the exception of the lower right corner which is off by 15 percent. Distribution and center position calibrations were performed for both lamps to ensure an equal heat flux to each surface.

Sample Preparation and Procedure

In-depth temperature profiles were measured for three of the six materials previously discussed. Samples were machined to 15 cm × 15 cm × 2 cm from larger blocks of material. The samples were machined on both sides and the edges. Tolerances were held to within ±0.1 cm. Either two or three 0.118-cm diameter holes were drilled approximately 7.5 cm deep to accommodate the thermocouples. Figure 72 depicts the sample dimensions and approximate locations of the thermocouples.

The exact location of the thermocouple was determined from x-rays of the samples with tungsten rods imbedded in the thermocouple holes.

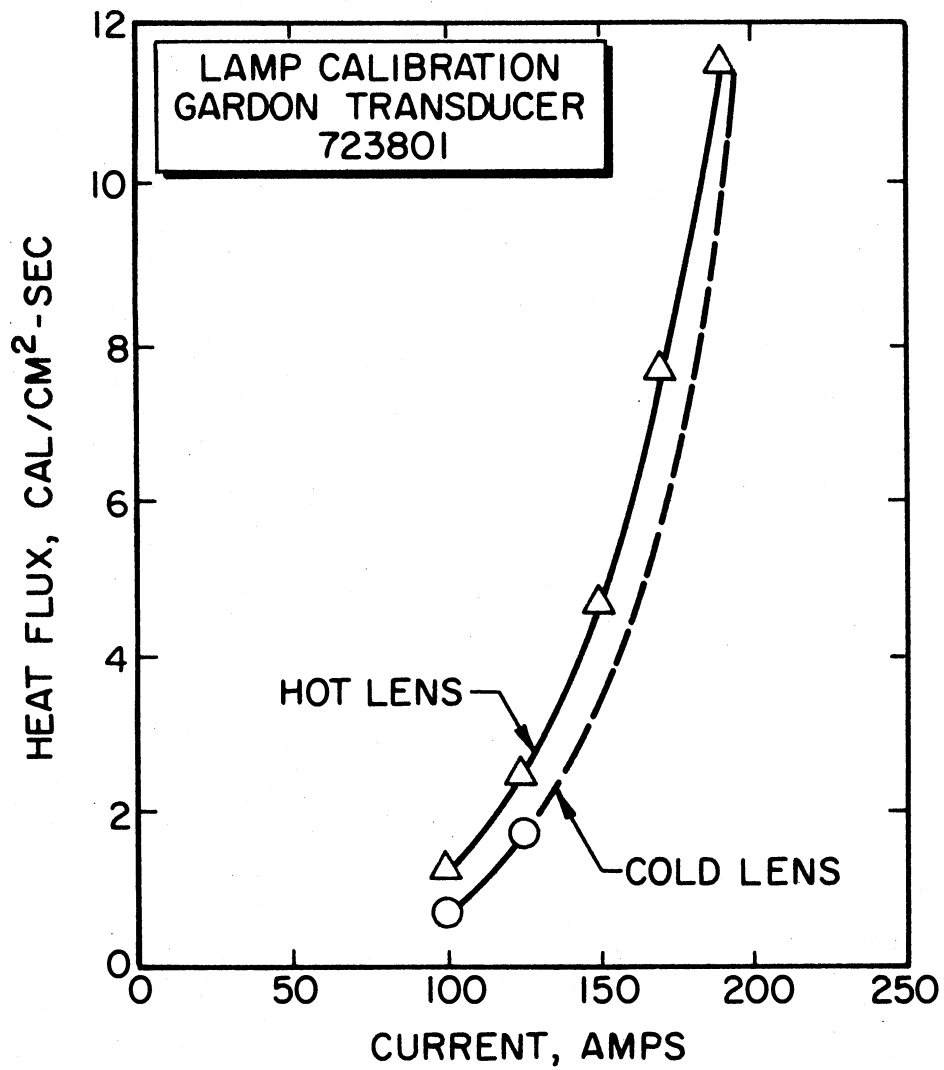


Figure 71. Calibration Curve for Tungsten Filament Lamps

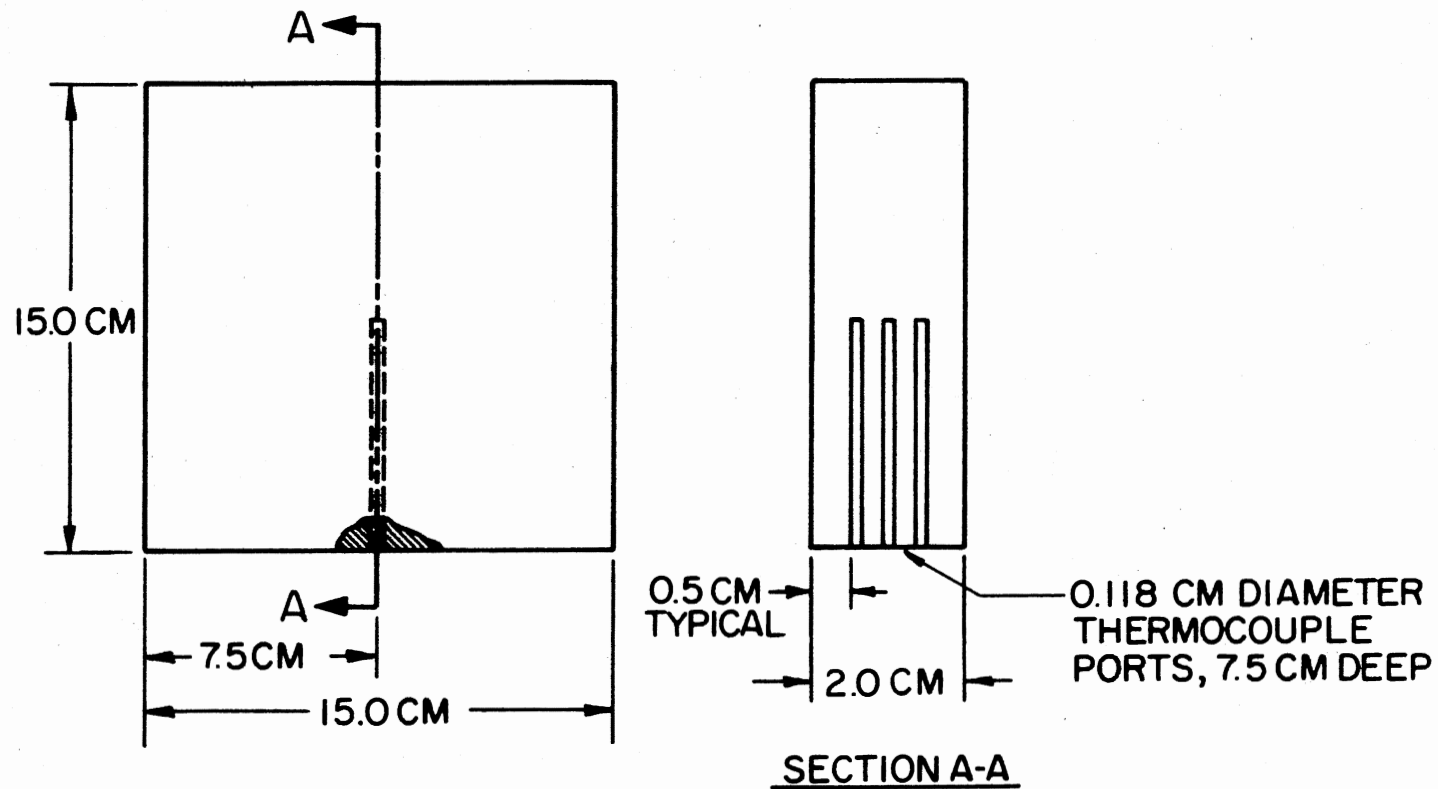


Figure 72. Sample Dimensions and Thermocouple Locations

If the sample and x-ray dimensions differed, the thermocouple locations were scaled according to the true sample dimensions.

TABLE XIV
HEAT FLUX DISTRIBUTION RELATIVE TO CENTER POSITION

Location	Magnitude of Heat Flux Relative to Center Position
Center	1.0
Upper Left	0.948
Upper Right	0.917
Lower Right	0.848
Lower Left	0.910

The sample dimensions were determined with a Brown and Sharpe Hite-Tronic height gauge at five locations on the 15-cm × 15-cm surface and two locations on each of the edges. The average values were used for all calculations. Samples were weighed on a Mettler Model P5N balance. The dimensions and density of each of the samples tested is shown in Table XV. A photograph of a virgin sample of MXBE-350 with thermocouples inserted is shown in Figure 73.

The emissivity of each material is different. For this reason, after machining, the surfaces were coated with lamp black. After

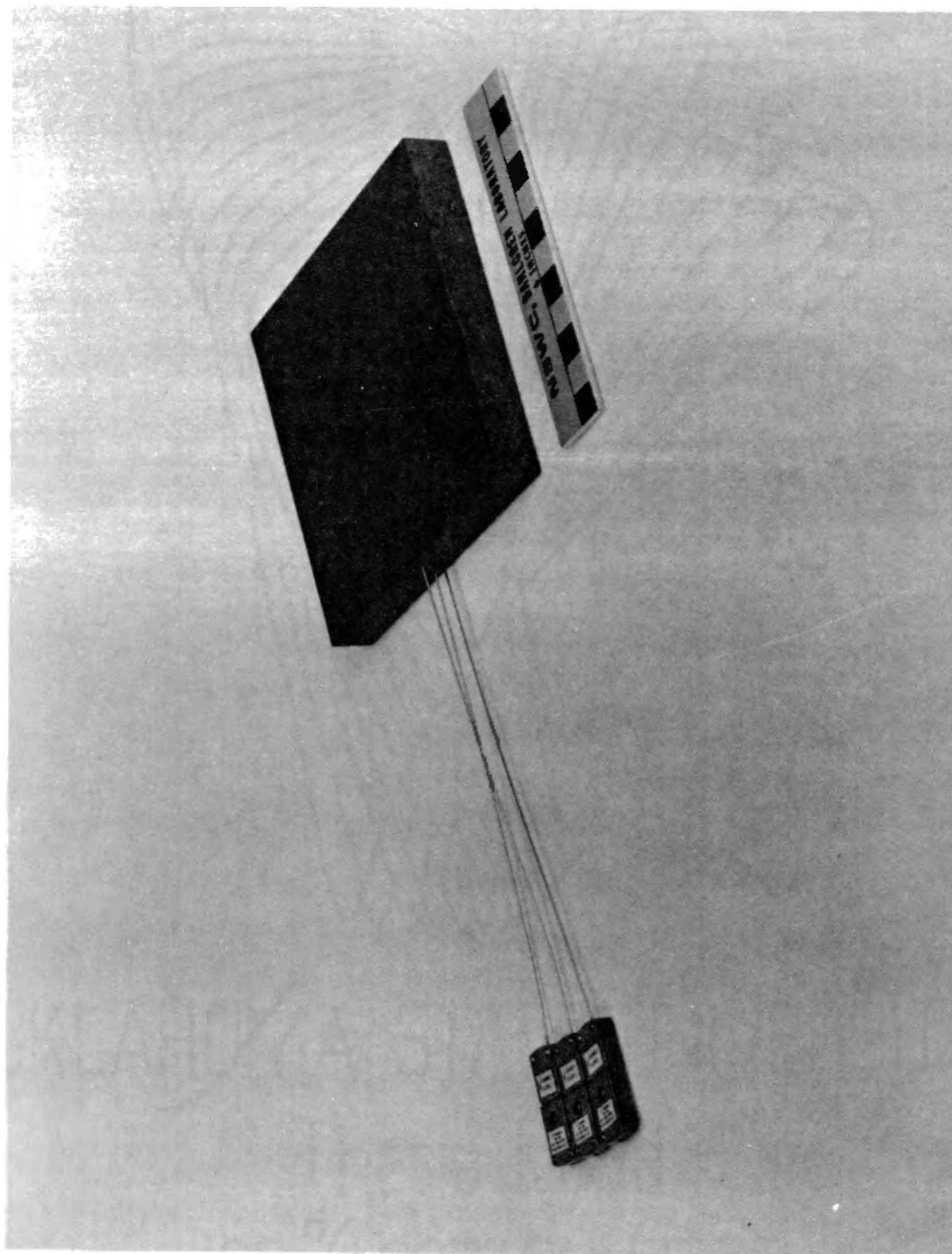


Figure 73. Sample of MXBE-350 Virgin Material with Thermocouples

coating, the samples were placed in a vacuum oven at 30°C for two days prior to testing in order to remove moisture. This resulted in weight losses of less than one percent. However, this procedure was continued throughout the work. After running, the samples were weighed again to determine their fraction of weight loss. Figure 74 is a photograph of a pyrolyzed sample of MXBE-350. The results of the temperature measurements are presented in Chapter VII.

TABLE XV
SUMMARY OF DIMENSIONS AND DENSITY OF MATERIALS
USED IN TEMPERATURE PROFILE MEASUREMENTS

Material	Dimensions (cm)	Virgin Material Density (gm/cm ³)	Number of Thermocouples
H41NE	15.08 × 15.00 × 1.99	1.81	3
MXBE-350	15.00 × 15.02 × 2.01	1.71	3
MXBE-350	15.00 × 15.02 × 2.05	1.70	2
FR-1	14.96 × 14.84 × 1.97	1.47	3

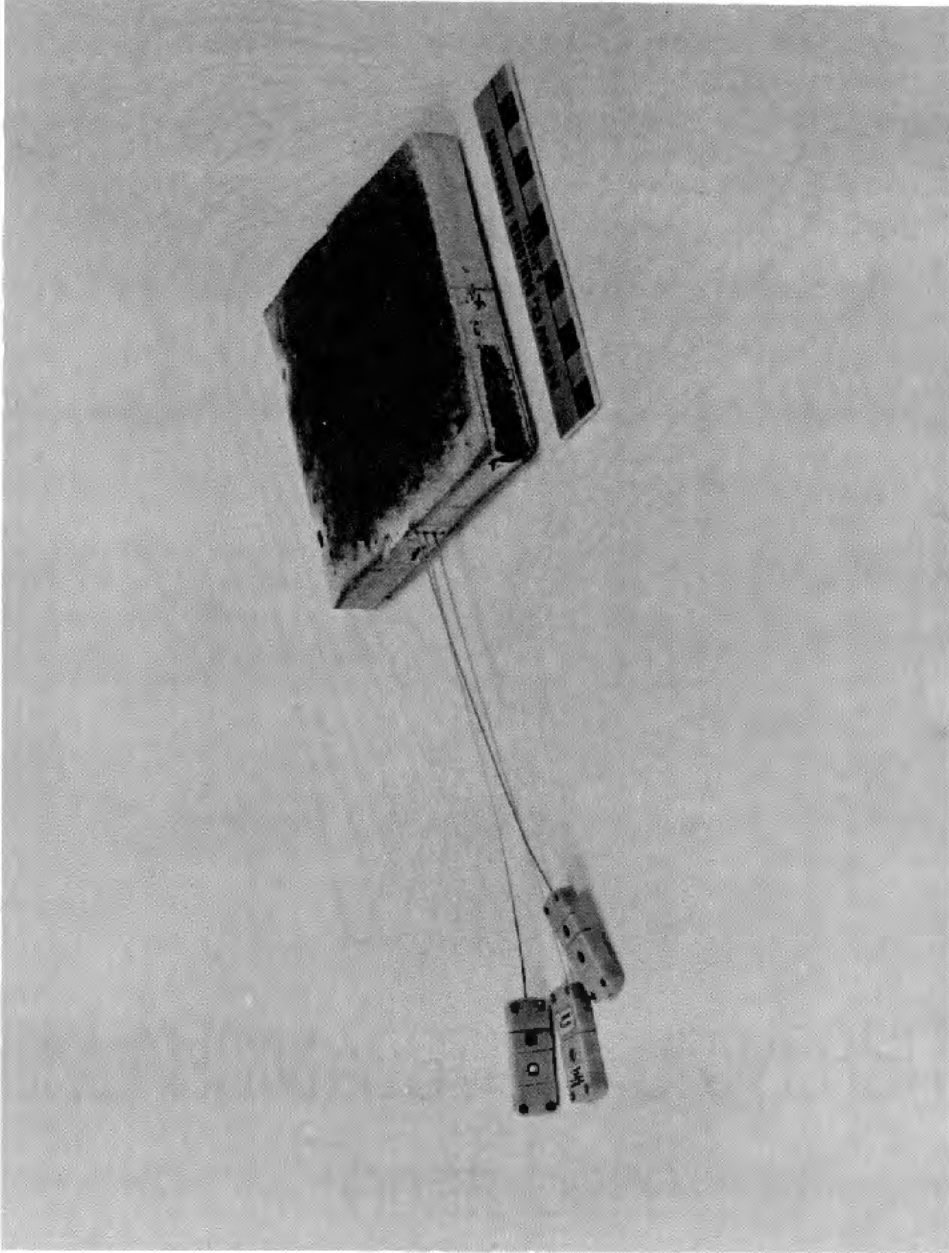


Figure 74. Sample of MXBE-350 After Pyrolysis

CHAPTER VII

COMPARISON OF CALCULATED AND EXPERIMENTAL TEMPERATURE PROFILES

Temperature profiles were measured for the materials listed in Table XV. With the exception of FR-1, these temperatures were compared to values calculated by the thermal model. Experimentally determined values for the kinetic parameters, specific heat, and heat of decomposition were used as input to the model. The thermal conductivity of the virgin material was estimated using published values. The thermal conductivity of the char was calculated by Equation (3). The thermal and kinetic properties used in the model are listed in Table XVI.

In-depth temperatures were measured for pyrolyzing H41NE exposed to a radiant heat flux of 2.2 cal/cm²-sec. The sample was heated for 600 seconds, at which time ignition occurred. Thermocouples were located at depths of 0.44, 0.60, and 0.64 cm. The results of these measurements are presented as data points in Figure 75. The solid lines represent the calculated values of the temperature, while the broken lines represent the nondimensional active material density, ρ_a/ρ_0 , at the same depths. Figure 76 depicts both the calculated temperatures and nondimensional active material density as a function of spatial location at 10, 150, 300, 450, and 600 seconds. The Fourier number used in the computer simulation was 0.24, with $\Delta x = 0.01$ cm.

TABLE XVI
 PROPERTIES USED IN TEMPERATURE CALCULATIONS
 FOR H41NE AND MXBE-350

Property	H41NE	MXBE-350
Virgin Density (gm/cm ³)	1.81	1.70
Final Char Density (gm/cm ³)	1.44	1.12
Virgin Thermal Conductivity (cal/cm-sec-°C)	7.25×10^{-4}	5.00×10^{-4}
Final Char Thermal Conductivity (cal/cm-sec-°C)	5.76×10^{-4}	3.30×10^{-4}
Virgin Specific Heat (Average) (cal/gm)	0.307	0.332
Final Char Specific Heat (at 0°C) (cal/gm)	0.173	0.185
Specific Heat of Volatiles (cal/gm)	0.24	0.24
Heat of Decomposition (cal/gm)	158.0	73.0
Average Activation Energy (kcal/gm-mole)	62.13	52.11
Pre-Exponential Factor (sec ⁻¹)	1.98×10^{29} 8.16×10^{18}	6.78×10^{44} 1.30×10^{16}
Order of Reaction	17.33 6.30	55.40 3.81
Emissivity	0.90	0.90

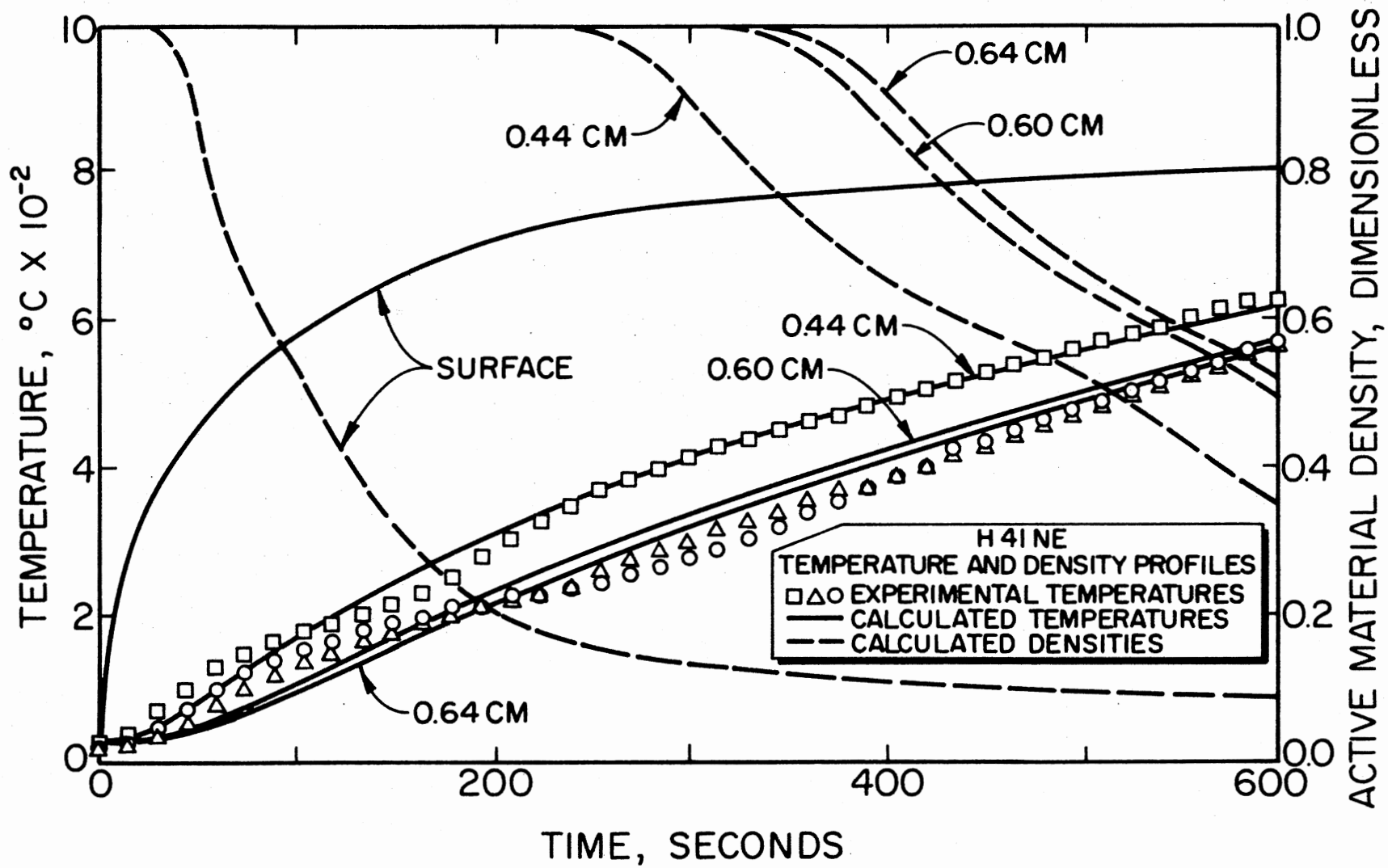


Figure 75. Calculated and Experimental Temperatures and Calculated Active Material Densities for H41NE

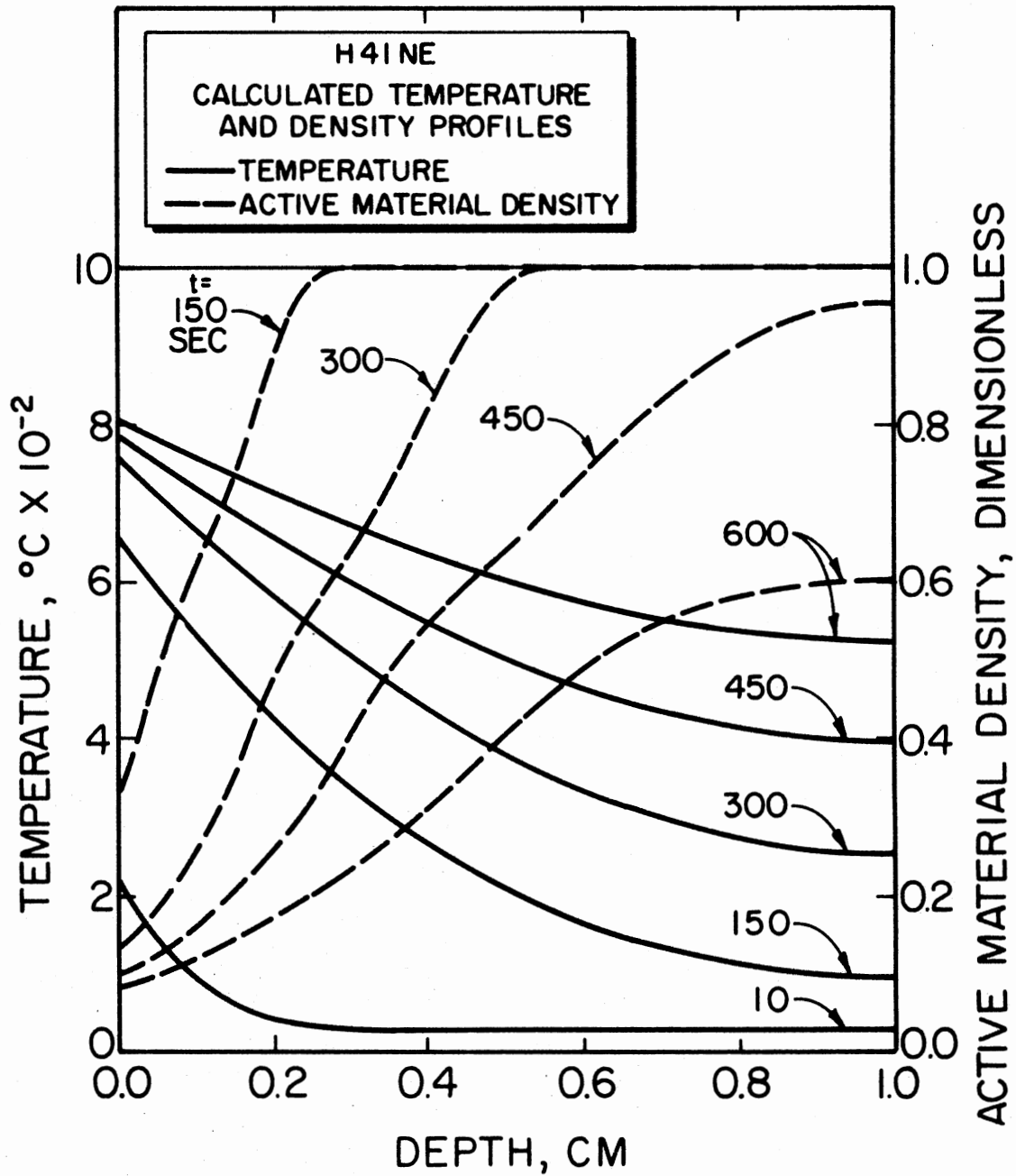


Figure 76. Calculated Spatial Dependent Temperatures and Active Material Densities for H41NE

The trends in the experimental data presented in Figure 75 are similar to those exhibited for wood at the lower temperatures. A low temperature endothermic reaction resulted in a temperature depression near 200°C. This same endothermic reaction is evident in the specific heat data shown in Figure 62. Unlike wood, however, after the initial temperature depression the temperatures are reasonably linear with time. The sharp temperature rise which usually accompanies the passage of the pyrolysis interface is not present. This is primarily a result of the high endothermic heat of decomposition of H41NE.

There is reasonably good agreement between the calculated and experimental temperatures for H41NE. The variations are thought to be due primarily to the lack of accurate temperature dependent thermal conductivity data for both the virgin and char components and the endothermic reaction which is not considered in the model. In order to evaluate the accuracy of the calculated temperatures, a statistical analysis of the data was performed for each thermocouple location. Additionally, overall errors were calculated based on the data from all three locations. The results of these computations are presented in Table XVII.

Two samples of MXBE-350 were run using heat fluxes of 4.7 and 2.3 cal/cm²-sec. The sample irradiated at 4.7 cal/cm²-sec contained thermocouples at depths of 0.40, 0.44, and 0.96 cm. The test was terminated upon ignition of the sample at approximately 255 seconds. The results of the calculated and experimental temperatures and calculated nondimensional active material densities are shown in Figure 77. The calculated spatial dependence of temperature and nondimensional active

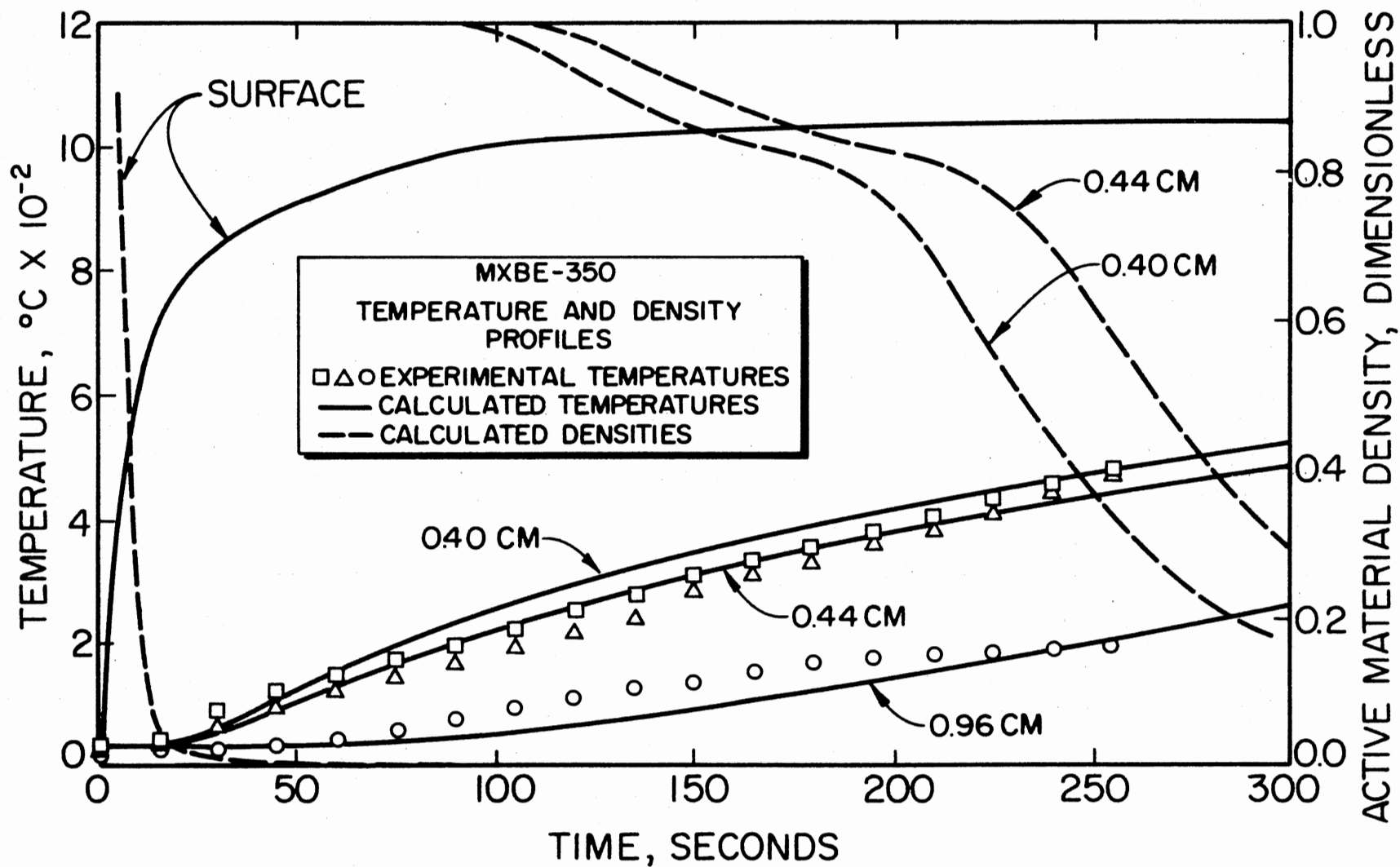


Figure 77. Calculated and Experimental Temperatures and Calculated Active Material Densities for MXBE-350, 255-Second Run

material density at 40, 75, 150, 225, and 300 seconds are presented in Figure 78. The Fourier number for this run was 0.11, with $\Delta x = 0.01$ cm.

TABLE XVII
STATISTICAL ANALYSIS OF CALCULATED VERSUS
EXPERIMENTAL TEMPERATURES FOR H41NE

Thermocouple Depth (cm)	Average Error (°C)	Standard Deviation (°C)	95% Confidence Interval (°C)	Number of Data Points
0.44	-2.48	14.0	-7.0 - 2.03	40
0.60	13.66	22.0	6.68 - 20.65	40
0.64	0.96	29.0	-8.37 - 10.29	40
Total	4.05	23.67	-0.27 - 8.37	120

As with H41NE, the temperature depressions near 200°C are present in MXBE-350. These depressions are not as evident in this data because of the short duration of the test. Again, there is reasonable agreement between the calculated and experimental temperatures. Table XVIII contains the statistical calculations for the MXBE-350 255-second run.

The second sample of MXBE-350 was irradiated at 2.3 cal/cm²-sec. Thermocouples were located at depths of 0.40 and 0.44 cm. Since no ignition occurred, the test was continued through completion of pyrolysis. The Fourier number for the computer run was 0.16, with

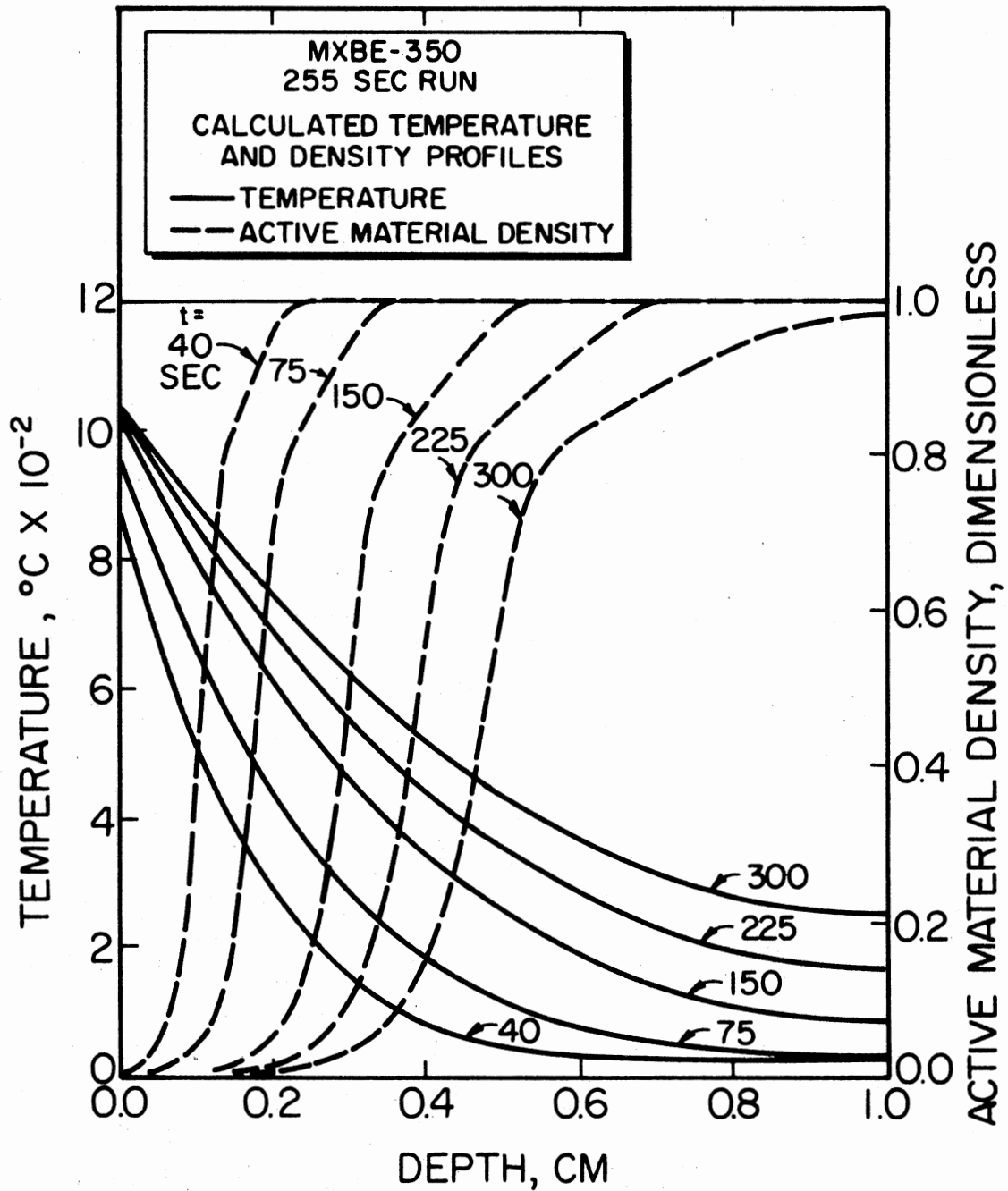


Figure 78. Calculated Spatial Dependent Temperatures and Active Material Densities for MXBE-350, 255-Second Run

$\Delta x = 0.01$ cm. The results of the experimental and calculated data are presented in Figure 79. The contents of Figure 79 are the same as for the two previous samples, with the exception of the addition of the calculated center temperature and active material density. Figure 80 shows the calculated spatial dependence of temperature and nondimensional active material density at 150, 300, 600, 900, and 1200 seconds.

TABLE XVIII
 STATISTICAL ANALYSIS OF CALCULATED VERSUS
 EXPERIMENTAL TEMPERATURES FOR
 MXBE-350, 255-SECOND RUN

Thermocouple Depth (cm)	Average Error (°C)	Standard Deviation (°C)	95% Confidence Interval (°C)	Number of Data Points
0.40	16.2	23.83	4.63 - 27.74	17
0.44	3.79	21.18	- 6.47 - 14.07	17
0.96	-27.55	23.63	-39.01 - -16.09	17
Total	- 2.52	29.14	-10.68 - 5.64	51

The temperature depressions are more evident in this particular test because of the longer duration and lower heating rate. Also, the effects of the pyrolysis of the center of the sample are apparent in the calculated temperatures. The experimental and calculated temperatures appeared to be approaching steady state near 600 seconds. When

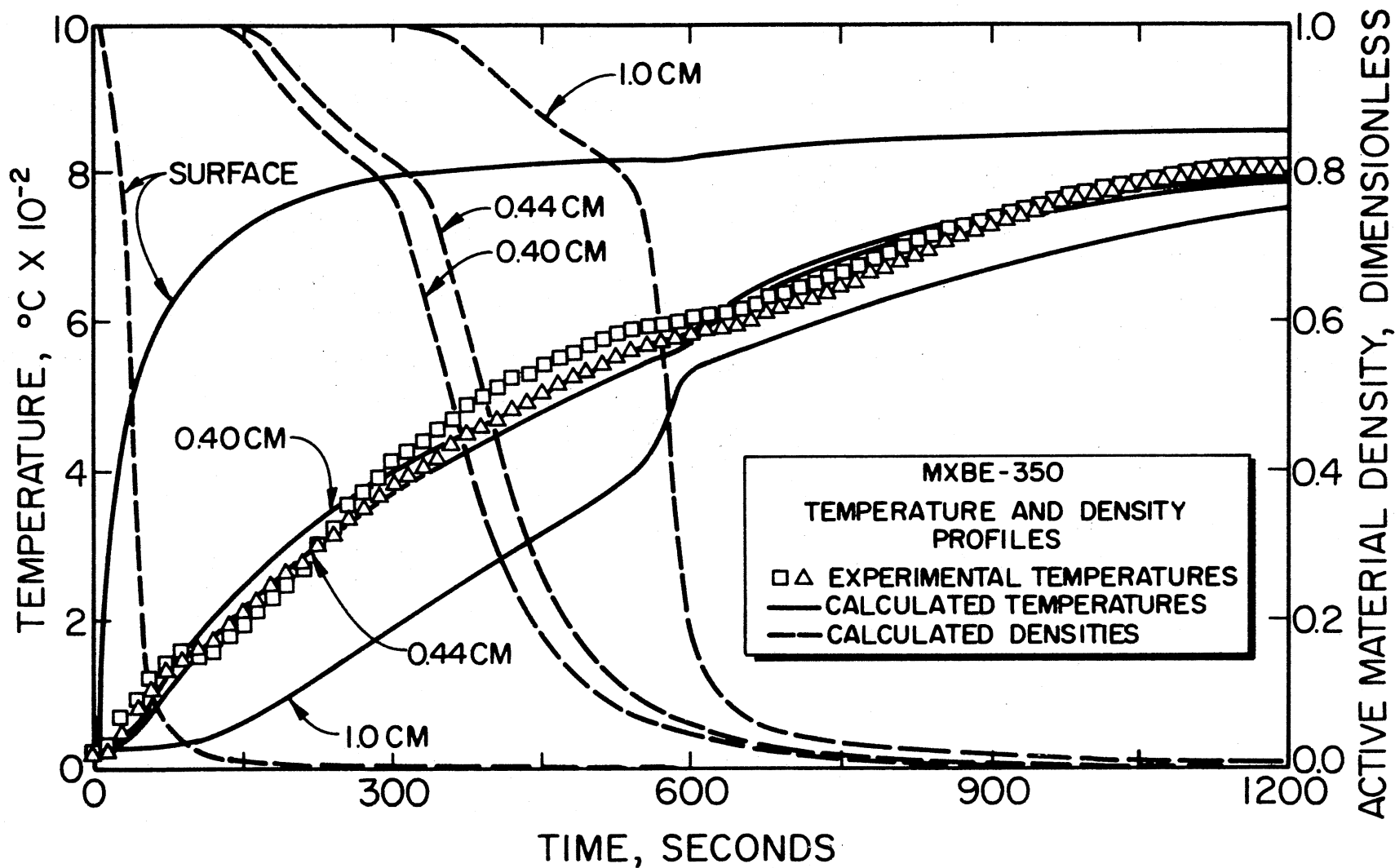


Figure 79. Calculated and Experimental Temperatures and Calculated Active Material Densities for MXBE-350, 1200-Second Run

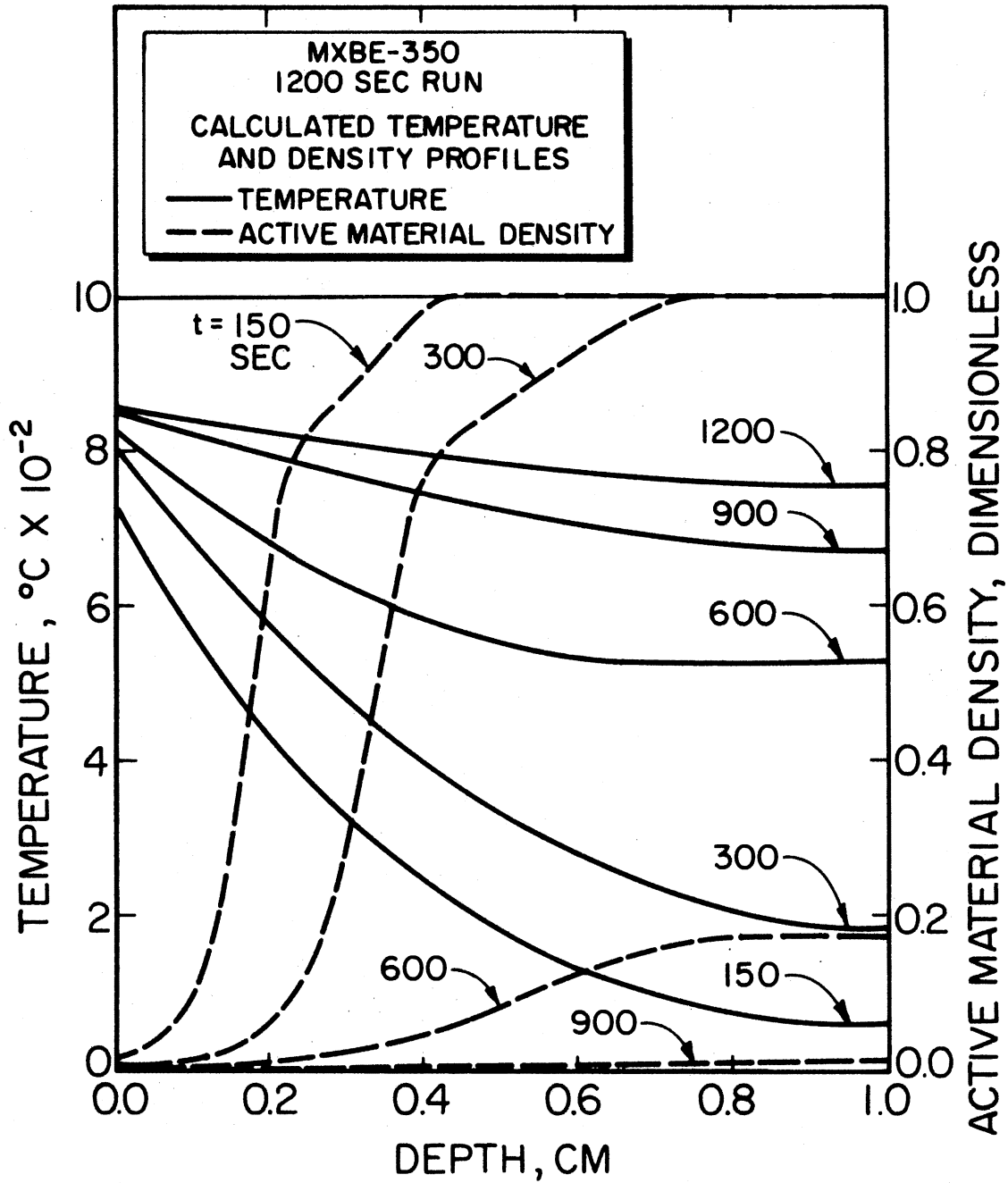


Figure 80. Calculated Spatial Dependent Temperatures and Active Material Densities for MXBE-350, 1200-Second Run

the pyrolysis interface approached the center of the sample, the exothermic reaction caused a sharp increase in the center temperature. This increase was propagated back through the char zone causing the inflection point in both the experimental and calculated temperatures near 600 seconds. The sample reached true steady state upon completion of the reaction at approximately 1200 seconds. The calculated temperatures were somewhat lower than the experimental values between 400-500°C. This is probably a result of inaccurate char thermal conductivity data. A much closer fit of the experimental data could have been obtained by modifying the estimated thermal conductivity. However, the results of the computations using the available data are within reason. The results of the statistical analysis for this particular run are presented in Table XIX.

TABLE XIX
 STATISTICAL ANALYSIS OF CALCULATED VERSUS
 EXPERIMENTAL TEMPERATURES FOR
 MXBE-350, 1200-SECOND RUN

Thermocouple Depth (cm)	Average Error (°C)	Standard Deviation (°C)	95% Confidence Interval (°C)	Number of Data Points
0.40	-3.48	25.48	- 9.11 - 2.29	80
0.44	-6.20	18.27	-10.28 - -2.11	80
Total	-4.84	22.13	- 8.30 - -1.30	160

A sample of FR-1 was irradiated at $2.2 \text{ cal/cm}^2\text{-sec}$. Thermocouples were located at depths of 0.40, 0.42, and 0.87 cm. Ignition of the sample occurred at approximately 150 seconds, however, the test was continued through complete decomposition. The results of this run are shown in Figure 81. Although these data were not compared to calculated values, they are included here because they exemplify the sharp temperature rise near the center of the sample which is frequently observed in wood. This is primarily because of the low heat of decomposition which is more typical of wood. This phenomenon is not generally observed in any type of ablative materials since they are generally exposed to levels of heat flux which overshadow the effects of the pyrolysis.

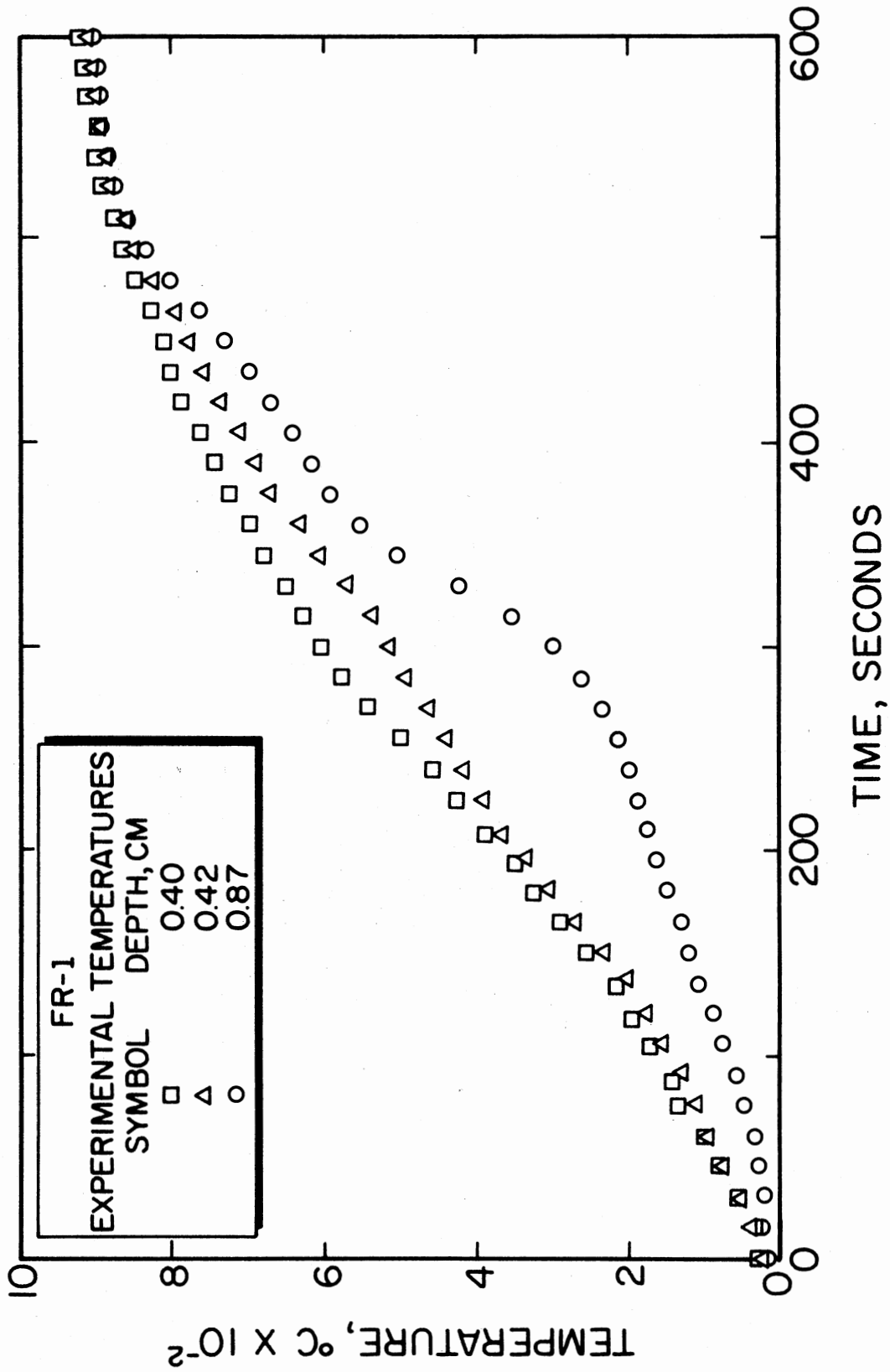


Figure 81. Experimental Temperatures for FR-1

CHAPTER VIII

DISCUSSION AND RECOMMENDATIONS

Kinetic Parameters

Experimental Technique and Data

All six of the materials tested have individual weight loss characteristics. However, with the exception of FR-2, they generally exhibit expected behavior. As the heating rate is increased, the fraction of weight remaining is shifted to the higher temperatures. At lower temperatures, FR-2 exhibits the same trends. After the temperature reaches approximately 400°C, however, the curves cross and the higher heating rate weight loss is less than the weight loss at slower heating rates. Figure 31 depicts this phenomenon. This behavior apparently is a result of the effects of pitch fiber on the reaction kinetics since FR-1 and FR-2 are identical with the exception of the fiber type. As shown in Figure 30, FR-1 exhibits expected characteristics.

As a result of the abnormal behavior of FR-2, application of Friedman's method led to negative activation energies for fractions of weight loss less than 0.83. This is clearly not realistic in the view of the physical meaning of activation energy. Therefore, activation energies calculated for values of weight loss less than 0.83 were not used. The end result was a rather poor correlation between the experi-

mental and calculated thermogravimetric data at the lower end of the weight loss curve.

With the exception of FR-2, the experimental data were extremely well behaved. The kinetic parameters calculated based on the data were well within the expected range. They closely reproduced the experimental thermograms.

Any changes in the experimental technique should be directed toward obtaining data at higher heating rates. However, as the heating rates are increased, the heat transfer rates to the sample become important. Sample geometry and thermal properties begin to play a major role in the rate of decomposition and thus affect the kinetic parameters. As a result, the task of developing a technique to produce reliable high heating rate data is a major undertaking in itself.

Data Analysis and Results

The average activation energies calculated by the methods of Flynn and Wall [24] and Friedman [22] agree within 7.5 percent in the worst case. There was less scatter of the data using the Flynn and Wall method. This was thought to be due primarily to the errors in measuring the derivatives of the weight loss used in Friedman's method.

With the exception of FR-2, the kinetic parameters were calculated based on data that represented at least 68 percent of the total weight loss. In contrast, Friedman's technique covered approximately 50 percent. As a result, large values of the order of reaction and pre-exponential factor were calculated for the first region. However, Friedman's results would have been similar had he considered the same range of decomposition.

In order to evaluate the effect of separating the reaction into two parts, a thermogram for H41NE was calculated using only the kinetic parameters for $w/w_0 \leq 0.91$. This corresponded approximately to the region of weight loss considered by Friedman. As shown by the broken lines in Figure 82, the calculated versus the experimental thermograms are in poor agreement.

By dividing the reaction into two separate weight loss regions, the reaction order and pre-exponential factor become empirical parameters that provide a "best fit" of the data. However, this method yields an extremely accurate reproduction of the thermograms over a wide range of heating rates. This is the desired result for kinetic parameters used in thermal models.

The technique of separating the weight loss curve into two regions results in kinetic parameters which reproduce the weight loss curves accurately. The only exceptions were FR-2, in which the activation energies for weight losses below 0.83 were not used. The other extreme was FR-1, for which the kinetic parameters were calculated based on over 91 percent of the total weight loss. As a result, FR-1 could have been fit with three sets of pre-exponential factors and orders of reaction to more accurately model the thermograms.

If the kinetics of decomposition of the materials of interest are independent of the rate of heating, the proposed method is valid. As stated previously, future work in this area should be directed toward obtaining experimental data at higher heating rates.

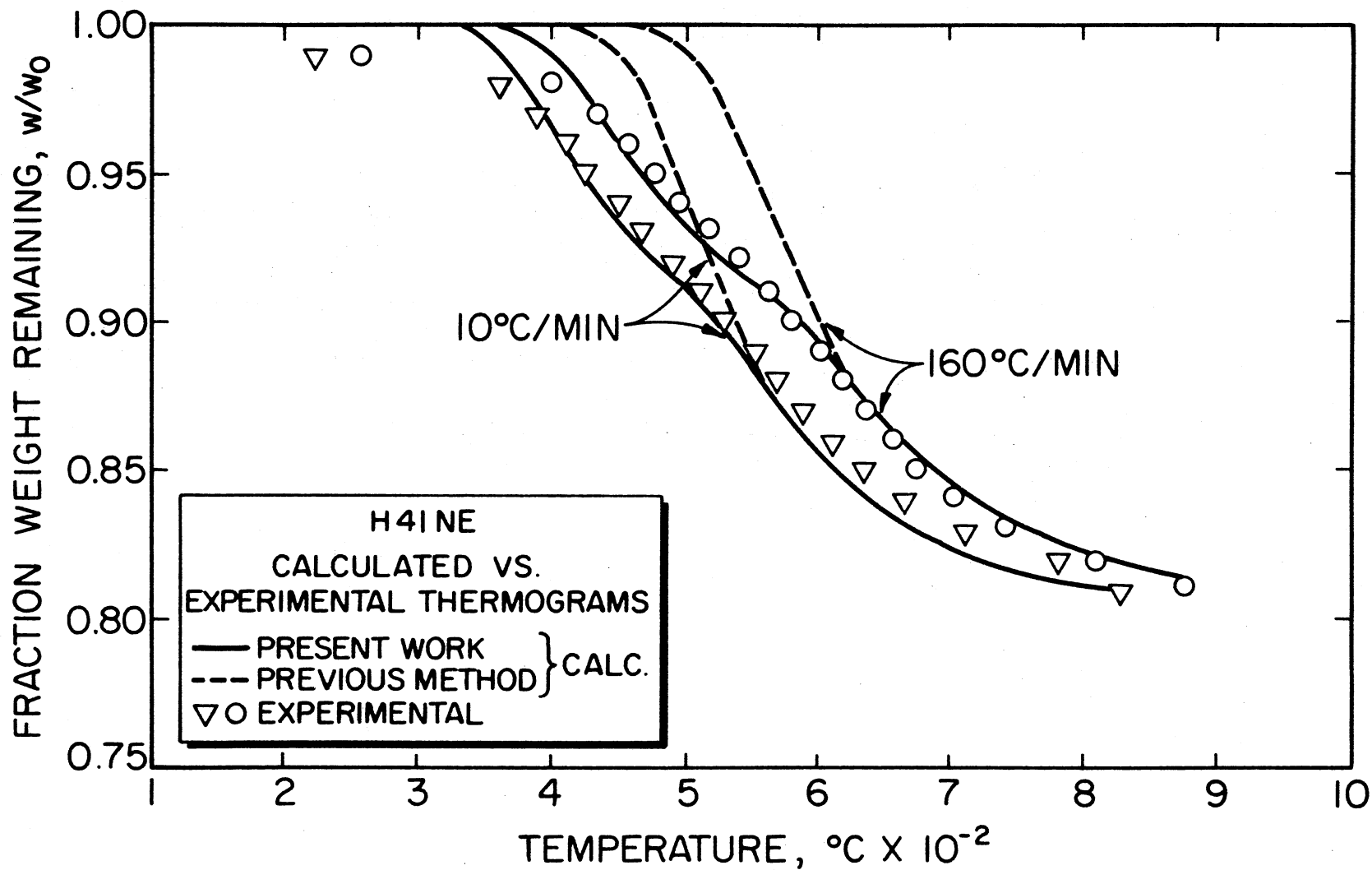


Figure 82. Comparison of Thermograms for H41NE Calculated Using Two Methods

Specific Heat and Heat of Decomposition

The method devised to measure specific heat and heat of decomposition during pyrolysis using differential scanning calorimetry is unique. Thermogravimetric data obtained at the same heating rate were used to calculate the instantaneous weight of the sample during the DSC scan. In addition, the effective range of the DSC-1B was extended by using a relationship similar to that proposed by Brennan [28]. This extension allowed the heat of decomposition to be calculated for materials in which completion of pyrolysis was past the temperature range of the instrument.

The accuracy of using TGA data to determine the temperature dependent weight of the DSC sample was determined by comparing the weights of H41NE heated by TGS and DSC at the same rate. The fraction of weight remaining was determined by weighing samples run in the DSC at 20°C/min to final temperatures of 189, 322, and 482°C. The DSC sample weights were compared to TGA sample weights heated at the same rate and to the same final temperature. The maximum error between the two methods was ± 0.02 fraction weight remaining. This results in ± 2 -percent error in the specific heat as well.

The accuracy of the DSC has been estimated for nonvolatile materials to be ± 0.3 percent by McNaughton and Mortimer [33]. This estimate seems extremely optimistic. However, if the accuracy were ± 3.0 percent for standard DSC measurements, the maximum error in the calculated data would be approximately ± 5.0 percent. For volatile materials this seems to be well within reason.

The greatest possible source of error is in the extrapolated char specific heat out to the intersection of the apparent virgin material

specific heat. Based on a linear least squares curve fit, the char specific heat was extrapolated 50 to 175°C past the experimental data. Therefore, any future work in this area should focus on measuring specific heat and heat of decomposition at temperatures up to at least 1000°C. Comparison of the heat of decomposition calculated in this work with data obtained at higher temperatures would be worthwhile.

Theoretical Model and Temperature Measurements

The thermal model satisfactorily predicts the time dependent temperatures in a pyrolyzing composite ablative material. The important physical phenomena which occur during pyrolysis were considered in its formulation. The most apparent omission was the modeling of the low temperature endothermic reaction near 200°C. As a result, the model does not closely represent the thermal response of the material through this temperature range. Differences between calculated and experimental temperatures of up to 40°C were observed. However, since this phenomenon occurred over a rather short temperature range, it had little effect on the overall accuracy of the calculations.

The accuracy of this model, like all thermal models, depends on the quality of the thermal and kinetic properties and the boundary conditions. With the exception of the virgin and char material thermal conductivity, all of the pertinent thermal properties and boundary conditions were measured and used as input to the model. Best estimates for the values of the virgin material thermal conductivities were obtained from reference [26]. The accuracy of the predictions of the model could have been greatly improved by using accurate temperature dependent thermal conductivities. The thermal conductivity of the

char is equally as important. It not only affects the magnitude of the temperature profiles, but the entire character of the predicted thermal response is changed as well.

The char thermal conductivity is perhaps the most elusive of the thermal properties. Values have been estimated ranging from a fraction of the virgin material thermal conductivity by Panton and Rittman [2] to many times the original value by Murty Kanury [6]. Part of the uncertainty is due to the diathermancy (combined conduction and radiation) of the materials being studied. The extent of this phenomenon is a function of the density of the char and the spectral distribution of the incident radiation. For low density chars exposed to short wavelength radiation, the effective thermal conductivity could increase significantly over the measured value. In fact, for some ablatives the diathermancy could become significant enough to change the requirements of the thermal model. If the interior of the sample reaches higher temperatures than the surface due to combined conduction and radiation, the present model is not adequate.

Future work on the model should include addition of a term to account for the endothermic reaction near 200°C, and efforts to model the secondary reactions between the char and pyrolysis gases. However, it is felt that the most significant errors in the present work are a result of the lack of accurate virgin and char thermal conductivities. As a result, temperature dependent thermal conductivities should be measured for the materials of interest. Also, significant efforts should be made to determine the effects of diathermancy on the char thermal conductivity of low density materials.

The experimental method was adequate to provide the needed temperature data to compare with predicted values. However, several small changes could improve the method. First, the sample holder should not contact the sample except at selected points. This would remove heat transfer effects resulting from the contact between the sample and the holder. Also, the sample should be smaller to improve the heat flux distribution over the surface. In addition, the in-depth temperatures should be measured at more locations to improve the thermal record for each material.

Continuation of this work should include as its first priority a study of the thermal conductivity of both the virgin and char materials and the addition of a term in the thermal model to account for the endothermic reaction observed in the experimental data.

BIBLIOGRAPHY

1. Bamford, C. H., J. Crank, and D. H. Malan, "The Combustion of Wood, Part I." Cambridge Phil. Soc. Proc., 42 (1946), pp. 166-182.
2. Panton, R. L. and J. G. Rittmann, Analytical Study of Pyrolysis Including Effects of Mass Loss and Competing Reactions. (Paper presented at Fall meeting of the Western States Section of the Combustion Institute, La Jolla, California, October 1969.)
3. Weatherford, W., Jr., "Mathematical Theory of Woodburning Mechanisms." (Unpublished paper prepared for the AIChE Journal, 1962.)
4. Thomas, P. H. and P. C. Bowes, "Some Aspects of the Self-Heating and Ignition of Solid Cellulosic Materials." British Journal of Applied Physics, 12 (1961), pp. 222-229.
5. Murty Kanury, A., "A Study of Transient Heat and Mass Transfer in Pyrolyzing Cellulose." (Unpublished M.S. thesis, University of Minnesota, Minneapolis, Minnesota, 1963.)
6. Murty Kanury, A. and P. L. Blackshear, Jr., "Some Considerations Pertaining to the Problem of Wood-Burning." Combustion Science and Technology, 1 (1970), pp. 339-355.
7. Munson, T. R. and R. J. Spindler, Transient Thermal Behavior of Decomposing Materials - Part I: General Theory and Application to Convective Heating. Avco Corporation RAD-TR-61-10, 1961.
8. Murty Kanury, A., "An Evaluation of the Physico-Chemical Factors Influencing the Burning Rate of Cellulosic Fuels and a Comprehensive Model for Solid Fuel Pyrolysis and Combustion." (Unpublished Ph.D. dissertation, University of Minnesota, Minneapolis, Minnesota, 1969.)
9. Kung, H.-C., "A Mathematical Model of Wood Pyrolysis." Combustion and Flame, 18 (1972), pp. 185-195.
10. Kratsch, K. M., L. F. Hearne, and H. R. McChesney, Theory for the Thermophysical Performance of Charring Organic Heat-Shield Composites. Lockheed Missile and Space Company Report No. LMSC-803099 2-60-63-7, October 1963.

11. Arai, N., "Transient Ablation of Teflon in Intense Radiative and Convective Environments." AIAA Journal, 17, No. 6 (1979), pp. 634-640.
12. Havens, J. A., "Thermal Decomposition of Wood." (Unpublished Ph.D. dissertation, University of Oklahoma, Norman, Oklahoma, 1969.)
13. Stamm, A. J., "Thermal Degradation of Wood and Cellulose." Industrial and Engineering Chemistry, 48, No. 3 (1956), pp. 413-417.
14. McNaughton, G. C., "Ignition and Charring Temperature of Wood." Wood Products, 50, No. 2, pp. 21-22.
15. Akita, K., Studies on the Mechanism of Ignition of Wood. Fire Research Institute of Japan, Report No. 9, 1959.
16. Flynn, J. H. and B. Dickens, "Steady State Parameter - Jump Methods and Relaxation Methods in Thermogravimetry." Thermochimica Acta, 15 (1976), pp. 1-16.
17. Freeman, E. S. and B. Carroll, "The Application of Thermoanalytical Techniques to Reaction Kinetics. The Thermogravimetric Evaluation of the Kinetics of the Decomposition of Calcium Oxalate Monohydrate." J. Phys. Chem., 62 (1958), p. 394.
18. Anderson, D. A. and E. S. Freeman, "The Kinetics of the Thermal Degradation of Polystyrene and Polyethylene." Journal of Polymer Science, 54 (1961), pp. 253-260.
19. Mickelson, R. W. and I. N. Einhorn, "The Kinetics of Polymer Decomposition Through Thermogravimetric Analysis." Thermochimica Acta, 1 (1970), pp. 147-158.
20. Baer, A. D., J. H. Hedges, J. D. Seader, K. M. Jayakar, and L. H. Wojcik, "Polymer Pyrolysis Over a Wide Range of Heating Rates." AIAA Journal, 15, No. 10 (1977), pp. 1398-1404.
21. Burningham, N. W. and J. D. Seader, "Determination of Kinetic Parameters for the Thermal Degradation of Polymers by the Quasilinearization Technique." Thermochimica Acta, 5 (1972), pp. 59-69.
22. Friedman, H. L., "Kinetics of Thermal Degradation of Char-Forming Plastics from Thermogravimetry. Application to a Phenolic Plastic." Journal of Polymer Science: Part C, 6 (1965), pp. 183-195.
23. Henderson, J. B., J. A. Wiebelt, M. R. Tant, and G. R. Moore, "Determination of the Kinetic Parameters for the Thermal Decomposition of Phenolic Ablative Materials by a Multiple Heating Rate Method." (Accepted for publication in Thermochimica Acta, 1980.)

24. Flynn, J. H. and L. A. Wall, "A Quick, Direct Method for the Determination of Activation Energy from Thermogravimetric Data." Polymer Letters, 4 (1966), pp. 323-328.
25. Pears, C. D., "Boxing Values for Thermal Conductivity and Heat Capacity of a CCA3/SC1008." (Letter to Air Force Materials Laboratory, Air Force Systems Command, Wright-Patterson AFB, Ohio, Contract No. F33615-76-C-5088, May 1978.)
26. "Intermetallics, Cerments, Polymers, Composite Systems (Vol. 6)." Thermophysical Properties of High Temperature Solid Materials. Ed. Y. S. Touloukian, 1967.
27. Dunlap, F., The Specific Heat of Wood. U.S. Department of Agriculture, Forest Service Bulletin No. 110, 1912
28. Brennan, W. P., B. Miller, and J. C. Whitwell, "An Improved Method of Analyzing Curves in Differential Scanning Calorimetry." I&EC Fundamentals, 8 (1969), pp. 314-318.
29. Brown, L. E., "An Experimental and Analytic Study of Wood Pyrolysis." (Unpublished Ph.D. dissertation, University of Oklahoma, Norman, Oklahoma, 1972.)
30. Kung, H.-C., "The Burning of Vertical Wooden Slabs." (Paper presented at the 15th Combustion Institute Symposium on Combustion, Tokyo, Japan, August 1974.)
31. Sykes, G. F., Jr., Decomposition Characteristics of a Char-Forming Phenolic Polymer Used for Ablative Composites. NASA Technical Note No. TN D-3810, 1967.
32. Tang, W. K. and W. K. Neill, "Effect of Flame Retardants on Pyrolysis and Combustion of α -Cellulose." Journal of Polymer Science: Part C, 6 (1964), pp. 65-81.
33. McNaughton, J. L. and C. T. Mortimer, Differential Scanning Calorimetry. (Reprinted from IRS: Physical Chemistry Series 2, 10 (1975).)
34. Davy, W. C., G. P. Menees, J. H. Lundell, and R. R. Dickey, "Hydrogen-Helium Ablation of Carbonaceous Materials: Numerical Simulation and Experiment." (Paper 78-866 presented at the Second AIAA/ASME Thermophysics and Heat Transfer Conference, Palo Alto, California, May 1978.)
35. Schaefer, J. W., T. J. Dahm, D. A. Rodriguez, J. J. Reese, Jr., and M. R. Wool, Studies of Ablative Material Performance for Solid Rocket Nozzle Applications. Final Report prepared for NASA Lewis Research Center, Cleveland, Ohio, March 1968.
36. Murty Kanury, A. and P. L. Blackshear, Jr., "An X-Ray Photographic Study of the Reaction of α -Cellulose Decomposition." Pyrodynamics, 4 (1966), pp. 285-298.

37. Wiebelt, J. A. and J. B. Henderson, Techniques to Predict Temperature Profiles in Pyrolyzing Alpha-Cellulose. Final Report, USAF, Eglin Air Force Base, Florida, 1973.
38. Martin, S., "Diffusion-Controlled Ignition of Cellulosic Materials by Intense Radiant Energy." Tenth Symposium (International) on Combustion Proceedings. The Combustion Institute, 1965, p. 877.
39. Ulrich, R. D. and A. G. Butcher, Post-Ignition Burning of Horizontal Wood Surfaces. Naval Weapons Center Report No. TP-5271, 1971.
40. Lincoln, K. A., "Flash Pyrolysis of Solid Fuel Materials by Thermal Radiation." Pyrodynamics, 2 (1963), p. 133.
41. Norem, S. D., M. J. O'Neill, and A. P. Gray, "The Use of Magnetic Transitions in Temperature Calibration and Performance Evaluation of Thermogravimetric System." Thermochemica Acta, 1 (1970), pp. 29-38.
42. Ginnings, D. C. and G. T. Furukawa, "Heat Capacity Standards for the Range 14 to 1200 K." Journal of the American Chemical Society, 75 (1953), pp. 522-527.

APPENDIX A

LISTING OF COMPUTER PROGRAM

```

PROGRAM PYRC(INPLT,OUTFUT,TAPE5=INPUT,TAPE6=OUTPUT)
REAL LT1,LT2,LT3,LT4,LT5
REAL K,KA,KC,KVICPT,KVSLP,MG,MGTEMP
DIMENSION TH(205),T(205),RHO(205),RHOH(205),RHCA(205),RHOC(205)
DIMENSION RHCAH(205)
DIMENSION TSTAT(4,90),TEX(4,90),TMEX(90),TME(90)
DIMENSION LT1(205),LT2(205),LT3(205),LT4(205),LT5(205)
DIMENSION CPA(205),CPC(205),CPS(205),ROCP(205),HA(205),HC(205)
DIMENSION MG(205),K(205),KA(205),KC(205),X(205),MG(205),
1 Z1(205),Z2(205),Z3(205),Z4(205)
DIMENSION A(105),RO(105)
DIMENSION IBLFF(800),RFL0T(5),PLT(300),PLT1(300),PLT2(300),
1 PLT3(300),PLT4(300),PLT5(300),PLT6(300),PLT7(300),PLT8(300),
1 PLT9(300),PLT10(300),PLT11(300),NOPLT(4)
101 FORMAT(1H1)
102 FORMAT(////,50X,*TIME=*,F10.5,4X,*QNET=*,F10.5,////)
103 FORMAT(40X,I4,5X,F6.3,5X,F6.2,5X,F7.4,5X,F4.1)
104 FORMAT(3X,I4,2X,F6.3,2X,F8.2,2X,F7.4,2X,F7.4,1X,1PE12.3,1X,
1 1PE12.3,1X,1PE12.3,1X,1PE12.3,1X,1PE12.2,2X,1PE12.4)
105 FORMAT(////,60X,*INPUT DATA*,////)
106 FORMAT(20X,*NX=*,I4,4X,*NT=*,I5,4X,*XMAX=*,
1 F6.2,4X,*TMAX=*,F6.1,4X,*TI=*,F6.1,4X,*QRAD=*,F6.2,////)
107 FORMAT(2X,*KVICPT=*,1PE12.3,4X,*KVSLP=*,1PE12.3,4X,
1 *VICPT=*,1PE12.3,4X,*VSLP=*,
1 1PE12.3,4X,*CICPT=*,1PE12.3,4X,*CSLP=*,1PE12.3,///,35X,
1 *CPC=*,1PE12.3,4X,*RHOV=*,1PE13.4,4X,*RHOF=*,1PE13.4,////)
108 FORMAT(40X,*EC=*,F4.2,5X,*EV=*,F4.2,5X,*AV=*,F4.2,5X,*AC=*,
1 F4.2,////)
109 FORMAT(10X,*QP=*,F6.1,4X,*RO1=*,F6.2,4X,*RO2=*,F6.2,4X,*CHNG=*,
1 F5.2,5X,*E=*,1PE14.4,4X,*A1=*,1PE11.2,4X,*A2=*,1PE11.2)
110 FORMAT(////,54X,*CALCULATED CONSTANTS*,////)
111 FORMAT(53X,*CX=*,F6.3,5X,*DT=*,F6.3,5X,///,35X,*C2=*,
1 F8.5,5X,*C3=*,F9.1,5X,*C4=*,F8.4,5X,*C5=*,F8.4)
DATA SIG,6/1.3E9E-12,1.986/
REAC(5,*)PTMX,RPLOT,NPRINT,NOPLT
WRITE(6,*)PTMX,RFL0T,NFRINT,NOPLT
WRITE(E,101)
REAC(5,*)NX,NT,XMAX,TMAX,TI,QRAD
READ(5,*)KVICPT,KVSLP,VICPT,VSLP,CICPT,CSLP,CPG,RHOV,RHOF
REAC(5,*)EC,EV,AV,AC
READ(5,*)E,RO1,RO2,A1,A2,CHNG,QP
WRITE(6,105)
WRITE(E,10E)NX,NT,XMAX,TMAX,TI,QRAD
WRITE(6,107)KVICPT,KVSLP,VICPT,VSLP,CICPT,CSLP,CPG,RHOV,RHOF
WRITE(E,108)EC,EV,AV,AC
WRITE(E,109)QP,RC1,RO2,CHNG,E,A1,A2

```

C
C
C
C
C
C
C
C
C
C

THE FOLLOWING ARE SET IN A DATA STATEMENT.

SIG = STEFAN-BOLTZM/N CONSTANT (CAL/SEC-CM**2-K**4)
R = GAS CONSTANT (CAL/GM-MOLE-K)

THE FOLLOWING ARE READ IN CN DATA CARDS

PTMX = MAXIMUM TEMPERATURE TO BE PLOTTED
RPLOT = VECTOR CONTAINING THE TIMES AT WHICH THE SPATIAL
TEMPERATURE AND DENSITY PROFILES ARE TO BE PLOTTED

C NPRINT = INTERVAL IN WHICH CALCULATED VARIABLES ARE PRINTED
 C NOPLCT = VECTOR CONTAINING NODE NUMBERS TO BE PLOTTED
 C NX = NUMBER OF SPATIAL NODES (INTEGER)
 C NT = NUMBER OF TIME NODES (INTEGER)
 C XMAX = HALF THICKNESS OF MATERIAL (CM)
 C TMAX = MAXIMUM RUN TIME (SEC)
 C TI = INITIAL SLAB TEMPERATURE (C)
 C QRAD = INCIDENT RADIANT HEAT FLUX (CAL/CM**2-SEC)
 C KV = THERMAL CONDUCTIVITY OF VIRGIN MATERIAL (CAL/CM-SEC-C)
 C VICPT = SPECIFIC HEAT OF VIRGIN MATERIAL AT T=0 (CAL/GM-C)
 C VSLP = SLOPE OF TEMPERATURE DEPENDENT SPECIFIC HEAT OF VIRGIN
 C MATERIAL (CAL/GM-C**2)
 C CICPT = SPECIFIC HEAT OF FINAL CHAR MATERIAL AT T=0 (CAL/GM-C)
 C CSLP = SLOPE OF TEMPERATURE DEPENDENT SPECIFIC HEAT OF FINAL
 C CHAR MATERIAL (CAL/GM-C**2)
 C CPG = SPECIFIC HEAT OF GASEOUS PRODUCTS (CAL/GM-C)
 C RHOV = DENSITY OF VIRGIN MATERIAL (GM/CC)
 C RHOFC = FINAL DENSITY OF CHAR (GM/CC)
 C AV = ABSORPTIVITY OF VIRGIN MATERIAL
 C EV = EMISSIVITY OF VIRGIN MATERIAL
 C AC = ABSORPTIVITY OF CHAR MATERIAL
 C EC = EMISSIVITY OF CHAR MATERIAL
 C E = AVERAGE ACTIVATION ENERGY (CAL/GM-MOLE)
 C A1 = PRE-EXPONENTIAL FACTOR FOR FIRST PART OF WEIGHT LOSS
 C REGION (1/SEC)
 C A2 = PRE-EXPONENTIAL FACTOR FOR SECOND PART OF WEIGHT LOSS
 C REGION (1/SEC)
 C RO1 = ORDER OF REACTION FOR FIRST PART OF WEIGHT LOSS REGION
 C RO2 = ORDER OF REACTION FOR SECOND PART OF WEIGHT LOSS REGION
 C CHNG = FRACTION OF WEIGHT LOSS DIVIDING THE TWO REGIONS
 C QP = HEAT OF PYROLYSIS (CAL/GM)

C THE FOLLOWING ARE CALCULATED IN THE PROGRAM

C T = TIME DEPENDENT TEMPERATURE IN PYROLYZING MATERIAL (C)
 C K = TIME DEPENDENT THERMAL CONDUCTIVITY (CAL/CM-SEC-C)
 C RHO = TIME DEPENDENT DENSITY (GM/CC)
 C RHOA = TIME DEPENDENT DENSITY OF ACTIVE MATERIAL (GM/CC)
 C RHOC = TIME DEPENDENT DENSITY OF CHAR MATERIAL (GM/CC)
 C CPS = TIME DEPENDENT SPECIFIC HEAT (CAL/GM-C)
 C CPA = TIME DEPENDENT SPECIFIC HEAT OF ACTIVE MATERIAL
 C (CAL/GM-C)
 C CPC = TIME DEPENDENT SPECIFIC HEAT OF CHAR MATERIAL (CAL/GM-C)
 C RCCP = TOTAL ENERGY CAPACITY (CAL/CC-C)
 C HA = ENTHALPY OF ACTIVE MATERIAL (CAL/GM)
 C HC = ENTHALPY OF CHAR MATERIAL (CAL/GM)
 C HG = ENTHALPY OF GASEOUS PRODUCTS (CAL/GM)

C CALCULATING TIME STEP (SEC)

C DT=TMAX/FLCAT(NT-1)

C CALCULATING SPACE BETWEEN NODES

C DX=XMAX/FLCAT(NX-1)

C
C

```

C      CALCULATING CCNSTANTS
C
C2=1.0-(RHOF/RHOV)
C3=-E/R
C4=RHOF/(RHOV-RHOF)
C5=RHOV/(RHCV-RHOF)
WRITE(6,110)
WRITE(6,111)CX,DT,C2,C3,C4,C5

C
C      INITIALIZING PROPERTIES AT TIME=0
C
TIME=0.0
DO 10 I=1,NX
  X(I)=DX*FLCAT(I-1)
  T(I)=TI
  TH(I)=TI
  RHO(I)=RHCV
  RHOH(I)=RHCV
  RHOA(I)=RHCV
  RHOAH(I)=RHCV
  MG(I)=0.0
  HA(I)=0.0
  HC(I)=0.0
  HG(I)=0.0
  A(I)=A1
  RC(I)=RO1
10 CONTINUE
  T(NX+1)=TI
  TH(NX+1)=TI
  RHO(NX+1)=RHCV
  RHOH(NX+1)=RHCV
  RHOA(NX+1)=RHCV
  RHOAH(NX+1)=RHCV
  X(NX+1)=X(NX)+CX
  QNET=0.0
  WRITE(6,101)
  WRITE(6,102)TIME,QNET
  NXL=NX+1

C
C      WRITING CCNCITIONS AT TIME=0
C
DO 20 I=1,NXL
20 WRITE(6,103)I,X(I),T(I),RHO(I),MG(I)

C
C      PLCT ROUTINES
C
PLT(NX+1)=0.0
PLT(NX+2)=XMAX/5.0
PLT8(NX+1)=0.0
PLT8(NX+2)=FTMX/5.0
PLT9(NX+1)=0.0
PLT9(NX+2)=1.0/5.0
CALL PLCTS(18UFF,800,1)
CALL CCIDNT(0.,3,3HJBH)
CALL PLCT(1.0,1.0,-3)
CALL AXIS(0.0,0.0,8HDEPTH-CH,-8,5.0,0.0,PLT(NX+1),PLT(NX+2))
CALL AXIS(0.0,5.0,1H .1,5.0,0.0,PLT(NX+1),PLT(NX+2))

```

```

CALL AXIS(0.0,0.0,13,TEMPERATURE-C,13,5.0,90.0,PLT8(NX+1),
1  PLT8(NX+2))
CALL AXIS(5.0,0.0,7,DENSITY,-7,5.0,90.0,PLT9(NX+1),PLT9(NX+2))
KFLT=0

```

C
C
C

```
STARTING TIME LOOP
```

```

IIST=15.0/DT
KKST=0
JJST=0
DO 30 J=1,NT

```

C
C
C

```
CALCULATING MATERIAL PROPERTIES
```

```

DO 40 I=1,NX
C=A(I)*DT*RHOV*EXP(C3/(T(I)+273.15))
RHO(I)=-C*((RHOH(I)-RHOV)/RHOV)**RO(I)+RHCH(I)
RHO(I)=(RHC(I)-RHOV)/C2
RHO(I)=RHC(I)-RHCA(I)
RAT=RHO(I)/RHOV
IF(RAT.LE.CHNG)A(I)=A2
IF(RAT.LE.CHNG)RC(I)=RC2
CPC(I)=CICPT+CSLP*T(I)
IF(T(I).GT.700.)CPC(I)=CICPT+700.*CSLP
CFA(I)=VICPT+VSLP*T(I)
IF(T(I).GT.700.)CFA(I)=VICPT+700.*VSLP
HC(I)=CPC(I)*(T(I)-TI)
HA(I)=CFA(I)*(T(I)-TI)
HG(I)=CPG*(T(I)-TI)
KA(I)=KVICPT+KVSLP*T(I)
IF(T(I).GT.600.0)KA(I)=KVICPT+KVSLP*600.0
KC(I)=RHOV*KA(I)/RHCV
IF(T(I).GT.225.0)KC(I)=RHOV*(KVICPT+KVSLP*225.0)/RHOV
KC(I)=0.7*KA(I)
K(I)=(RHOA(I)/RHOV)*KA(I)+((1.-RHO(I)/RHOV)/C2)*KC(I)
RCCP(I)=RHOA(I)*CFA(I)+RHOV(I)*CPC(I)
CFS(I)=RCCP(I)/RHC(I)

```

```

+0 CCNTINUE
RHO(NX+1)=RHC(NX-1)
RHCA(NX+1)=RHCA(NX-1)
K(NX+1)=K(NX-1)

```

C
C
C

```
CALCULATING GAS MASS FLUX
```

```

MGTEMP=0.0
DO 50 N=1,NX
I=NX-N+1
FUNC=-(DX/DT)*(RHC(I)-RHOH(I))
IF(N.EQ.1.CF.N.EQ.NX)FUNC=FUNC/2.0
MGTEPF=MGTEMP+FUNC
MG(I)=MGTEMP

```

```

50 CCNTINUE
MG(NX)=0.0

```

C
C
C

```
CALCULATING BOUNDARY CONDITIONS
```

```
Q=(GRAC/4.0)*(TIME+DT)
```



```

IF (TIME.GE.4.0) Q=QRAO
QG=(0.80/225.0)*(TIME+DT)
IF (TIME.GT.225.0) QG=0.80
Q=QG+Q
QNET=AV*C-EV*SIG*(TH(1)+273.0)**4
TEMP=QNET+K(1)*(TH(2)-TH(1))/DX
TEMP=TEMP+HG(1)*CPG*(TH(2)-TH(1))
TEMP=TEMP+(CX/(2.*DT))*(TG(1)+QP+C4*HC(1)-C5*HA(1))*
1 (R+C(1)-RHCH(1))
C6=RHO(1)*CPS(1)*DX/(2.0*DT)
T(1)=(TEMP+C6*T+(1))/C6
C
C
C
CALCULATING NEW TEMPERATURES
DO 60 I=2,NX
Z1(I)=(K(I)*DT)/(ROCP(I)*DX**2)
Z2(I)=DT/(4.0*DX**2*ROCP(I))
Z3(I)=(HG(I)*CPG*DT)/(ROCP(I)*DX)
Z4(I)=(R+C(I)-RHCH(I))/ROCP(I)
LT1(I)=Z1(I)*(TH(I+1)-2.0*TH(I)+TH(I-1))
LT2(I)=Z2(I)*(K(I+1)-K(I-1))*(TH(I+1)-TH(I-1))
LT3(I)=Z3(I)*(TH(I)-TH(I-1))
LT4(I)=Z4(I)*(HG(I)+QP-HA(I)*C5+C4*HC(I))
T(I)=TH(I)+LT1(I)+LT2(I)+LT3(I)+LT4(I)+LT5(I)
50 CONTINUE
DO 85 I=1,NX
TH(I)=T(I)
RHCA(I)=RHCA(I)
85 RPOF(I)=R+C(I)
T(NX+1)=T(NX-1)
RHCA(NX+1)=RHCA(NX-1)
TH(NX+1)=T(NX-1)
RHCH(NX+1)=RHC(NX-1)
TIME=TIME+DT
JJST=JJST+1
IF (IIST.NE. JJST) GO TO 25
KKST=KKST+1
THE(KKST)=TIME
TSTAT(1, KKST)=T(NOPLT(2))
TSTAT(2, KKST)=T(NOPLT(3))
TSTAT(3, KKST)=T(NOPLT(4))
TSTAT(4, KKST)=T(NOPLT(4))
JJST=0
25 CCNTINUE
KPRINT=KPRINT+1
IF (KPRINT.LT.NPRINT) GO TO 45
KPLT=KPLT+1
WRITE(6,101)
WRITE(6,102) TIME, QNET
DO 80 I=1, NX
WRITE(6,104) I, X(I), T(I), RHO(I), RHOA(I), HG(I), PG(I), HA(I), HC(I)
1 , K(I), RCCP(I)
80 CCNTINUE
KPRINT=0

```

```

C
C
C
LOADING TIME, TEMPERATURE AND NON-DIMENSIONAL DENSITY INTO
PLCTING VECTORS AT SPECIFIED DEPTHS
C

```

```

PLT1(KPLT)=TIME
PLT2(KPLT)=T(NOPLT(1))
PLT3(KPLT)=RHOA(NOPLT(1))/RHOV
PLT4(KPLT)=T(NOPLT(2))
PLT5(KPLT)=RHCA(NOPLT(2))/RHOV
PLT6(KPLT)=T(NOPLT(3))
PLT7(KPLT)=RHCA(NOPLT(3))/RHOV
PLT10(KPLT)=T(NOPLT(4))
PLT11(KPLT)=RHCA(NOPLT(4))/RHOV
45 CONTINUE
DO 70 I=1,5
IF(J.EC.IFIX(RPLCT(I)/CT))GO TO 65
70 CONTINUE
GC TO 30
55 CONTINUE
DO 75 I=1,NX
PLT(I)=X(I)
PLT8(I)=T(I)
PLT9(I)=RHCA(I)/RHOV
75 CONTINUE
CALL LINE(PLT,PLT8,NX,1,0,0)
CALL LINE(PLT,PLT9,NX,1,0,0)
30 CONTINUE
C
C
C
PLCT ROUTINES
PLT1(KPLT+1)=0.0
PLT1(KPLT+2)=TMAX/8.0
PLT2(KPLT+1)=0.0
PLT2(KPLT+2)=PTMX/5.0
PLT3(KPLT+1)=0.0
PLT3(KPLT+2)=1.0/5.0
CALL PLCT(10.0,0.0,-3)
CALL AXIS(0.0,0.0,8HTIME-SEC,-8,8,0,0.,PLT1(KPLT+1),PLT1(KPLT+2))
CALL AXIS(0.0,5.0,1H,1,8,0,0,0,PLT1(KPLT+1),PLT1(KPLT+2))
CALL AXIS(0.0,0.0,13HTEMPERATURE-C,13,5,0,90.0,PLT2(KPLT+1),
1 PLT2(KPLT+2))
CALL AXIS(8.0,0.0,7HDENSITY,-7,5,0,90.0,PLT3(KPLT+1),PLT3(KPLT+2))
CALL LINE(PLT1,PLT2,KPLT,1,0,0)
CALL LINE(PLT1,PLT3,KPLT,1,0,0)
DO 90 I=1,KPLT
PLT2(I)=PLT4(I)
30 PLT3(I)=PLT5(I)
CALL LINE(PLT1,PLT2,KPLT,1,0,0)
CALL LINE(PLT1,PLT3,KPLT,1,0,0)
DO 95 I=1,KPLT
PLT2(I)=PLT6(I)
95 PLT3(I)=PLT7(I)
CALL LINE(PLT1,PLT2,KPLT,1,0,0)
CALL LINE(PLT1,PLT3,KPLT,1,0,0)
DO 55 I=1,KPLT
PLT2(I)=PLT10(I)
55 PLT3(I)=PLT11(I)
CALL LINE(PLT1,PLT2,KPLT,1,0,0)
CALL LINE(PLT1,PLT3,KPLT,1,0,0)
CALL PLCT(0.,0.,999)
CALL STAT(TSTAT,TME)
STOP
END

```

```

SUBROUTINE STAT(TSTAT,TME)
DIMENSION TSTAT(4,90),TEX(4,90),TMEX(90),TME(90)
10 FORMAT(30X,F10.5,5X,F10.5,5X,F10.5,5X,F10.5)
C
C   N = NUMBER OF DATA PCINTS FOR EACH NODE
C   M = NUMBER OF NODES OF DATA
C
READ(5,*)N,M
WRITE(6,*)N,M
DO 1 J=1,N
READ(5,*)(TMEX(J),(TEX(I,J),I=1,M))
WRITE(6,10)(TMEX(J),(TEX(I,J),I=1,M))
1 WRITE(6,10)(TME(J),(TSTAT(I,J),I=1,M))
STAT7=0.0
STAT8=0.0
M=M-2
DO 3 I=1,M
STAT2=0.0
STAT3=0.0
DO 2 J=1,N
STAT6=TSTAT(I,J)-TEX(I,J)
STAT7=STAT6+STAT7
STAT8=STAT6**2+STAT8
STAT1=TSTAT(I,J)-TEX(I,J)
STAT2=STAT1+STAT2
2 STAT3=STAT1**2+STAT3
STAT4=STAT2**2/FLOAT(N)
VAR=(STAT3-STAT4)/FLOAT(N-1)
SC=SQRT(VAR)
XBAR=STAT2/FLOAT(N)
SX=SQRT(VAR/FLOAT(N))
COF1=XBAR-2.*SX
COF2=XBAR+2.*SX
WRITE(6,*)STAT2,STAT3,STAT4,VAR,SD,XBAR,SX,COF1,COF2
3 CONTINUE
STAT9=STAT7**2/FLOAT(N*M)
VAR=(STAT8-STAT9)/FLOAT(N*M-1)
SC=SQRT(VAR)
XBAR=STAT7/FLOAT(N*M)
SX=SQRT(VAR/FLOAT(N*M))
COF1=XBAR-2.*SX
COF2=XBAR+2.*SX
WRITE(6,*)STAT7,STAT8,STAT9,VAR,SD,XBAR,SX,COF1,COF2
RETURN
END

```

APPENDIX B

THERMOGRAVIMETRIC DATA

TABLE XX

WEIGHT LOSS AND RATE OF WEIGHT LOSS DATA FOR H41NE

w/w_0	Heating Rate 160°C/min $w_0 = 7.9306$		Heating Rate 100°C/min $w_0 = 7.4272$		Heating Rate 80°C/min $w_0 = 7.8858$		Heating Rate 40°C/min $w_0 = 7.6769$		Heating Rate 20°C/min $w_0 = 7.1357$		Heating Rate 10°C/min $w_0 = 7.4106$	
	T(°C)	$(-1/w_0)(dw/dt)$ (1/min)	T(°C)	$(-1/w_0)(dw/dt)$ (1/min)	T(°C)	$(-1/w_0)(dw/dt)$ (1/min)	T(°C)	$(-1/w_0)(dw/dt)$ (1/min)	T(°C)	$(-1/w_0)(dw/dt)$ (1/min)	T(°C)	$(-1/w_0)(dw/dt)$ (1/min)
0.98	403.0	0.0203	390.0	0.0106	400.0	0.0151	371.7	0.0051	370.6	0.0042	363.3	0.0026
0.97	436.0	0.0496	432.3	0.0312	430.0	0.0304	412.2	0.0146	398.6	0.0083	392.0	0.0047
0.96	460.0	0.0683	454.9	0.0436	452.0	0.0384	437.1	0.0195	423.6	0.0105	415.6	0.0059
0.95	480.0	0.0786	476.5	0.0498	472.0	0.0415	456.9	0.0215	441.2	0.0112	430.0	0.0062
0.94	500.0	0.0827	497.1	0.0517	492.0	0.0415	479.7	0.0215	460.9	0.0110	452.5	0.0061
0.93	521.0	0.0815	421.9	0.0504	514.0	0.0393	495.3	0.0203	481.7	0.0102	469.9	0.0058
0.92	544.0	0.0773	543.5	0.0479	539.0	0.0378	521.2	0.0191	504.6	0.0097	492.5	0.0054
0.91	566.0	0.0773	565.1	0.0470	561.0	0.0382	542.0	0.0193	528.4	0.0099	514.0	0.0054
0.90	586.0	0.0808	586.7	0.0485	581.0	0.0413	563.8	0.0206	548.2	0.0107	531.4	0.0058
0.89	605.8	0.0866	608.4	0.0533	602.9	0.0445	584.6	0.0223	567.9	0.0112	556.0	0.0062
0.88	623.5	0.0922	627.6	0.0571	620.7	0.0465	604.1	0.0234	587.6	0.0116	571.4	0.0063
0.87	640.3	0.0953	645.8	0.0580	639.5	0.0462	621.3	0.0236	606.9	0.0112	591.9	0.0063

TABLE XX (Continued)

w/w_0	Heating Rate 160°C/min $w_0 = 7.9306$		Heating Rate 100°C/min $w_0 = 7.4272$		Heating Rate 80°C/min $w_0 = 7.8858$		Heating Rate 40°C/min $w_0 = 7.6769$		Heating Rate 20°C/min $w_0 = 7.1357$		Heating Rate 10°C/min $w_0 = 7.4106$	
	T(°C)	$(-1/w_0)(dw/dt)$ (1/min)	T(°C)	$(-1/w_0)(dw/dt)$ (1/min)	T(°C)	$(-1/w_0)(dw/dt)$ (1/min)	T(°C)	$(-1/w_0)(dw/dt)$ (1/min)	T(°C)	$(-1/w_0)(dw/dt)$ (1/min)	T(°C)	$(-1/w_0)(dw/dt)$ (1/min)
0.86	659.0	0.0934	664.0	0.0567	659.3	0.0426	640.5	0.0221	627.5	0.0097	612.8	0.0054
0.85	676.7	0.0831	687.0	0.0482	686.0	0.0332	665.7	0.0176	651.1	0.0083	635.6	0.0049
0.84	705.2	0.0657	717.7	0.0380	720.6	0.0259	698.1	0.0140	685.6	0.0059	668.2	0.0038

TABLE XXI

WEIGHT LOSS AND RATE OF WEIGHT LOSS DATA FOR H41D

w/w_0	Heating Rate 160°C/min $w_0 = 7.3061$		Heating Rate 100°C/min $w_0 = 7.8094$		Heating Rate 80°C/min $w_0 = 7.0392$		Heating Rate 40°C/min $w_0 = 7.9664$		Heating Rate 20°C/min $w_0 = 7.5368$		Heating Rate 10°C/min $w_0 = 7.6958$	
	T(°C)	$(-1/w_0)(dw/dt)$ (1/min)	T(°C)	$(-1/w_0)(dw/dt)$ (1/min)	T(°C)	$(-1/w_0)(dw/dt)$ (1/min)	T(°C)	$(-1/w_0)(dw/dt)$ (1/min)	T(°C)	$(-1/w_0)(dw/dt)$ (1/min)	T(°C)	$(-1/w_0)(dw/dt)$ (1/min)
0.97	400.0	0.0160	407.1	0.0190	397.7	0.0125	382.7	0.0060	380.6	0.0038	367.1	0.0019
0.96	437.0	0.0454	437.7	0.0385	431.3	0.0303	418.6	0.0152	412.4	0.0086	397.4	0.0040
0.95	461.0	0.0682	459.2	0.0507	451.6	0.0405	440.1	0.0210	431.9	0.0114	418.6	0.0057
0.94	480.0	0.0825	478.6	0.0580	468.9	0.0465	456.5	0.0240	450.3	0.0127	436.7	0.0064
0.93	497.0	0.0913	495.9	0.0613	486.2	0.0497	474.0	0.0254	466.7	0.0131	449.8	0.0065
0.92	516.0	0.0944	513.3	0.0618	504.5	0.0500	491.4	0.0255	483.1	0.0130	467.0	0.0064
0.91	534.0	0.0958	529.6	0.0608	522.8	0.0492	508.8	0.0250	498.5	0.0126	486.1	0.0062
0.90	552.0	0.0958	548.0	0.0607	539.0	0.0483	525.2	0.0245	516.0	0.0123	499.2	0.0061
0.89	568.0	0.0965	567.4	0.0616	557.3	0.0492	542.7	0.0246	534.4	0.0125	519.4	0.0062
0.88	587.0	0.1010	582.7	0.0645	573.6	0.0509	561.1	0.0256	548.8	0.0131	533.5	0.0066
0.87	601.0	0.1063	600.0	0.0691	589.9	0.0546	575.5	0.0274	566.2	0.0142	549.7	0.0071
0.86	616.7	0.1143	613.9	0.0731	606.1	0.0581	592.9	0.0291	580.6	0.0149	562.8	0.0074

TABLE XXI (Continued)

w/w_0	Heating Rate 160°C/min $w_0 = 7.3061$		Heating Rate 100°C/min $w_0 = 7.8094$		Heating Rate 80°C/min $w_0 = 7.0392$		Heating Rate 40°C/min $w_0 = 7.9664$		Heating Rate 20°C/min $w_0 = 7.5368$		Heating Rate 10°C/min $w_0 = 7.6958$	
	T(°C)	$(-1/w_0)(dw/dt)$ (1/min)	T(°C)	$(-1/w_0)(dw/dt)$ (1/min)	T(°C)	$(-1/w_0)(dw/dt)$ (1/min)	T(°C)	$(-1/w_0)(dw/dt)$ (1/min)	T(°C)	$(-1/w_0)(dw/dt)$ (1/min)	T(°C)	$(-1/w_0)(dw/dt)$ (1/min)
0.85	632.4	0.1196	627.8	0.0759	620.2	0.0607	605.8	0.0303	595.9	0.0154	577.9	0.0075
0.84	645.2	0.1230	640.8	0.0755	635.4	0.0609	617.5	0.0299	608.7	0.0150	591.0	0.0073
0.83	658.0	0.1224	656.7	0.0718	649.5	0.0581	634.2	0.0281	625.1	0.0138	608.4	0.0064
0.82	674.7	0.1150	672.6	0.0639	665.7	0.0519	647.9	0.0247	638.7	0.0118	626.8	0.0053
0.81	692.4	0.0983	697.5	0.0501	686.9	0.0418	670.4	0.0201	661.9	0.0096	649.1	0.0043
0.80	715.1	0.0787	727.3	0.0379	714.2	0.0317	697.8	0.0154	689.0	0.0073	676.2	0.0032
0.79	753.5	0.0560	768.1	0.0250	751.6	0.0224	732.1	0.0112	722.9	0.0052	715.9	0.0021

TABLE XXII

WEIGHT LOSS AND RATE OF WEIGHT LOSS DATA FOR MXBE-350

w/w_0	Heating Rate 160°C/min $w_0 = 7.8020$		Heating Rate 100°C/min $w_0 = 7.8451$		Heating Rate 80°C/min $w_0 = 7.9097$		Heating Rate 40°C/min $w_0 = 7.8589$		Heating Rate 20°C/min $w_0 = 7.9766$		Heating Rate 10°C/min $w_0 = 7.8000$	
	T(°C)	$(-1/w_0)(dw/dt)$ (1/min)	T(°C)	$(-1/w_0)(dw/dt)$ (1/min)	T(°C)	$(-1/w_0)(dw/dt)$ (1/min)	T(°C)	$(-1/w_0)(dw/dt)$ (1/min)	T(°C)	$(-1/w_0)(dw/dt)$ (1/min)	T(°C)	$(-1/w_0)(dw/dt)$ (1/min)
0.99	255.9	0.0172	242.6	0.0121	234.0	0.0094	217.7	0.0046	212.2	0.0023	200.2	0.0010
0.98	305.5	0.0352	288.3	0.0245	284.0	0.0204	268.5	0.0104	257.5	0.0055	247.2	0.0029
0.97	334.4	0.0565	316.2	0.0388	314.0	0.0322	298.3	0.0168	284.5	0.0085	272.7	0.0042
0.96	356.1	0.0728	341.1	0.0482	335.0	0.0388	317.2	0.0197	304.8	0.0097	295.2	0.0049
0.95	376.1	0.0793	360.0	0.0507	355.0	0.0403	337.1	0.0201	326.0	0.0097	313.8	0.0050
0.94	391.9	0.0875	379.1	0.0553	374.1	0.0436	357.0	0.0219	345.3	0.0105	330.5	0.0053
0.93	407.7	0.1015	393.2	0.0704	388.1	0.0559	373.8	0.0277	362.3	0.0143	349.1	0.0068
0.92	419.2	0.1318	404.2	0.0905	401.2	0.0742	385.7	0.0382	373.7	0.0186	363.3	0.0092
0.91	428.7	0.1702	412.2	0.1120	408.2	0.0931	393.7	0.0463	385.2	0.0244	373.6	0.0114
0.90	432.9	0.1965	417.3	0.1370	415.3	0.1085	399.6	0.0550	390.4	0.0278	379.7	0.0132
0.89	439.2	0.2152	425.3	0.1546	423.3	0.1236	406.6	0.0615	397.6	0.0298	388.0	0.0145
0.88	444.5	0.2587	431.3	0.1706	427.3	0.1379	413.5	0.0667	407.0	0.0325	395.2	0.0156

TABLE XXII (Continued)

w/w_0	Heating Rate 160°C/min $w_0 = 7.8020$		Heating Rate 100°C/min $w_0 = 7.8451$		Heating Rate 80°C/min $w_0 = 7.9097$		Heating Rate 40°C/min $w_0 = 7.8589$		Heating Rate 20°C/min $w_0 = 7.9766$		Heating Rate 10°C/min $w_0 = 7.8000$	
	T(°C)	$(-1/w_0)(dw/dt)$ (1/min)	T(°C)	$(-1/w_0)(dw/dt)$ (1/min)	T(°C)	$(-1/w_0)(dw/dt)$ (1/min)	T(°C)	$(-1/w_0)(dw/dt)$ (1/min)	T(°C)	$(-1/w_0)(dw/dt)$ (1/min)	T(°C)	$(-1/w_0)(dw/dt)$ (1/min)
0.87	450.8	0.2775	435.3	0.1807	434.3	0.1440	418.5	0.0714	411.1	0.0342	401.4	0.0165
0.86	454.0	0.2947	440.4	0.1917	438.3	0.1508	424.4	0.0751	418.4	0.0365	408.6	0.0176
0.85	461.3	0.3111	444.4	0.1980	444.4	0.1560	429.4	0.0772	425.7	0.0390	412.7	0.0187
0.84	464.5	0.3233	451.4	0.2038	448.4	0.1602	435.3	0.0803	429.8	0.0409	418.9	0.0197
0.83	470.8	0.3298	455.4	0.2080	454.4	0.1644	440.3	0.0827	436.1	0.0433	423.0	0.0209
0.82	476.1	0.3397	460.4	0.2126	458.4	0.1679	444.3	0.0853	439.2	0.0450	430.2	0.0224
0.81	481.3	0.3454	465.5	0.2175	464.5	0.1702	447.2	0.0881	444.4	0.0464	433.3	0.0238
0.80	484.5	0.3495	471.5	0.2208	470.5	0.1741	453.2	0.0905	449.6	0.0469	439.5	0.0249
0.79	490.8	0.3527	474.5	0.2227	474.5	0.1757	457.2	0.0925	452.7	0.0464	442.6	0.0251
0.78	495.0	0.3561	478.5	0.2240	478.5	0.1757	463.1	0.0933	458.9	0.0449	448.7	0.0251
0.77	499.2	0.3561	484.5	0.2231	484.5	0.1735	466.1	0.0930	463.1	0.0419	450.8	0.0250
0.76	504.5	0.3552	487.6	0.2191	488.6	0.1663	472.0	0.0905	469.3	0.0374	457.0	0.0241

TABLE XXII (Continued)

w/w_0	Heating Rate 160°C/min $w_0 = 7.8020$		Heating Rate 100°C/min $w_0 = 7.8451$		Heating Rate 80°C/min $w_0 = 7.9097$		Heating Rate 40°C/min $w_0 = 7.8589$		Heating Rate 20°C/min $w_0 = 7.9766$		Heating Rate 10°C/min $w_0 = 7.8000$	
	T(°C)	$(-1/w_0)(dw/dt)$ (1/min)	T(°C)	$(-1/w_0)(dw/dt)$ (1/min)	T(°C)	$(-1/w_0)(dw/dt)$ (1/min)	T(°C)	$(-1/w_0)(dw/dt)$ (1/min)	T(°C)	$(-1/w_0)(dw/dt)$ (1/min)	T(°C)	$(-1/w_0)(dw/dt)$ (1/min)
0.75	512.9	0.3486	494.6	0.2116	495.6	0.1546	476.0	0.0853	475.5	0.2098	460.1	0.0226
0.74	516.0	0.3356	501.6	0.1967	502.6	0.1363	482.9	0.0763	484.9	0.0198	464.2	0.0200
0.73	523.4	0.3126	506.6	0.1628	510.6	0.1033	490.9	0.0616	498.4	0.0115	472.4	0.0158

TABLE XXIII

WEIGHT LOSS AND RATE OF WEIGHT LOSS DATA FOR MXB-360

w/w_0	Heating Rate 160°C/min $w_0 = 7.7894$		Heating Rate 100°C/min $w_0 = 7.3376$		Heating Rate 80°C/min $w_0 = 7.1716$		Heating Rate 40°C/min $w_0 = 7.2935$		Heating Rate 20°C/min $w_0 = 7.5161$		Heating Rate 10°C/min $w_0 = 7.5213$	
	T(°C)	$(-1/w_0)(dw/dt)$ (1/min)	T(°C)	$(-1/w_0)(dw/dt)$ (1/min)	T(°C)	$(-1/w_0)(dw/dt)$ (1/min)	T(°C)	$(-1/w_0)(dw/dt)$ (1/min)	T(°C)	$(-1/w_0)(dw/dt)$ (1/min)	T(°C)	$(-1/w_0)(dw/dt)$ (1/min)
0.98	320.0	0.0333	317.2	0.0245	314.2	0.0224	297.6	0.0111	298.6	0.0067	277.2	0.0027
0.97	351.0	0.0560	347.0	0.0379	343.1	0.0329	325.3	0.0162	326.3	0.0086	306.0	0.0040
0.96	377.3	0.0659	370.9	0.0407	368.2	0.0351	349.1	0.0173	348.1	0.0082	329.0	0.0041
0.95	402.6	0.0610	404.6	0.0308	394.5	0.0277	376.3	0.0130	382.4	0.0055	355.0	0.0029
0.94	439.1	0.0497	438.3	0.0313	429.9	0.0255	410.7	0.0125	418.5	0.0072	391.3	0.0029
0.93	469.4	0.0605	466.1	0.0397	454.2	0.0332	439.1	0.0167	442.0	0.0084	422.6	0.0040
0.92	493.7	0.0668	491.9	0.0413	482.6	0.0361	466.4	0.0175	469.5	0.0082	445.8	0.0041
0.91	521.1	0.0629	518.6	0.0357	505.9	0.0323	489.7	0.0151	497.1	0.0068	473.0	0.0035
0.90	553.5	0.0561	553.4	0.0319	535.2	0.0282	519.0	0.0134	527.7	0.0064	506.3	0.0031
0.89	589.9	0.0523	587.1	0.0313	568.7	0.0271	555.5	0.0130	562.5	0.0063	537.5	0.0031
0.88	624.2	0.0503	622.1	0.0304	598.9	0.0259	588.9	0.0122	601.3	0.0056	575.8	0.0029
0.87	660.3	0.0463	664.4	0.0249	635.3	0.0231	628.0	0.0106	647.2	0.0041	615.7	0.0024

TABLE XXIV

WEIGHT LOSS AND RATE OF WEIGHT LOSS DATA FOR FR-1

w/w_0	Heating Rate 160°C/min $w_0 = 7.6956$		Heating Rate 100°C/min $w_0 = 7.8715$		Heating Rate 80°C/min $w_0 = 7.6218$		Heating Rate 40°C/min $w_0 = 7.7786$		Heating Rate 20°C/min $w_0 = 7.4357$		Heating Rate 10°C/min $w_0 = 7.5964$	
	T(°C)	$(-1/w_0)(dw/dt)$ (1/min)	T(°C)	$(-1/w_0)(dw/dt)$ (1/min)	T(°C)	$(-1/w_0)(dw/dt)$ (1/min)	T(°C)	$(-1/w_0)(dw/dt)$ (1/min)	T(°C)	$(-1/w_0)(dw/dt)$ (1/min)	T(°C)	$(-1/w_0)(dw/dt)$ (1/min)
0.99	133.1	0.0472	125.5	0.0338	118.8	0.0297	108.0	0.0164	100.6	0.0106	93.7	0.0051
0.98	150.5	0.0830	142.3	0.0593	136.5	0.0546	125.7	0.0286	117.7	0.0169	110.0	0.0083
0.97	162.0	0.1089	156.1	0.0760	149.3	0.0678	137.5	0.0378	128.8	0.0207	120.2	0.0107
0.96	174.2	0.1292	166.9	0.0897	161.0	0.0773	146.3	0.0411	138.9	0.0221	129.4	0.0113
0.95	186.4	0.1403	177.8	0.0941	169.9	0.0794	156.1	0.0424	148.9	0.0218	138.6	0.0113
0.94	198.6	0.1420	188.6	0.0930	182.7	0.0773	166.0	0.0410	160.0	0.0199	150.8	0.0103
0.93	211.8	0.1361	204.4	0.0859	195.5	0.0706	177.8	0.0371	170.9	0.0175	162.0	0.0090
0.92	225.0	0.1245	217.1	0.0753	208.3	0.0613	191.5	0.0315	183.8	0.0147	173.7	0.0076
0.91	244.3	0.1055	232.9	0.0633	224.0	0.0513	207.3	0.0256	199.6	0.0114	190.1	0.0058
0.90	266.6	0.0807	255.5	0.0457	244.7	0.0375	227.0	0.0191	222.4	0.0081	212.4	0.0038
0.89	298.1	0.0561	286.1	0.0306	273.3	0.0248	254.6	0.0119	258.0	0.0046	252.2	0.0021
0.88	329.6	0.0617	317.6	0.0351	307.7	0.0255	294.9	0.0113	295.6	0.0066	288.1	0.0032

TABLE XXIV (Continued)

w/w_0	Heating Rate 160°C/min $w_0 = 7.6956$		Heating Rate 100°C/min $w_0 = 7.8715$		Heating Rate 80°C/min $w_0 = 7.6218$		Heating Rate 40°C/min $w_0 = 7.7786$		Heating Rate 20°C/min $w_0 = 7.4357$		Heating Rate 10°C/min $w_0 = 7.5964$	
	T(°C)	$(-1/w_0)(dw/dt)$ (1/min)	T(°C)	$(-1/w_0)(dw/dt)$ (1/min)	T(°C)	$(-1/w_0)(dw/dt)$ (1/min)	T(°C)	$(-1/w_0)(dw/dt)$ (1/min)	T(°C)	$(-1/w_0)(dw/dt)$ (1/min)	T(°C)	$(-1/w_0)(dw/dt)$ (1/min)
0.87	346.9	0.0750	342.2	0.0470	333.3	0.0358	320.5	0.0171	319.4	0.0087	313.3	0.0042
0.86	368.1	0.0816	361.2	0.0490	353.0	0.0386	344.1	0.0184	341.1	0.0089	335.6	0.0042
0.85	387.3	0.0816	379.9	0.0485	375.4	0.0380	365.4	0.0181	365.1	0.0090	357.1	0.0043
0.84	407.4	0.0816	404.7	0.0492	394.8	0.0386	386.1	0.0188	387.4	0.0094	378.7	0.0047
0.83	425.6	0.0839	424.3	0.0516	416.3	0.0409	407.8	0.0200	408.7	0.0104	401.4	0.0051
0.82	445.8	0.0886	440.9	0.0556	436.7	0.0440	426.4	0.0217	426.9	0.0114	419.9	0.0055
0.81	460.9	0.0959	460.5	0.0601	454.1	0.0470	445.0	0.0238	441.1	0.0121	438.4	0.0057
0.80	479.0	0.1019	477.1	0.0638	471.4	0.0509	460.5	0.0248	459.3	0.0124	454.9	0.0057
0.79	493.2	0.1055	493.6	0.0652	487.8	0.0520	479.2	0.0253	476.5	0.0118	475.5	0.0053
0.78	511.3	0.1059	510.2	0.0639	504.1	0.0512	496.7	0.0244	491.7	0.0113	494.1	0.0049
0.77	527.4	0.1016	529.8	0.0593	520.4	0.0479	513.3	0.0226	514.0	0.0101	518.8	0.0045
0.76	547.6	0.0929	548.4	0.0544	541.9	0.0433	536.0	0.0203	535.2	0.0093	542.5	0.0043

TABLE XXIV (Continued)

w/w_0	Heating Rate 160°C/min $w_0 = 7.6956$		Heating Rate 100°C/min $w_0 = 7.8715$		Heating Rate 80°C/min $w_0 = 7.6218$		Heating Rate 40°C/min $w_0 = 7.7786$		Heating Rate 20°C/min $w_0 = 7.4357$		Heating Rate 10°C/min $w_0 = 7.5964$	
	T(°C)	$(-1/w_0)(dw/dt)$ (1/min)	T(°C)	$(-1/w_0)(dw/dt)$ (1/min)	T(°C)	$(-1/w_0)(dw/dt)$ (1/min)	T(°C)	$(-1/w_0)(dw/dt)$ (1/min)	T(°C)	$(-1/w_0)(dw/dt)$ (1/min)	T(°C)	$(-1/w_0)(dw/dt)$ (1/min)
0.75	567.8	0.0837	571.2	0.0488	563.3	0.0392	558.8	0.0188	559.5	0.0089	564.1	0.0043
0.74	592.0	0.0754	596.0	0.0447	588.9	0.0361	582.6	0.0177	582.8	0.0087	589.8	0.0043
0.73	620.0	0.0694	621.7	0.0427	612.6	0.0344	609.3	0.0173	609.3	0.0087	614.0	0.0043
0.72	645.0	0.0664	647.4	0.0415	639.1	0.0337	631.3	0.0173	634.8	0.0089	637.0	0.0042
0.71	673.0	0.0647	676.1	0.0412	665.5	0.0335	657.0	0.0173	657.3	0.0086	662.0	0.0039
0.70	702.0	0.0641	703.8	0.0409	690.0	0.0331	682.8	0.0168	687.0	0.0077	686.0	0.0036
0.69	737.0	0.0615	740.4	0.0381	724.2	0.0314	711.4	0.0153	719.7	0.0065	715.0	0.0033
0.68	770.0	0.0564	770.1	0.0334	758.5	0.0270	745.7	0.0130	754.4	0.0054	747.0	0.0030
0.67	811.1	0.0495	810.9	0.0295	794.3	0.0240	781.0	0.0113	794.6	0.0046	783.9	0.0025

TABLE XXV

WEIGHT LOSS AND RATE OF WEIGHT LOSS DATA FOR FR-2

w/w_0	Heating Rate 160°C/min $w_0 = 7.3750$		Heating Rate 100°C/min $w_0 = 7.3284$		Heating Rate 80°C/min $w_0 = 7.5891$		Heating Rate 40°C/min $w_0 = 7.7749$		Heating Rate 20°C/min $w_0 = 7.6085$		Heating Rate 10°C/min $w_0 = 7.7427$	
	T(°C)	$(-1/w_0)(dw/dt)$ (1/min)	T(°C)	$(-1/w_0)(dw/dt)$ (1/min)	T(°C)	$(-1/w_0)(dw/dt)$ (1/min)	T(°C)	$(-1/w_0)(dw/dt)$ (1/min)	T(°C)	$(-1/w_0)(dw/dt)$ (1/min)	T(°C)	$(-1/w_0)(dw/dt)$ (1/min)
0.99	139.9	0.0450	130.4	0.0322	128.6	0.0290	115.9	0.0139	109.7	0.0085	101.9	0.0043
0.98	156.2	0.0748	151.1	0.0554	147.3	0.0472	134.5	0.0242	127.8	0.0138	121.2	0.0068
0.97	173.2	0.0974	166.9	0.0680	164.0	0.0571	148.3	0.0293	139.9	0.0154	134.5	0.0077
0.96	187.4	0.1087	180.7	0.0730	178.8	0.0577	164.0	0.0300	153.9	0.0150	149.8	0.0074
0.95	203.6	0.1094	196.5	0.0708	193.5	0.0535	177.8	0.0270	169.9	0.0133	164.0	0.0063
0.94	222.9	0.1014	210.3	0.0643	209.3	0.0453	196.5	0.0221	186.8	0.0110	183.4	0.0049
0.93	243.3	0.0866	230.9	0.0542	230.9	0.0364	219.1	0.0167	209.5	0.0084	209.5	0.0035
0.92	270.7	0.0675	255.5	0.0423	260.5	0.0262	253.6	0.0113	242.2	0.0057	242.5	0.0023
0.91	300.2	0.0588	285.1	0.0356	296.9	0.0269	284.1	0.0117	279.8	0.0062	279.3	0.0032
0.90	323.5	0.0679	307.7	0.0413	320.5	0.0353	312.6	0.0163	306.5	0.0083	302.6	0.0040
0.89	344.9	0.0793	328.4	0.0498	342.2	0.0377	335.3	0.0176	330.2	0.0085	326.9	0.0039
0.88	363.1	0.0796	349.1	0.0504	363.2	0.0345	358.2	0.0161	354.0	0.0080	349.2	0.0039

TABLE XXV (Continued)

w/w_0	Heating Rate 160°C/min $w_0 = 7.3750$		Heating Rate 100°C/min $w_0 = 7.3284$		Heating Rate 80°C/min $w_0 = 7.5891$		Heating Rate 40°C/min $w_0 = 7.7749$		Heating Rate 20°C/min $w_0 = 7.6085$		Heating Rate 10°C/min $w_0 = 7.7427$	
	T(°C)	$(-1/w_0)(dw/dt)$ (1/min)	T(°C)	$(-1/w_0)(dw/dt)$ (1/min)	T(°C)	$(-1/w_0)(dw/dt)$ (1/min)	T(°C)	$(-1/w_0)(dw/dt)$ (1/min)	T(°C)	$(-1/w_0)(dw/dt)$ (1/min)	T(°C)	$(-1/w_0)(dw/dt)$ (1/min)
0.87	386.3	0.0731	372.6	0.0461	385.7	0.0339	384.0	0.0165	378.3	0.0084	375.6	0.0041
0.86	406.4	0.0738	394.3	0.0458	411.2	0.0364	405.7	0.0177	399.6	0.0091	398.3	0.0045
0.85	428.6	0.0776	415.0	0.0486	432.6	0.0401	429.5	0.0199	419.8	0.0100	420.9	0.0050
0.84	448.8	0.0835	435.7	0.0524	449.0	0.0441	448.1	0.0219	439.1	0.0110	439.5	0.0052
0.83	465.9	0.0904	455.4	0.0574	467.3	0.0476	466.7	0.0233	459.3	0.0113	461.1	0.0052

2
VITA

Jack Bradford Henderson

Candidate for the Degree of

Doctor of Philosophy

Thesis: AN ANALYTICAL AND EXPERIMENTAL STUDY OF THE PYROLYSIS OF
COMPOSITE ABLATIVE MATERIALS

Major Field: Mechanical Engineering

Biographical:

Personal Data: Born in Caney, Kansas, July 29, 1943, the son of
Mr. and Mrs. H. J. Henderson.

Education: Graduated from Copan High School, Copan, Oklahoma in
May, 1961; received Bachelor of Science in Mechanical Engi-
neering degree from the University of Tulsa in 1972; received
Master of Science degree from Oklahoma State University in
1973; completed requirements for the Doctor of Philosophy
degree at Oklahoma State University in December, 1980.

Professional Experience: Junior Engineer, Butler-Culvern and
Associates, summer 1972; graduate research assistant, School
of Mechanical Engineering, Oklahoma State University, 1972-
1973; mechanical engineer, Naval Surface Weapons Center, 1974;
mechanical engineer, Army Corps of Engineers, 1974-1976;
research associate, School of Mechanical and Aerospace
Engineering, Oklahoma State University, 1976-1978; mechanical
engineer, Naval Surface Weapons Center, 1978 to present.